DOCTOR OF SCIENCE (DSC)

The Development of p-type Transparent Conducting Oxide Materials using Atomic Layer Deposition

Innocent, Jerome

Award date:
2020

Awarding institution:
University of Bath

The Development of p-type Transparent Conducting Oxide Materials using Atomic Layer Deposition

Jerome William Francis Innocent

A thesis submitted for the degree of

Doctor of Philosophy

University of Bath

Department of Chemistry

June 2020

Acknowledgements

My most sincere thanks is extended to Dr. Andrew Johnson. I shall be forever grateful for your friendship, guidance and ability to pull ideas out of a hat. You have made the past four years an unforgettable experience.

Similarly my thanks goes to all members of Johnson group past and present: Sam, Jeff, Emily, Matt, Kerry, Prem, Pete, Andrew, Andy and Andy. Special thanks goes to Jamie and Hannah who have endured my presence the longest.

My thanks must also go to those who made this work possible. I would like to thank everyone at PragmatIC Printing Ltd for their input and funding. I would like to thank the MC^2 instrumentation team, in particular Dr. Phillip Fletcher whose expertise was invaluable. The greatest of thanks goes to Dr. Mari Napari who has been a fantastic friend and mentor. Without your expertise in PEALD this thesis may have gone a very different direction. Thanks to Jackie Muggleton, your kind words and encouragement were enormously helpful.

Though none of my family ever understood what I was doing, it goes without saying that without their support the completion of this thesis would not have been possible. Thanks dad for proof reading my Masters report in 2014, sorry I didn't acknowledge you on that. Thanks to Mum, someday I may earn enough to pay taxes and be able to return for your immense generosity in kind. Finally, I would like to thank Dr. Amelia Langley. How anyone can tolerate me at work and home for this long is a miracle. Your contribution to the last four years cannot be quantified, thank you.

Declaration

The work contained within this thesis was conducted by the author at the University of Bath between October 2016 and October 2020. It represents the author's own work, except where specific reference is made to the contrary. This thesis does not exceed the prescribed limit, including tables, references and appendices.

Contents

List of Figures

List of Tables

Chapter 1

An Introduction to Transparent Semiconducting Metal Oxides and Atomic Layer Deposition

Contents

1.1 Chapter Abstract

The semiconductor industry is constantly expanding to accommodate new technologies and materials, but a deficit in p-type semiconducting materials has begun to emerge. To combat this deficiency, p-type semiconducting materials including transparent binary metal oxides, which have potential application in flexible, transparent technologies, have become a key topic of academic and industrial research. Among these materials NiO, a wide bandgap transparent p-type semiconductor is of interest.

This chapter provides a synopsis of band theory and the basic chemistry of semiconductors. As well as a more detailed discussion as to how semiconductivity arises in different transparent semiconducting metal oxides including; SnO, Cu_2O and NiO is also provided. Furthermore, atomic layer deposition (ALD), the fundamental chemistry behind it and plasma-enhanced ALD (PEALD) will be discussed.

1.2 Semiconducting Metal Oxides

1.2.1 NiO

Transparent semiconducting oxides (TSOs) are ubiquitous and key to the advancement of microelectronics, energy storage, gas sensing and optoelectronics.[1–4] The demands for these materials are constantly changing and to meet that demand it is atomic layer deposition (ALD), which can deposit thin films on the micro to nanoscale, that has become a leading TSO deposition technology. It is therefore essential that ALD continues to advance in order to meet the demands of emerging technologies.

Essential to the progression of semiconductor industry is the development of p-type TSOs such as the metal oxides ZnO, Cu_2O, SnO and NiO. Each material has its particular strengths and weaknesses, for example ZnO is commonly an n-type material and it is only through doping with nitrogen or phosphorus that it becomes p-type semiconducting.[5] Though currently, p-type ZnO is hindered because doping processes are not reliable enough reproducibly manufacture devices on a large scale.[6, 7] Cu_2O and SnO are both intrinsically p-type. However, CuO is restricted by a narrow optical bandgap and as such has limited optical transparency and SnO is oxidatively unstable and readily oxidises in atmosphere to SnO_2, an n-type semiconductor.[8, 9] In contrast, NiO which is oxidatively stable and an intrinsic p-type is therefore of great interest.

Nickel oxide is a wide band gap (3.6-4 eV) p-type semiconducting material. NiO has been synthesised by both physical and chemical methods including magnetron sputtering [10], sol-gel [11, 12], e-beam evaporation [13] and ALD[14, 15]. Though as discussed in this thesis, despite the ALD of NiO being well established, it is limited in its reliability and therefore application. Within this body of work, new plasma-enhanced ALD (PEALD) methods for the growth of NiO which can synthesise conformal films on an 8" wafer scale are presented. The optimised PEALD methods have been utilised to produce NiO co-catalysed photoanodic devices and applied as co-cycles in a new nickel ferrite PEALD process.

1.2.2 Semiconductor Physics

Materials can be broadly categorised by their resistivity as conductors, insulators and semiconductors. To explain how each of these material types differs electronically, molecular orbital theory must be expanded to bulk materials with vastly more bonding interactions. The illustration in **Fig 1.1** shows how sodium has the ground state electronic configuration of $1\,s^2\,2\,s^2\,2\,p^6\,3\,s^1$ with each electron at a discrete energy level. With the formation of a Na-Na bond, molecular orbital theory dictates that for each in-phase bonding interaction there will be a higher energy out of phase anti-bonding interaction e.g. σ_{1s} and $\sigma*_{1s}$, which have been simplified to 1s and $1s^*$ in **Fig 1.1**. In bulk sodium, there are many more bonding interactions such that for Na_n, the number of possible energy levels will increase by a factor n. As the number of energy levels

increases, the separation between each energy level becomes sufficiently small such that they can be considered a continuum or band of energy. These are the basic principles of band theory which can provide a simple explanation of conductivity.

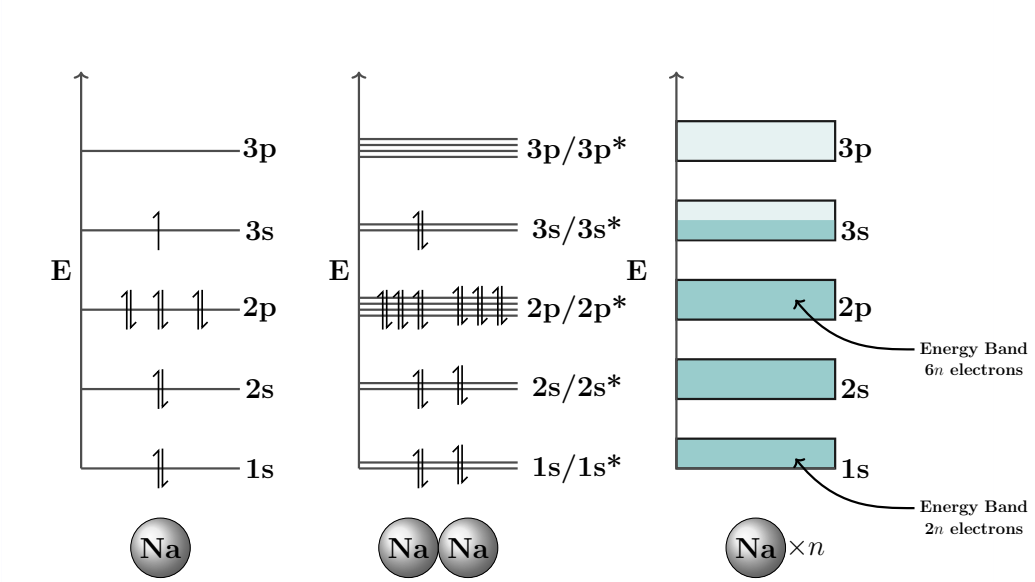

Figure 1.1. Left: *Atomic orbitals of sodium* ***Middle:*** *Molecular orbitals of sodium* ***Right:*** *Na_n atoms within solid sodium*

Conductivity arises from the movement of electrons. In the case of Na, it is the promotion of the electrons in the highest occupied molecular orbital (HOMO) $3s$ to $3s*$ the lowest unoccupied molecular orbital (LUMO). For a single Na-Na interaction this energy is significant but, for the bulk Na_n, band theory tells us the HOMO-LUMO gap has been reduced until the energy difference is negligible. Consequently, Na HOMO electrons can efficiently move from HOMO to LUMO and as such, sodium is a good conductor of electrons.

For conducting metals the band gap (E_g) between the valence and conduction bands is 0 eV. As the bandgap increases so does the resistivity of a material, as illustrated by **Fig 1.2**. Band theory dictates that intrinsic semiconductors are materials with a small enough bandgap that electrons can be promoted into the conduction band from thermal excitation, leaving positive holes in the valence band. When semiconductors are placed in an electric field with sufficient bias, the concentration of electrons in the conduction band is sufficient for the conduction of electricity. In conrtast, an insulating material's bandgap is sufficiently wide that, regardless of an electric field, the concentration of electrons in the conduction band is negligible and there is no conduction.

Crystalline silicon is the archetypal intrinsic semiconductor. The bandgap is sufficiently small that thermal excitation can promote valence electrons into the conduction and as an electron is promoted there is effectively a positive hole left in the valence band/crystal lattice. Above 0 K,

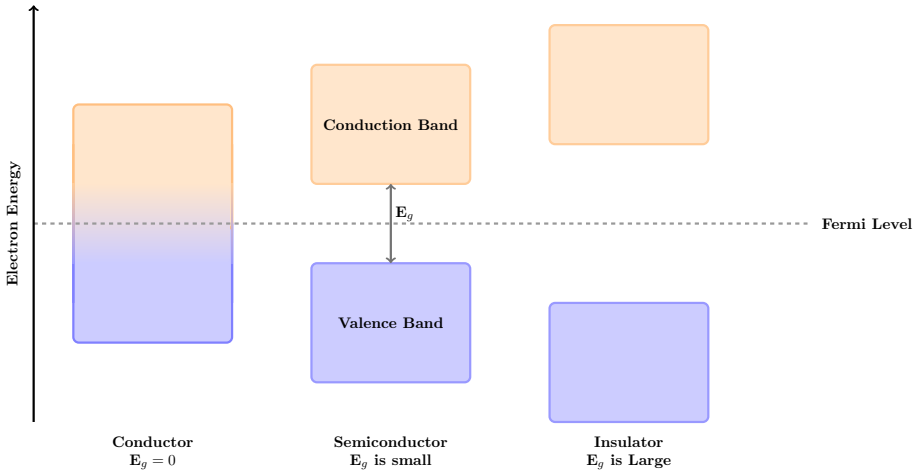

Figure 1.2. *Band theory of conductors, insulators and semiconductors*

electrons are promoted and recombine with generated holes such that at any given moment, the number of holes is equal to the number of promoted electrons. When an electric field is applied there are sufficient electron hole pairs that the electrons flow, driving holes in the opposite direction to electrons. In a semiconductor the number of charge carriers i.e. the number of electron-hole pairs is still sufficiently small that at room temperature the conductivity is poor and to increase conductivity either the concentration of holes or electrons must be increased.[16]

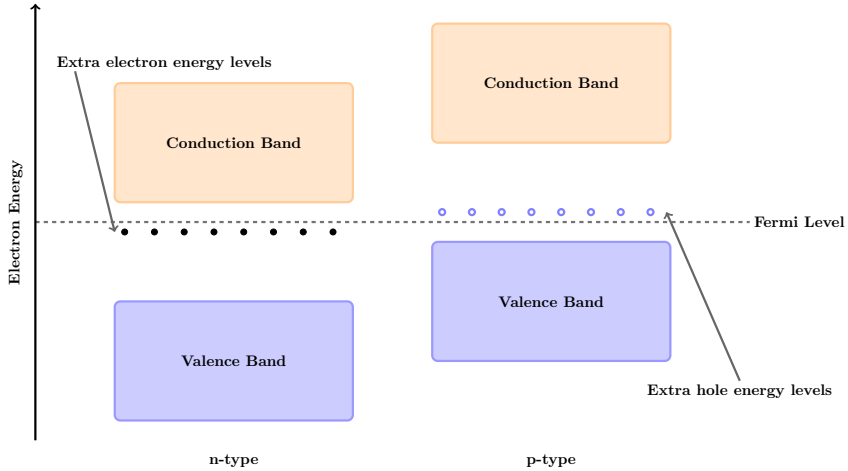

Figure 1.3. *n-type and p-type semiconductors*

To alter the electronic structure of a semiconductor the number of electron holes (n_h) and excited electrons (n_e) can be increased. In the example of crystalline silicon each silicon atom within the lattice has four two electron Si-Si covalent bonds. To increase the number of electrons the crystalline lattice can be doped and a silicon atom replaced with elements with a greater number of electrons e.g. phosphorus. Every phosphorus atom within the lattice will, on average have four two electron Si-P covalent bonds, with one free electron remaining. The free electron requires less thermal energy for promotion to the conduction band, lowering the conduction band closer to the

Fermi level (energy level which has a 50% probability of being filled by an electron). The number of free electrons at any given moment is greater than the number of holes, and as such, electrons are the majority charge carriers and the material is classed as an n-type semiconductor.[16]

Conversely, For electron holes to be majority charge carriers the silicon lattice can be doped with elements with fewer electrons such as boron. On average boron defects will have three two electron B-Si bonds and an electron deficient 1 electron B-Si bond, effectively leaving a positive hole. Each boron dopant will increase the number of available electron holes such that the Fermi level moves closer the band edge, as illustrated by **Fig 1.3**.[16] As the electron holes are at a greater concentration than free electrons, the positive holes are the majority charge carriers and the material is defined as a p-type semiconductor. n and p-type semiconductors which have been engineered by doping are known as extrinsic semiconductors. It is the application of extrinsic silicon materials in metal oxide field effect transistors (MOSFET) that launched modern electronics as they are now ubiquitous in modern electronic devices.

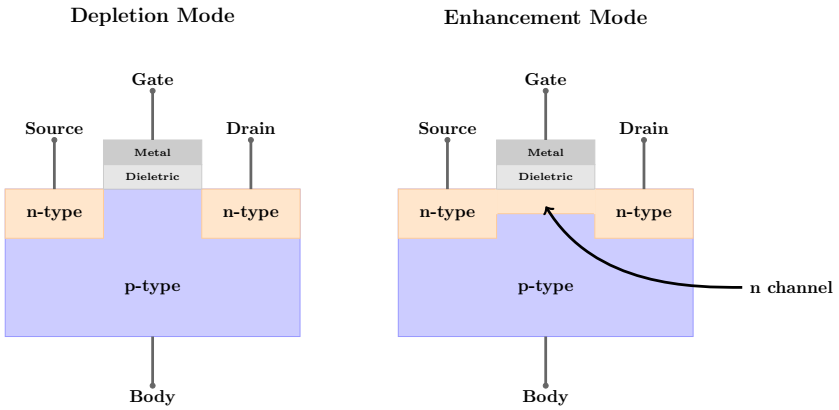

Figure 1.4. *Basic n-MOSFET structure when "switched off" in depletion mode and the formation of a conducting n-channel when "switched on" in enhancement mode*

MOSFETs are ubiquitous throughout electronics and are one of the simplest building blocks of the logic gates which makes up transistors. Shown in **Fig 1.4** is the basic structure of an n-MOSFET device, a p-type doped silicon substrate with two areas that are highly n-doped act as source and drain terminals. Atop the device is an insulating dielectric layer with a metal contact which acts as the gate. When no voltage is applied through the gate the device remains in an off state and no current can flow through the source-drain contacts. When a bias is applied through the gate, electrons move toward it and holes are repelled, creating an electron rich area across the two n-terminals. With sufficient bias, the n-channel becomes saturated with electrons and current can flow from source to drain and the device is switched on. By regulating the current through the gate terminal a MOSFET can be rapidly switched on and off and by combining MOSFET units the logic gates which define all of modern computing can be built. Whilst many of the principles behind transistors remain the same, the demands of a transistor have expanded. Additional features such as transparency and flexibility are

key targets for future devices and silicon technology alone is no longer sufficient because of its inflexibility and opacity. Organic and inorganic metal oxide semiconductors, which have greater transparency and flexibility, are rapidly increasing in research output and device application. Organic semiconducting materials are not the focus of this thesis, for the interested reader there are comprehensive reviews available.[17, 18]

1.2.3 Transparent Semiconducting Metal Oxides

At first glance the idea of transparent conducting materials are incongruous. Typically transparent materials, such as silicon based glasses, are insulating and conducting materials, typically metals are opaque. However, transparent semiconducting metal oxides (TSOs) are a wide and diverse group of materials. There are numerous n-type and p-type materials which have seen application within microelectronics, photovoltaics, gas sensing and batteries to name a few.[1–4] Though, it is n-type materials which dominate the electronics market. Materials such as indium doped tin oxide (ITO), fluorine-doped tin oxide (FTO), doped zinc oxides and indium-gallium zinc oxide which are ubiquitous in microelectronic and optoelectronic applications.[19–23] Thus far, p-type materials have not been able to match the performance of n-type materials and the demand for high performance transparent p-type materials is increasing.

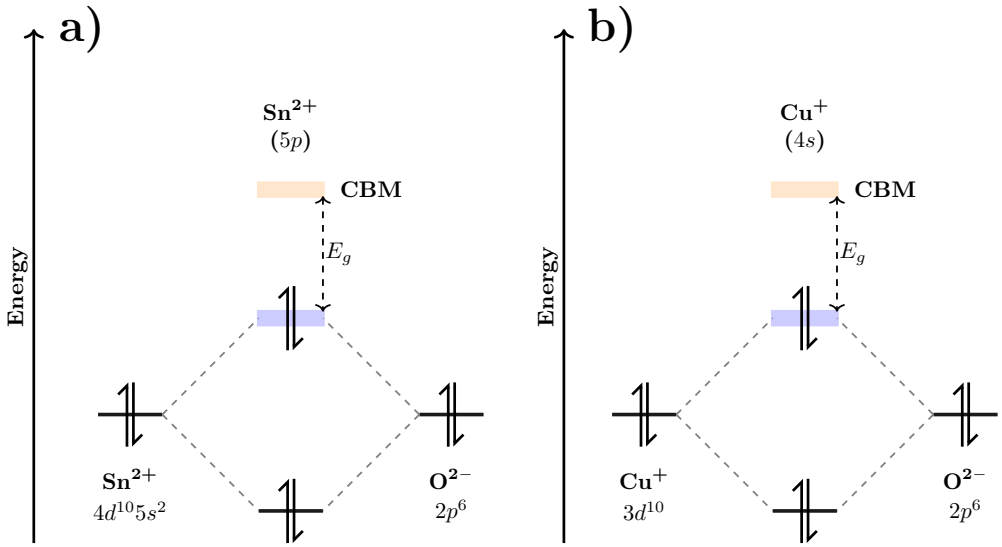

Figure 1.5. *Illustrations of the valence band maximum hybridisation in a) SnO and b) Cu_2O. Reproduced from illustration in literature.[24]*

The development of high performance p-type TSOs has been hindered in part, because charge mobility of p-type TSOs is poor when compared to n-type TSOs. Generally for n-type TSOs, conduction is a result of lattice oxygen vacancies which generate extra metal electrons. The electrons have high mobility because the conduction band maximum of an n-type, such as ITO, is comprised of diffuse *s*-orbitals. The orbitals are sufficiently large that they overlap with adjacent metal orbitals and form a wide conduction band. Furthermore, because of the large

atomic radii of the heavy metal cations, even in amorphous structures there is sufficient orbital overlap that electrons have high mobility, which reduces the demand on material production.[23–25] Conversely, it has been suggested that p-type TSOs have a greater localisation of the valence band maximum (VBM) because it is comprised of oxygen $2p$ orbitals, that are localised.[24] Consequently, p-types have a restricted band overlap and generally hole mobility is poor.[24, 26, 27]

Understanding how to improve hole mobility has been key to developing efficient p-type materials and when Kawazoe *et al* published the first transparent p-type semiconducting delafossite $CuAlO_2$, they developed a criteria for hole mobility in TSOs.[28] The report outlined that closed shell $d^{10}s^0$ metals such as Cu^+ had sufficiently close band energies to the O$2p$, that hybridisation can occur between orbitals increasing the dispersion of the O$2p$ VBM and as a consequence hole mobility is improved.[28, 29] With regards to conductivity the delafossite $CuAlO_2$, was far behind the current n-type materials of the time. However, the development of a p-type TSO framework meant that the number of TSO materials rapidly expanded to include more delafossites, spinels, perovskites and corundum type oxides.[30–34]

TSOs are not limited to ternary crystal systems. The binary metal oxides Cu_2O, SnO and NiO are also p-type TSOs, but not all abide to the criteria established by Kawazoe *et al.*[24, 28] In Cu_2O the Cu^+ ion has the closed shell [Ar]d^{10} s^0 electronic configuration and hybridizes with the $O2p$ orbitals increasing hole mobility.[27, 28] It has been calculated that in SnO the Sn^{2+} $5s$ orbitals hybridise to form a dispersed VBM which promotes the movement of positive holes.[24] However, in NiO the conduction method is different. The Ni^{2+} ions within NiO have a d^8 configuration and do not have a closed shell, nor do they possess s-electrons to hybridise with $O2p$ bands. To understand the conduction in NiO it is first relevant to discuss how conduction generally arises in binary transition metal oxides.

Binary transition metal oxides generally possess geometry in which a transition metal cation is occupied in octahedral site within the lattice and the conductivity arises from d-orbital overlap. Electrons move through partially filled valence bands and when d-orbital overlap is sufficient, the materials are metallic conductors. For example the cubic systems TiO and VO both have rocksalt structures and the Ti^{2+} and V^{2+} cations have d^2 and d^3 electronic configurations respectively. The t_{2g} HOMO bands in each material are partially filled and there is sufficient overlap between d_{xy}, d_{xz} and d_{yz} orbitals such that metal-metal conduction is possible, as illustrated by **Fig 1.6**.[35] NiO is a p-type semiconducting metal oxide with a band gap of 3.6-4.0 eV and it is an interesting example of a material which band theory dictates is semiconducting but stoichiometric NiO is in fact insulating. Similar to TiO and VO, NiO has the cubic rocksalt structure. Each Ni atom has octahedral geometry and is coordinated to six oxyanions. The Ni^{2+} cations within NiO are isoelectronic with $[Ni(H_2O)_6]^{2+}$ as each Ni^{2+} cation within the NiO cubic lattice, possesses octahedral geometry and has six O^{2-} sigma donor ligands. As such, each NiO is a 20 electron

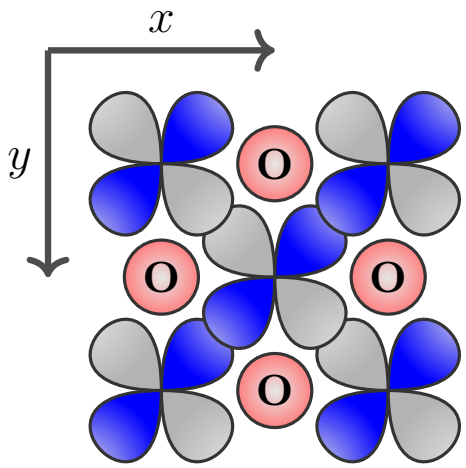

Figure 1.6. *Illustration of the overlapping d_{xy} valance orbitals in cubic conducting transition metal oxides TiO and VO.*

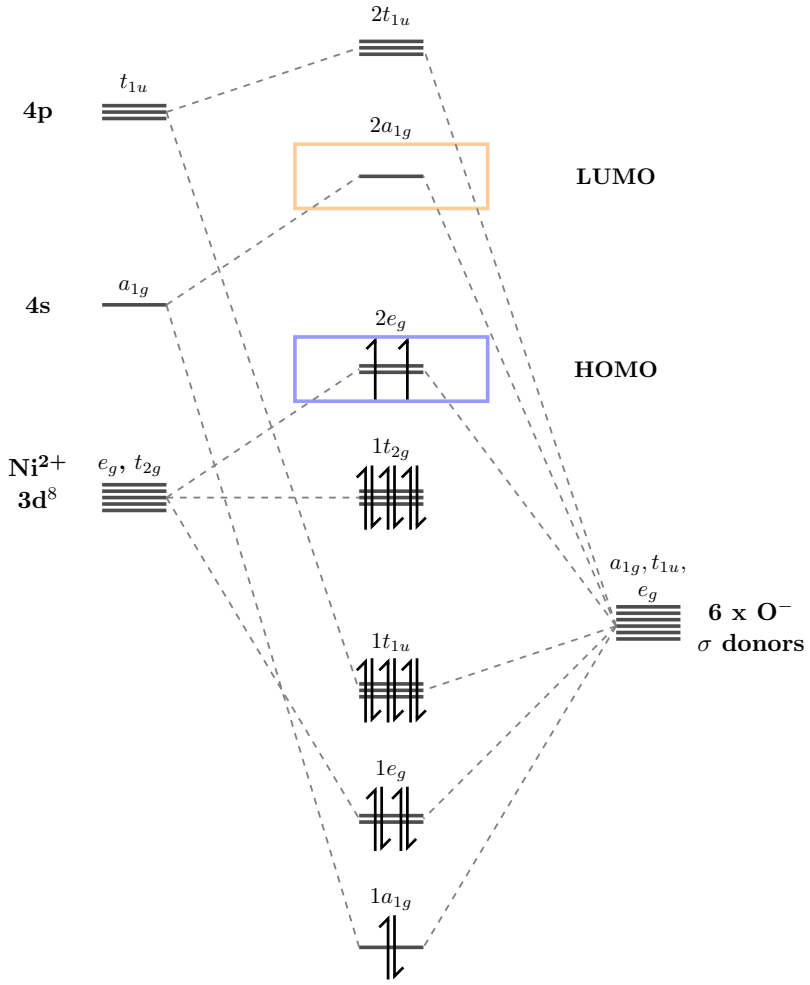

Figure 1.7. *Molecular orbital diagram of the NiO HOMO and LUMO orbitals in octahedral Ni^{2+}.*

system with its d-orbitals partially filled as shown by **Fig 1.7**. The e_g HOMO orbitals of Ni^{2+} are partially filled and as such, each NiO molecule has space within the HOMO orbital for an excited electron to occupy. According to band theory, with space in the partially filled HOMO orbital metallic conduction should be possible. However, stoichiometric NiO is insulating. The assumption of band theory is that the d-orbitals of Ni can interact with surrounding Ni d orbitals to form a continuous band through which electrons can move, in the instance of NiO the d orbitals are localised and the energy required to move electrons between atoms is too great and the material is insulating.[36, 37]

Band theory breaks down for NiO because of two reasons, the first is that it does not account for localisation of the HOMO d-orbitals. Shown in the partial MO diagram in **Fig 1.7**, the t_{2g} (d_{xy}, d_{xz}, d_{yz}) Ni^{2+} orbitals are filled. The HOMO ${e_g}^*$ set which are partially filled and have space for additional conducting electrons, are orientated along the x, y and z axes and are aligned with the with the oxygen anions. Metallic conduction requires orbital overlap between the Ni atoms. However, as the HOMO orbital set are not Ni-Ni aligned there is no overlap and metallic conduction is impossible, as illustrated by **Fig 1.8**.

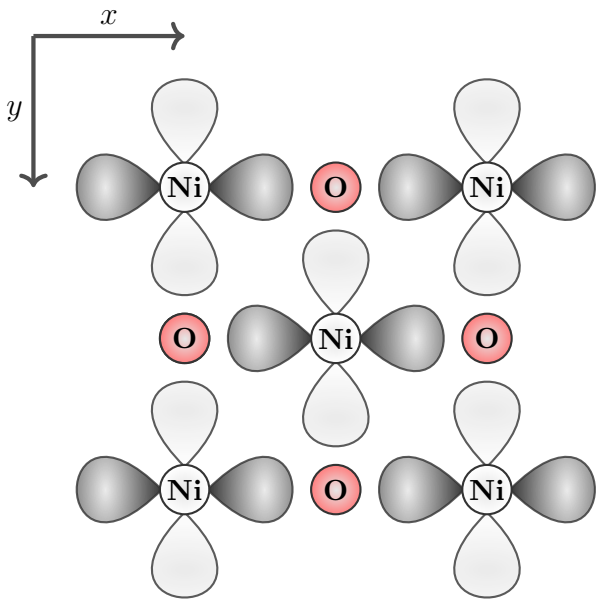

Figure 1.8. *Illustration of the NiO $d_{x^2-y^2}$ pointing directly toward oxide ions and unable to form an e_g band.*

The second reason for the breakdown of band theory with regards to NiO can be explained by Mott-Hubbard breakdown. Mott-Hubbard breakdown[36, 37] accounts for electron interactions and the band gap of a material (U) can be calculated as a function of ionisation energy (I) and electron affinity(A) such that:

$$U = I - A$$

If a material is conducting the energy loss from ionisation will be negated by the energy gained

moving an electron to an unoccupied site. If the ionisation energy is low or the electron affinity high the material will be conducting.[36, 37] Pauli exclusion principle dictates that two electrons with the same quantum number must have opposite spins.[38] If an electron is promoted into the partially filled ${e_g}^*$ HOMO energy level in stoichiometric NiO, it must have opposite spin. Adding an electron with opposite spin will increase electron-electron repulsion, meaning electron affinity (A) is low and the band gap of stoichiometric NiO is wide and therefore insulating.[36, 37]

While stoichiometric NiO is an insulator, substoichiometric NiO is an intrinsic semiconductor. This can be attributed to the innate presence of Ni^{3+} ions within the lattice which are prevalent as point defects. Fortunately for materials synthesis, point defects are thermodynamically favourable because they increase disorder and increase the Gibbs free energy of the system ($\Delta G = \Delta H - T\Delta S$). The Ni^{3+} defects also act as extra electron holes facilitating charge transfer. Ni^{2+}–Ni^{3+} transfer is favourable because the electron affinity is greater when electrons are promoted into Ni^{3+} holes. Electrons do not have to pair within the d^7 ${e_g}^*$ set meaning an electron promoted into a Ni^{3+} HOMO orbital has a lower value of A and the band gap is reduced.[36, 37]

To conclude, band theory does not account for the localised Ni d-orbitals or electron pair repulsion in the Ni HOMO e_g set. It is the presence of the Ni^{3+} ions throughout the lattice that provide positive holes and act as a current carrier for the material. Ni^{3+} ions help to reduce the materials bandgap making conduction possible. Because Ni^{3+} point defects are thermodynamically favoured, ALD synthesised NiO in practice should be semiconducting.

1.3 Atomic Layer Deposition

Atomic layer deposition (ALD) has an interesting history because it was independently developed by two groups. Initially Soviet groups in the 1960s developed molecular layering, while atomic layer epitaxy (ALE) was developed in Finland in the 1970s, which then became the more commonly known ALD.[39, 40] Though literature is limited from the Soviet era, Suntola *et al* developed ALD as a method for the production of flat panel displays and as such ALD has always been connected with the electronics industry.[39]

ALD has now expanded across the periodic table and precursors exist for huge variety of materials.[41, 42] However, ALD came to the world's attention when Intel utilised an ALD deposited HfO_2 high-k dielectric layer in their processor design.[43, 44] Prior to this technological advancement, processor technology had come to a crux in development which traditional silicon based devices could not overcome. The dielectric silicon layer could not be further reduced in size as it would allow current to leak and the n-channel breaks down, (**Fig 1.4**). HfO_2 was one of the target oxides that had a greater dielectric constant (k) than silicon, which meant a HfO_2 di-electric could be thinner than silicon, yet more insulating and could overcome the issue with current leak. The HfO_2 nanolayer grown by ALD accessed smaller transistor technology than ever before and ALD became invaluable to the transistor market and the world.

1.3.1 Fundamentals of ALD

Chemical vapour deposition (CVD) is a versatile technique commonly performed at low pressure and used to grow inorganic films ranging from metals, metal oxides, metal chalcogenides, metal nitrides and metal sulfides.[42, 45–47] In a typical CVD process a substrate is exposed to one or more chemical reagents which either react or thermally decompose to deposit the desired material.[48] Any unwanted reaction byproducts and excess precursor are removed by the reactor gas flow. The advantage of CVD is its diversity, depending upon the desired material the reactor chamber configurations and chemical delivery method can be altered to specification. However, for the ultra-thin, highly uniform coatings required in the manufacturing of complex nano-electronics, CVD does not always have the necessary precision or ability to coat high aspect ratio substrates.

ALD is a CVD technique which grows inorganic films on the nano to micron scale. ALD processing typically relies on two chemical precursors, one metal precursor and co-reagent typically an oxidant e.g. trimethylaluminium (TMA) and water. Precursors are introduced in the gas phase to the reaction chamber in discrete pulses where they react with the substrate surface. The gas-solid reactions are separated by inert gas purges which remove reaction by-products and unreacted precursor. Consequently ALD is broadly defined by the pulse/purge/pulse/purge method illustrated in **Fig 1.9**. Film thickness increases linearly with respect to the number of ALD cycles as the growth per cycle (GPC) is constant. This a consequence of the self-limiting

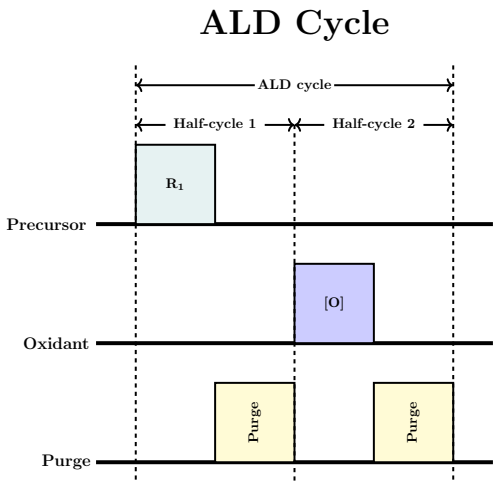

Figure 1.9. *Illustration of an ALD cycle*

ALD growth mechanism whereby a gas phase precursor can only react with available surface sites, once the surface is saturated the excess precursor is purged out leaving only a monolayer of material on the substrate surface, as illustrated in **Fig 1.10**. The self-terminating chemical reactions with sufficiently long purging ensures that there is no mixing of the two reactive species and eliminates film growth by another mechanism, ensuring the GPC is saturation limited.

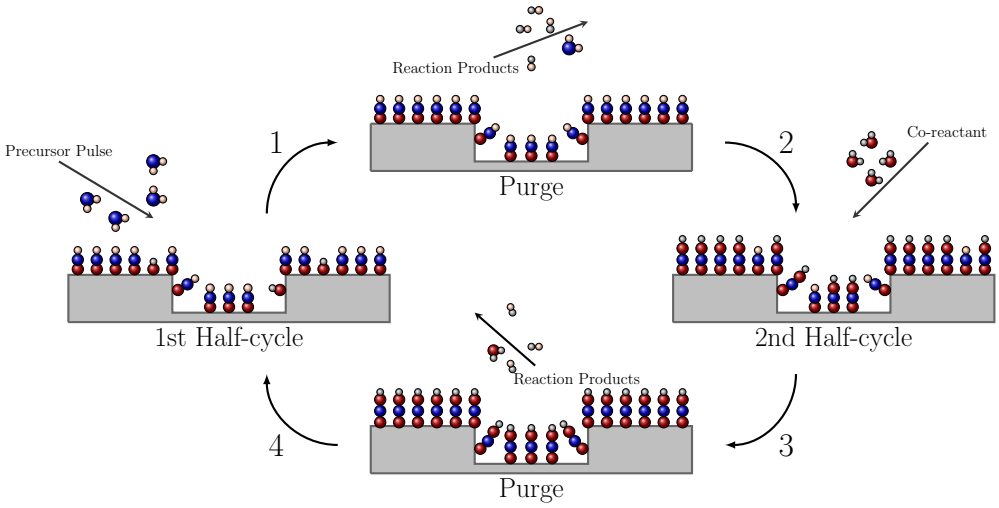

Figure 1.10. *Illustration of an ALD reaction cycle.*

The advantage of ALD over other CVD methods is a result of the discrete pulses and constant GPC. As growth is limited to a single mono-layer per-cycle, films can be grown with precision that other CVD methods cannot match. This is especially effective in high aspect ratio substrates

whereby ALD can uniformly coat the substrate and maintain surface features e.g. nanorods and trenches as shown in **Fig 1.11**.[49] Provided the substrate surface is also homogeneous with a uniform distribution of reactive sites, an optimised ALD process can deposit with a high degree of uniformity. Furthermore, as all reaction by-products are removed by purging cycles there are low concentrations of defects and impurities compared to other CVD techniques.

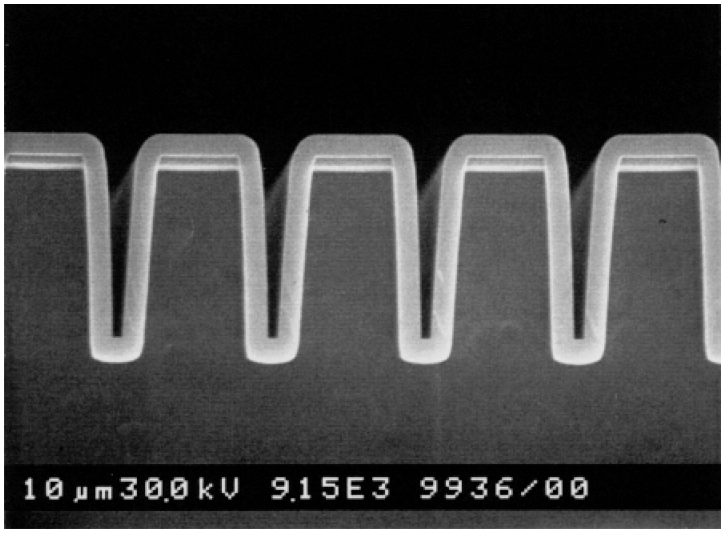

Figure 1.11. *Cross-sectional SEM image of a Si trench structure with a 200 nm Al_2O_3 ALD deposited film, adapted with permission from Wiley Publishing.[49]*

To verify whether an ALD process is self-limiting, the growth rate must saturate with respect to the precursor delivery. Shown in **Fig 1.12a** is an illustration of a model ALD growth rate with respect to precursor delivery time. As precursor delivery time is increased so should the GPC until the concentration of precursor in the deposition chamber matches the number of surface binding sites. Once all binding sites have been saturated, regardless of an increase in precursor concentration the overall GPC should remain constant.[50] If the growth rate continues to increase the growth mechanism is not self-limiting and therefore not ALD. Common flaws which result in non-surface limited growth are the condensation of precursor on the substrate or thermal decomposition of the precursor, both of which can often be compensated for by varying the reactor or precursor temperature.

It is a convention in ALD literature is to define the thermal range in which the growth of a film is self-limiting, referred to as process thermal window. **Fig 1.12b** shows how between temperatures **A** and **B** the GPC remains constant, though above and below these two temperatures the GPC varies as a result of precursor decomposition, desorption, condensation or low reactivity. In this example it is between **A** and **B** that the process thermal window can be defined, as within that range the GPC is constant.[51] A thermal window is not essential for an ALD process. An ALD process can have a thermally dependent GPC, yet there is no requirement in literature to define a range in which the GPC is constant.[52] A thermal window is helpful to engineer two separate

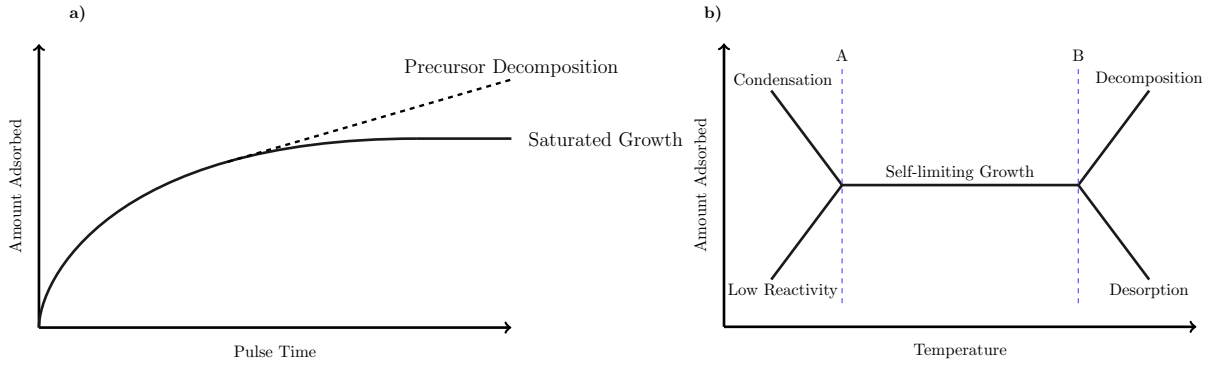

Figure 1.12. *a) ALD and non-ALD growth dependency on precursor delivery time b) Thermal modelling of ALD growth and potential causes of deviation from model ALD systems*

ALD processes together or when selecting and ALD process for film growth on thermally sensitive substrate.

1.3.2 Metal Oxide ALD Oxidation Sources and Precursors

TMA and Water

ALD is defined by the self-limiting growth mechanism, the GPC and thermal window of a process are therefore defined by the chemistry of the chemical precursors. Essential for an ALD precursor is that it is volatile, completes surface reactions swiftly and cleanly, it is thermally stable, does not self-decompose and that it does not etch the material or dissolve into the film surface. Furthermore, it is desirable that the precursors are safe to handle, inexpensive and produce by-products which are volatile and do not react with the substrate. Finding a compound which is suitably volatile, thermally stable and highly reactive can be challenging, precursor chemistry is therefore a compromise of all these traits. Rarely does a precursor meet all these requirements, though trimethyl aluminium (TMA) is perhaps an exception.

One of the most frequently published ALD materials is Al_2O_3. The first publications concerning the ALD of Al_2O_3 emerged in the 1990's with the precursors triethylaluminium (TEAL), aluminium trichloride and TMA.[53–56] Since those early publications the number of ALD papers concerning TMA has accounted for up to a quarter of all ALD publications each year, as shown by **Fig 1.13**. The success of Al_2O_3 is due, in part, to the chemistry of the precursor TMA.

TMA is a liquid at room temperature, which readily evaporates at reduced pressure. It rapidly and cleanly reacts with water and the only by-product, methane (**1.1**), is volatile and non-reactive. TMA is relatively inexpensive because there is a high demand for Al_2O_3 as a high-k dielectric layer. The only potential flaw is that TMA reacts violently when exposed to water and, as such, must be handled with caution.[57] Though that exceptional reactivity is perhaps why TMA is the perfect precursor and why it meets nearly every requirement.

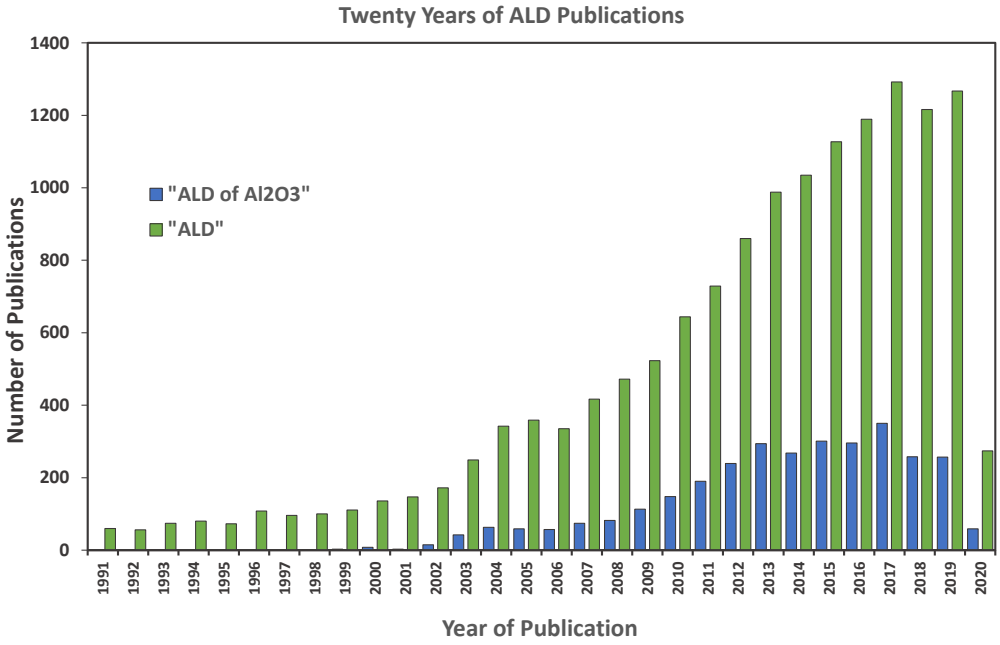

Figure 1.13. *Trends in the number of research articles concerning "ALD" and the "ALD of Al_2O_3" in the last twenty years. (status April 2020) The search was run in published abstracts using Web of Science.*

$$\mathrm{Al(CH_3)_3} + \frac{3}{2}\,\mathrm{H_2O} \longrightarrow \frac{1}{2}\,\mathrm{Al_2O_3} + 3\,\mathrm{CH_4} \tag{1.1}$$

$$||\mathrm{-OH} + \mathrm{Al(CH_3)_3} \longrightarrow ||\mathrm{-O-Al(CH_3)_2} + \mathrm{CH_4} \tag{1.2}$$

$$||\mathrm{-O-Al(CH_3)_2} + \mathrm{H_2O} \longrightarrow ||\mathrm{-O-Al(CH_3)OH} + \mathrm{CH_4} \tag{1.3}$$

$$2\,||\mathrm{-OH} + \mathrm{Al(CH_3)_3} \longrightarrow ||\mathrm{(-O)_2-Al(CH_3)} + 2\,\mathrm{CH_4} \tag{1.4}$$

The overall surface reaction for a TMA and water ALD process is given in **R1.1**. This can be subsequently divided into two half reactions, when the TMA is pulsed into the chamber (**R1.3**) and when water is pulsed into the chamber (**R1.4**). A third reaction is possible between two adjacent hydroxyl groups shown in **R1.1**.[58] It was surmised by Puurunen *et al*, in a comprehensive review of ALD in 2005, that the TMA/H_2O process works as a representative model for ALD because it is inherently a thermal process relying solely on self-terminating reactions.[59]

Oxidants for Metal oxide ALD

The requirements for a thermal ALD precursors are a challenge for synthetic chemists and attaining the "Goldilocks compound" of each element will remain an engaging synthetic challenge. However, ALD is not limited to water, and for metal oxides films alternative oxidants can be utilised. More reactive oxidants can compensate for low reactivity of a metal precursor, or can

access ALD deposition on thermally sensitive or hydrophilic substrates. TMA has proven to be versatile in this regard and has been demonstrated to deposit Al_2O_3 with alternative oxidation sources including O_3, H_2O_2 and O_2 plasma.[52, 60–62] These alternative oxidation sources as well as molecular O_2 are all potential oxidants for metal oxide precursors which lack the necessary reactivity for ALD growth with water.[63]

ALD investigations utilising O_3, H_2O_2, O_2 can generally be completed without modification of an ALD tool and similar to H_2O processes, have been demonstrated to grow uniform films on complex substrate geometries. In contrast, plasma-enhanced ALD (PEALD) which utilises reactive oxygen radicals requires an additional plasma ignition source and because plasma is directional and radicals can terminate before reaching complex geometries, generally PEALD films grow with lower uniformity, especially on high aspect ratio or 3D substrates.[64–66] Despite the limitations of PEALD it is of particular interest to this study as it can facilitate rapid growth of metal oxides even with relatively unreactive metal precursors.

PEALD

Plasma is energetically the fourth state of matter and is compromised of charged particles which balance out to a near electronically neutral medium. The advantage to PEALD and O_2 plasma, is that its strongly oxidising and generally facilitates fast reactions with short purge times which can be utilised at room temperature.[62] Furthermore, film growth often has a short nucleation delay and linear growth rates are achieved after a few PEALD cycles. It is an effective oxidant which can eliminate the requirement for highly reactive precursors, relaxing the overall demands of ALD precursor design. For example, in a study by Napari *et al*, nickel(II) acetylacetonate ($Ni(acac)_2$) was used a precursor for the PEALD of NiO. $Ni(acac)_2$ is air stable and does not have the necessary reactivity to complete ALD reactions with H_2O, it is only from the application of O_2 plasma that ALD deposition with $Ni(acac)_2$ is enabled.

Oxygen plasma comprised of highly reactive ionising gases including O^*, O_2^+, O_2^-, O_3, O, O^+ and O^- and as such, compared to H_2O, determining a concise reaction mechanism can be challenging. A study by Heil *et al*, monitored the PEALD reactions between O_2 plasma and surface chemisorbed TMA with mass spectrometry and a quartz crystal microbalance (QCM).[67] It was proposed that O_2 plasma pulses resulted in combustion reactions with chemisorbed TMA forming CO, CO_2 and H_2O. Additionally Naumann *et al*, proposed that after prolonged plasma pulses, high temperatures and high plasma powers, the chemisorption of TMA onto the surface can be hindered due to plasma damage.[68] Consequently, the films Al:O ratio is reduced and carbon content increased.[68] Balancing the variables in PEALD is therefore challenging but when optimised effectively, high quality films can be synthesised.

$$O_2 + e^- \longleftrightarrow 2\,O^\bullet \tag{1.5}$$

Plasma is generated and sustained in an ALD or CVD reactor by applying a DC bias, typically

sourced from a microwave (MW) or radio frequency (RF) pulse, over gases such as $H_2/O_2/NH_3$. Free electrons, which are present in low concentration due to ionising background radiation and cosmic rays, accelerate in the electrical field and with sufficient kinetic energy (applied voltage) the electrons collide with and ionise other gaseous species creating reactive radicals and ions, such as in **equation 1.5**.[69] The ions in turn are accelerated in the electrical field and continue to generate more species, as well as, recombine in self-eliminating reactions.[69] The generation of plasma is dependent on the voltage applied and not the temperature of the reactor, for this reason plasma can be generated and used in PEALD processes at room temperature or below.

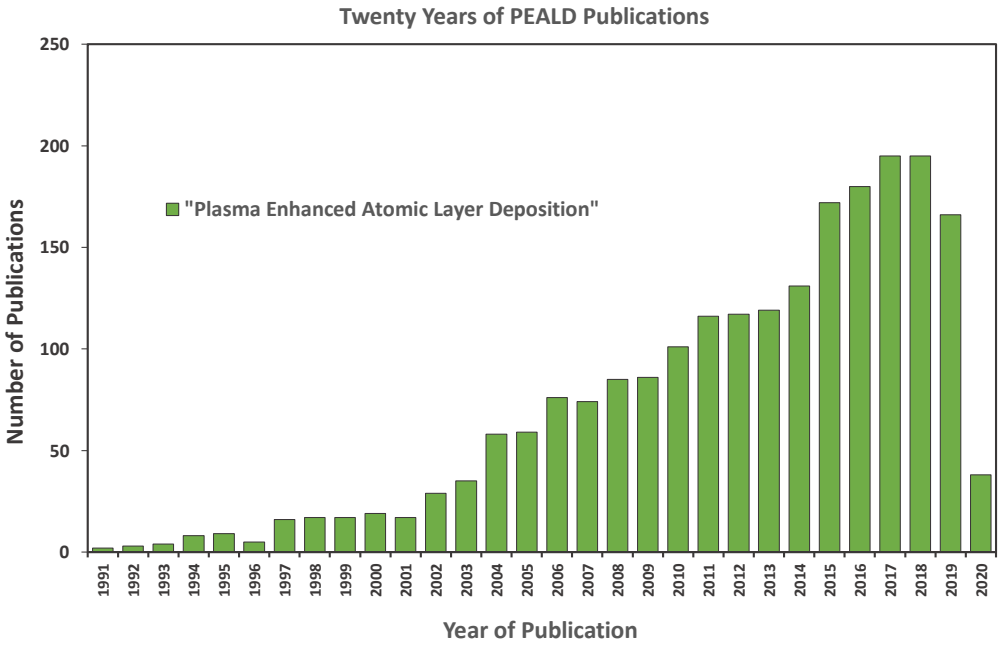

Figure 1.14. *Trends in the number of online research articles concerning "plasma enhanced atomic layer deposition". (status April 2020) The search was run in published abstracts using Web of Science.*

Since the initial development of PEALD in 1991 there has been a steady increase in the number of PEALD publications per year, see **Fig 1.14**, which is a partially a consequence of PEALD technology becoming more accessible.[70] PEALD reactors can generally be divided into three types direct, remote and radical enhanced. In direct plasma reactors the plasma generation occurs within the same chamber as the substrate, with the substrate typically positioned on the grounded plasma generation plate. In remote plasma configurations, the plasma generation occurs in a separate chamber to the substrate. Radical enhanced plasma describes configurations where only the plasma radicals have sufficient lifetime to interact with the deposition substrate.[71, 72]

Within this body of work a Beneq TFS-200 has been utilised for all experimental PEALD processing. In this reactor type the plasma gas flows directly through the plasma electrode which ignites the plasma with a radio frequency (RF) pulse (13.56 MHz) with the substrate sitting on the ground electrode. Because the plasma is generated in the main deposition chamber, a greater concentration of reactive species can reach the substrate before extinction and as such, shorter RF pulses can be applied for saturated growth.

1.4 Project Scope and Thesis Overview

The general scope of this project was to design and evaluate new NiO ALD precursors and deposition processes, with the ambition to develop an ALD method for the growth of NiO which could be scaled to wide area deposition. Due to the success of the investigation, the scope of the project expanded to develop new applications of the NiO PEALD method including i) utilisation in photovoltaics ii) enhancement of the NiO conductivity by controlled ALD doping with group one elements, iii) development of a new Fe_2O_3 PEALD method for integration with NiO PEALD supercycles for the synthesis of nickel ferrite.

1.4.1 Chapter Overview

Chapter 2

Chapter 2 will provide a general review of literature concerning the ALD of NiO utilising water as an oxygen source. This will include novel PEALD experimental data, as well as, repetitions of previously reported NiO ALD processes on a Beneq TFS-200 tool. Furthermore, this chapter will present a systematic investigation of a new PEALD method for the growth of NiO utilising the precursor $Ni(DMAMP)_2$.

Chapter 3

Chapter 3 will present a discussion on the current NiO ALD methods utilising cyclopentadienyl compounds, as well as a review of current PEALD methods for the growth of NiO. Two new direct plasma methods for the PEALD of NiO using $NiCp_2$ are detailed, with both methods compared and the iterative optimisation of the second method provided. Following on from this work, the 3D substrate coverage and co-catalytic activity of a NiO layer on TiO_2 nanorods is assessed and data from experiments attempting to dope NiO with group one elements are presented.

Chapter 4

Chapter 4 details the current literature on the ALD deposition of Fe_2O_3 and nickel ferrite. Given the gap in literature for the PEALD of Fe_2O_3, the optimisation of a new method utilising dimethylferrocene is provided ($Fe(MeCp)_2$). Following on from this, a new process for the growth of nickel ferrite by NiO and Fe_2O_3 supercycling is presented.

Chapter 5

Chapter 5 details attempts to expand on the current catalogue of NiO ALD precursors, several compounds were synthesised, characterised and analysed for application as ALD precursors. Furthermore, a consequence of the salt-metathesis reactions used to synthesise nickel compounds

was that a series of group one aminoalkoxides were isolated. Their structures and volatility were analysed and their potential as ALD precursors is discussed.

Bibliography

[1] E. Fortunato, P. Barquinha and R. Martins, *Adv. Mater.*, 2012, **24**, 2945–2986.

[2] J. Lee, L. Meng and Y. Yang, in *Futur. Semicond. Oxides Next-Generation Sol. Cells*, Elsevier, 2018, pp. 241–265.

[3] A. Oprea, D. Degler, N. Barsan, A. Hemeryck and J. Rebholz, in *Technol. Appl.*, Elsevier, 2018, pp. 61–165.

[4] S. Fang, D. Bresser and S. Passerini, *Adv. Energy Mater.*, 2020, **10**, 1902485.

[5] A. Janotti and C. G. Walle, *Reports Prog. Phys.*, 2009, **72**, 126501.

[6] J. C. Fan, K. M. Sreekanth, Z. Xie, S. L. Chang and K. V. Rao, *Prog. Mater. Sci.*, 2013, **58**, 874–985.

[7] U. Ozgur, D. Hofstetter and H. Morkoc, *Proc. IEEE*, 2010, **98**, 1255–1268.

[8] J. Kwon, S. Kwon, T. Jung, K. Nam, K. Chung, D. Kim and J. Park, *Appl. Surf. Sci.*, 2013, **285**, 373–379.

[9] J. Han, Y. J. Chung, B. K. Park, S. K. Kim, H. Kim, C. G. Kim and T. Chung, *Chem. Mater.*, 2014, **26**, 6088–6091.

[10] Y. Chen, Y. Sun, X. Dai, B. Zhang, Z. Ye, M. Wang and H. Wu, *Thin Solid Films*, 2015, **592**, 195–199.

[11] N. Wang, C. Q. Liu, C. Q. L. B. Wen, H. L. Wang, S. M. Liu, W. W. Jiang, W. Y. Ding and W. P. Chai, *Thin Solid Films*, 2016, **616**, 587–593.

[12] S. R. Nalage, M. A. Chougule, S. Sen, P. B. Joshi and V. B. Patil, *Thin Solid Films*, 2012, **520**, 4835–4840.

[13] K. I. Lee, Y. R. Denny, H. J. Kang and N. S. Park, *New Phys. Sae Mulli*, 2014, **64**, 492–496.

[14] M. Utriainen, M. Kröger-Laukkanen and L. Niinistö, *Mater. Sci. Eng. B*, 1998, **54**, 98–103.

[15] Y. Koshtyal, D. Nazarov, I. Ezhov, I. Mitrofanov, A. Kim, A. Rymyantsev, O. Lyutakov, A. Popovich and M. Maximov, *Coatings*, 2019, **9**, 301.

[16] M. Grundmann, *The Physics of Semiconductors*, Springer International Publishing, Cham, 2016.

[17] V. Coropceanu, H. Li, P. Winget, L. Zhu and J. Brédas, *Annu. Rev. Mater. Res.*, 2013, **43**, 63–87.

[18] C. Wang, H. Dong, L. Jiang and W. Hu, *Chem. Soc. Rev.*, 2018, **47**, 422–500.

[19] K. L. Chopra, S. Major and D. K. Pandya, *Thin Solid Films*, 1983, **102**, 1–46.

[20] K. Fleischer, E. Norton, D. Mullarkey, D. Caffrey and I. V. Shvets, *Materials (Basel).*, 2017, **10**, 1019.

[21] Z. Wang, P. K. Nayak, J. A. Caraveo-Frescas and H. N. Alshareef, *Adv. Mater.*, 2016, **28**, 3831–3892.

[22] E. Fortunato and R. Martins, *Phys. status solidi - Rapid Res. Lett.*, 2011, **5**, 336–339.

[23] N. Tiwari, A. Nirmal, M. R. Kulkarni, R. A. John and N. Mathews, *Inorg. Chem. Front.*, 2020, **7**, 1822–1844.

[24] Z. W. Wang, P. K. Nayak, J. A. Caraveo-Frescas and H. N. Alshareef, *Adv. Mater.*, 2016, **28**, 3831–3892.

[25] K. Nomura, H. Ohta, A. Takagi, T. Kamiya, M. Hirano and H. Hosono, *Nature*, 2004, **432**, 488–492.

[26] K. H. L. Zhang, K. Xi, M. G. Blamire and R. G. Egdell, *J. Phys. Condens. Matter*, 2016, **28**, 383002.

[27] C. Guillén and J. Herrero, *Mater. Res. Express*, 2019, **7**, 016411.

[28] H. Kawazoe, M. Yasukawa, H. Hyodo, M. Kurita, H. Yanagi and H. Hosono, *Nature*, 1997, **389**, 939–942.

[29] G. Hautier, A. Miglio, G. Ceder, G. M. Rignanese and X. Gonze, *Nat. Commun.*, 2013, **4**, 1–7.

[30] M. A. Marquardt, N. A. Ashmore and D. P. Cann, Thin Solid Films, 2006, pp. 146–156.

[31] K. Fleischer, E. Norton, D. Mullarkey, D. Caffrey and I. Shvets, *Materials (Basel).*, 2017, **10**, 1019.

[32] X. C. Huang, J. Y. Zhang, M. Wu, S. Zhang, H. Y. Xiao, W. Q. Han, T. L. Lee, A. Tadich, D. C. Qi, L. Qiao, L. Chen and K. H. Zhang, *Phys. Rev. B*, 2019, **100**, 115301.

[33] F. Deschler, D. Neher and L. Schmidt-Mende, *Perovskite semiconductors for next generation optoelectronic applications*, 2019.

[34] S. Fujita, M. Oda, K. Kaneko and T. Hitora, Jpn. J. Appl. Phys., 2016, p. 1202A3.

[35] A. Wold, K. Dwight, A. Wold and K. Dwight, in *Solid State Chem.*, Springer Netherlands, 1993, pp. 90–124.

[36] B. H. Brandow, *Adv. Phys.*, 1977, **26**, 651–808.

[37] S. Hüfner, *Adv. Phys.*, 1994, **43**, 183–356.

[38] J. L. Heilbron, *Hist. Stud. Phys. Sci.*, 1983, **13**, 261–310.

[39] T. Suntola and J. Hyvarinen, *Annu. Rev. Mater. Sci.*, 1985, **15**, 177–195.

[40] R. Puurunen, *Chem. Vap. Depos.*, 2014, **20**, 332–344.

[41] A. L. Johnson and J. D. Parish, in *ACS Symp. Ser.*, American Chemical Society, 2018, vol. 1311, pp. 1–53.

[42] R. W. Johnson, A. Hultqvist and S. F. Bent, *Mater. Today*, 2014, **17**, 236–246.

[43] P. Packan, S. Cea, H. Deshpande, T. Ghani, M. Giles, O. Golonzka, M. Hattendorf, R. Kotlyar, K. Kuhn, A. Murthy, P. Ranade, L. Shifren, C. Weber and K. Zawadzki, 2008 IEEE Int. Electron Devices Meet., 2008, pp. 1–4.

[44] K. Mistry, R. Chau, C.-H. Choi, G. Ding, K. Fischer, T. Ghani, R. Grover, W. Han, D. Hanken, M. Hattendorf, J. He, C. Allen, J. Hicks, R. Huessner, D. Ingerly, P. Jain, R. James, L. Jong, S. Joshi, C. Kenyon, K. Kuhn, K. Lee, C. Auth, H. Liu, J. Maiz, B. McIntyre, P. Moon, J. Neirynck, S. Pae, C. Parker, D. Parsons, C. Prasad, L. Pipes, B. Beattie, M. Prince, P. Ranade, T. Reynolds, J. Sandford, L. Shifren, J. Sebastian, J. Seiple, D. Simon, S. Sivakumar, P. Smith, D. Bergstrom, C. Thomas, T. Troeger, P. Vandervoorn, S. Williams, K. Zawadzki, M. Bost, M. Brazier, M. Buehler and A. Cappellani, 2007 IEEE Int. Electron Devices Meet., 2007, pp. 247–250.

[45] S. M. George, *Chem. Rev.*, 2010, **110**, 111–131.

[46] T. Hatanpää, M. Ritala and M. Leskelä, *Coord. Chem. Rev.*, 2013, **257**, 3297–3322.

[47] R. L. Puurunen, *Chem. Vap. Depos.*, 2014, **20**, 332–344.

[48] H. O. Pierson, *Handbook of Chemical Vapor Deposition*, Elsevier, 1992.

[49] M. Ritala, M. Leskelä, J. Dekker, C. Mutsaers, P. J. Soininen and J. Skarp, *Chem. Vap. Depos.*, 1999, **5**, 7–9.

[50] C. H. L. Goodman and M. V. Pessa, *J. Appl. Phys.*, 1986, **60**, R65–R82.

[51] M. Ritala and J. Niinistö, in *Chem. Vap. Depos.*, Royal Society of Chemistry, Cambridge, 2008, pp. 158–206.

[52] J. L. van Hemmen, S. B. S. Heil, J. H. Klootwijk, F. Roozeboom, C. J. Hodson, M. C. M. van de Sanden and W. M. M. Kessels, *J. Electrochem. Soc.*, 2007, **154**, G165.

[53] R. Huang and A. H. Kitai, *J. Electron. Mater.*, 1993, **22**, 215–220.

[54] M. Ritala, H. Saloniemi, M. Leskelä, T. Prohaska, G. Friedbacher and M. Grasserbauer, *Thin Solid Films*, 1996, **286**, 54–58.

[55] A. W. Ott, J. W. Klaus, J. M. Johnson and S. M. George, *Thin Solid Films*, 1997, **292**, 135–144.

[56] S. J. Yun, J. S. Kang, M. C. Paek and K. Nam, *J. Korean Phys. Soc.*, 1998, **33**, 170.

[57] H. Hu, J. Zhu, M. Chen, T. Guo and F. Li, *Appl. Surf. Sci.*, 2018, **441**, 295–302.

[58] T. Weckman and K. Laasonen, *Phys. Chem. Chem. Phys.*, 2015, **17**, 17322–17334.

[59] R. L. Puurunen, *J. Appl. Phys.*, 2005, **97**, 121301.

[60] S. D. Elliott, G. Scarel, C. Wiemer, M. Fanciulli and G. Pavia, *Chem. Mater.*, 2006, **18**, 3764–3773.

[61] J. F. Fan and K. Toyoda, *Jpn. J. Appl. Phys.*, 1993, **32**, L1349–L1351.

[62] T. O. Kääriäinen and D. C. Cameron, Plasma Process. Polym., 2009.

[63] J. A. Singh, N. F. W. Thissen, W. Kim, H. Johnson, W. M. M. Kessels, A. A. Bol, S. F. Bent and A. J. M. Mackus, *Chem. Mater.*, 2018, **30**, 663–670.

[64] J. W. Elam, G. Xiong, C. Y. Han, H. H. Wang, J. P. Birrell, U. Welp, J. N. Hryn, M. J. Pellin, T. F. Baumann, J. F. Poco and J. H. Satcher, *J. Nanomater.*, 2006, **2006**, 1–5.

[65] V. Cremers, R. L. Puurunen and J. Dendooven, *Conformality in atomic layer deposition: Current status overview of analysis and modelling*, 2019.

[66] J. Chang and J. P. Chang, *J. Phys. D. Appl. Phys.*, 2017, **50**, 253001.

[67] S. B. Heil, P. Kudlacek, E. Langereis, R. Engeln, M. C. Van De Sanden and W. M. Kessels, *Appl. Phys. Lett.*, 2006, **89**, 131505.

[68] F. Naumann, J. Reck, H. Gargouri, B. Gruska, A. Blümich, A. Mahmoodinezhad, C. Janowitz, K. Henkel and J. I. Flege, *J. Vac. Sci. Technol. B*, 2020, **38**, 014014.

[69] A. Grill, *Cold plasma in materials fabrication : from fundamentals to applications*, IEEE Press, 1994, p. 257.

[70] M. De Keijser and C. Van Opdorp, *Appl. Phys. Lett.*, 1991, **58**, 1187–1189.

[71] H. B. Profijt, S. E. Potts, M. C. M. van de Sanden and W. M. M. Kessels, *J. Vac. Sci. Technol. A Vacuum, Surfaces, Film.*, 2011, **29**, 050801.

[72] H. C. M. Knoops, T. Faraz, K. Arts and W. M. M. Kessels, *J. Vac. Sci. Technol. A*, 2019, **37**, 030902.

Chapter 2

Deposition of NiO with $Ni(DMAMP)_2$

Contents

2.1 Abstract

NiO is a p-type semiconducting transparent metal oxide and its synthesis by atomic layer deposition (ALD) has been known for over twenty years. The faults with precursor reactivity remain to date and new precursors and processes are required to address these issues. To ensure that the results of new processes are comparable to current literature, a series of depositions were performed using the $Ni(DMAMP)_2$ (nickel(II)dmamp=1-dimethylamino-2-methyl-2-propanolate, $-OCMe_2CH_2NMe_2$) and water. The attempts to emulate literature found that NiO growth rate couldn't be matched. To understand the process faults the $Ni(DMAMP)_2$ precursor was utilised in a novel plasma-enhanced ALD (PEALD) process. The $Ni(DMAMP)_2$ PEALD process was studied iteratively to ensure that film growth was saturation limited and that growth rate had been maximised. The $Ni(DMAMP)_2$ PEALD process was found to consistently and reliably produce NiO though the thermal window for the process is limited by the thermal stability of $Ni(DMAMP)_2$.

2.2 Introduction

The ALD of NiO has been known since the late 90's, one of the more notable studies from that period was completed by Utriainen *et al*, which explored the use of a range of oxidation sources including water (H_2O) and ozone (O_3).[1] Three nickel precursors $Ni(apo)_2$ (apo=2-amino-pent-2-en-4-onato), $Ni(acac)_2$ (acac=acetylacetonato) and $Ni(dmg)_2$ (dmg=dimethyl-glyoximato) (see **Fig. 2.1**) were all analysed and it was determined that regardless of nickel precursor and O_3 was essential to producing crystalline materials.[1] Limited precursor reactivity was believed to prevent crystalline NiO growth with H_2O and since this report there has been a search for a highly reactive thermally stable NiO ALD precursor. Summarised in **Table 2.1** are the NiO ALD processes which have since reported growth of NiO with from a thermal ALD with water as an oxygen source. In all the reports shown in **Table 2.1** there are only two publications which have reported crystalline NiO.[2, 3] Despite the development of new precursors the issue with low reactivity has not been entirely addressed.

Precursor Temperature (°C)	**Oxygen Source**	**Deposition Temperature (°C)**	**Growth Rate (nm/cycle)**	**Reference**
$Ni(acac)_2$	H_2O	250	0.06	[1, 2]
$Ni(apo)_2$	H_2O	250	-	[1]
$Ni(dmg)_2$	H_2O	250	-	[1]
$Ni(DMAMP)_2$	H_2O	90-150	0.08	[4]
$Ni(DMAMB)_2$	H_2O	140	0.14	[5]
$Ni(Cp)_2$	H_2O	270-330	-	[6]
$Ni(THD)_2$	H_2O	205-260	0.015-0.035	[3, 7]
$Ni(amd)_2$	H_2O	90-200	0.050-0.075	[8–10]

Table 2.1. *Comparison of NiO ALD processes which utilise water as an oxygen source.*

Given that water ALD process generally do not produce crystalline NiO it is pertinent to ask whether it is necessary for ALD methods to produce crystalline materials. A detailed review by Miikkulainen *et al* summarised that crystallinity was generally an indicator of film purity and therefore it can be concluded that crystallinity is a preferred trait for an ALD process. [11] Though generally, depending on the application, the requirements of an ALD grown material can vary. Several reports suggest that amorphous NiO could be utilised in both thin film transistors and photovoltaics and post deposition annealing or UV/O_3 treatments have been shown to influence film crystallinity and electronics, potentially negating the demands of an ALD process.[12–15] It can therefore be concluded that though a desirable trait, the growth of crystalline NiO by ALD is not necessarily essential.

To start the investigation into NiO ALD, a process from literature was studied as to benchmark

any new ALD processes and films against during the course of the project. The $Ni(DMAMP)_2$ and water process was selected for three reasons i) the process has a fast growth rate with a short ALD cycle, ii) previous experience within the research group of handling DMAMP compounds meant $Ni(DMAMP)_2$ could quickly and easily be produced iii) modification of the ligand can be performed by altering either the amine or oxirane used in synthesis which may lead to improved ALD precursors.[4, 16]

Aminoalkoxides have been synthesised for a variety of main group and transition metal compounds and their volatility has seen them utilised in CVD and ALD processes.[17–21] It was therefore presumed that the NiO process reported by Yang *et al* would be easily reproduced on the Beneq TFS-200 tool. Unfortunately the method as published did not reliably produce NiO films and despite alterations to the process parameters the results by Yang *et al* could not be reproduced.

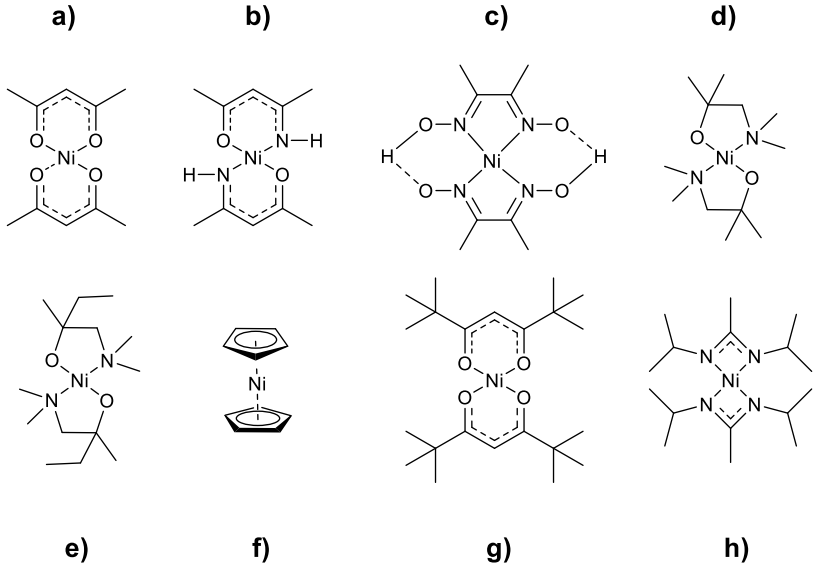

Figure 2.1. *The NiO ALD precursors (a) $Ni(acac)_2$ and (b) $Ni(apo)_2$ c) $Ni(dmg)_2$ d) $Ni(DMAMP)_2$ e) $Ni(DMAMB)_2$ f) $Ni(Cp)_2$ g) $Ni(THD)_2$ h) $Ni(amd)_2$*

A recent review by Sønsteby *et al* discusses the issues of reproducibility in ALD processes.[22] The review highlights how changes in substrate, precursor handling and ALD tool can result in deviations from results published in literature. For the experimental deposition performed in this report, all $Ni(DMAMP)_2$ precursor was synthesised and handled under an inert atmosphere and there was no systematic error that could be attributed to an equipment fault. In an attempt to explain the data, a series of depositions were performed utilising oxygen plasma instead of water. As discussed in chapter one PEALD uses reactive oxygen plasma to compensate for poor precursor reactivity. It was hypothesised a $Ni(DMAMP)_2$ PEALD processes could match the growth rate achieved by Yang *et al* and with more experimental data the reasons for the process failure could be elucidated.

2.3 Experimental

All depositions were performed on a Beneq TFS-200 reactor using a direct capacitively-coupled plasma configuration. The $Ni(DMAMP)_2$ was kept in a HS300 stainless steel container and heated to 100 °C, details of the synthesis of $Ni(DMAMP)_2$ are in Chapter **5.5**. For the chemicals utilised in chapter 3 and 4, specifically $NiCp_2$ and $Fe(MeCp)_2$, both were purchased from STREM chemical and used without further purification. For ALD processing both the $NiCp_2$ and $Fe(MeCp)_2$ were kept in kept in HS300 stainless steel containers and held at 60 °C $NiCp_2$ and 70 °C respectively. For the deposition of potassium, KO^tBu (97%) was purchased from Sigma Aldrich and used without further purification, for deposition it was held in the HS300 stainless steel container at 170 °C. To avoid condensation of precursors, nitrogen (N_2) was used as carrier gas and as a purging gas. O_2 and N_2 were used in the plasma system and maintained at 50 sccm and 200 sccm respectively throughout the deposition process. A 13.56 MHz RF power source (CESAR 133, Advanced Energy) and impedance matching network (Navio, Advanced Energy) system was used to generate O_2 plasma and for all deposition the reactor pressure was kept between 4-8 millibar with a constant feed of 200 sccm of N_2.

Ellipsometry was used to measure film thickness with all measurements were performed on a J. A. Woollam Variable-Angle SE Spectroscopic Ellipsometer and modelled using the CompleteEASE software suite. SiO_2 substrates were measured prior to deposition, the native oxide thickness measured then following deposition film thickness was remeasured with an additional B-spline layer on the native oxide model. The fit was optimised by the CompleteEASE software. With the assistance of collaborators at Cambridge University, X-ray diffraction (XRD) and X-ray reflectivity (XRR) measurements were used to determine film density using a Bruker D8 X-ray diffractomer with CuK incident x-ray. Further x-ray reflectivity measurements were completed at Bath University using powder X-ray diffraction (XRD) (Bruker D8 XRD system) and a STOE STADI P in reflection mode.

Time-of-flight elastic recoil detection analysis (ToF-ERDA) was used to discover the elemental compositions of films. A 13.6 MeV $^{79}Br^{7+}$ ion beam was used to measure the film composition and the data was analysed with Potku analysis software. Further elemental analysis was performed with an Escalab 250XI (Thermo Fischer Scientific) microprobe for all X-ray photoelectron spectroscopy (XPS) measurements. Raman spectroscopy, utilised a Renishaw inVia confocal microscope with 325 nm UV laser in the backscattering configuration. The surface roughness was estimated using atomic force microscopy (AFM). AFM was performed in contact mode on either a Veeco Multimode Nanoscope III using Bruker SNL-10 tips or a Nanosurf Flex-Axiom using Budget Sensors Contact-G tips. Analysis of images was completed in Gwyddion and the root-mean-squared (RMS) roughness values were calculated from 2×2 µm areas. The band gap of the NiO films grown onto borosilicate glass (0.7 mm thick) were determined from UV-Visible spectra and were recorded on a PerkinElmer Lambda 750 S UV/VIS/NIR Spectrometer. A Tauc plot

was used to calculate the optical band gap, with the square root of the product of the absorption coefficient and photon energy ($-(aE)^{0.5}$) plotted versus photon energy.[23]

2.4 Results and Discussion

2.4.1 ALD and PEALD deposition of NiO using $Ni(DMAMP)_2$

To begin the investigation into NiO ALD processes, the precursor $Ni(DMAMP)_2$ (**Fig 2.1**) was used in a series of deposition experiments with water as a co-oxidant. The intention was to benchmark the Beneq TFS-200 ALD tool used in our investigation with a NiO process already optimised in literature. **Table 2.2** summarises the deposition experiments completed using $Ni(DMAMP)_2$ and H_2O onto SiO_2 substrates. Precursor delivery and purge times initially matched the optimised process defined by Yang *et al* but when results did not align with those in literature the $Ni(DMAMP)_2$ delivery times, holding temperature, purge times, reactor temperature and number of ALD cycles were all systematically varied. The influence of processes manipulation on film thickness monitored by ellipsometry. In all instances the method was unable to achieve the results published by Yang *et al* given that, not once was a growth rate of 0.08 nm/cycle achieved nor was there a consistent film growth rate, with identical experiments yielding different film thicknesses.

Reactor Temperature(°C)	**Number of Cycles**	**Average Thickness (nm)**	**Growth Rate (nm/cycle)**	**Sequence**
150	425	7.86	0.0185	(5/10/5/10)
150	425	6.92	0.0163	(4/5/3/5)
150	425	3.33	0.0078	(2.5/10/5/10)
150	850	9.66	0.0114	(5/10/5/10)
120	425	2.76	0.0065	(5/10/5/10)
150	425	1.86	0.0044	(5/10/5/10)
150	425	5.00	0.0118	(5/10/5/10)
150	425	4.29	0.0101	(5/10/5/10)
120	425	5.94	0.0140	(5/10/5/10)
150	425	11.40	0.0268	(2/10/5/10)

Table 2.2. *Results of ALD experiments completed using variations of the $Ni(DMAMP)_2$ and H_2O method reported by Yang et al.[4] $Ni(DMAMP)_2$ was held at* 100 °C

As no trend was observed between deposition parameters and film thickness for the $Ni(DMAMP)_2$ experiments, it is difficult to define why the experiments performed in this study could not match literature. One significant difference between our study and the study by Yang *et al* is the ALD tool used to perform the depositions. The Beneq TSF-200 used in this investigation is a commercial ALD tool which can reliably produce ALD films. The study by Yang *et al* was completed on a prototype reactor with no known specifications.[4] As the reported growth rate could not be matched in our study, it is possible that the growth rate achieved by Yang *et al* was not saturation limited. Either some mixing of precursors occurred or the reactor temperature

was not adequately controlled and precursor decomposition influenced the observed film growth rate.

From the ALD experiments performed in this study, it may be concluded that the $Ni(DMAMP)_2$ precursor is not a suitable precursor for H_2O based ALD process on a Beneq TFS-200. From direct experience handling $Ni(DMAMP)_2$ it can be noted that when exposed to atmosphere the precursor has remarkable stability. The dark green compound, over a period of hours, begins to lighten in colour and presumably co-ordinate water. Given how slowly the compound reacts with atmosphere, the precursor appears to lack the necessary reactivity observed in other H_2O based ALD precursors.[24, 25]

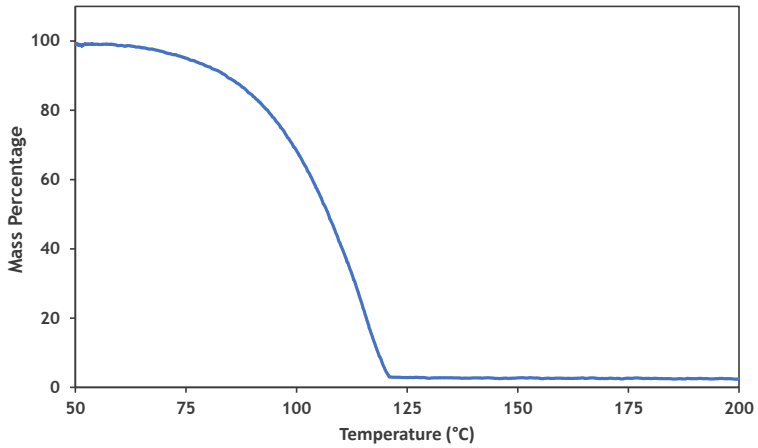

Figure 2.2. *Thermogravimetric analysis of the $Ni(DMAMP)_2$ precursor performed in an inert atmosphere*

It has been concluded that $Ni(DMAMP)_2$ is too inert to facilitate ALD growth with H_2O but it is volatile at 100 °C and is potentially suited to more reactive ALD precursors such as O_3 or O_2 plasma. By comparison $Ni(DMAMB)_2$, an alternative nickel aminoalkoxide shown in **Fig 2.1**, has been reported to effectively grow NiO using O_3, which demonstrates the suitability of the nickel aminoalkoxides as NiO ALD precursors with stronger oxidants. It was hypothesised that PEALD utilising strongly oxidising O_2 plasma may make up for the deficient reactivity of the $Ni(DMAMP)_2$ and facilitate the deposition of NiO.

For the initial $Ni(DMAMP)_2$ studies the PEALD cycle for the $Ni(DMAMP)_2$ process utilised a 5 s $Ni(DMAMP)_2$ pulse into a closed chamber with a 3 s residency period. The exhaust valve was then opened and a 10 s N_2/O_2 purge was used to end the first half-cycle. For the second half-cycle, a 4 s O_2 plasma pulse was followed by a 3 s N_2/O_2 purge meaning the overall PEALD cycle in this process was 5(3)s/10 s/4 s/3 s. The $Ni(DMAMP)_2$ was held at 100 °C, the reactor temperature held at 150 °C and the O_2 plasma pulse was ignited by a 100 W radio frequency (RF) signal. The plasma gas flow was controlled by mass flow controllers which delivered 50

sccm of O_2 and 200 sccm of diluting N_2. In 425 PEALD cycles onto SiO_2, a NiO film with an average thickness of 17.99 nm was grown with a deviation in thickness of 2.78%, with the film thinning toward the reactor outlet. With a growth rate of 0.042 nm/cycle and XRD showing the film to have weak reflections we can associate with the cubic (200) plane of NiO, the process is an improvement on the equivalent $Ni(DMAMP)_2$ and H_2O process. To confirm that O_2 plasma is necessary for deposition, the second deposition experiment utilised the same method, but no plasma ignition was performed, an illustration of these methods is shown in **Fig 2.3**. In the second experiment no film growth was observed suggesting no reaction between $Ni(DMAMP)_2$ and the molecular O_2 occurs at 150 °C and that plasma ignition is necessary to facilitate film growth.

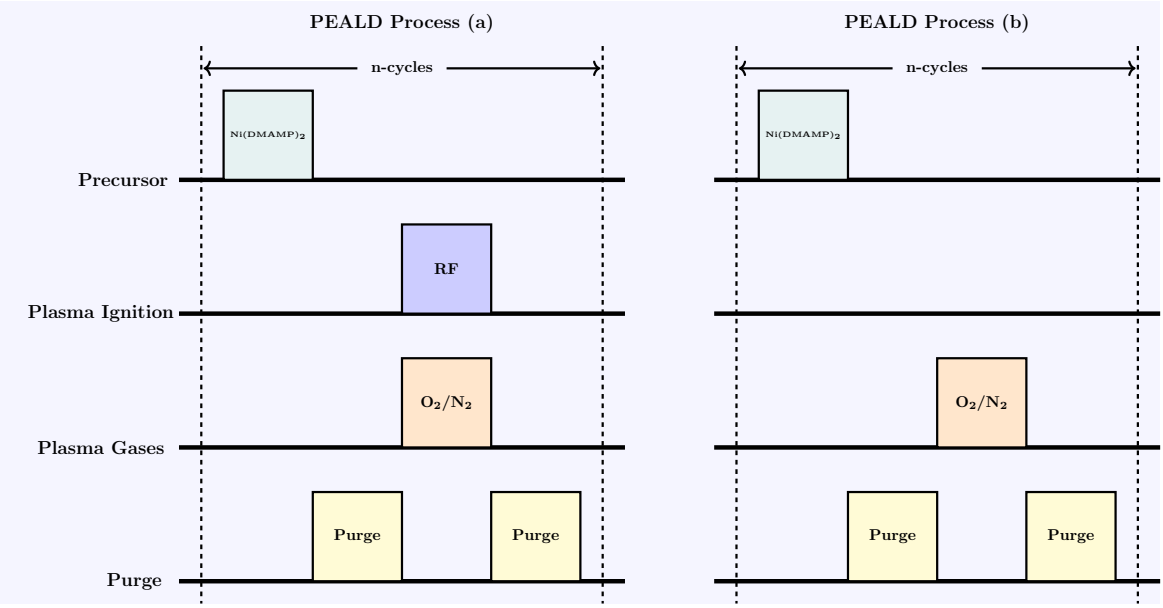

Figure 2.3. *A schematic of a) the initial PEALD method using Ni(DMAMP)$_2$ and O_2 plasma and b) experiment 2 with no plasma ignition*

Initial PEALD experiments confirmed that $Ni(DMAMP)_2$ requires plasma to facilitate the growth of NiO. To ascertain whether the process was surface saturation limited the deposition parameters were fully optimised by iteratively altering precursor pulse, purge and plasma delivery times and measuring the effect on growth rate. **Fig 2.4** shows the results of the $Ni(DMAMP)_2$ PEALD optimisation experiments performed.

Shown in **Fig 2.4** as the $Ni(DMAMP)_2$ pulse time is reduced from 5-0.5 s there is a minor reduction in growth rate (5%). To ensure that the process growth rate could reduce as a consequence of $Ni(DMAMP)_2$ delivery, an experiment was performed where the $Ni(DMAMP)_2$ was held at 70 °C. This would lower the vapour pressure of the precursor and ensure a lower dose of $Ni(DMAMP)_2$ would be delivered to the deposition chamber. When a 1 s pulse was utilised with the $Ni(DMAMP)_2$ held at 70 °C, the reduction in $Ni(DMAMP)_2$ temperature resulted in a 25% reduction in growth rate to 0.031 nm/cycle, proving the process can be constrained by

$Ni(DMAMP)_2$ concentration.

The $Ni(DMAMP)_2$ delivery pulse optimisation confirms that a 1 s $Ni(DMAMP)_2$ pulse is sufficient for saturation. The additional precursor-substrate interaction time provided by the residency period did not significantly alter the overall growth rate, as shown by **fig 2.4b**. However, the 3 s residency period correlated with the fastest growth rate and as such the 3 s residency step was performed in all further depositions. To ensure that a 5 s purge time completely purged all unwanted chemical species and prevented CVD film growth, the final $Ni(DMAMP)_2$ control experiment increased purge times to 30 s. In this experiment the overall growth rate was unchanged confirming that a purge time of 5 s eliminated any unwanted side reactions.

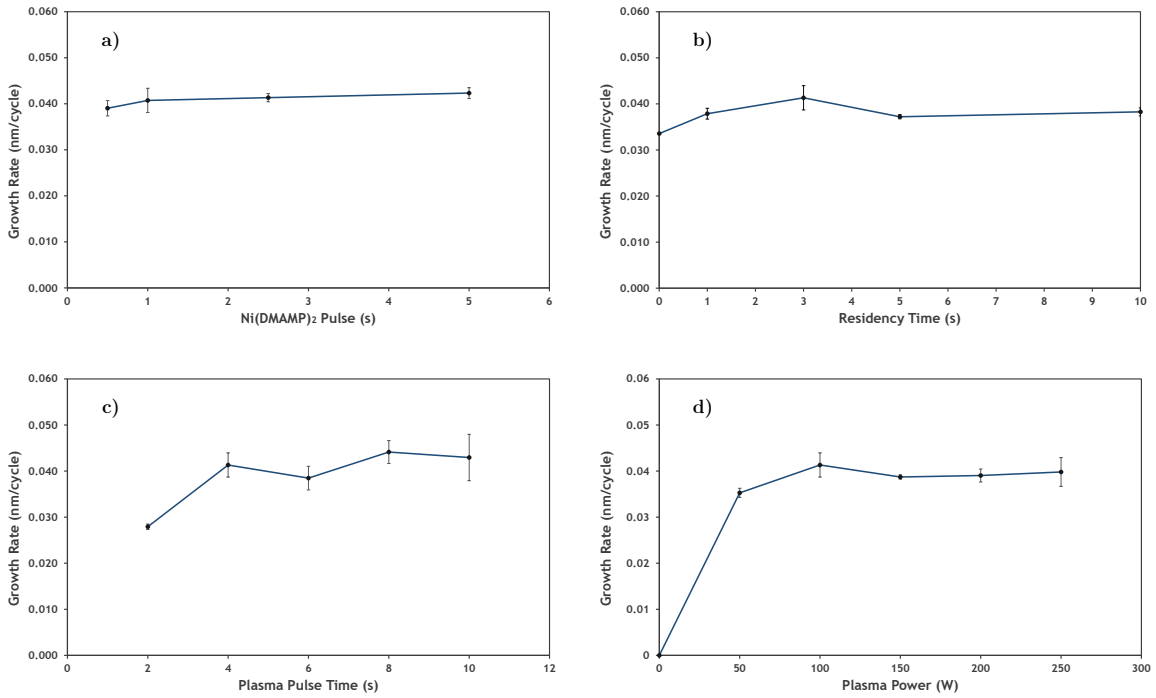

Figure 2.4. *Process optimisation experiments a) Effect of Ni(DMAMP)$_2$ pulse time on growth rate, b) Effect of residency time on NiO growth rate, c) Effect of plasma pulse length of growth rate, d) Effect of plasma power on NiO growth rate*

The $Ni(DMAMP)_2$ PEALD process was found to be more susceptible to changes in plasma conditions than it was to changes to the $Ni(DMAMP)_2$ delivery. Shown in **Fig 2.4c**, saturation is achieved after a 4 s RF pulse. As longer pulses of plasma are used the variation in sample thickness increases with the overall error increasing from 2% to 11% and the longer plasma exposures reducing film uniformity. From the results of the $Ni(DMAMP)_2$ and O_2 plasma experiments the final process was concluded as a 1 s $Ni(DMAMP)_2$ pulse with a 3 s residency period followed by a 5 s N_2 purge then a 4 s O_2 plasma pulse with a 3 s N_2 purge (1(3)s/5s/4s/3s). The optimised

process was used for all further $Ni(DMAMP)_2$ PEALD depositions.

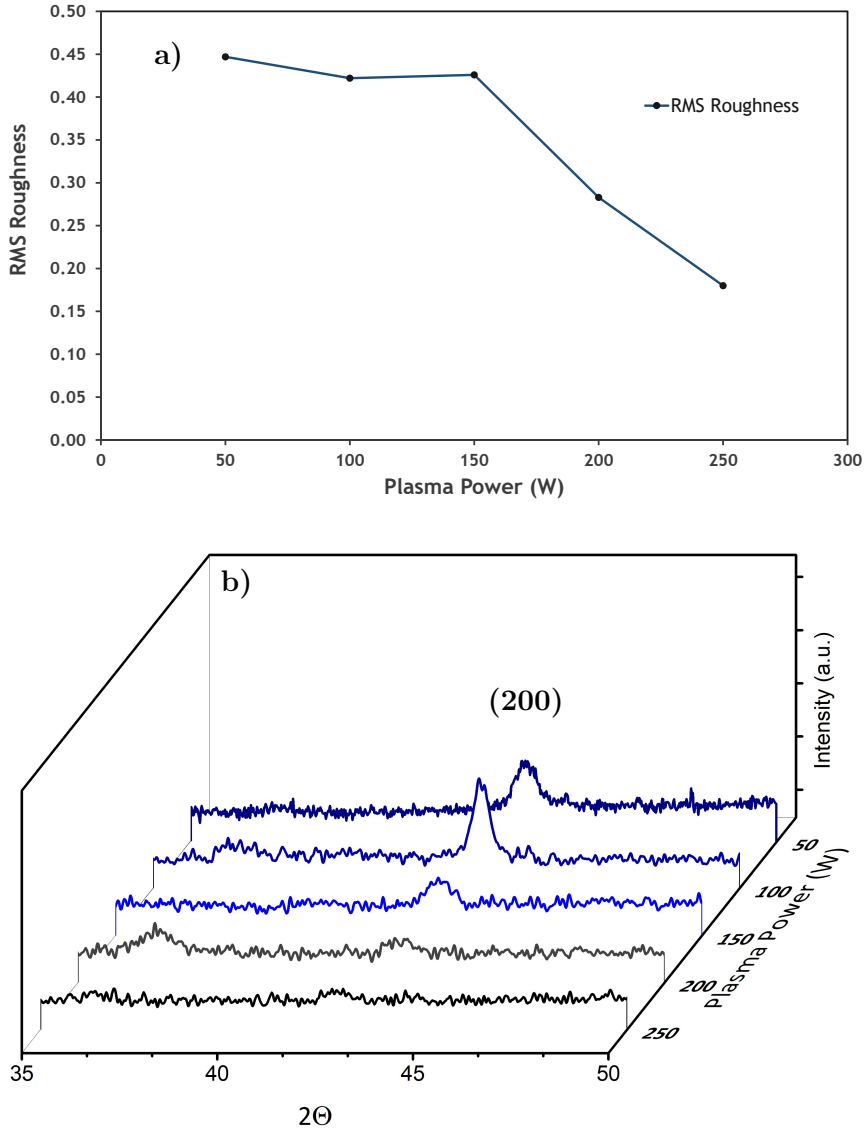

Figure 2.5. *How altering the RF plasma power applied in the $Ni(DMAMP)_2$ PEALD process effects NiO a) film roughness and b) crystallinity)*

To ascertain what plasma power is optimal for the $Ni(DMAMP)_2$ process, a series of depositions were completed varying plasma power from 50-250 W, the results of which are shown in **fig 2.4d**. A RF plasma pulse between 100-250 W grew films at a rate of approximately 0.04 nm/cycle and when power was lowered to 50 W a reduction in growth rate was observed to 0.035 nm/cycle. Analysing the films with XRD and AFM concludes that the properties of the film are also influenced by plasma power. **Fig 2.5** shows that at higher plasma powers the roughness of the

films reduces and the crystallinity in the (200) plane is greatest at 100 W. The tests confirm that though NiO growth is possible at lower plasma power, 100 W appears to be the optimal power for film crystallinity.

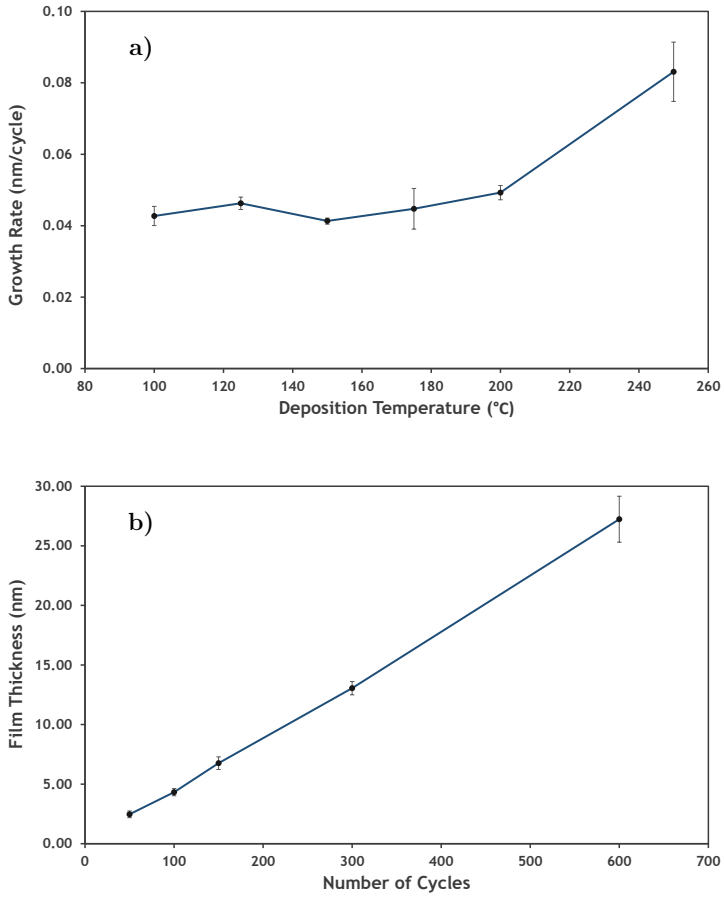

Figure 2.6. *a) Effect of reactor temperature on the growth rate of the Ni(DMAMP)$_2$ PEALD process b) Linearity of growth achieved with the Ni(DMAMP)$_2$ PEALD method.*

The optimised Ni(DMAMP)$_2$ PEALD method was subsequently used in a series of depositions between 100-250 °C to investigate a potential the thermal window for the process. Theoretically the process should have the same thermal window as the method proposed by Yang *et al* as the two processes are limited by the thermal stability of the Ni(DMAMP)$_2$ precursor. The data in **Fig 2.6a** show that above 175 °C the NiO growths rate increases which is in agreement with the study performed by Yang *et al*. From the experiments performed in this study the thermal window can be defined as between 100-150 °C. The 12% deviation in film thickness observed in the deposition at 175 °C may be a result of thermal decomposition of the Ni(DMAMP)$_2$ and as such it has not been included in the thermal window.

The Ni(DMAMP)$_2$ PEALD process has demonstrated excellent reproducibility. This is compounded by the results in **Fig 2.6b**, whereby the process has shown to maintain a linear growth rate with respect to the number of PEALD cycles. To better determine the quality of the films, further characterisation was completed using XPS, UV-Vis and Raman spectroscopy. The Raman and UV-Vis spectra shown in **Fig 2.7** are consistent with cubic NiO. The films were found to have optical bandgap of 3.8 eV and the Raman scattering profile is consistent with NiO Raman data in literature.[26, 27] The first-order transverse optical (TO) and longitudinal optical (LO) phonons and second-order (2TO and 2LO) phonons match with those in the report by Mironova-Ulmane *et al* and similarly the 2M band is absent when a 325 nm excitation source is used.[27]

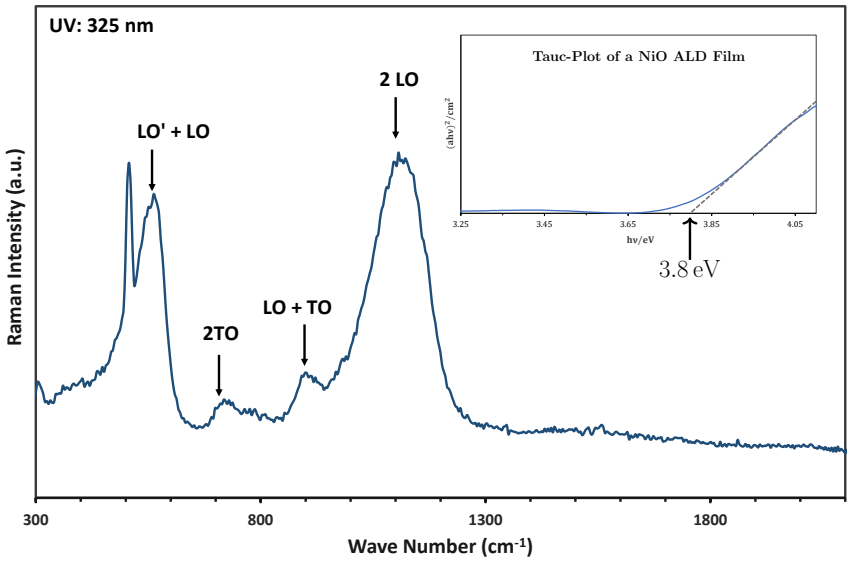

Figure 2.7. *Raman spectra of a Ni(DMAMP)$_2$ PEALD deposited NiO onto SiO_2 inset: Tauc plot calculated from the transmission and reflection data from a Ni(DMAMP)$_2$ NiO sample grown onto borosilicate glass.*

A sample of NiO grown on SiO_2 was measured by XPS to ascertain the overall Ni:O ratio. Accurately interpreting the stoichiometry of NiO samples with XPS is difficult due to the complexity of the Ni2p peak.[28] **Fig 2.8** depicts the assignments made for all Ni2p3/2, O1s and C1s scans which are based on approximations used in current literature.[29] A basic fitting of the XPS spectra was completed and charge corrected to the C1s = 284.8 eV with signature Ni 2P3/2 and O1S peaks at 853.7 eV and 529.24 eV respectively. From the low resolution survey spectrum it is apparent that the NiO sample is carbon rich with 13.2*at.*% carbon detected and nickel deficient with an overall Ni:O ratio of 0.58. The high resolution scans are in good agreement with this assessment. The O1s scan in **Fig 2.8b** has a broad shoulder consistent with the presence of organic species and the C1s scan also shows the distinct presence of carbonyl and

carboxylic species. From the high resolution scans the Ni:O ratio is calculated as 0.65 with the film containing 18*at.*% carbon.

Given that the XRD data possesses reflections which can be associated with reflections of the (200) plane of cubic NiO, it may be expected that the XPS data would yield a Ni:O ratio near to 1:1. However, it must be noted that XPS is an extremely surface sensitive technique and can identify both crystalline and non-crystalline material. Conversely, XRD analysis can only detect reflections associated with crystalline matter. It can only be postulated, due to a lack of further stoichiometric analysis, that the crystalline 1:1 NiO, does not make up the bulk of the film. The nickel deficient Ni:O ratio of 0.65 may instead infer that there are a large number of Ni2+ vacancies within the lattice, which is desirable for p-type behaviour and that there is significant oxygen content present due to carboxylic and carbonyl species. So whilst cubic NiO can be detected by XRD, XPS analysis shows that the films are contaminate rich which reduces the overall Ni:O ratio below 1:1.

2.5 Conclusions

The current literature concerning the deposition of NiO using the precursors $Ni(DMAMP)_2$ and H_2O has been concluded to be inaccurate. When tested on a commercial ALD reactor the results were inconsistent with literature and the method was unreliable. A new $Ni(DMAMP)_2$ PEALD process has been developed and optimised. The PEALD process consistently produces NiO films ordered in the (200) plane which grow at a rate of 0.040 nm/cycle. The thermal window is restricted to 100-150 °C, which is a consequence of the thermal instability of $Ni(DMAMP)_2$. XPS analysis of NiO grown at 150 °C shows that within the thermal window films contains carbon impurities and UV-VIS measurements show that the films have an optical bandgap of 3.8 eV. The PEALD process has been concluded as superior to the water process in that it can reliably produce NiO films but the high levels of impurities mean that the process cannot be used to produce high quality NiO films.

The investigations reported within this chapter, with the precursor $Ni(DMAMP)_2$, have resulted in a new PEALD process. The process is reliable but the concentration of carbon impurities may limit its potential impact. To improve on the process, a nickel precursor which has similar volatility but greater thermal stability is required.

2.6 References

[1] M. Utriainen, M. Kröger-Laukkanen and L. Niinistö, *Mater. Sci. Eng. B*, 1998, **54**, 98–103.

[2] M. Utriainen, M. Kröger-Laukkanen, L. S. Johansson and L. Niinistö, *Appl. Surf. Sci.*, 2000, **157**, 151–158.

[3] E. Lindahl, J. Lu, M. Ottosson and J. O. Carlsson, *J. Cryst. Growth*, 2009, **311**, 4082–4088.

[4] T. S. Yang, W. T. Cho, M. Kim, K. S. An, T. M. Chung, C. G. Kim and Y. Kim, *J. Vac. Sci. Technol. A*, 2005, **23**, 1238–1243.

[5] B. So, Y. You, K. Kim, J. Hwang, W. Cho, S. S. Lee, T. Chung, Y. K. Lee, C. G. Kim, K. An, Y. Kim, Y. K. Lee and W. Seo, *Electrochem. Solid-State Lett.*, 2007, **10**, J61–J64.

[6] M. Daub, M. Knez, U. Goesele and K. Nielsch, *J. Appl. Phys.*, 2007, **101**, 09J111.

[7] E. Lindahl, M. Ottosson and J. O. Carlsson, *Chem. Vap. Depos.*, 2009, **15**, 186–191.

[8] J. W. Shim, C. Fuentes-Hernandez, A. Dindar, Y. Zhou, T. M. Khan and B. Kippelen, *Org. Electron.*, 2013, **14**, 2802–2808.

[9] E. Thimsen, A. B. F. Martinson, J. W. Elam and M. J. Pellin, *J. Phys. Chem. C*, 2012, **116**, 16830–16840.

[10] R. Zhao, S. Xiao, S. Yang and X. Wang, *Chem. Mater.*, 2019, **31**, 5172–5180.

[11] V. Miikkulainen, M. Leskelä, M. Ritala and R. L. Puurunen, *J. Appl. Phys.*, 2013, **113**, 21301.

[12] J. Chen, T. Chen, L. Lai, P. Li, H. Liu, Y. Hong and D. Liu, *Materials (Basel).*, 2015, **8**, 4273–4286.

[13] W. Xu, J. Zhang, Y. Li, L. Zhang, L. Chen, D. Zhu, P. Cao, W. Liu, S. Han, X. Liu and Y. Lu, *J. Alloys Compd.*, 2019, **806**, 40–51.

[14] G. Atak and Ö. D. Coşkun, *Solid State Ionics*, 2017, **305**, 43–51.

[15] R. Islam, G. Chen, P. Ramesh, J. Suh, N. Fuchigami, D. Lee, K. A. Littau, K. Weiner, R. T. Collins and K. C. Saraswat, *ACS Appl. Mater. Interfaces*, 2017, **9**, 17201–17207.

[16] C. Hsu, H. Su, C. Hou, J. Shyue and F. Tsai, *Nanotechnology*, 2015, **26**, 385201.

[17] J. Han, Y. J. Chung, B. K. Park, S. K. Kim, H. Kim, C. G. Kim and T. Chung, *Chem. Mater.*, 2014, **26**, 6088–6091.

[18] J. W. Park, H. S. Jang, M. Kim, K. Sung, S. S. Lee, T. M. Chung, S. Koo, C. G. Kim and Y. Kim, *Inorg. Chem. Commun.*, 2004, **7**, 463–466.

[19] R. E. Agbenyeke, B. K. Park, T. M. Chung, C. G. Kim and J. H. Han, *Appl. Surf. Sci.*, 2018, **456**, 501–506.

[20] Y. Chi, P. F. Hsu, C. S. Liu, W. L. Ching, T. Y. Chou, A. J. Carty, S. M. Peng, G. H. Lee and S. H. Chuang, *J. Mater. Chem.*, 2002, **12**, 3541–3550.

[21] S. H. Yoo, H. Choi, H. Kim, B. K. Park, S. S. Lee, K. An, Y. K. Lee, T. Chung and C. G. Kim, *Eur. J. Inorg. Chem.*, 2011, **2011**, 1833–1839.

[22] H. H. Sønsteby, A. Yanguas-Gil and J. W. Elam, *J. Vac. Sci. Technol. A*, 2020, **38**, 020804.

[23] P. Makuła, M. Pacia and W. Macyk, *How To Correctly Determine the Band Gap Energy of Modified Semiconductor Photocatalysts Based on UV-Vis Spectra*, 2018.

[24] A. Devi, *Coord. Chem. Rev.*, 2013, **257**, 3332–3384.

[25] S. E. Koponen, P. G. Gordon and S. T. Barry, *Polyhedron*, 2016, **108**, 59–66.

[26] D. Lockwood, M. Cottam and J. Baskey, *J. Magn. Magn. Mater.*, 1992, **104-107**, 1053–1054.

[27] N. Mironova-Ulmane, A. Kuzmin, I. Steins, J. Grabis, I. Sildos and M. Pärs, *J. Phys. Conf. Ser.*, 2007, **93**, 012039.

[28] A. P. Grosvenor, M. C. Biesinger, R. S. Smart and N. S. McIntyre, *Surf. Sci.*, 2006, **600**, 1771–1779.

[29] M. C. Biesinger, B. P. Payne, L. W. M. Lau, A. Gerson and R. S. C. Smart, *Surf. Interface Anal.*, 2009, **41**, 324–332.

2.7 Supplementary Information

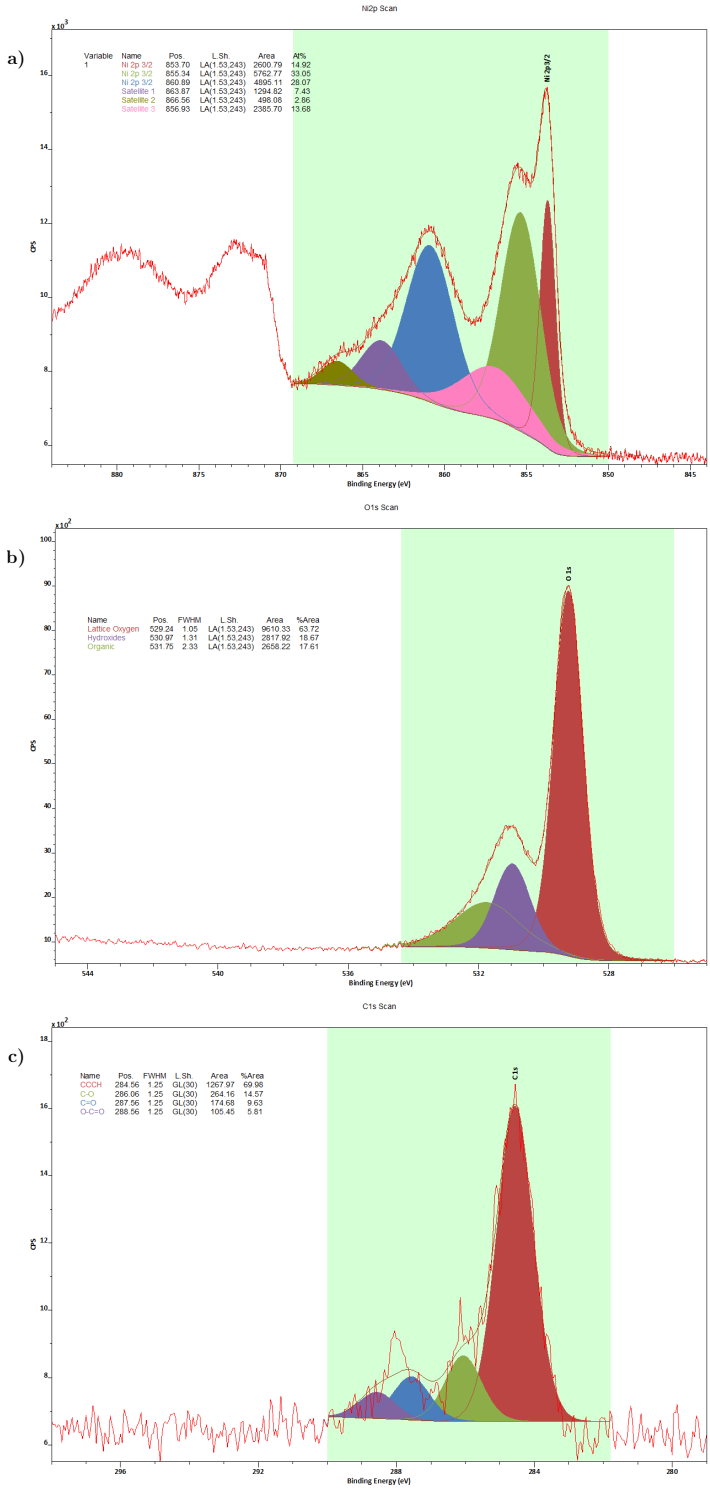

Figure 2.8. *XPS Spectra of a NiO sample grown at* 150 °C *onto* SiO_2 *using the* $Ni(DMAMP)_2$ *PEALD process a) Ni2p scan, b) O1s scan, c) C1s scan*

Chapter 3

PEALD of NiO using Nickel Metallocene Precursors

Contents

3.1 Abstract

Metallocenes, for a variety of elements, have seen application as CVD and ALD precursors due to their volatility and reactivity. Nickelocene ($NiCp_2$), an air sensitive and relatively volatile compound has been utilised in PEALD processes for the growth of NiO though the processes reported in literature are restricted by long cycle times and carbon impurities. To determine whether the process may be improved two alternative $NiCp_2$ PEALD methods which utilise direct plasma ignition have been investigated. Full materials characterisation by XRD, XPS, XRR, Raman, AFM, UV-Vis and ToF-ERDA have been performed and the process, which was iteratively optimised, provides NiO with negligible impurities via reduced cycle times and improved on the $NiCp_2$ PEALD processes in literature.

Electronic characterisation of the $NiCp_2$ PEALD films found the NiO to be insulating. In order to increase the NiO conductivity, positive holes can be introduced which increases charge carrier concentration. This can be achieved either by increasing the concentration of Ni^{2+} vacancies in the lattice or by substituting nickel atoms for group one species. Two PEALD methods were investigated as a means to alter the NiO conductivity. In the first method, a reductive NH_3 plasma cycle was supercycled as a means to reduce the oxygen content of the NiO. The second series of experiments attempted to supercycle potassium into the films and increase conductivity through potassium doping.

PEALD processes due to their directionality are generally considered ineffective at coating 3D substrates. In order to assess film coverage onto 3D substrates, a NiO layer grown from 600 PEALD cycles was grown onto TiO_2 nanorods. Through FE-SEM imaging the film coverage has been shown to maintain minor 3D features and the incorporation of the NiO layer was determined to improve the overall photo-anodic performance of the TiO_2 nanorods.

Chapter Publications:

Parts of this chapter are prepared for submission to Journal of Materials Advances.

Jerome W. F. Innocent, Mari Napari, Andrew L. Johnson, Thom R. Harris-Lee, MiriamRegue, Timo Sajavaara, Judith L. MacManus-Driscoll, Frank Marken and Feras Alkhalil. Atomic Scale Surface Modification of TiO_2 3D Nano-Arrays: Plasma Enhanced Atomic Layer Deposition of NiO for Photocatalysis.

Special Acknowledgements

Special thanks go to mari Napari, Thom Harris-Lee and Miriam Regue for their contribution to the work on NiO nanorarrays and Timo Sajavaara for completing ToF-ERDA characterisation.

3.2 Introduction

3.2.1 ALD of NiO using Metallocenes and O_3

Metallocenes are compounds which contain at least one metal carbon bond to a C_5H_5 anion ligand and have the general formula $(C_5H_5)_2M$. They are a diverse and well documented class of organometallics which rapidly developed after the discovery of ferrocene in 1951. Metallocenes can be synthesised for nearly every metal in the periodic table and have been prolifically used as olefin polymerisation catalysts.[1] It is the stability, reactivity and volatility of metallocenes which make them excellent precursors for ALD and CVD. A range of both metal and metal oxides have been grown using metallocenes including groups 2-4 and the transition metals. [2]

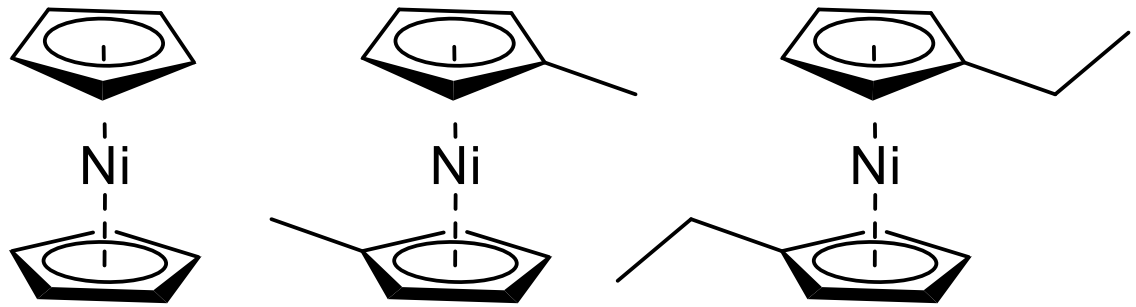

Figure 3.1. *Metallocenes $NiCp_2$, $Ni(MeCp)_2$ and $Ni(EtCp)_2$.*

Some of the most widely reported precursors for the deposition of NiO are the metallocenes $NiCp_2$, $Ni(MeCp)_2$ and $Ni(EtCp)_2$, shown in **Fig 3.1**. All three metallocenes are volatile, reactive and have been utilised as CVD and ALD precursors.[3–6] Elegantly, from $NiCp_2$ $\rightarrow Ni(MeCp)_2$ $\rightarrow Ni(EtCp)_2$ as the alkyl substituent on the C_5H_5 ring increases in size the melting point of the metallocene decreases and the precursor becomes more volatile. The increased alkyl size disrupts intermolecular pi-pi stacking and increases volatility. However, the substitution also reduces the thermal stability of the metallocene, demonstrated by $Ni(MeCp)_2$ and $Ni(EtCp)_2$ both requiring refrigeration as they are prone to thermal decomposition at room temperature. The relative stability and cost of the nickel metallocenes are compared in **Table 3.1**.

Ozone (O_3) facilitates fast ALD reactions that require short purging times at low temperatures and its high electrochemical potential (2.08 V) facilitates reactions with precursors that are otherwise non-reactive to molecular oxygen or water. As $NiCp_2$ is cheap, stable, volatile but non-reactive to water and O_2, it is understandable that the $NiCp_2 + O_3$ process is one of the most widely used in research.[3, 7–24]

Precursor	Melting point (°C)	Stability	Cost per 100 g
$NiCp_2$	173	air-sensitive	£4
$Ni(MeCp)_2$	34-36	air-sensitive, requires refrigeration	£69
$Ni(EtCp)_2$	liquid boils at 90 °C	air-sensitive, requires refrigeration	£82

Table 3.1. *Nickel cyclopentadienyl compounds as presented by STREM chemical April 2020.*

Summarised in **Table 3.2** are publications which reported the growth of NiO using nickel cyclopentadienyl compounds and O_3. There are significantly more reports concerning the utilisation of $NiCp_2$ and O_3 compared to $Ni(MeCp)_2/O_3$ and $Ni(EtCp)_2/O_3$. This is due in part to the ease of handling, cost and thermal stability of $NiCp_2$. The initial report by Lu *et al,* investigated the effect of deposition temperature on the growth rate of NiO using the precursors $NiCp_2$ and $Ni(EtCp)_2$ and O_3.[7] The investigation determined that $NiCp_2$ was the superior precursor in terms of growth rate, film structure and composition. Proceeding publications adapted the $NiCp_2$ ALD process for the growth of NiO onto a versatile array of substrates for applications in gas sensing, oxygen evolution and photocatalysis and microwave absorption.

$$Ni^{2+}(OH)_2 + O_3 \longrightarrow Ni^{4+}O(OH)_2 + O_2 \tag{3.1}$$

$$Ni^{4+}O(OH)_2 + O_3 \longrightarrow Ni^{2+}(OH)_2 + 2\,O_2 \tag{3.2}$$

$$2\,Ni^{4+}O(OH)_2 \longrightarrow 2\,Ni^{2+}(OH)_2 + O_2 \tag{3.3}$$

$$3\,Ni^{4+}O(OH)_2 \longrightarrow Ni^{2+}(OH)_2 + 2\,Ni^{3+}O(OH) + H_2O + O_2 \tag{3.4}$$

The development of NiO ALD processes has focused on processes which use O_3. However, a study by Stoyanova *et al,* demonstrated that NiO catalytically decomposes O_3 at temperatures as low as -50 °C.[29] A consequence of O_3 decomposition is a possible concentration gradient across the ALD reaction chamber which may result in incomplete ALD half reactions in areas of low O_3 concentration. As a film increases in surface area and the rate of O_3 decomposition increases, an increased O_3 concentration gradient may result in either significant film growth gradients or potentially negate further growth of NiO layers. As part of the study it was proposed that in the presence of O_3, NiO reversibly oxidises from Ni^{2+} to Ni^{4+} but may also form Ni^{3+} as shown in equations (1-4).[29] Evidence of O_3 decomposition during ALD processing might therefore result in a combination of non-uniform film growth and a high concentration of Ni^{3+}/significant nickel vacancies in the lattice.

In a study by Utriainen *et al,*, a series of NiO ALD precursors and oxidation sources were investigated.[30] In all the O_3 processes investigated there was a significant gradient in film

Precursor	Deposition Temperature (°C)	Growth Rate (nm/cycle)	Orientation	Substrate	Reference
$NiCp_2$	150-300	0.08-0.32	(200)	Si(100)	[7]
	150	-	-	Graphene	[8]
	150	-	-	ZnO	[25]
	200	-	-	Al_2O_3	[9]
	200	0.012	(200)	SiO_2	[10]
	270	-	-	Carbon Fibre	[11]
	280	-	(200)	CNTs	[12]
	300	-	-	Al_2O_3	[3]
	300	-	(111)	Si, Ni, Pt, W, TiN	[13]
	150	0.03	(200)	CNTs	[14]
	270-330	-	-	TiO_2	[15]
	120	-	(200)	Graphene	[16]
	200	0.05	-	FTO	[17]
	150	-	-	CNCs	[18]
	180-280	0.035	(200)	CNTs	[19]
	275	0.063	(200)	FTO	[20]
	100-300	-	(111)/(200)	Si	[21]
	230	-	(200)	Si(111)	[22]
	200	0.031-0.04	(111)	CNTs	[23]
	120-200	-	(200)	CNTs	[24]
$Ni(MeCp)_2$	150-250	0.048-0.084	(111)	W, Pt, Ru	[26]
$Ni(EtCp)_2$	150-300	0.039-0.089	(200)	Si(100)	[7, 27]
	250	0.028	(200)	Alumina	[28]

Table 3.2. *O_3 oxidised NiO ALD processes reported with the metallocenes $NiCp_2$, $Ni(MeCp)_2$ and $Ni(EtCp)_2$.*

thickness across the deposition chamber. By increasing pulse lengths of both the precursors and O_3 the gradient was reduced to a 3% thickness variation across the chamber. The leading edges of the NiO films were noted to have reduced transparency, greater conductivity and a reduced d-value to the bulk film. The effect was attributed to formation of lattice defects and nickel vacancies. Both the deposition gradient and the concentration of nickel vacancies, which is proportional to Ni^{3+} count, could be attributed to the O_3 decomposition and evidence of the effects noted by Stoyanova *et al,* shown by equation 4.

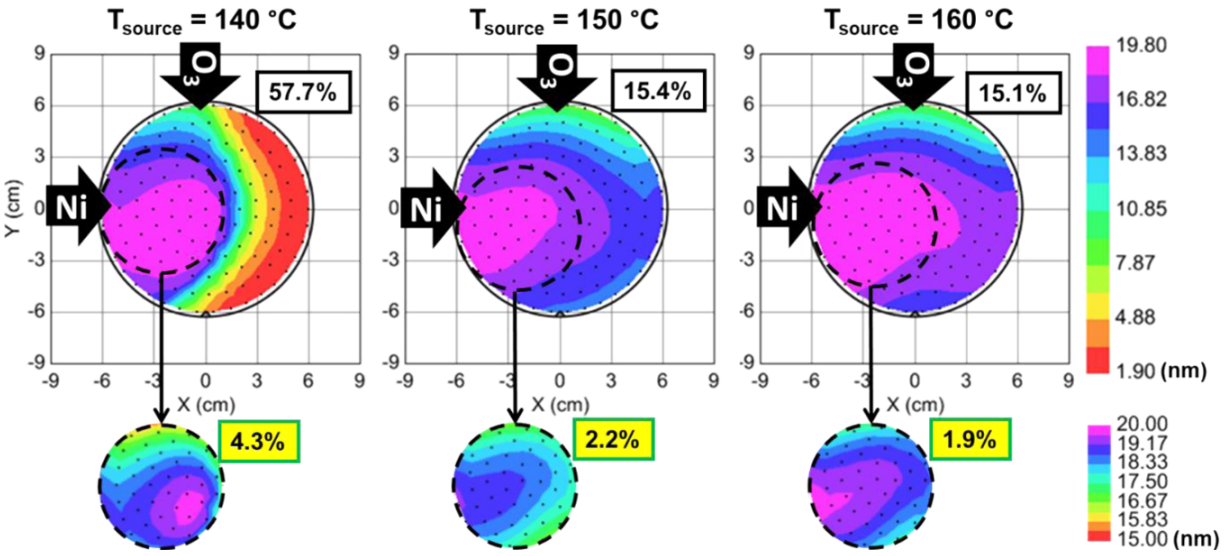

Figure 3.2. *Thickness maps of ALD deposited NiO, completed with 150 cycles of O_3 and Ni(^{tBu2}DAD)$_2$. Percentage non-conformity across the full wafer is displayed to top right of each wafer.[31]*

A publication by Holden *et al,*, reported a novel ALD process with Ni(^{tBu2}DAD)$_2$ and O_3. The publication reinforces the argument that O_3 grows non-uniform NiO films.[31] Shown in **Fig 3.2** are wafer maps of the as deposited NiO films, which display a significant growth gradient across each wafer. Comparing the results presented by Holden *et al,* to current literature is challenging as detailed wafer mapping is uncommon. Similarly, the thickness dependence on growth rate is often presented without error bars, meaning there is no clear description of uniformity of NiO films grown by O_3 ALD. [32] For example a report by Zhang *et al,* which details a novel NiO precursor and O_3 fails to report on the uniformity of the films or to present error bars for its process optimisation. [33]

Ozone is a commonly used as oxidation source in NiO ALD. Initial NiO ALD precursors, including $NiCp_2$, displayed limited reactivity towards water. In contrast O_3 is preferable to water as an oxidation source for NiO ALD as it facilitates fast reactions, with competitive growth rates and requires shorter purge times.[30, 32] The $NiCp_2$ and O_3 ALD process is widely reported because it is cost effective and has a competitive growth rate. It remains unanswered whether O_3 is an appropriate oxidation source for all NiO ALD process and applications. Ambiguous reports ensure there is no clear conclusion as to how uniform NiO films are when O_3 is used to grow thick

films or over large surface areas. Continuing to investigate and develop new NiO ALD process with alternative oxidation sources is therefore necessary to ensure there is a library of processes suitable for a diverse set of applications. This may include the development of new nickel oxide precursors and investigations with alternative oxidation sources.

3.2.2 Nickel and NiO PEALD Processes Utilising Metallocenes

Plasma-enhanced atomic layer deposition (PEALD) commonly displays rapid reactivity, requires short purge times and enables low temperature deposition. It has similar advantages to O_3 but is limited by its directionality as generally plasma is accelerated perpendicular to the generation plate and results in an angle of incidence that is approximately normal to the surface. On flat substrates this is not limiting but in 3D structures this can inhibit radical contact with film substrate. Furthermore, when growing on high aspect ratio substrates the reaction kinetics can be limited by radicals recombining before complete surface saturation occurs. In complex 3D structures that contain trenches and channels this results in growth gradients and thinning of films as demonstrated by **Fig 3.3**.[34] Despite the limitations of PEALD, it remains an effective method for the growth of metal oxides, including NiO. Several processes have been reported for the growth of both NiO (O_2 plasma) and Ni metal (NH_3 and H_2 plasmas) using PEALD, a number of which concern the use of nickel metallocenes.[4, 26, 35–41]

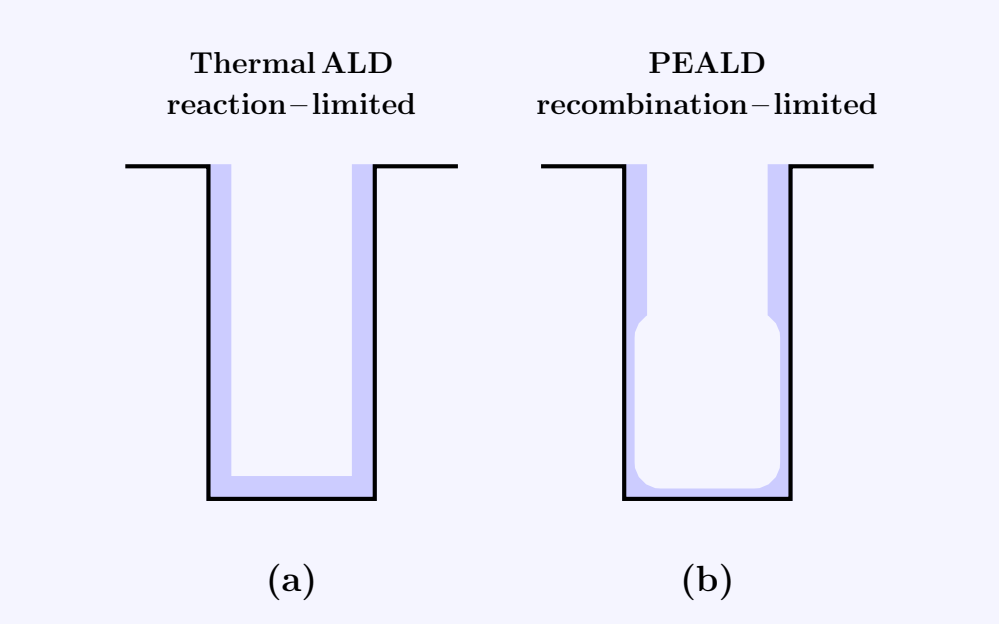

Figure 3.3. *Illustration of two deposition regimes a) reaction-limited growth in which reactions occur simultaneously covering the entire substrate uniformly, b) recombination-limited in which grow occurs everywhere but with a reduced rate towards the bottom of 3D features.*

Compared to O_3 ALD processes, there are fewer publications concerning the growth of NiO by PEALD and there are limited publications applying PEALD NiO processes. Summarised in **Table 3.3** are publications which have reported NiO ALD deposition with PEALD processes. Initial developments were reported by Song *et al,* in 2012 and focused on the growth of NiO using $Ni(MeCp)_2$ onto Pt, Ru and W substrates. [26] The study demonstrated that PEALD was a viable method for the growth of NiO but it was six years before a follow up study on $NiCp_2$ was reported.[35]

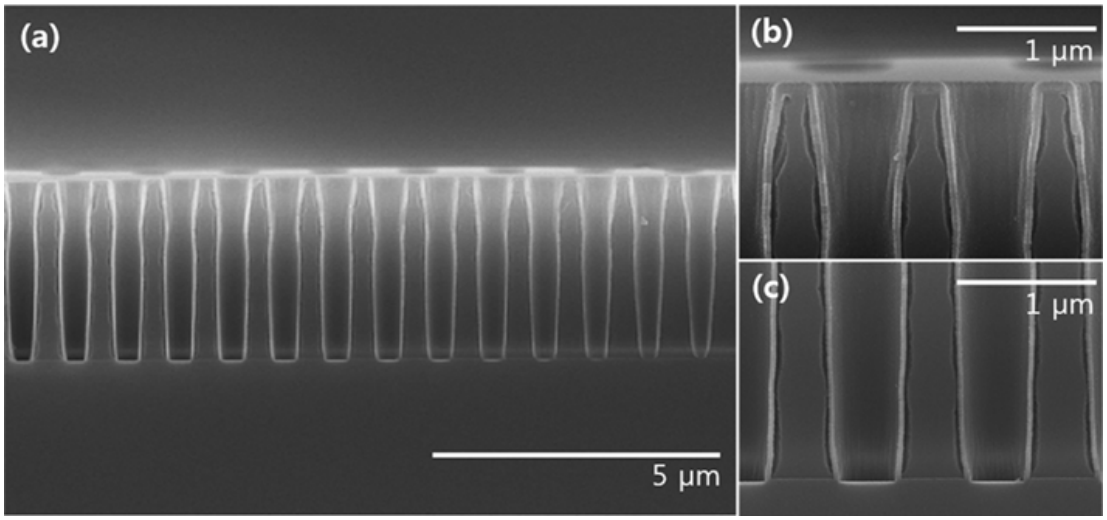

Figure 3.4. *(a) Cross-sectional SEM of NiO deposited at 250 °C using a PEALD process with the magnified channel top and bottom shown in (b) and (c) respectively.[37]*

A novel PEALD process reported by Hufnagel *et al,* developed a method for the growth of NiO using $Ni(Cp)_2$ and O_2 plasma.[35] The process had a narrow thermal window between 225-275 °C but a fast growth rate of up to 0.044 nm/cycle. The process required exceptionally long plasma pulses and triple pulses of $Ni(Cp)_2$ were necessary to reach saturation. Despite the fast growth rate, long PEALD cycles mean growing films of more than a few nanometres in thickness is expensive in regards to time and materials. A second study of the PEALD of NiO with $NiCp_2$ by Koshytal *et al,* reported a wider growth window and a reduced growth rate of 0.011-0.012 nm/cycle. The process reported that single $NiCp_2$ pulses were required but the reduced growth rate and an abundance of carbon impurities (12 at.% carbon), mean that the process is impractical for the growth of pure NiO. The high carbon content is possibly a result of the $NiCp_2$ being held at 115 °C. Although this increased the vapour pressure, in our experience, $NiCp_2$ will decompose when held above 70 °C for a prolonged period, likely resulting in volatile carbon species evacuating into the reactor, which may be incorporated into the films.

The volatile alkyl-substituted metallocenes $Ni(MeCp)_2$ and $Ni(EtCp)_2$ have also been investigated for use in NiO PEALD processing. The thermal window of the $Ni(MeCp)_2$ and $Ni(EtCp)_2$ systems is reported to be wider than the $NiCp_2$ process. Given that $Ni(MeCp)_2$ and $Ni(EtCp)_2$ both decompose at room temperature and are generally considered less stable than $NiCp_2$ it is possible that there is a contribution of precursor decomposition to film growth at high temperature. However, $Ni(EtCp)_2$ PEALD reports mention low carbon content within the thermal window and that carbon content is reduced at higher temperatures which is in agreement with the equivalent O_3 ALD process. In contrast, no composition analysis was presented in any $Ni(MeCp)_2$ PEALD reports and so determining the contribution of precursor decomposition to film growth rate is impossible. [7, 37]

Precursor	Thermal Window	Growth Rate (nm/cycle)	Precursor Temperature	Preferred Orientation	Roughness	Ni:O:C Ratio	Reference
$NiCp_2$	225- 275 °C	0.042	50 °C	(200)	<1 nm	47:52:1	[35]
$NiCp_2$	200- 300 °C	0.011-0.012	115 °C	(022)	0.34 nm	47:41:12	[4]
$Ni(MeCp)_2$	250- 300 °C	0.011-0.012	115 °C	-	-	-	[4]
$Ni(MeCp)_2$	150-250 °C	0.48 (Pt), 0.58 (Ru), 0.84 (W)	50 °C	-	-	-	[26]
$Ni(MeCp)_2$	150 °C	0.032	55 °C	(200)	-	-	[36]
$Ni(EtCp)_2$	100-325 °C	0.037	50 °C	(200)	1.412 nm	47:52:1	[37]
$Ni(acac)_2$	175-300 °C	-	-	(200)	2 nm	40:57:0.5	[38]

Table 3.3. *Nickel Cyclopentadienyl and acetylacetonate PEALD processes.*

Significantly, there have been very few publications which have utilised any of the NiO PEALD processes. This is likely to be due in part to the slow half-cycle times and significant carbon impurities. Whereas the equivalent O_3 process is fast and is reported to grow pure NiO, improving the process could prompt further application and research as $NiCp_2$ is possibly the cheapest and most easily handled NiO ALD precursor available. Using a different reactor set up and precursor delivery method, the $NiCp_2$ process could achieve the growth rate observed by Hufnagel *et al,* without significant impurities. This is compounded by the studies completed with $Ni(MeCp)_2$ and $Ni(EtCp)_2$ where growth rates of 0.032 and 0.037 nm/cycle have been achieved with low carbon content. The $Ni(EtCp)_2$ process has also demonstrated excellent step coverage on high aspect ratio substrates as shown by **Fig 3.4**. It is interesting if similar results can be achieved using an improved $NiCp_2$ PEALD process, thereby eliminating the main disadvantage of PEALD compared to thermal processes.

The use of nickel metallocenes is not limited to NiO growth. Three further publications have reported the application of $NiCp_2$ and $Ni(EtCp)_2$ as precursors for the deposition of Ni metal films. [39–41] The publications present two methodologies; one is the thermal deposition of NiO with a secondary reduction step using H_2 plasma, alternatively a single step Ni metal deposition process can be performed with $NH_3/N_2/H_2$ plasmas. Both methods demonstrate that $NiCp_2$ is an effective precursor for the deposition of conductive Ni metal.

ALD and PEALD offer control of film growth on the nano to micro scale, as $NiCp_2$ can be used to effectively grow both NiO and Ni.[40] An interesting thought experiment is whether mixing of a NiO and a Ni metal process could control the stoichiometry of the film by altering the oxygen content. NiO is semiconducting because of nickel vacancies and Ni^{3+} ions which act as electron holes and facilitate charge transfer. Theoretically, in a perfectly stoichiometric NiO sample with a 1:1 ratio of Ni:O, all charges would be balanced and the material would be insulating. It is sub-stoichiometric, imperfect NiO which is semiconducting. If the ratio of Ni:O can be controlled then electronic properties of the material could be tuned to the needs of the application. Stoichiometric control could be achieved in a supercycled PEALD process where upon NiO is deposited using an oxidative step, with additional reductive plasma steps which remove oxygen. The ratio of Ni:O could therefore effectively be controlled by altering the ratio of reductive and oxidative plasma cycles. $NiCp_2$ could be a precursor for such a process as it has been shown to effectively deposit NiO and Ni films with PEALD processes.

Using a commercial Beneq TFS-200 ALD reactor fitted with a plasma head, investigations were made to improve the $NiCp_2$ and O_2 PEALD process. The tool was used in a direct plasma configuration and two methods were developed; the first method utilised a conventional ALD system whereby discrete pulses of plasma gases are introduced to the reaction chamber and then ignited with a radio frequency pulse. The second method utilised a constant flow of plasma gas into the reaction chamber with reactions only initiated by plasma ignition. Film stoichiometry,

uniformity, crystallinity, optical and electronic properties of the as deposited films have been assessed.

The $NiCp_2$ PEALD processes were used in three further investigations. The first investigation applied a reductive NH_3 plasma cycle between O_2 cycles in an attempt to alter the overall Ni:O ratio and the stoichiometry, crystallinity and optical properties of the as deposited films were monitored as a function of O_2:NH_3 plasma pulses. The second study looked at the overall effectiveness of the PEALD process as a method for depositing onto high aspect ratio substrates. TiO_2 nanorods (TiO_2NRs) grown by solvothermal methods were used as a substrate for the growth of NiO. The effectiveness of the NiO layer as a co-catalyst for the photocatalytic splitting of water was then assessed. The final study looked at altering the electronic properties of the NiO by controlled doping of potassium by PEALD supercycles.

3.3 Results and Discussion

3.3.1 Development of the Pulsed $NiCp_2$ PEALD Process

The overall aim of $NiCp_2$ PEALD experiment was to produce a method for the growth of NiO using $NiCp_2$ that utilises short cycle times but produces uniform, high purity NiO films. Initial experiments developing the $NiCp_2$ PEALD process adopted previous literature procedures and advice from the $NiCp_2$ supplier STREM. STREM advised that the $NiCp_2$ precursor can decompose at when held above 70 °C for prolonged periods, as such the precursor was held at 60 °C for all depositions. To maximise precursor carry over, the process was programmed to pressurise the precursor container with a short pulse of N_2. Prior research from within the group has found this to be an effective method of increasing precursor carry over and an effective means of reducing the precursor delivery pulse times required for saturated ALD growth. Both steps were taken to ensure minimal carbon contamination within films and maximise precursor delivery.

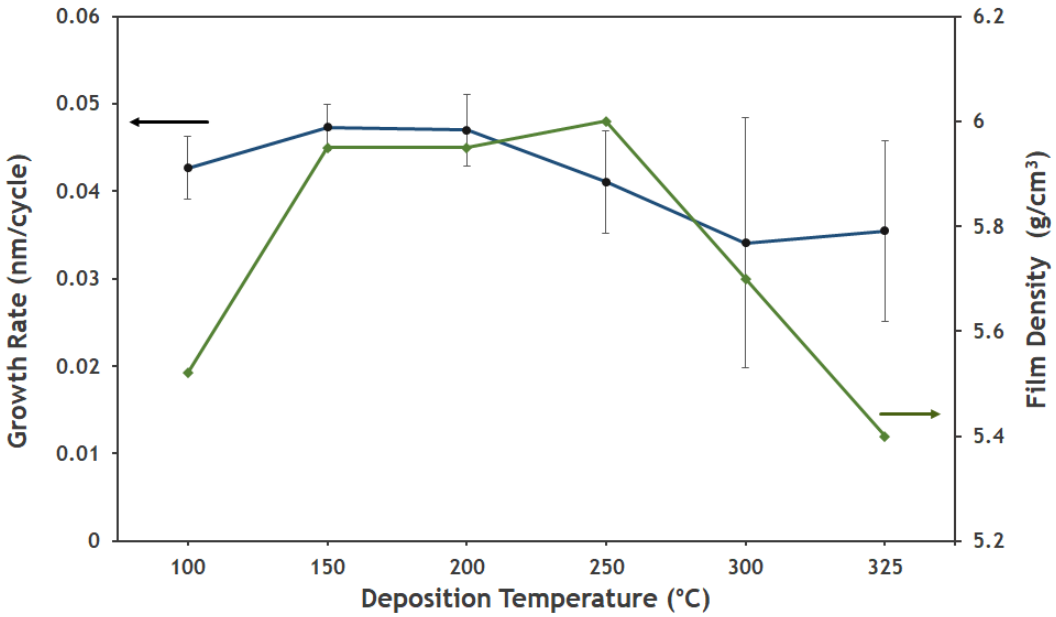

Figure 3.5. *Thermal window and density of the pulsed $NiCp_2$ PEALD process. The green line presents the density calculated by XRR.*

For precursor pulse times and purge times the process utilised an 8 s $NiCp_2$ pulse with a 5 s N_2 purge and a 3 s O_2/N_2 pulse with a 5 s N_2 purge (8 s/5 s/3 s/5 s). The pulses were estimated to be sufficient for saturation and incorporated purges long enough purges to avoid mixing of co-reagents. For the plasma, 50 sccm of O_2 was supplied with a further 200 sccm of diluting N_2 and the plasma was ignited with 100 W radio frequency (RF) pulse. The initial test depositions were completed at 250 °C, which sits within the reported thermal window for other $NiCp_2$ PEALD processes. As the process utilised a conventional segregation of precursors and reactive gases

this process will be referred to as the pulsed $NiCp_2$ PEALD method.

Shown in **Fig 3.5** is the effect of deposition temperature on the pulsed $NiCp_2$ deposition process. The NiO at low temperatures (100 °C) grows at 0.045 nm/cycle (as determined by ellipsometry) and it reduces to 0.032 nm/cycle at 250 °C. To further understand this behaviour, films were measured by x-ray reflectivity (XRR) to determine the film density at each deposition temperature. The density of the as deposited films mimics a conventional ALD thermal profile, with a thermal window between 150-250 °C and a reduction in density either side of the window thermal. Between 150-250 °C the density remains greater than 5.9 g cm^{-3} and can be considered the growth window. The reduction in density above 300 °C has been attributed to the partial decomposition of the $NiCp_2$ precursor and a probable increase in carbon content in the film. Below 150 °C the lower film density is presumably a result of poor adsorption of $NiCp_2$ to the substrate and a reduction in film crystallinity.

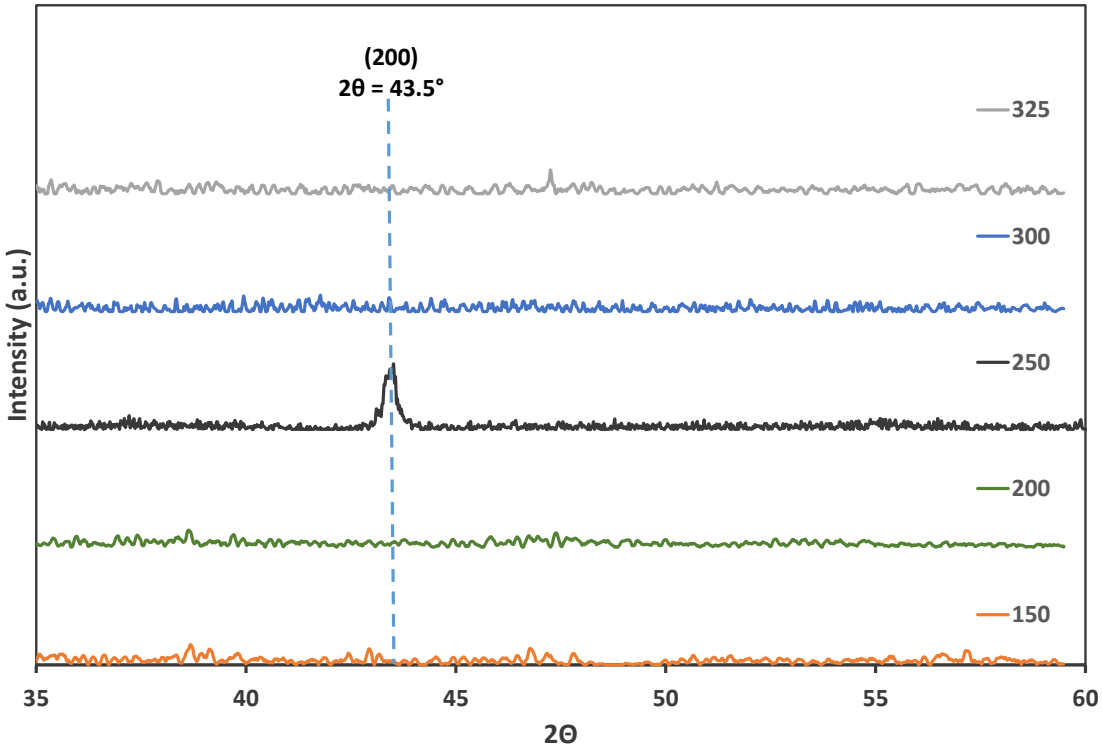

Figure 3.6. *XRD patterns of the NiO films grown using the pulsed PEALD process between 150-325 °C.*

Film uniformity is an important marker for any ALD process. Thermal ALD processes are expected to be highly uniform with negligible deviation across the deposition chamber. PEALD is often attributed to non-uniform processes which have significant gradients across the deposition chamber. In the $NiCp_2$ pulsed process, depositions tended to grow faster at the reactor inlet and thinned toward the exhaust, resulting in non-uniform film growth. This gradient significantly increased above 200 °C which could be attributed to partial precursor decomposition or a poorly optimised process. Given that that general consensus in literature agrees that 250 °C sits within

the thermal window for the a $NiCp_2$ process, it is probable that the poorly optimised method is detrimental to overall film uniformity. Furthermore, XPS analysis of the films deposited at 250 °C do not support an argument of precursor decomposition as films were determined to have negligible carbon and nitrogen content. The non-uniform growth cannot be attributed to a single parameter and is likely a complex combination of chamber gas dynamics, plasma effects and precursor chemistry.

Shown in **Fig 3.6** are the XRD patterns of the as deposited NiO films. The densest film deposited at 250 °C, is the only film to show significant crystallinity. Similar to many NiO ALD reports, the films were orientated in the (200) plane and did not strongly reflect in the (111) plane. Because of the crystallinity at 250 °C and the consistent film density between 150-250 °C, the thermal window for the pulsed $NiCp_2$ process can be defined between 150-250 °C.

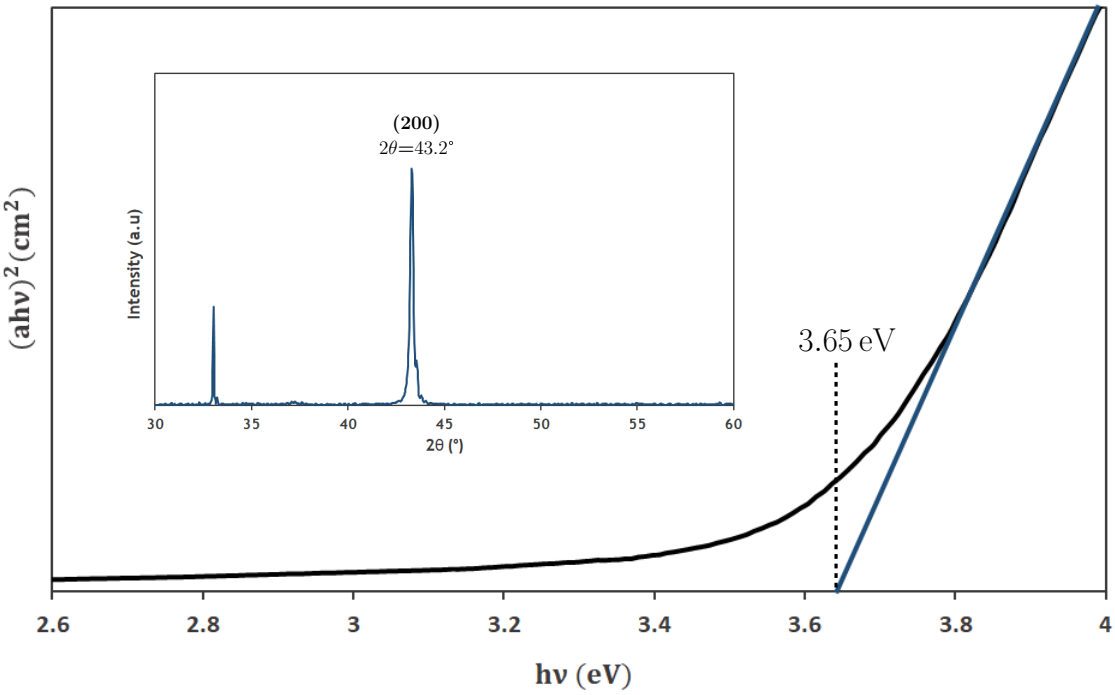

Figure 3.7. *Tauc plot calculated from the transmission and reflection data of a 100 nm film on borosilicate glass. Inset is the XRD pattern from a 100 nm NiO film deposited onto SiO_2.*

A 100 nm sample of NiO was grown onto SiO_2 and borosilicate glass at 250 °C. These samples were analysed with UV-VIS spectroscopy, Raman spectroscopy, XRD, AFM, FE-SEM and ToF-ERDA. As with the thinner films deposited at 250 °C, the films are aligned in the (200) plane as shown in **Fig 3.6**. Diffraction intensity increased with film thickness and the film is highly orientated with no other diffraction peaks detected. Shown in **Fig 3.8** is the FE-SEM image of the 100 nm sample, which confirms the accuracy of the ellipsometry modelling and verifies the film to be approximately 100 nm. The film was smooth with the route mean square roughness

(RMS) a 2x2 µm section calculated as 1.928 nm.

The films grown onto glass are dark grey in colour but remain transparent. Shown in **Fig 3.7** is a Tauc plot calculated from the transmission and reflection data of a 100 nm NiO sample deposited onto borosilicate glass at 250 °C using the pulsed $NiCp_2$ PEALD process. The optical bandgap was calculated to be 3.65 eV which correlates with an expected value for NiO (3.2-3.8 eV).

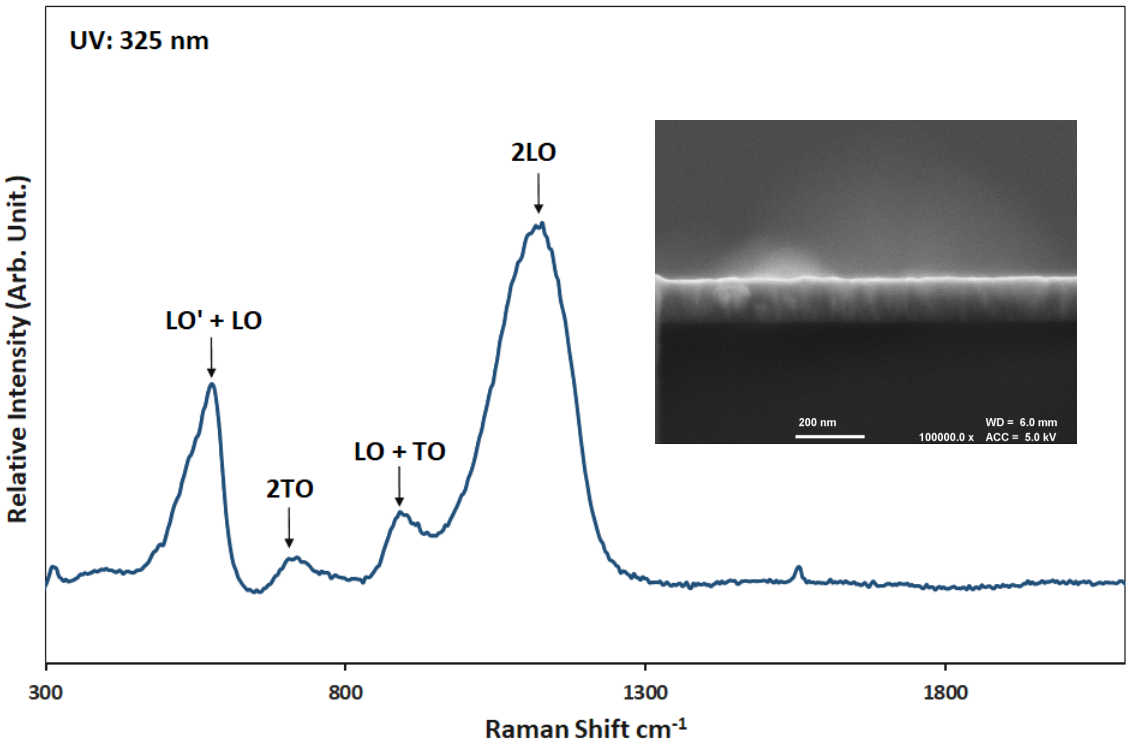

Figure 3.8. *Raman scattering of a 100 nm NiO film deposited onto SiO_2 using a 325 nm excitation source. Inset is an FE-SEM image of the 100 nm film.*

In the literature studies presented in this report, XRD, XPS, and IR are frequently utilised in the analysis of ALD deposited NiO films and, though several reports detail the Raman scattering of NiO it has not been extensively utilised as an analytical technique in ALD.[42–44] Theoretically NiO of perfect stoichiometry, containing no vacancies in its cubic lattice, has no asymmetric stretches and is Raman inactive. This is not the case for non-stoichiometric NiO. Vacancies within the lattice create asymmetry, enabling Raman spectroscopy as a means of NiO characterisation. **Fig 3.8** shows the room temperature Raman scattering of a 100 nm NiO sample oriented in the (200) plane. The excitation was caused by a UV source (3.81 eV/325 nm). The scattering profile is consistent with NiO Raman data in literature.[42, 44] The first-order transverse optical (TO) and longitudinal optical (LO) phonons and second-order (2TO and 2LO) phonons match with those in the report by Mironova-Ulmane et al, and similarly the 2M band is absent when a 325 nm excitation source is used. ToF-ERDA stoichiometric analysis estimates the films have an approximate Ni:O ratio of 0.71 which his consistent with the argument that NiO must be

non-stoichiometric to be Raman active.

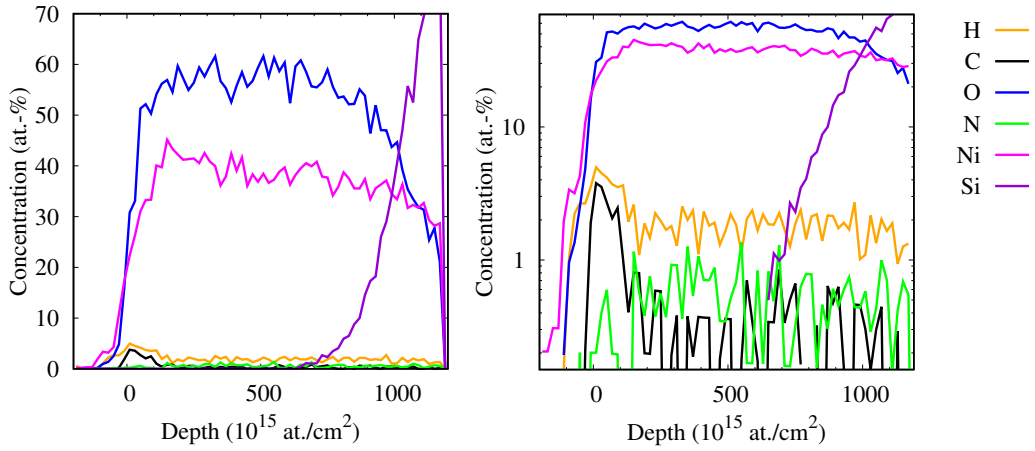

Figure 3.9. *ToF-ERDA depth profiles of a 100 nm NiO sample on SiO_2 shown with both standard (left) and logarithmic scale (right).*

Despite this positive set of results, the $Ni(Cp)_2$ pulsed PEALD method was found to leave solid deposits in the plasma head gas distribution channels. This was deemed a consequence of the plasma gases pulsing from a steady flow during plasma ignition and shutting off for the gas purges. We hypothesised that a steady flow of gas from the channels would stop the formation of the film within the plasma head and would not inhibit the film growth and reduce the maintenance cost associated with the process.

Conclusions

The pulsed process designed in this investigation utilised significantly shorter $NiCp_2$ pulses than the method used utilised Hufnagel *et al,* and achieved a similar growth rate of 0.042-0.047 nm/cycle. The pulsed $NiCp_2$ process addressed the issues presented by previous $NiCp_2$ PEALD publications, such that the process requires only short pulse times for both the $Ni(Cp)_2$ and plasma delivery for the growth of crystalline NiO. However, further amendments to the recipe were required to ensure that the reactor health over multiple processes does not degrade and compromise process reproducibility.

3.3.2 NiO Stoichiometric control with O_2:NH_3 Plasma Supercycles

The pulsed $NiCp_2$ PEALD process produced films with a Ni:O ratio of approximately 0.7. It is possible to adjust the electronic properties of the films by altering the overall stoichiometry. Changing the ratio of Ni:O will adjust the overall film electronics as nickel vacancies will be charge balanced by the presence of Ni^{3+} ions within the lattice. Ni^{3+} ions act as the majority carries in p-type conducting NiO as they act as electron holes. By increasing the concentration of Ni^{3+} it is possible to increase the conductivity. Therefore a PEALD process which can control the overall ratio of Ni:O is of significant interest.

O_2:NH_3 Ratio	at.%C	at.%N	at.% O	at.% Ni
Oxygen	1.7	0.0	58.8	39.5
9:1	1.7	0.7	58.8	38.7
4:1	2.7	0.5	58.3	38.5
2:1	2.3	0.6	58.4	38.7
1:1	2.6	0.7	58.4	38.3

Table 3.4. *Stoichiometry of NiO deposited with mixed O_2 and NH_3 plasma as determined by XPS.*

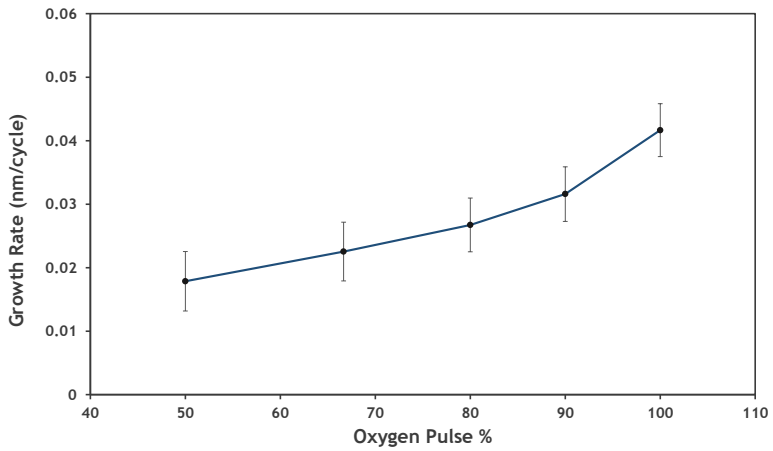

Figure 3.10. *Effect of altering the ratio of O_2:NH_3 plasma cycles on the growth rate of NiO on SiO_2 at* 250 °C.

In order to alter the overall NiO ratio in the NiO films, the flow $NiCp_2$ process was adjusted to include an additional reductive step. There are examples of both NH_3 and H_2 plasmas being used to deposit Ni metal and theoretically either could be supercycled within the flow $NiCp_2$ process.[39–41] NH_3 plasma was chosen over H_2 because in our experience H_2 completely reduces all NiO present to Ni metal and it is probable that only Ni metal would be deposited. NH_3 is less reductive and could potentially offer greater control of the overall stoichiometry. By changing the ratio of O_2:NH_3 plasmas it was hypothesised that the overall Ni:O ratio could be controlled

with PEALD processing.

The $NiCp_2$ pulsed PEALD process was used as a benchmark and depositions were completed with O_2:NH_3 ratios of 1:1, 2:1, 4:1 and 9:1. 80 sccm of NH_3 was pulsed into the reaction chamber with 200 sccm of diluting N_2 and the plasma ignited with a 100 W radio frequency signal. For each deposition experiment 1200 PEALD cycles were completed at 250 °C. Films were deposited onto SiO_2, Si(100) and borosilicate glass respectively. Film growth rates were monitored by ellipsometry and film crystallinity was measured by XRD. The optical bandgaps were calculated from Tauc plots and stoichiometric analysis was completed using XPS.

Shown in **Fig 3.10** are the growth rates observed in PEALD depositions from the $NiCp_2$ PEALD process and PEALD depositions with O_2:NH_3 ratios of 1:1, 2:1, 4:1 and 9:1. There is a linear relationship between the number of NH_3 cycles and the reduction in growth rate. Furthermore, as the number of NH_3 plasma cycles is increased the growth gradient across the films also increases with the percentage error adjusting from 10-26%. The effect of the NH_3 plasma is hard to determine from growth rates alone. Analysis of the XPS results shows that alterations if the films can be attributed to an increase in carbon and nitrogen impurities as shown in **table 4**. However, the reductive plasma step appears to have failed to alter the overall Ni:O ratio as it remains constant for all depositions.

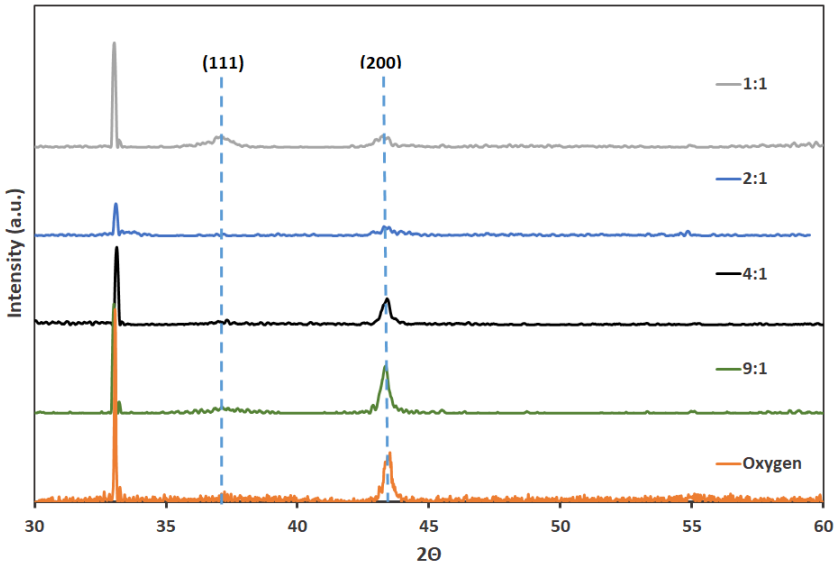

Figure 3.11. *XRD patterns of $NiCp_2$ PEALD deposited NiO supercycled with NH_3 plasma.*

Although there was no obvious alteration of overall stoichiometry, PXRD analysis suggests that a weak reflection at 37° is consistent with NiO orientated in the (111) direction. The (111) reflection was only observed in the samples synthesised when the NH_3:O_2 ratio is equal to 1:1. Evidently the NH_3 plasma is altering the film orientation. The reduction in the intensity of the (200) peak is attributed to the reduction of the NiO film thickness and a loss in effective reflection of the incident X-rays. Though the reflections associated with NiO orientated in the

(111) direction may only be attributed to a reorientation as it was not present in the films with a lower ratio of NH_3. Further evidence of the NH_3 plasma altering the NiO properties can be seen in the optical bandgaps calculated from Tauc plots. Shown in **Fig 3.12**, the depositions completed with O_2:NH_3 ratios of 9:1 and 5:1 as well as O_2 only process, have a bandgap of 3.65 eV, as the number of NH_3 plasma cycles is increased the bandgap increases to 3.7 eV as seen in the depositions with 2:1 and 1:1 ratios.

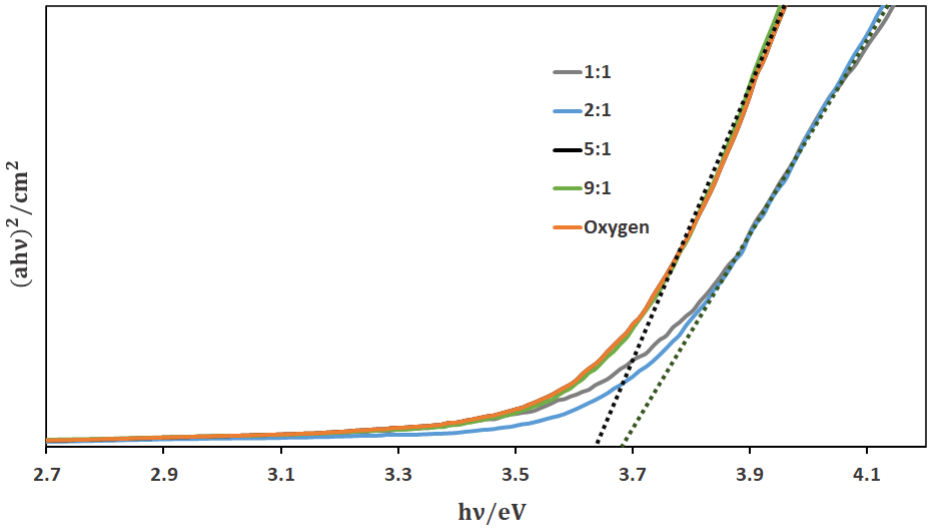

Figure 3.12. *Optical bandgaps of NiO samples deposited with a O_2:NH_3: plasma ratios of 1:1, 2:1, 5:1 and only O_2.*

XPS data suggest that altering the O_2:NH_3 plasma ratio is an ineffective method for altering the stoichiometry of the NiO. There is also evidence of some structural change given the presence of the (111) peak and alteration in optical bandgap in samples with a higher percentage of nitrogen plasma pulses. Whether this is a consequence of the NH_3 plasma pulses or by repeated plasma exposure was not explored further.

Conclusions

The initial hypothesis was that the reductive plasma step may alter the overall film stoichiometry by reducing Ni^{2+} species to Ni metal species. In this set of experiments the plasma O_2:NH_3 ratio did not alter stoichiometry. If this study was to be taken further, a comparative H_2:O_2 plasma study may be of value. Given how effective H_2 is at reducing NiO to Ni, the process would likely be Ni dominant and only a small quantity of oxygen may be left in the films. If conducted, the overall number of H_2 plasma pulses would need to be kept relatively low and consequently the process may only be appropriate in thicker films. Yet, no study of this kind has been completed or reported in literature and collecting evidence of any stoichiometric variation which scales with the number of H_2 PEALD pulses would be of interest.

3.3.3 $NiCp_2$ Flow PEALD Process

Throughout the $NiCp_2$ pulsed deposition experiments the condition of the Beneq TFS-200 ALD tool was noted to significantly deteriorate with the plasma head growing a thick insulating film of unknown composition. The material eventually inhibited plasma generation and made ignition of O_2 plasma impossible. During this period the tool was not limited to NiO depositions and monitoring the health of the tool was impractical on a run-to-run basis. In an attempt to improve the reactor health and decrease the downtime caused by maintenance, alternative gas flow regimes were investigated. Maintaining a constant gas flow through the plasma head would theoretically avoid drawing precursors within the instrument, due to the continuous positive flow of gases. As such, the $NiCp_2$ PEALD process was adapted from the pulsed methodology discussed in **3.3.1** to an alternative flow regime.

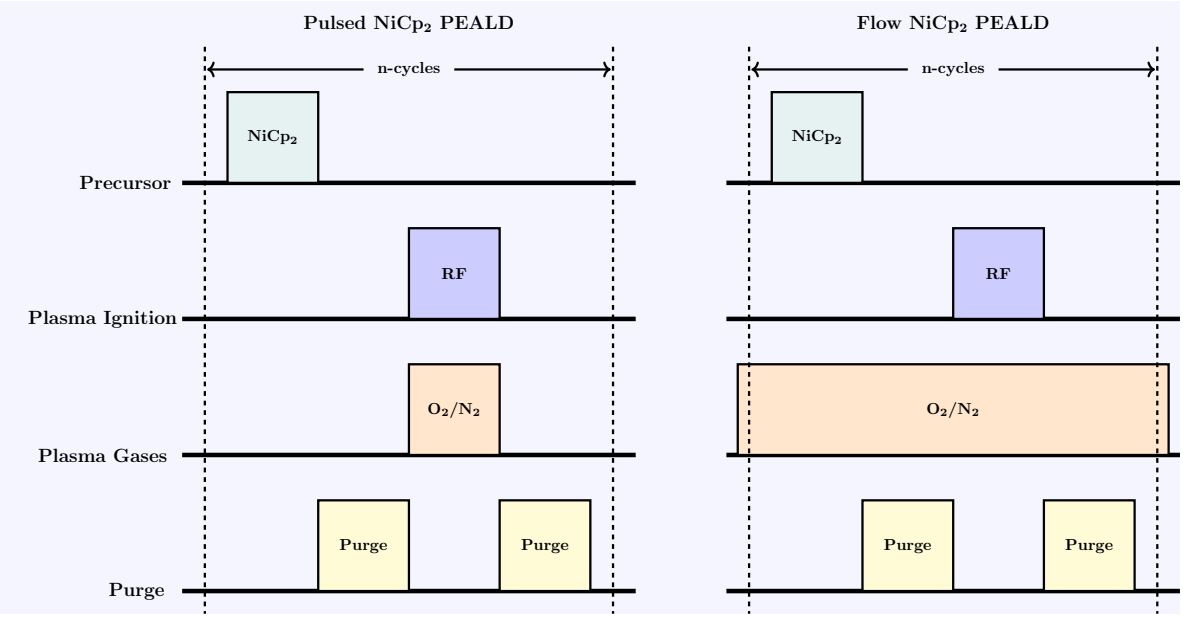

Figure 3.13. *Schematic of the Flow and Pulsed $NiCp_2$ PEALD processes.*

The $NiCp_2$ PEALD process was adapted from a pulsed to a flow process, whereby the plasma gases, specifically O_2, remain throughout each half-cycle are utilised as purging gases and reactivity is initiated by plasma ignition. Though O_2 and nickel precursor are mixed between half-cycles, provided no reaction occurs without plasma ignition then surface limited growth will be maintained and the process will still be ALD in nature. Shown in **Fig 3.13**, is the new proposed flow PEALD method compared to the pulsed PEALD method.

Initial investigations were completed at 250 °C and the $NiCp_2$ pulse was kept to 8 s. The O_2 was delivered by mass flow controller with a constant flow of 50 sccm with a 200 sccm dilution of N_2. Oxygen was delivered to the chamber throughout the process, reactions were initiated by a 50 W, 4 s plasma ignition and followed by 10 s N_2 purges between pulses of plasma and $NiCp_2$. Initial process performance was monitored by film growth rates determined by ellipsometry.

Two control experiments were completed for the $NiCp_2$ flow PEALD process. The first control study consisted of 300 cycles of $NiCp_2$ and O_2 plasma, with reactions initiated by RF pulses. The second control test consisted of 300 PEALD cycles without plasma ignition. The control test without plasma ignition did not produce any material measurable by ellipsometry. The plasma ignition test was successful and a NiO 10-10.5 nm film was grown, at 0.034 nm/cycle. Importantly, film uniformity across the chamber for the flow $NiCp_2$ process (10%) improved on that of the pulsed $NiCp_2$ pulsed process (29%) and films had significantly reduced thickness gradients. Despite the small reduction in growth rate compared to the pulsed $NiCp_2$ process (0.04 nm/cycle), the flow $NiCp_2$ pulsed process was successful and no CVD reaction occurred between the O_2 and $NiCp_2$.

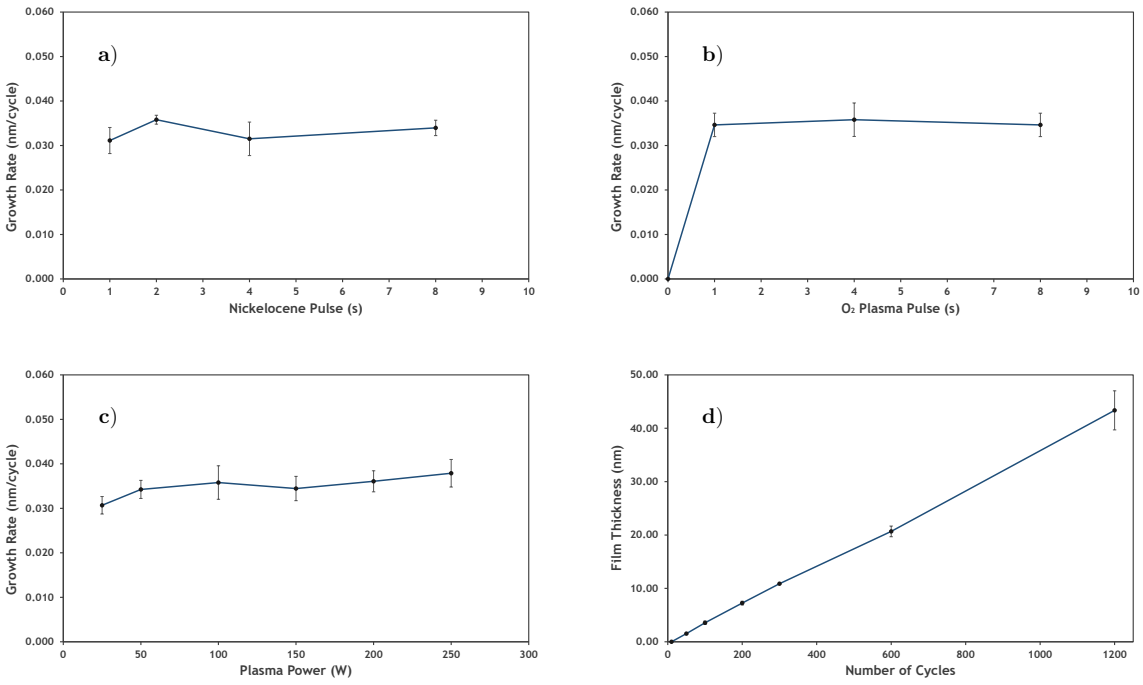

Figure 3.14. *a) Growth rate of NiO with respect to the pulse length of Ni(Cp)$_2$ b) Growth rate as a function of plasma pulse time c) Growth rate of NiO as a function of plasma power d) NiO film thickness deposited with varying numbers of PEALD cycles.*

Following the successful control deposition experiments, the flow $NiCp_2$ PEALD depositions were fully optimised to ensure complete half-cycle saturation and that growth rate had been maximised. Shown in **Fig 3.14** are the saturation experiments for the flow $NiCp_2$ PEALD process. The $NiCp_2$ delivery pulses were incrementally reduced from 8 s to 1 s. From the saturation curve in **3.15a** it is evident that only a 2 s pulse of $NiCp_2$ is required for saturated growth at 0.034 nm/cycle. This is attributed to the precursor carry over enhancement by the short pre-

pulse pressurisation step. Further optimisation of the plasma half-cycle found that a 2 s RF pulse with a power of 50 W was sufficient for saturated growth. The final optimisation study confirmed there was no mixing of reactive species and an experiment with 10 s N_2 purges between half-cycles resulted in no change to either the growth rate or NiO uniformity. Thus proving that purges of 5 seconds are sufficient between half-cycles.

The optimisation experiments performed for the $NiCp_2$ flow process have determined that one PEALD cycle consists of; a 2 s $NiCp_2$ pulse followed by a 5 s N_2 purge, and the second half-cycle a 2 s plasma ignition followed by a second 5 s N_2 purge (2 s/5 s/2 s/5 s). Throughout the PEALD cycle a continuous flow of the O_2 (50 sccm) and N_2 (200 sccm) were determined to initiate NiO growth only when ignited with an RF pulse between 50-250 watts.

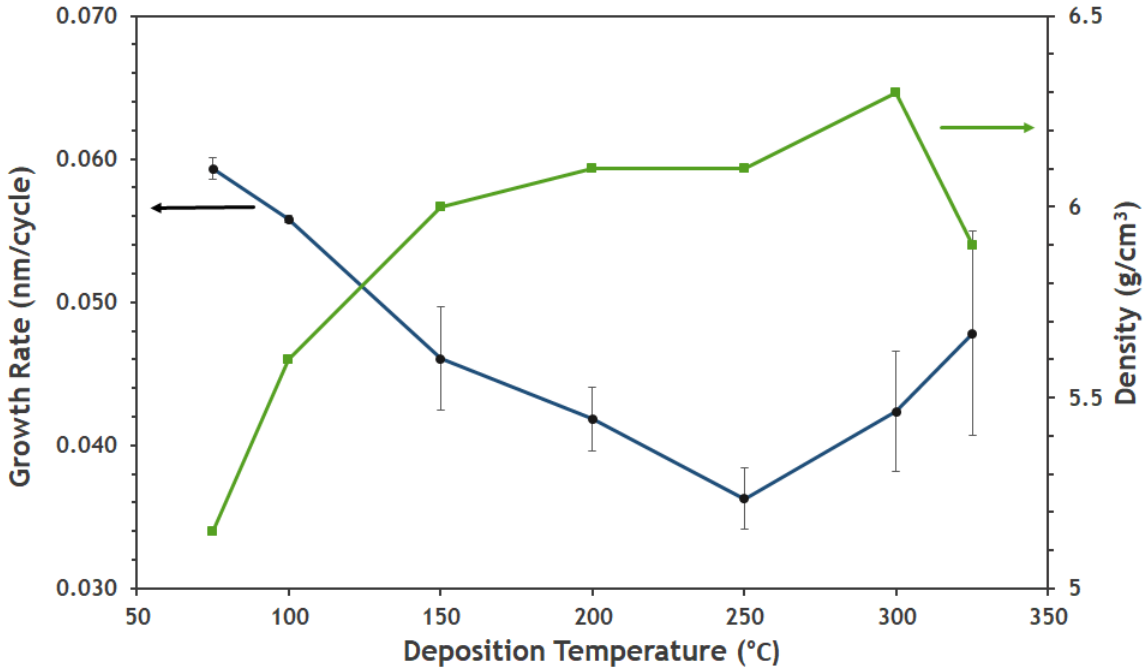

Figure 3.15. *Film growth rate and density of NiO grown between 75-325 °C.*

Using the optimised process the linearity of the growth rate with respect to the number of deposition cycles was measured between 10-1200 cycles. Shown in **3.14 d**, NiO wasn't quantifiable by ellipsometry from 10 PEALD cycles but from the following 50-1200 cycles the NiO film consistently grew at a rate of 0.036 nm/cycle. The films also displayed excellent uniformity with less than 10% variation across the chamber. Overall, the relationship between growth rate is linear with only a short onset of 10 PEALD cycles necessary to initiate NiO growth.

The thermal window for the pulsed $NiCp_2$ PEALD process was determined to be 150-250 °C (**Fig 3.5**), the flow process thermal window is potentially wider and lies between 150-300 °C. Shown in **Fig 3.15** is the growth dependence on reactor chamber temperature and the resulting film

density. As the reactor temperature is increased from 75-250 °C there is a significant reduction in growth rate from 0.060-0.036 nm/cycle, which correlates with an increase in density from 5.1-6.1 g cm^{-3}. Between 250-325 °C the growth rate increases from 0.036-0.048 nm/cycle and the film density increases to a maximum of 6.3 g cm^{-3} before reducing to 5.9 g cm^{-3}. The exact mechanism of densification cannot be monitored on the TFS-200 as no in-situ analysis may be performed. However, the film density directly correlates to film crystallinity. Shown in **Fig 3.16**, with increasing deposition temperature the films begin to show greater alignment in the (200) plane. The increase in film density can therefore be attributed to an increase in film crystallinity and the subsequent reduction at 325 °C a result of precursor decomposition. The thermal window for the growth of NiO using the flow $NiCp_2$ PEALD process can be concluded to lie between 150-300 °C.

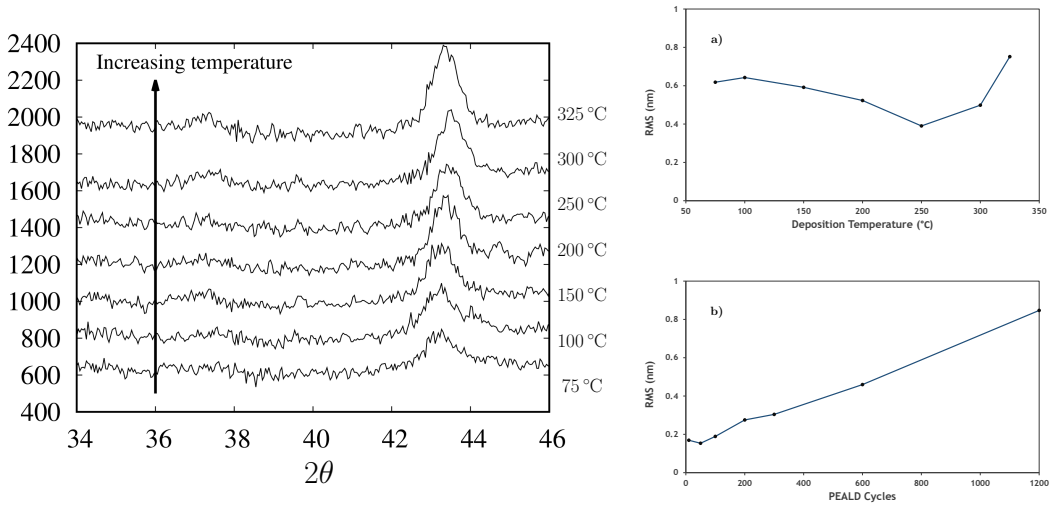

Figure 3.16. *Order in the (200) plane of NiO films grown between 75-325 °C a)Film roughness as a function deposition temperature b)Film roughness variation with increasing PEALD cycles.*

Ideally ALD films should be as smooth as possible, with a smoother film generally indicating controlled layer by-layer growth resulting from fewer surface defects and layer-by-layer growth consistent with the ALD model. The surface roughness of the flow $NiCp_2$ PEALD films was analysed by AFM. A 2x2 µm area was measured and the route mean square (RMS) roughness calculated for a series of samples deposited at varying temperatures and of differing thickness. **Fig 3.16a** shows the effect of deposition temperature on film roughness. From the study it is clear that the roughness correlates to film growth rate. The comparatively slower growth rates observed between 200-300 °C have the lowest the RMS values and as deposition rate increases so does the overall roughness. In addition, roughness increased linearly with film thickness with the film grown from 1200 PEALD cycles calculated to be the roughest with an RMS of 0.847

nm. Shown in **Fig 3.17** are the AFM images of films deposited between 10-1200 cycles all of which are featureless as expected of smooth ALD deposited films.

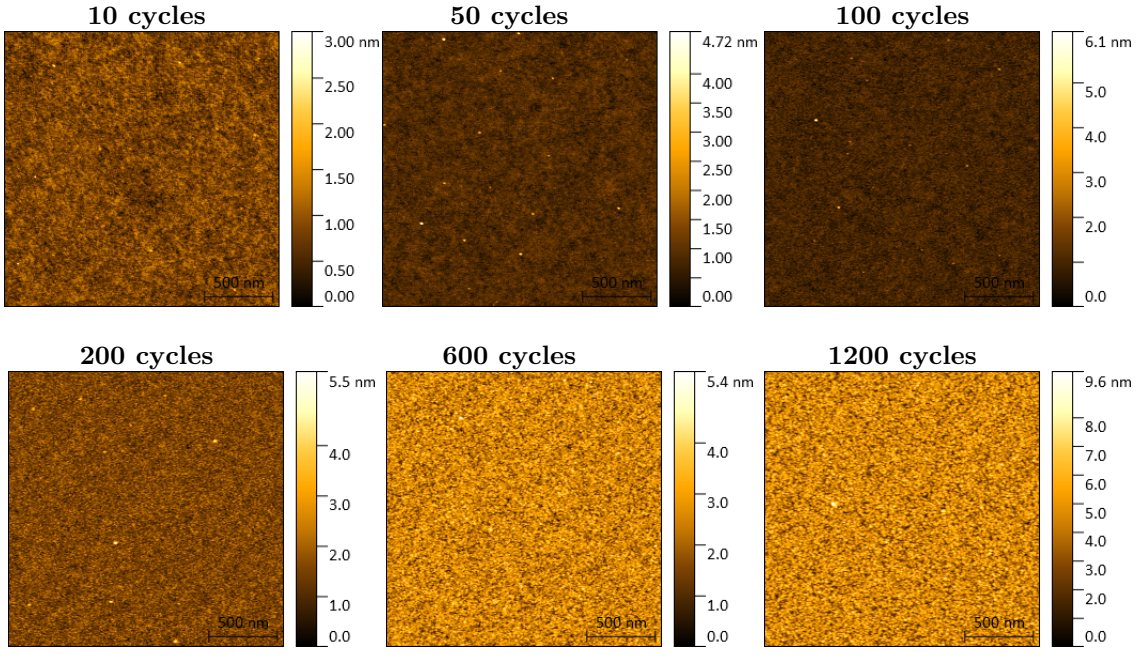

Figure 3.17. *AFM images of 2x2 µm areas of films grown from 10-1200 $NiCp_2$ PEALD cycles.*

It was hypothesised, that the $NiCp_2$ flow PEALD process produces identical material to that of the pulsed $NiCp_2$ PEALD process. The optical and structural properties of the NiO films grown at 250 °C using both the pulsed and flow processes were compared to determine whether the processes are equivalent. All XRD measurements of flow deposited NiO films possess a peak at 43°, consistent with cubic NiO orientated in the (200) direction. A NiO film was grown onto borosilicate glass at 250 °C using the flow PEALD process and was analysed by UV-Vis spectroscopy. The band-gap was calculated with a Tauc-plot and it was determined to be 3.65 eV and equal to the bandgap of the pulsed PEALD processed NiO.

As part of the comparison between the pulsed and flow PEALD deposited NiO, Raman measurements of two 30 nm films were completed. A publication by Dietz *et al,* reported that NiO with a 1:1 Ni:O ratio has a different Raman spectrum to sub-stoichiometric, oxygen rich NiO.[43] Stoichiometric NiO was reported to have low intensity peaks within the 400-600 cm^{-1} region, whereas the oxygen rich NiO was shown to have a significantly more intense first order scattering within the same region. From the experimental results obtained in this study all samples can be considered oxygen rich as corroborated by XPS and ToF-ERDA measurements. This is in line with the study by Dietz *et al*, as demonstrated by the Raman spectra in **Fig 3.18**, both the flow and pulse PEALD deposited NiO showcase intense peaks between 400-600 cm^{-1}. Furthermore, the spectra are near identical, as can be seen by the overlay inset it **Fig 3.18**.

The flow and pulse $NiCp_2$ PEALD deposited NiO samples both have a density of 6 $g\,cm^{-3}$ and

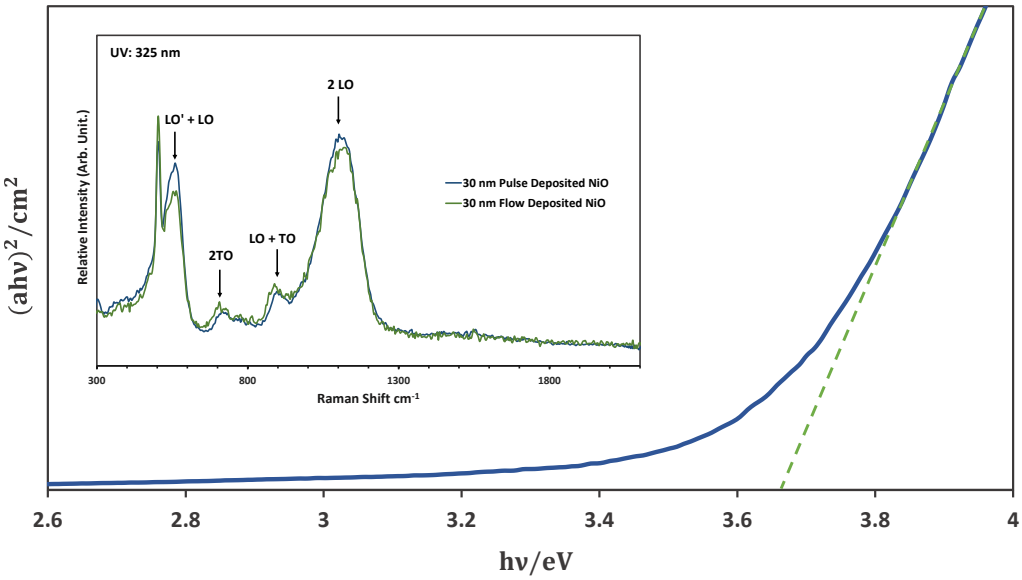

Figure 3.18. *Tauc plot of a NiO film grown by the flow PEALD process using $NiCp_2$, inset are the Raman spectra of 30 nm NiO films grown by both pulsed and flow methods.*

as shown in **Figs 3.15** and **Fig 3.5**, they produce NiO preferentially aligned in the (200) plane and have an optical band gap of 3.65 eV. Further similarities are that the growth rates for both processes are near equivalent (0.035-0.04 nm/cycle) and the thermal windows overlap (150-250 °C). Overall for both processes film coverage is excellent with only a slight deviation in film thickness across the deposition chamber. No XPS or ToF-ERDA measurements were completed on the flow deposited films but, given the similarity between the pulsed and flow processes, the flow $NiCp_2$ deposited films are believed to have a similar oxygen rich NiO stoichiometry, as verified by Raman measurements. To conclude both process from analysis of the structural and optical properties and deemed to grow identical films.

As part of the investigation into the flow PEALD NiO, it was hoped that the overall stoichiometry of the NiO films could be correlated between XPS and Raman spectroscopy. Dietz *et al*, reported that the overall stoichiometry of NiO alters the Raman spectra of the films but literature confirming this trend with XPS and ToF-ERDA is measurements is scarce. Within this study, normalising and integrating the regions between 400-600 cm^{-1} and 900-1250 cm^{-1} can give a rough estimate of the ratio of the LO + 2LO peaks, but correlating this with the sample stoichiometry is not trivial. The 400-600 cm^{-1} region contains the NiO peaks LO' and LO as well as a peak from the SiO_2 substrate. Even assuming that the LO' and LO have equal contribution to the peak intensity, the influence of the SiO_2 substrate cannot be accounted for and as such, an accurate quantification of the LO' + LO peaks cannot be ascertained and the overall stoichiometry cannot be attained by Raman spectroscopy. To use Raman to quantitatively estimate

the stoichiometry of NiO is not possible within the scope of this project. However, completing a study such as this would be an interesting contribution to the field.

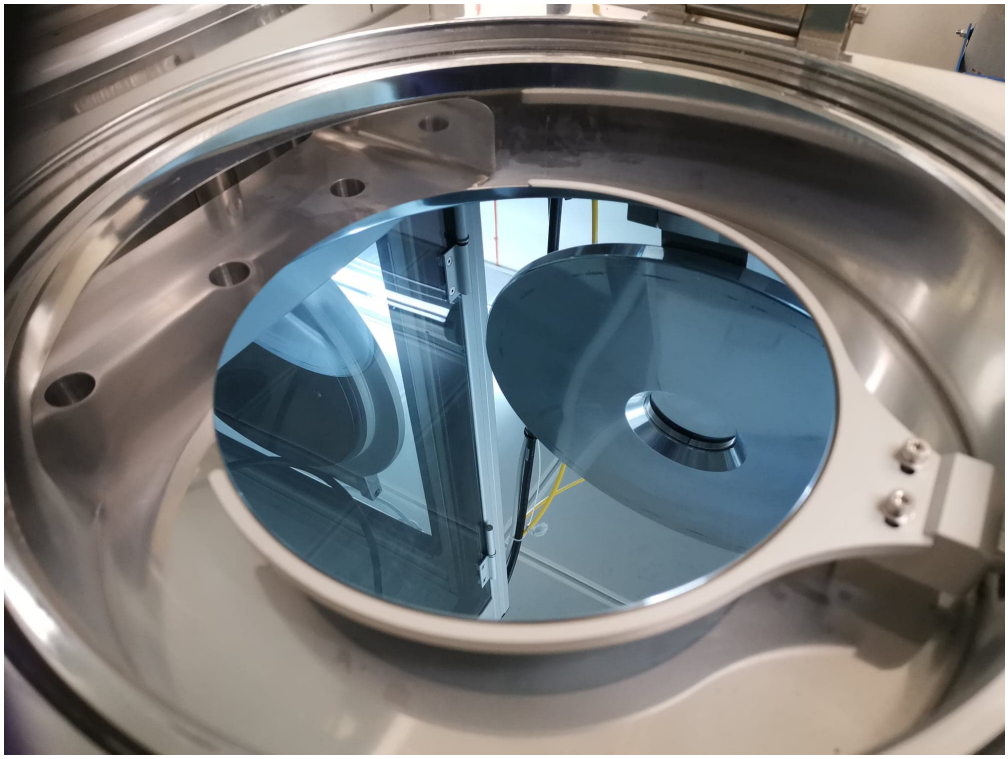

Figure 3.19. *A 20 nm NiO film grown by the flow PEALD process using $NiCp_2$ onto an 8" SiO_2 wafer.*

Growth Method	**Resistivity ($\Omega\,cm^{-1}$)**	**Mobility ($cm^3\,V^{-1}\,s$)**	**Carrier Concentration (cm^{-3})**
$NiCp_2$ Flow PEALD	$1.31 * 10^4$	0.2	$2.5 * 10^{15}$

Table 3.5. *Electrical properties of NiO deposited by flow $NiCp_2$ PEALD*

As part of a collaboration between Pragmatic Printing and several research groups multiple samples of NiO were grown and their electronic characteristics analysed. The overall project aim was to develop a thin film transistor (TFT) which utilised a PEALD/ALD deposited NiO layer. Shown in **Fig 3.19** is a 20 nm NiO film grown at 250 °C on a 8" SiO_2 wafer. The substrate filled the entire deposition chamber and yet the NiO is entirely free of blemishes and has remarkable uniformity, which demonstrates the scalability of the flow $NiCp_2$ PEALD process. A separate sample which was successfully electronically characterised was a 100 nm NiO film on borosilicate glass. Hall Measurements analysis with a four-point-probe showed the NiO had resistivity of $1.31 \times 10^4\,\Omega\,cm$ and p-type conductivity with holes as majority carriers. The hole density was measured to be $2.5{\times}10^{15}$ cm^{-3} with a mobility of 0.2 cm^2Vs^{-1}. Despite showing p-type conductivity none of the samples which were analysed displayed the switching characteristics essential for application in TFTs. This has been attributed to the overall resistivity of the films

and unfortunately no NiO TFTs were produced within this study.

Conclusions

The optimised flow $NiCp_2$ PEALD process has a thermal window between 150-300 °C in which it displays a growth rate of 0.036-0.046 nm/cycle and grows NiO aligned in the (200) plane with a density of $6.0\,g\,cm^{-3}$. It is sub-stoichiometric with an approximate Ni:O ratio of 0.7 and is p-type semiconducting with an optical bandgap of 3.65 eV. It is the most reliable, reproducible and efficient NiO deposition method that has been used within this volume of work. The process efficiently uses a cheap precursor with short cycle times, the films are free of carbon and nitrogen impurities and the flow method has been demonstrated to scale up without further optimisation. It is an excellent method for the growth of NiO. Given that it is unsuitable in TFTs, research focused on developing applications for the PEALD grown NiO as well as altering the overall electronic properties of the films.

3.3.4 PEALD grown NiO, a Co-catalytic Layer for Photoanodic Water Splitting

Titanium dioxide TiO_2, is an n-type semiconducting metal oxide that is well established as a material for the photoanodic catalytic splitting of water.[45–47] It is not within the scope of this report to review TiO_2 as a photocatalytic material, for the interested reader there are some comprehensive reviews covering the subject.[48, 49] Of relevance to this work is that NiO layers can have been demonstrated to enhance the photocatalytic activity of TiO_2 and several reports have documented significant performance improvements from the addition of NiO. [50–54] NiO enhances the photocatalytic current of TiO_2 because the materials have aligned bandgaps and when in contact form P-N junctions. The junction increases charge separation and improves and prolongs charge lifetimes by reducing recombination probability. Shown in **Fig 3.20** is the conduction mechanism for NiO/TiO2 adapted from Rasheed *et al.*[51] It demonstrates that with incident light an electron from the valence band of TiO_2 is promoted into the TiO_2 conduction band. The excited electron's hole in the TiO_2 valence band are then shifted into the NiO valence band which inhibits electron hole recombination in the TiO_2. This relationship ensures that at any given time there are more electrons than in the TiO_2 conduction band than there are holes in the valence band and reduces the chance of recombination and prolongs charge lifetimes, increasing catalytic turnover.[51]

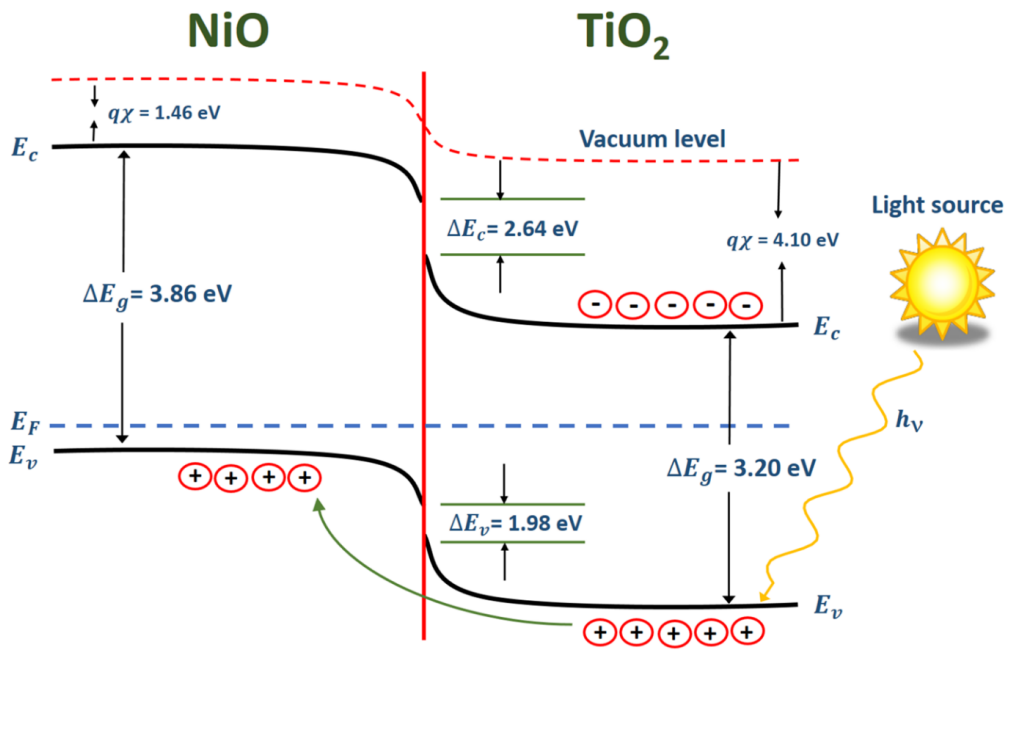

Figure 3.20. *Conduction mechanism at the p-n junction of TiO_2 and NiO. Adapted from Rasheed et al.[51]*

Titanium dioxide TiO_2, can be grown into a variety of structures such as nano-flowers and nano-rods.[55] Increasing the surface area of the TiO_2 may improve photocatalytic performance and it provides an interesting substrate for the growth of NiO by PEALD. Depositing a NiO layer onto the high aspect ratio TiO_2 can be used to show the effectiveness of the flow $NiCp_2$ PEALD method for growth onto 3D structures. In order to test the overall NiO PEALD coverage, TiO_2 nanorods (TiO_2-NRs) were grown via solvothermal synthesis onto fluorine-doped tin oxide (FTO), using the method utilised in the study by Zhang *et al.*[56] The TiO_2-NRs were analysed structurally with XRD, Raman, SEM, EDX and the photocatalytic activity was measured using a one sun lamp solar simulation. A second set of TiO_2-NRs were coated with 20 nm of NiO grown using the optimised $NiCp_2$ flow PEALD method at 250 °C. The NiO/TiO_2-NRs were then compared to the TiO_2-NRs both structurally and as photocatalysts.

When coated with NiO the white TiO_2-NRs turn a dull grey in colour and when analysed by XRD the NiO layer is undetectable. Shown in **Fig 3.21** the 20 nm of NiO is weakly diffracting and cannot be differentiated from the baseline. FTO dominates the spectra with only a few weakly diffracting TiO_2 peaks detectable. Noticeably, there is no difference between the TiO_2-NRs and the NiO coated TiO_2-NRs as such the orientation of the NiO could not be determined.

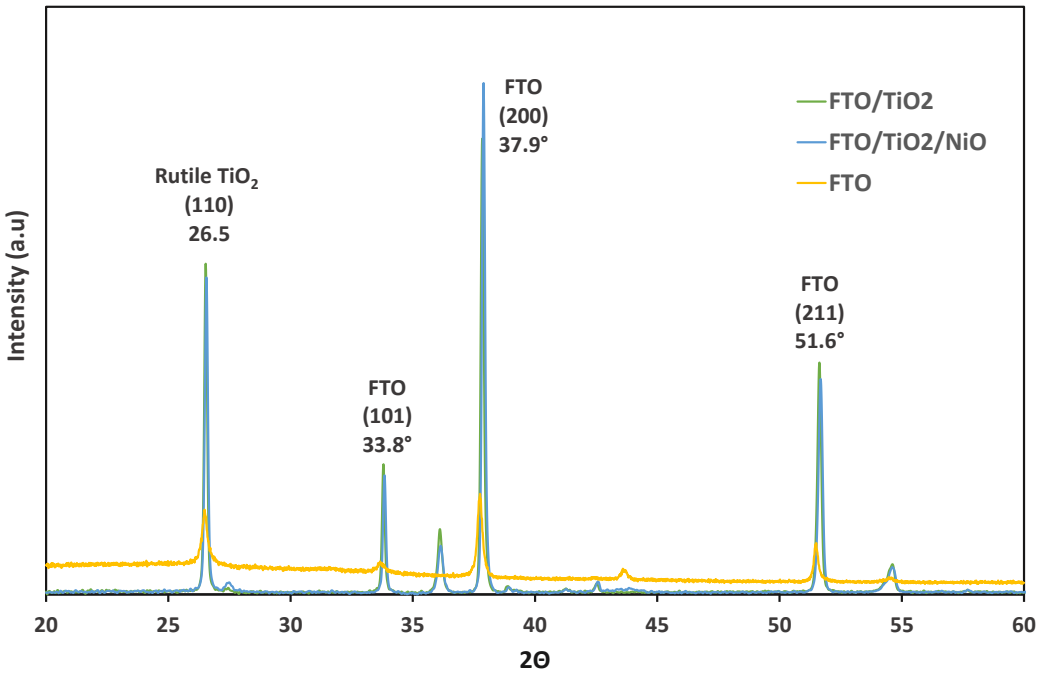

Figure 3.21. *XRD patterns from the TiO_2-NRs and NiO coated TiO_2-NRs.*

Raman measurements were completed for the TiO_2NRs and the NiO coated TiO_2NRs using a 385 nm UV light source. Shown in **Fig 3.22** are the baseline corrected Raman spectra collected of both samples. There is no significant difference between the coated and uncoated TiO_2NRs.

Signature rutile TiO_2 peaks can be identified in **Fig 3.22** at 612 cm^{-1} (A_{1g}), 236 cm^{-1} (B_{1g}) and 826 cm^{-1} (B_{2g}).[57] None of the Raman peaks observed from the NiO samples grown on SiO_2 (**Fig 3.8**) can be detected.

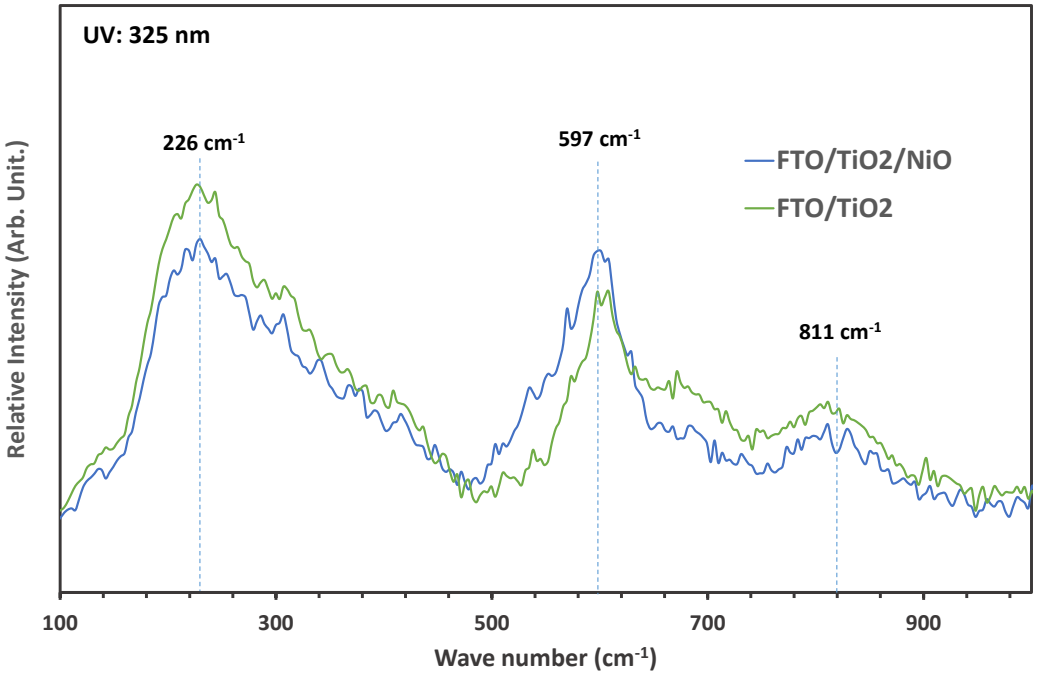

Figure 3.22. *Raman spectra of the TiO_2–NRs and NiO coated TiO_2–NRs.*

To confirm adhesion of the NiO onto the TiO_2–NRs, SEM microscopy was paired with EDX, samples of the NiO coated TiO_2–NRs were imaged and the elemental composition obtained. Shown in **Fig 3.23 (a)** is a control sample section of FTO which was masked during NiO deposition which did not exhibit any Ni peaks, but an intense peak ascribed to the presence of Sn confirmed the sample was FTO and scotch tape was sufficient to mask deposition. **Fig 3.23 (b)** and **(c)** are SEM-EDX scans of two different samples of the TiO_2–NRs coated in NiO. In both sample scans, Ni was detected suggesting it has bound to the TiO_2–NRs during PEALD deposition. Furthermore, looking at **Fig 3.23 (c)** the surface of the NiO/TiO_2–NRs is uniform and spatial voids remain across the substrate surface suggesting the material has a large surface area suitable for photochemical water splitting.

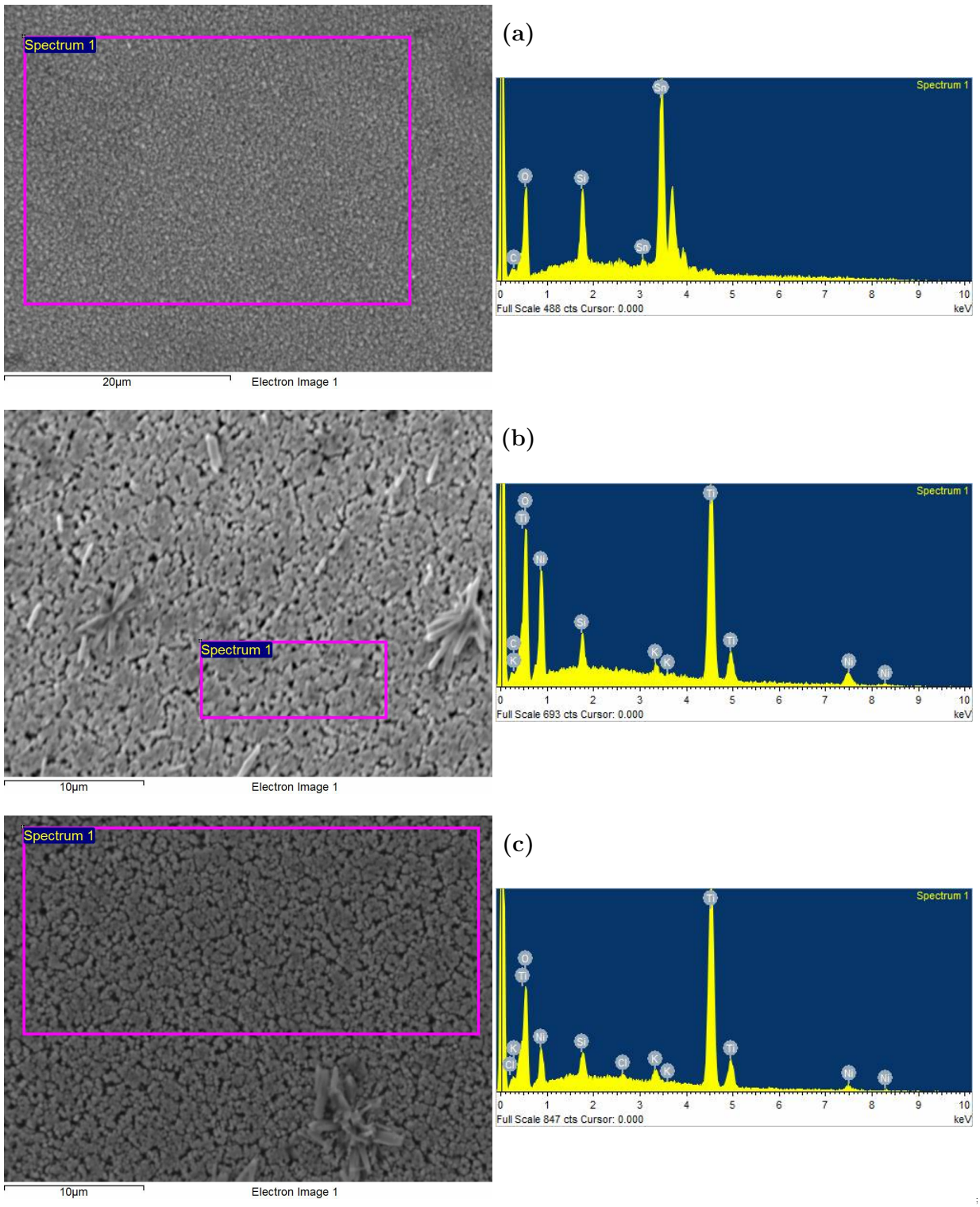

Figure 3.23. *(a) SEM-EDX imaging analysis of a control section of FTO (b) and (C) SEM-EDX of NiO coated TiO_2−NRs.*

SEM-EDX confirms the NiO has coated the TiO_2 – NRs but to determine the uniformity of NiO coverage on individual nanorods and whether the high aspect ratio of the nanorods is maintained, FE-SEM imaging was conducted. **Fig 3.24** shows FE-SEM images of TiO_2 – NRs before **(a-c)** and after **(d-f)** coating with 20 nm of NiO. Inset into **3.24a** is an image of one of the surface defects seen previously in the TiO_2 – NRs in SEM imaging. The defects consist of randomly dispersed TiO_2 – NRs clustered together. The bulk of the TiO_2 – NRs are aligned roughly perpendicular to the FTO with large spatial voids between nanorod clusters. The TiO_2 – NRs are approximately 1 µm in length and between 100-200 nm in width. In the top down view shown in **3.24c** the nanorods can clearly be seen clustering at the surface some of which agglomerate into a continuous film. Very few of the nanorods remain singular. This highlights that the TiO_2 – NRs are not an ideal substrate for testing the uniformity of coverage of an ALD method. Depending on the uniformity of the TiO_2 – NRs sample, there may already be a continuous film of TiO_2 prior to NiO coverage.

Comparing the FE-SEM images of the TiO_2 and NiO/TiO_2 – NRs shown in **Fig 3.24** there are some notable differences in structure between the samples. The image in **Fig 3.24d** shows the NiO/TiO_2 – NRs have clustered and an almost continuous film has formed over the surface. Another difference between the samples is that the NiO-TiO_2 – NRs nanorods in **Fig 3.24e** are longer than TiO_2 – NRs **Fig 3.24b** at roughly 2 µm in length. Few singular NiO/TiO_2 – NRs remain with many clustered into groups of nanorods varying in width from 100-400 nm. **Fig 3.24f** provides an angled view of the NiO/TiO_2 – NRs, some definition of the nanorods remains at the surface as well as some large spatial voids. Overall the NiO looks to have coated the nanorods leaving large spatial voids and maintaining a high surface area. The variation between nanorod samples means no specific comparisons can be drawn between pre-coated and coated nanorods. The NiO PEALD process may sacrifices some of the substrate surface area, but in applications where ultra high surface area is not important the flow $NiCp_2$ process adequately coats the substrate and maintains some definition of surface features. For a more comprehensive assessment of the $NiCp_2$ flow PEALD uniformity on high aspect ratio substrates, a substrate with greater homogeneity is required.

From the FE-SEM and SEM-EDX imaging it is notable that several large clusters which protrude across the TiO_2 – NR surface which can be seen in both **Fig 3.23 (b)** and **(c)**. These defects suggest that the TiO_2-NRs have significant variations in uniformity between samples and make comparing the NiO-coated and uncoated nanorods difficult even with high resolution FE-SEM. However, to effectively assess whether the NiO is an effective addition to the nanorods, photo-electrochemical (PEC) measurements were compared of NiO/TiO_2 – NRs and TiO_2 – NRs.

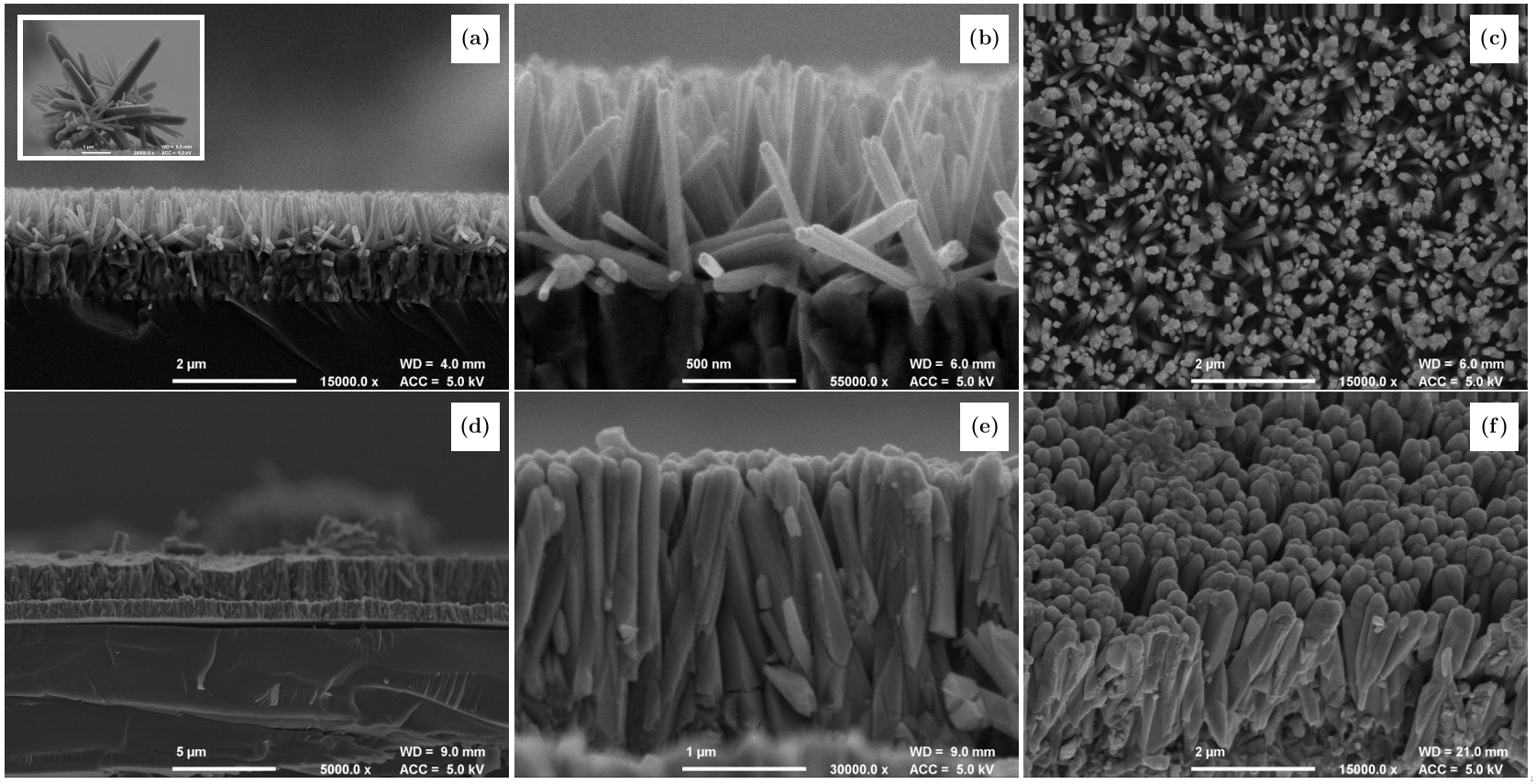

Figure 3.24. *(a-c) FE-SEM images of TiO_2NRs grown onto FTO, (e-f) TiO_2NRs coated with 20 nm of PEALD deposited NiO.*

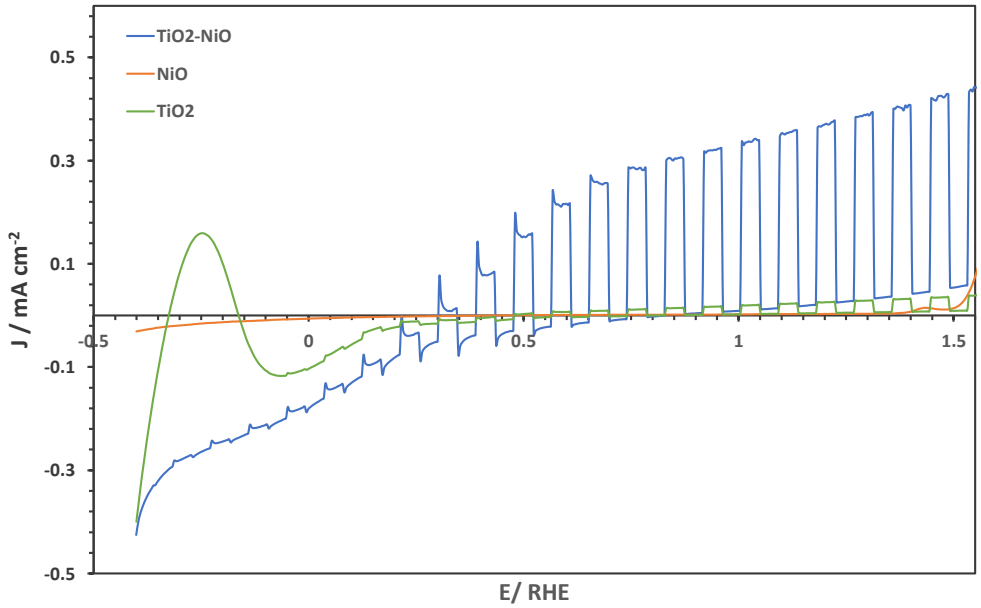

Figure 3.25. *j-V curves measured in 1M KOH (pH=13.6) of pristine TiO_2, pristine NiO and NiO/TiO_2 samples. All measurements were performed under 1 sun chopped illumination (AM 1.5G, 100 mW cm^{-2}) from back-side illumination.*

TiO_2 nanorods with and without NiO coating were tested in a photoelectrochemical cell (PEC) cell to evaluate the effect of NiO loading on the PEC performance. **Fig.3.25** shows j-V curves of TiO_2, NiO and TiO_2–NiO samples measured from back-side illumination. No photocurrent response was detected for the pristine NiO control sample and pristine TiO_2 nanorods exhibited the lowest PEC performance of 0.03 mA cm^{-2} at 1.23 V_{RHE} under simulated solar light. Incorporation of a 20 nm layer of NiO on top of TiO_2 improved the PEC performance by a factor of 12, achieving a value of ca. 0.38 mA cm^{-2} at 1.23 V_{RHE}. In fact, a significant improvement in the PEC performance was achieved in all the potential window range studied. As expected a smaller onset potential was observed in TiO_2–NiO samples in comparison with pristine TiO_2.[51] At low bias (0 to 0.5 V_{RHE}), large anodic photocurrent transients appeared in TiO_2–NiO samples, indicating trapping of photogenerated holes at the electrode-electrolyte interface. This is a common feature also observed in other TiO_2 systems loaded with different co-catalysts.[58, 59] At larger bias, these photocurrent transients disappeared and an efficient charge transfer occurred. The results show that incorporation of a 20 nm layer of NiO on top of TiO_2 is demonstrated to be an effective approach to successfully improve the PEC performance of TiO_2-NRs.

Given that no alterations were made to the $Ni(Cp)_2$ PEALD process to account for the diffusion limitations in 3D substrates nor was the NiO thickness optimised for performance, this short study has shown remarkable success. Future work will focus on adjusting the PEALD deposi-

tion sequence to in order to improve the 3D substrate coverage. By systematically altering the precursor and plasma pulse lengths we aim to compensate for the diffusion limitations of 3D substrates and improve the NiO coverage.[60] Furthermore, in order to improve device photocurrents the thickness of films will be altered and post deposition device annealing as well as O_3/UV treatments will be investigated.[61]

Conclusions

The NiO/TiO_2 study was completed to assess the $NiCp_2$ PEALD deposition uniformity on high aspect ratio substrates. Approximately 20 nm of NiO from 600 $NiCp_2$ PEALD cycles was grown onto solvothermally synthesised TiO_2-NRs. From SEM-EDX and FE-SEM imaging it can be concluded that the TiO_2-NRs were coated uniformly with a layer of NiO which reduced the overall definition of individual nanorods but the samples maintained a relatively high surface area. Furthermore, the NiO/TiO_2 samples were shown to have an improved photoanodic response when stimulated by a one sun lamp after coating with the NiO with a peak current of $0.38\,\mathrm{mA\,cm^{-2}}$ at 1.23 V_{RHE}. In conclusion a NiO PEALD deposition method has been shown to be a suitable for the growth of photoanodic co-catalysts on complex substrate geometries, work on improving the PEALD process for increased photoanodic response, is currently under investigation.

3.3.5 Supercycled PEALD Processes and the growth of Potassium doped NiO

NiO is p-type semiconducting with a bandgap of 3.6-4 eV. The electronic structure of NiO can be modified by the addition of group one monovalent ions including Li^+, Na^+ or K^+. Doping NiO with a group one ion can increase p-type conductivity as for every M^+ to preserve electronic neutrality and oxidise to Ni^{3+}.[62, 63] Ni^{3+} ions can be considered positive holes and are the majority carriers in p-type electronics. Doping with M^+ ions and increasing the concentration of Ni^{3+} increases hole carrier concentration and results in improved conductivity. Shown in **Table 3.6** is a comparison of the electrical properties of the experimentally produced NiO deposited by flow $NiCp_2$ PEALD and group one doped NiO presented in literature. It is evident that the NiO produced by flow $NiCp_2$ PEALD is comparatively resistive, with a 10^4 increase in resistivity compared to both doped and undoped NiO samples presented in literature. The overall electrical performance of the PEALD deposited films is limited and for electronic applications needs improvement.

Dopant	**Growth Method**	**Resistivity $\Omega\,cm^{-1}$**	**Mobility ($cm^3\,V^{-1}\,s$)**	**Carrier Concentration (cm^{-3})**	**Reference**
-	$NiCp_2$ Flow PEALD	$1.31 * 10^4$	0.2	$2.5 * 10^{15}$	-
Li	Pulsed Laser	-	0.05	$6.13 * 10^{22}$	[64]
Li	RF Sputtering	-	0.1-1	$1 * 10^{17}$	[65]
-	e-beam	33.57	6.2	$4.86 * 10^{15}$	[66]
Na	e-beam	11.57	-	$2.85 * 10^{16}$	[66]
K	Sol-Gel	23.7	13	$9 * 10^{16}$	[67]
K	Pulsed Plasma	0.235	0.37	$7.18 * 10^{19}$	[68]

Table 3.6. *Electrical properties of NiO deposited by flow $NiCp_2$ PEALD compared to NiO doped with group one monovalent ions.*

One application of NiO in electronics is as a hole transport layer (HTL) in applications such as solar cells. ALD deposited NiO has an advantage over other deposition CVD deposition methods because ALD films generally have lower roughness, with smoother films possessing fewer grain boundaries which improves charge transfer and increases solar cell efficiency. [36, 69–71] The performance of the NiO HTL can be improved by doping with monovalent group 1 ions, as such an ALD method which can grow doped NiO could have a positive impact in photovoltaics.[72–74] Given the demand for a PEALD method which can produce a doped NiO ALD film, it

was hypothesised that suitable group one precursors could be supercycled with the $NiCp_2$ flow PEALD process to controllably dope the NiO film.

A report by Østreng *et al*, evaluated sodium tert-butoxide (NaO^tBu) and potassium tert-butoxide (KO^tBu) on a Beneq TFS-200. In the study both precursors were supercycled with TMA and water/O_3. [75] The NaO^tBu had a thermal window between 225-375 °C and the KO^tBu a thermal window between 250-300 °C. Both the NaO^tBu and KO^tBu thermal windows lie within that of the flow $NiCp_2$ PEALD process and can be supercycled together. **Fig 3.26** is a schematic of the proposed supercycle procedure. Theoretically, varying the number of NiO cycles "n" to either the NaO^tBu or KO^tBu will control the overall stoichiometric ratio of Ni:Na/K and feasibly dope the NiO controllably by PEALD.

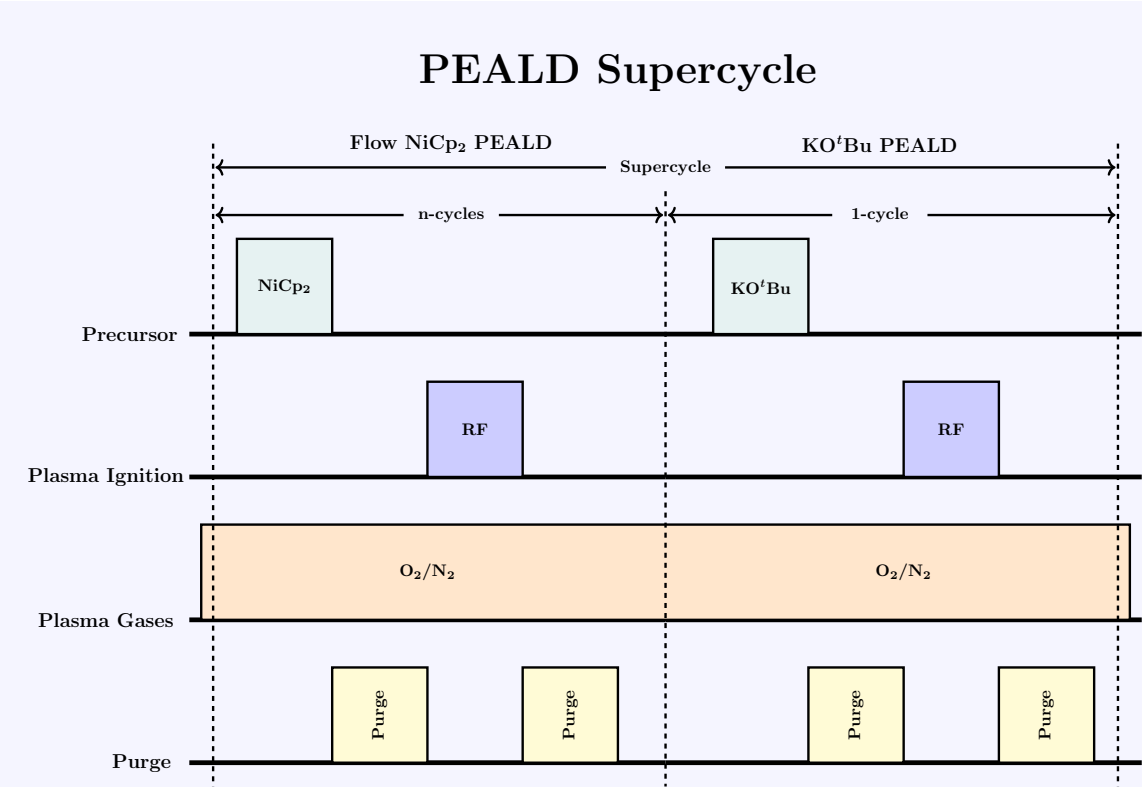

Figure 3.26. *An illustration of the potassium doped NiO supercycle.*

For the PEALD supercycle investigations the KO^tBu was chosen over alternative potassium precursors because the study by Østreng *et al*, was completed on a Beneq TFS-200, the same tool for the NiO PEALD processes. As the KO^tBu was optimised on the same tool as the investigation, no further alterations to the precursor delivery pulses should be necessary for initial investigations. The precursor is also low cost and commercially available. Østreng *et al,* did not investigate O_2 plasma as oxidation source, though it was hypothesised that precursor delivery time and purge times could be kept the same when supercycled and that O_2 plasma would still facilitate film growth.

In total, two experimental depositions where completed. For the first deposition the optimised flow $NiCp_2$ PEALD process was cycled in a 5:1 ratio with the KO^tBu process used by Østreng *et al*, (1 s/5 s/2 s/5 s). The reactor was held at 250 °C, the $NiCp_2$ and KO^tBu held at 60 °C and 170 °C respectively. The O_2 and N_2 plasma gases were continuously flowed into the chamber throughout the process and a plasma power of 100 W was applied. In total 460 supercycles were completed and the samples analysed by PXRD, Raman and SEM-EDX.

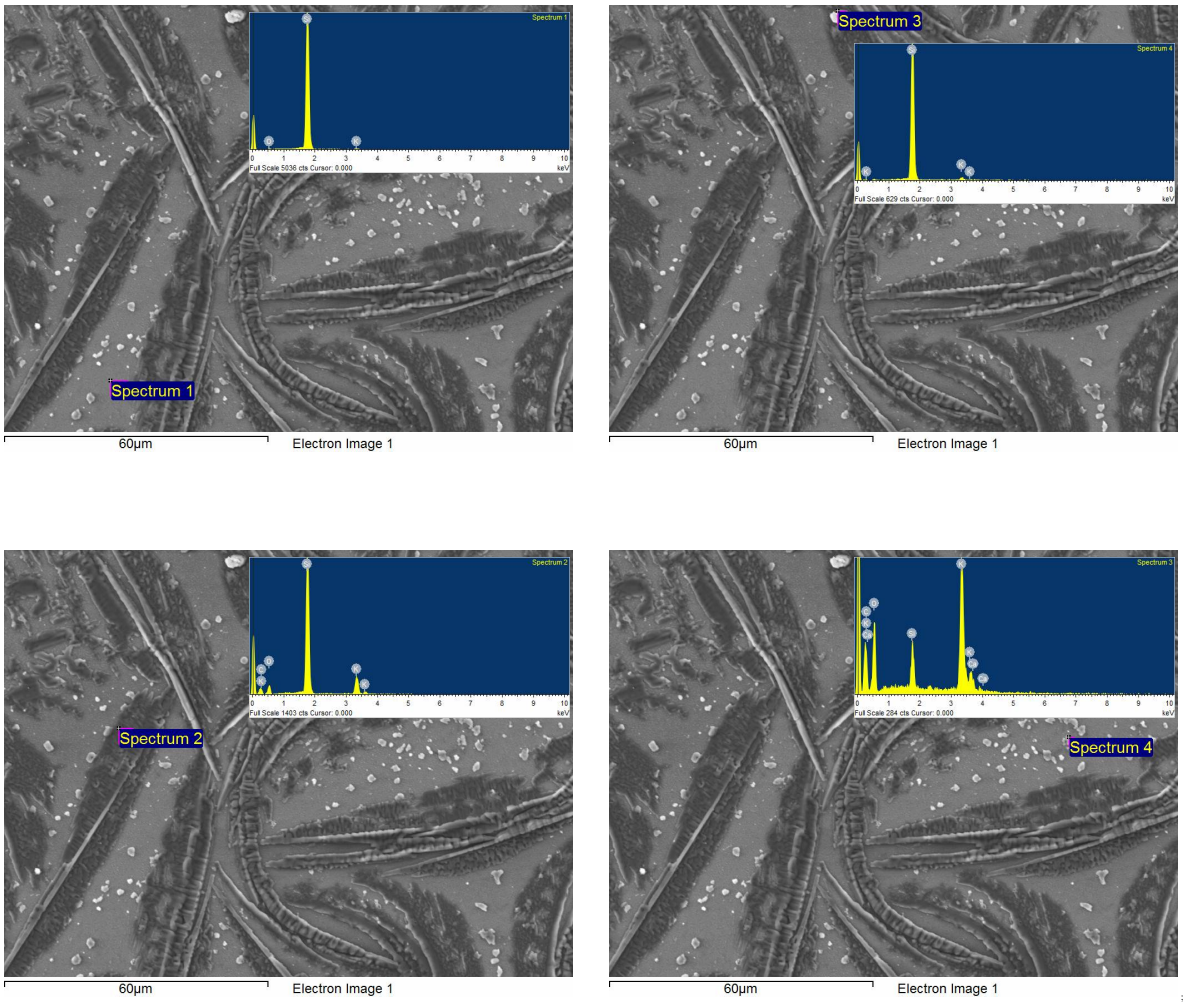

Figure 3.27. *SEM-EDX analysis of a film grown from 460 PEALD supercycles of KO^tBu and $NiCp_2$ in a 1:5 ratio.*

The films produced from the 5:1 ratio Ni:K, at least to the naked eye, looked to be poorly uniform with blistered surfaces. Before removing from the load lock, under vacuum the films appeared non-uniform, with a significant deposition gradient from reactor inlet to outlet. When removed from vacuum, the films rapidly deteriorated and formed small crystallites across the surface, some of these features can be seen in **fig 3.28**. The surface features small crystallites scattered between rough crystalline edges. EDX analysis shows that in **Fig3.27** there is significant potassium and carbon incorporation indicative of the presence of K_2CO_3. Analysis shows that sections of film contain no detectable potassium and in no EDX spectra was nickel observed. Raman

analysis, the results of which are shown in **Fig 3.28**, confirms the presence of K_2CO_3 with the $\nu 1(A\prime 1)$ peaks observable at 1030 cm^{-1} and 1060 cm^{-1}.[76] Furthermore, the XRD measurements in **Fig 3.28** show the films are polycrystalline with many peaks matching with K_2CO_3 and $KHCO_3$. All analysis indicates the film contains K_2CO_3 and $KHCO_3$ which is a likely result of spontaneous reactions between CO_2 and surface KOH observed when the films were exposed to atmosphere.

The first deposition experiment with the Ni:K, 5:1 ratio produced flawed films with no observable nickel content. To improve the process two changes were made for experiment 2. The overall ratio of Ni:K was altered to 20:1 and the plasma gases were flowed for the NiO but pulsed into the chamber for the KO^tBu half cycles. The changes were made to prevent the growth of K_2CO_3 and ensure there was no CVD reaction between the O_2 and KO^tBu. Despite the precautions, the films grown with a 20:1 ratio displayed significant gradients in thickness across each sample. SEM-EDX imaging in **Fig 3.29** shows the films are smoother than those grown in 5:1 ratios (**Fig3.27**), though crystallites are still scattered across the surface. The EDX scans of the crystallites (**Fig3.29**) show that they have significantly higher potassium content than the bulk film, (**Fig3.29**) with only the bulk film having any detectable nickel content.

The samples grown with a PEALD Ni:K ratio of 20:1 were measured by Raman spectroscopy. When viewed with a microscope the films were found to be nonhomogeneous. Sections of the surface resemble a conventional, smooth ALD film. However, scattered randomly across the surface were small crystallites. The two environments on the surface have significantly different Raman spectra. The spectra from the scattered crystallites matches the Raman spectra for $KHCO_3$ and the smoother sections closely match the Raman spectra for NiO, as shown in **Fig 3.30b**.[77] XRD measurements verify the presence of triclinic $KHCO_3$ ordered in the (10-2) plane. It can be concluded that surface exposed KOH facets reacted with atmospheric CO_2 and formed large $KHCO_3$ crystallites. This is consistent with the study by Østreng *et al*, which reported carbonates in films with high potassium content.[75]

No further depositions were completed in this short study as the use of KO^tBu was detrimental to the ALD reactor. Thick black films deposited around the gas distribution channels into the chamber which were attributed to the decomposition of the KO^tBu. From the small sample set investigated in this study it is difficult to gauge the overall success of the investigation. The SEM-EDX analysis confirmed that potassium had been incorporated into the structure of the NiO films when grown with a Ni:K ratio of 20:1. The film uniformity in both depositions was poor, with deposition gradients visible to the naked eye across 1x1 cm samples. In the report by Østreng *et al* it was noted that in the 1:1 Al:K depositions, growth gradients were present with films thickening toward the reactor outlet. This was associated to a hygroscopic film retaining water and provoking uncontrolled growth and it was stated that there was no evidence of thermal decomposition. However, this is not in agreement with the results of the study performed with

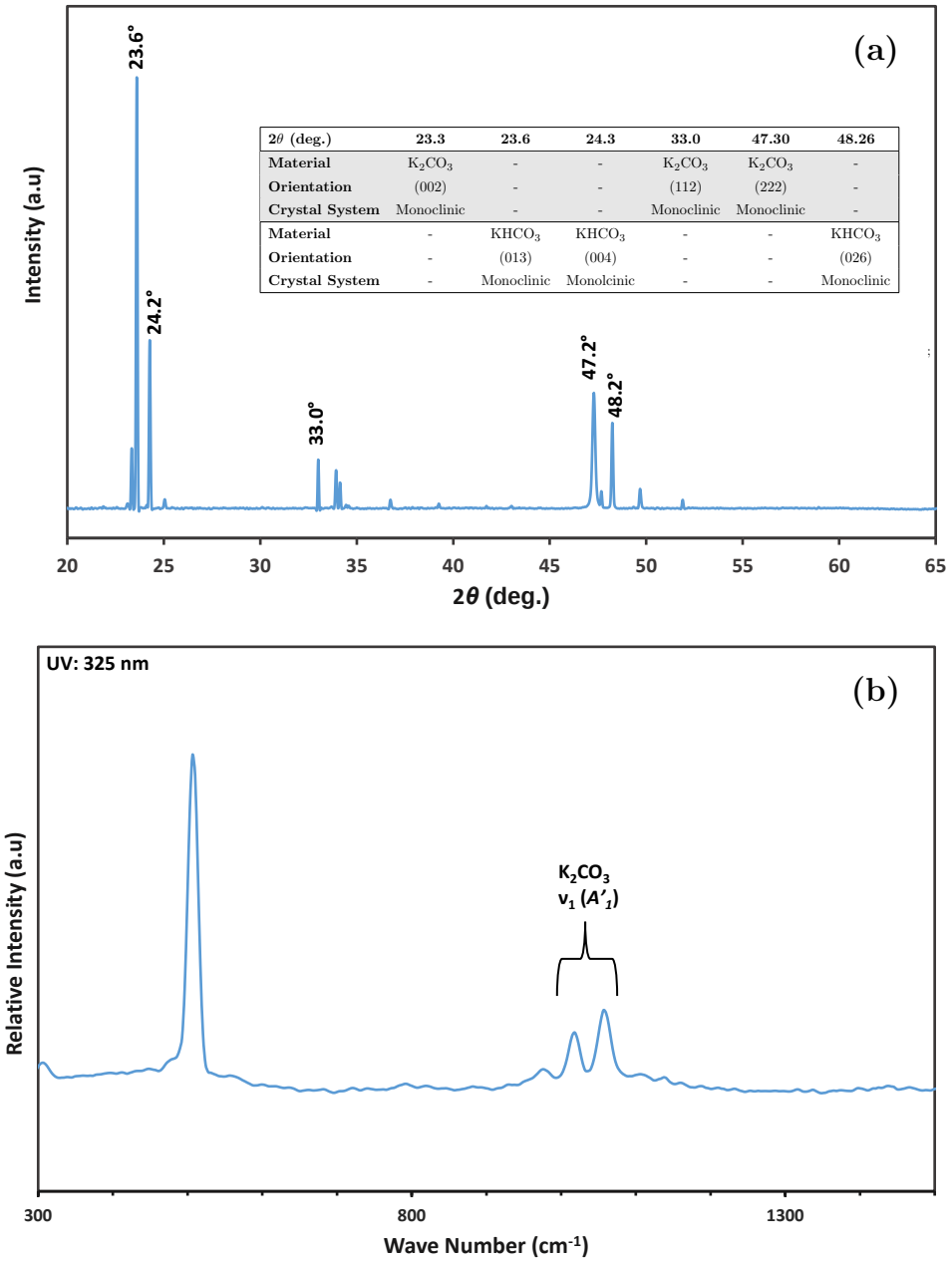

2θ (deg.)	23.3	23.6	24.3	33.0	47.30	48.26
Material	K_2CO_3	-	-	K_2CO_3	K_2CO_3	-
Orientation	(002)	-	-	(112)	(222)	-
Crystal System	Monoclinic	-	-	Monoclinic	Monoclinic	-
Material	-	$KHCO_3$	$KHCO_3$	-	-	$KHCO_3$
Orientation	-	(013)	(004)	-	-	(026)
Crystal System	-	Monoclinic	Monolcinic	-	-	Monoclinic

Figure 3.28. *a) XRD and b) Raman analysis of film grown from 460 PEALD supercycles of KO^{t}Bu and $NiCp_2$ in a 1:5 ratio.*

Ni:K. No water was used in the process and significant precursor decomposition has been noted to occur within the chamber. Therefore the growth gradients and poor film uniformity have been ascribed to the decomposition of the KO^{t}Bu.

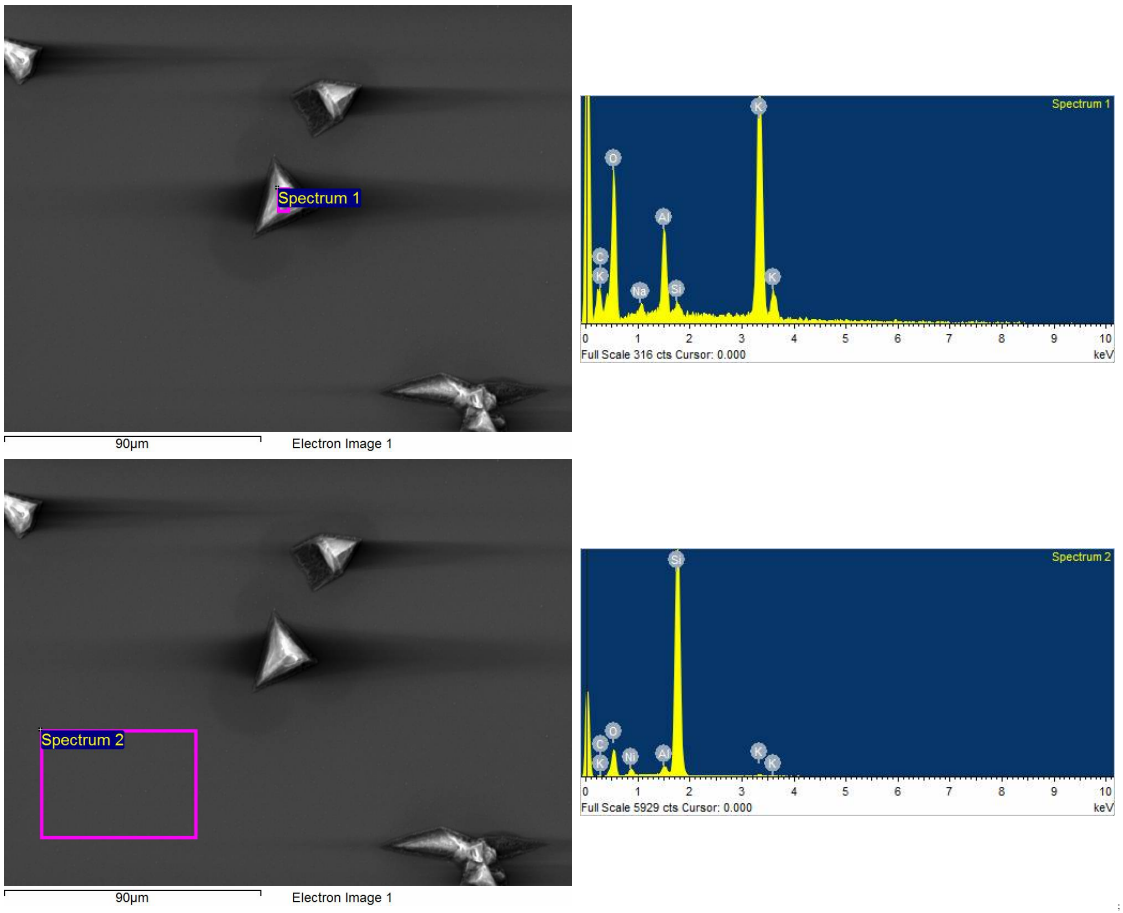

Figure 3.29. *SEM-EDX analysis of a film grown from 460 PEALD supercycles of KO^{t}Bu and NiCp$_2$ in a 1:20 ratio.*

Conclusions

This investigation set out to controllably dope NiO with potassium by supercycling a KO^{t}Bu PEALD cycle within the NiCp$_2$ PEALD process. Reducing the number of KO^{t}Bu PEALD cycles relative to NiCp$_2$ improved the overall film uniformity (Ni:K = 20:1). This is attributed to the lower volume of potassium introduced into the process. Going forward the introduction a capping layer of Al_2O_3 to impede reactions with atmospheric CO_2 may significantly increase film lifetimes. Without a suitable potassium ALD precursor, the study was concluded before a reliable potassium doped NiO process could be developed. To fully develop a satisfactory K-doping process would require an alternative potassium precursor which has been optimised to the same tool as a NiO process. Given the opportunity it would be interesting to investigate the potassium 2-Dimethylamino-2-methylpropanoate (KDMAMP) or Potassium bis(trimethylsilyl)amide (KHMDS) precursors as alternative potassium sources and attempt to incorporate either with the NiCp$_2$ flow PEALD method.

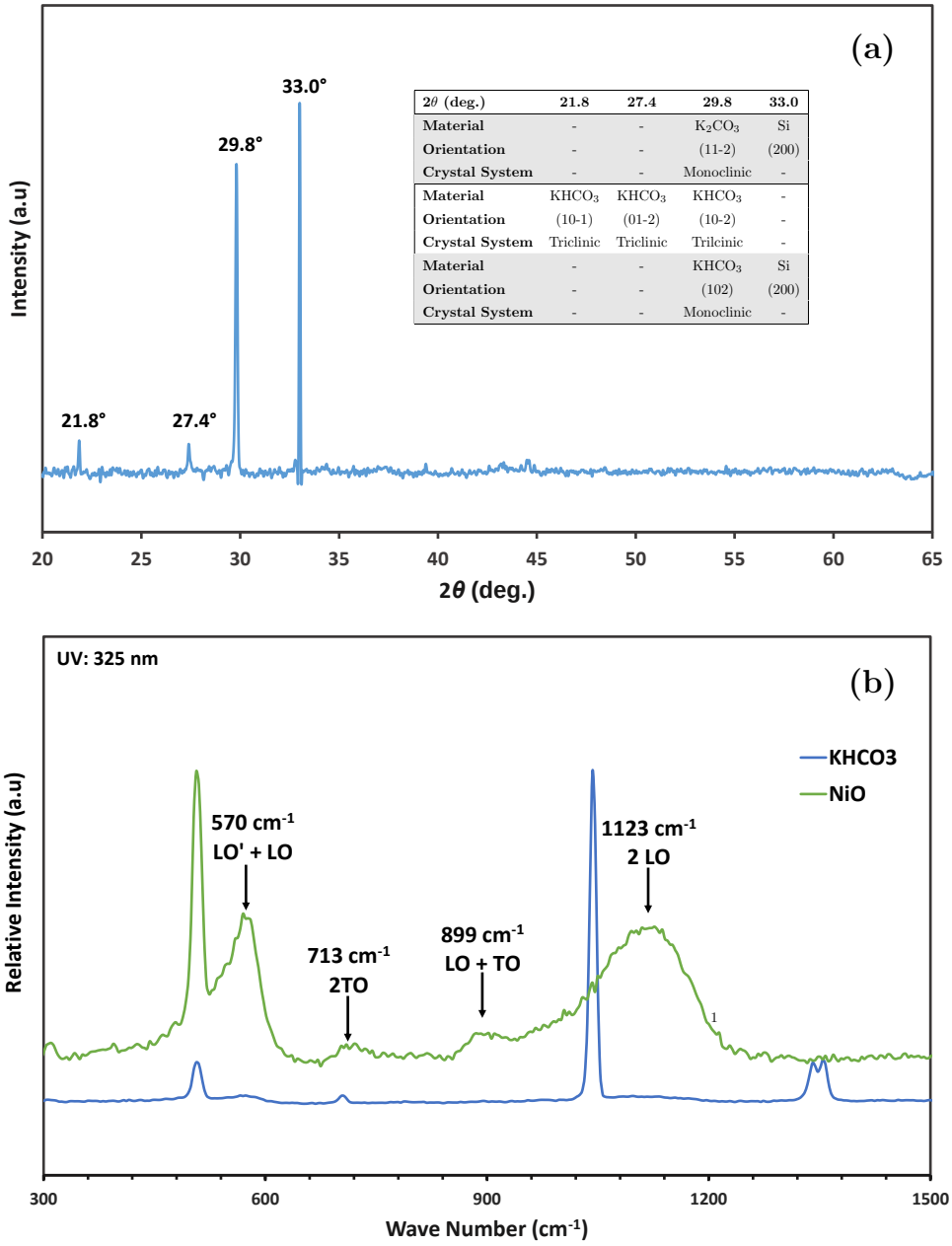

2θ (deg.)	21.8	27.4	29.8	33.0
Material	-	-	K_2CO_3	Si
Orientation	-	-	(11-2)	(200)
Crystal System	-	-	Monoclinic	-
Material	$KHCO_3$	$KHCO_3$	$KHCO_3$	-
Orientation	(10-1)	(01-2)	(10-2)	-
Crystal System	Triclinic	Triclinic	Trilcinic	-
Material	-	-	$KHCO_3$	Si
Orientation	-	-	(102)	(200)
Crystal System	-	-	Monoclinic	-

Figure 3.30. *a) XRD and b) Raman analysis of a film grown from 460 PEALD supercycles of KO^tBu and $NiCp_2$ in a 1:20 ratio.*

3.4 Conclusions

Within this body of work two PEALD methods for the growth of NiO have been developed. Both utilise the precursor $NiCp_2$ and oxygen plasma however the processes differed by the purges gases utilised during deposition. The first "pulsed" process utilised standard N_2 purge cycles with discreet addition of O_2 during plasma ignition step. The second "flow" process utilised N_2/O_2 purges and O_2 remained flowing into the chamber during the addition of $NiCp_2$. It was determined that plasma ignition was necessary to facilitate the growth of NiO and no CVD growth occurred between O_2 purge gas and $NiCp_2$.

Both the flow and pulsed methods produced NiO with densities of $6\,\mathrm{g\,cm^{-3}}$, as determined by XRR, which is just under that of bulk NiO ($6.68\,\mathrm{g\,cm^{-3}}$). Furthermore, each process produced cubic NiO aligned in the (200) plane with Raman estimating they have a similar Ni:O ratio of 0.7. Given the overlap of the process thermal windows as well as structural and optical similarities the flow and pulsed process have been concluded as equivalent.

Given the insulating behaviour of NiO films, attempts were made to alter the overall stoichiometry of the NiO with the addition of a reductive NH_3 plasma step. XPS analysis determined that regardless of the ratio of NH_3:O_2 plasmas the stoichiometry remained unaffected. The 1:1 NH_3:O_2 process did however alter the crystallinity with an increased alignment in the cubic (111) plane.

The flow $NiCp_2$ PEALD method was used to grow a thin NiO film onto TiO_2-NRs to assess whether the high surface area could be maintained. Both TiO_2-NRs and NiO coated TiO_2-NRS were imaged with FE-SEM and it was found that a continuous film of NiO was deposited over clusters of the nanorods but spatial voids remained. Overall it appears the surface area of the TiO_2-NRs was significantly reduced but due to batch to batch variation of the nanorods it is impossible to accurately compare coated and uncoated systems. Generally the 3D nature of the material was maintained and when the photocatalytic activity of the materials was tested the NiO was shown to increase photocatalytic current. The flow $NiCp_2$ is therefore suitable for growing co-catalytic NiO onto complex 3D TiO_2-NRs, though the method was never fully optimised and feasibly much thinner layers which better conserve 3D geometries may be as effective.

Finally, attempts were made to improve the overall conductivity of the flow $NiCp_2$ PEALD NiO by potassium doping. KO^tBu was utilised as a potassium precursor in PEALD supercycles which altered the ratio of Ni:K. Depositions were completed in ratios of 5:1 and 20:1, in both instances poorly uniform films were produced which rapidly reacted with atmospheric CO_2 to form potassium carbonates. The KO^tBu precursor was found to decompose before entering the reaction chamber and was deemed unsuitable as a potassium precursor for the desired process. No further attempts were made to introduce potassium with supercycles, though alternative potassium precursors and the application of an Al_2O_3 capping layer could yet yield a method

whereby $NiCp_2$ PEALD supercycles can be controllably doped with potassium.

The $NiCp_2$ PEALD methods discussed in this chapter are the best method for growing NiO by PEALD/ALD investigated in this body of work. The flow $NiCp_2$ method reliably produces uniform, crystalline NiO and it has proven to be versatile by growing NiO onto a diverse array of substrates. Importantly, it makes use of a cheap, commercially available precursor and the short cycle times mean that thin NiO films can be grown with short processing times. As the method has been developed on a commercially available PEALD reactor the method should be highly reproducible may improve the quality of research utilising PEALD deposited NiO.

[1] J. B. P. Soares and A. E. Hamielec, *Polym. React. Eng.*, 1995, **3**, 131–200.

[2] A. L. Johnson and J. D. Parish, in *ACS Symp. Ser.*, American Chemical Society, 2018, vol. 1311, pp. 1–53.

[3] A. Pereira, J. L. Palma, J. C. Denardin and J. Escrig, *Nanotechnology*, 2016, **27**, 345709.

[4] Y. Koshtyal, D. Nazarov, I. Ezhov, I. Mitrofanov, A. Kim, A. Rymyantsev, O. Lyutakov, A. Popovich and M. Maximov, *Coatings*, 2019, **9**, 301.

[5] H. L. Lu, G. Scarel, C. Wiemer, M. Perego, S. Spiga, M. Fanciulli and G. Pavia, *J. Electrochem. Soc.*, 2008, **155**, H807.

[6] L. Brissonneau, A. Reynes and C. Vahlas, *Chem. Vap. Depos.*, 1999, **5**, 281–290.

[7] H. L. Lu, G. Scarel, C. Wiemer, M. Perego, S. Spiga, M. Fanciulli and G. Pavia, *J. Electrochem. Soc.*, 2008, **155**, H807–H811.

[8] G. Wang, Z. Gao, G. Wan, S. Lin, P. Yang and Y. Qin, *Nano Res.*, 2014, **7**, 704–716.

[9] Z. Gao, M. Dong, G. Wang, P. Sheng, Z. Wu, H. Yang, B. Zhang, G. Wang, J. Wang and Y. Qin, *Angew. Chemie Int. Ed.*, 2015, **54**, 9006–9010.

[10] D. Alburquenque, M. Del Canto, C. Arenas, F. Tejo, A. Pereira and J. Escrig, *Thin Solid Films*, 2017, **638**, 114–118.

[11] R. Zhang, H. Wei, W. Si, G. Ou, C. Zhao, M. Song, C. Zhang and H. Wu, *Materials (Basel).*, 2016, **10**, 15.

[12] J. Zhang, C. Chen, W. Yan, F. Duan, B. Zhang, Z. Gao and Y. Qin, *Catal. Sci. Technol.*, 2016, **6**, 2112–2119.

[13] A. Lamperti, S. Spiga, H. L. Lu, C. Wiemer, M. Perego, E. Cianci, M. Alia and M. Fanciulli, *Microelectron. Eng.*, 2008, **85**, 2425–2429.

[14] L. Yu, G. G. G. Wang, G. Wan, G. G. G. Wang, S. Lin, X. Li, K. Wang, Z. Bai and Y. Xiang, *Dalt. Trans.*, 2016, **45**, 13779–13786.

[15] M. Daub, M. Knez, U. Goesele and K. Nielsch, *J. Appl. Phys.*, 2007, **101**, 09J111.

[16] X. Xu, G. Wang, G. Wan, S. Shi, C. Hao, Y. Tang and G. Wang, *Chem. Eng. J.*, 2020, **382**, 122980.

[17] J. G. Baker, J. R. Schneider, J. A. Garrido Torres, J. A. Singh, A. J. M. Mackus, M. Bajdich and S. F. Bent, *ACS Appl. Energy Mater.*, 2019, **2**, 3488–3499.

[18] L. Yu, G. Wan, Y. Qin and G. Wang, *Electrochim. Acta*, 2018, **268**, 283–294.

[19] Y. Fan, Y. Wu, G. Clavel, M. H. Raza, P. Amsalem, N. Koch and N. Pinna, *ACS Appl. Energy Mater.*, 2018, **1**, 4554–4563.

[20] K. L. Nardi, N. Yang, C. F. Dickens, A. L. Strickler and S. F. Bent, *Adv. Energy Mater.*, 2015, **5**, 1500412–n/a.

[21] C. Ros, T. Andreu, J. David, J. Arbiol and J. R. Morante, *J. Mater. Chem. A*, 2019, **7**, 21892–21902.

[22] J. Bachmann, A. Zolotaryov, O. Albrecht, S. Goetze, A. Berger, D. Hesse, D. Novikov and K. Nielsch, *Chem. Vap. Depos.*, 2011, **17**, 177–+.

[23] M. H. Raza, K. Movlaee, S. G. Leonardi, N. Barsan, G. Neri and N. Pinna, *Adv. Funct. Mater.*, 2019, 1906874.

[24] M. H. Raza, K. Movlaee, Y. Wu, S. M. El-Refaei, M. Karg, S. G. Leonardi, G. Neri and N. Pinna, *ChemElectroChem*, 2019, **6**, 383–392.

[25] G. Wang, X. Peng, L. Yu, G. Wan, S. Lin and Y. Qin, *J. Mater. Chem. A*, 2015, **3**, 2734–2740.

[26] S. J. Song, S. W. Lee, G. H. Kim, J. Y. Seok, K. J. Yoon, J. H. Yoon, C. S. Hwang, J. Gatineau and C. Ko, *Chem. Mater.*, 2012, **24**, 4675–4685.

[27] H. L. Lu, G. Scarel, X. L. Li and M. Fanciulli, *J. Cryst. Growth*, 2008, **310**, 5464–5468.

[28] M. K. S. Barr, L. Assaud, Y. Wu, C. Laffon, P. Parent, J. Bachmann and L. Santinacci, *Electrochim. Acta*, 2015, **179**, 504–511.

[29] M. Stoyanova, P. Konova, P. Nikolov, A. Naydenov, S. Christoskova and D. Mehandjiev, *Chem. Eng. J.*, 2006, **122**, 41–46.

[30] M. Utriainen, M. Kröger-Laukkanen and L. Niinistö, *Mater. Sci. Eng. B*, 1998, **54**, 98–103.

[31] K. E. K. Holden, C. L. Dezelah and J. F. Conley, *ACS Appl. Mater. Interfaces*, 2019, **11**, 30437–30445.

[32] P. A. Premkumar, M. Toeller, C. Adelmann, J. Meersschaut, A. Franquet, O. Richard, H. Tielens, B. Brijs, A. Moussa, T. Conard, H. Bender, M. Schaekers, J. Kittl, M. Jurczak and S. Van Elshocht, *Chem. Vap. Depos.*, 2012, **18**, 61–69.

[33] Y. Zhang, L. Du, X. Liu and Y. Ding, *Appl. Surf. Sci.*, 2019, **481**, 138–143.

[34] H. C. M. Knoops, E. Langereis, M. C. M. van de Sanden and W. M. M. Kessels, *J. Electrochem. Soc.*, 2010, **157**, G241.

[35] A. G. Hufnagel, A. K. Henß, R. Hoffmann, O. E. O. Zeman, S. Häringer, D. Fattakhova-Rohlfing and T. Bein, *Adv. Mater. Interfaces*, 2018, **5**, 1701531.

[36] D. Koushik, M. Jošt, A. Dučinskas, C. Burgess, V. Zardetto, C. Weijtens, M. A. Verheijen, W. M. M. Kessels, S. Albrecht and M. Creatore, *J. Mater. Chem. C*, 2019, **7**, 12532–12543.

[37] S. Ji, W. Jang, J. Son and D. Kim, *Korean J. Chem. Eng*, 2018, **35**, 2474–2479.

[38] M. Napari, T. N. Huq, T. Maity, D. Gomersall, K. M. Niang, A. Barthel, J. E. Thompson, S. Kinnunen, K. Arstila, T. Sajavaara, R. L. Z. Hoye, A. J. Flewitt and J. L. MacManus-Driscoll, *InfoMat*, 2020, inf2.12076.

[39] J. Chae, H. Park and S. Kang, *Electrochem. Solid-State Lett.*, 2002, **5**, C64–C66.

[40] Y. Wang, Z. Ding, Q. Liu, W. Liu, S. Ding and D. W. Zhang, *J. Mater. Chem. C*, 2016, **4**, 11059–11066.

[41] P. Motamedi, K. Bosnick, K. Cui, K. Cadien and J. D. Hogan, *ACS Appl. Mater. Interfaces*, 2017, **9**, 24722–24730.

[42] N. Mironova-Ulmane, A. Kuzmin, I. Steins, J. Grabis, I. Sildos and M. Pärs, *J. Phys. Conf. Ser.*, 2007, **93**, 012039.

[43] R. E. Dietz, G. I. Parisot and A. E. Meixner, *Phys. Rev. B*, 1971, **4**, 2302–2310.

[44] D. Lockwood, M. Cottam and J. Baskey, *J. Magn. Magn. Mater.*, 1992, **104-107**, 1053–1054.

[45] M. Gao, L. Zhu, W. Ong, J. Wang and G. W. Ho, *Catal. Sci. Technol.*, 2015, **5**, 4703–4726.

[46] R. Li, Y. Weng, X. Zhou, X. Wang, Y. Mi, R. Chong, H. Han and C. Li, *Energy Environ. Sci.*, 2015, **8**, 2377–2382.

[47] A. Naldoni, M. Altomare, G. Zoppellaro, N. Liu, S. Kment, R. Zbořil and P. Schmuki, *ACS Catal.*, 2019, **9**, 345–364.

[48] J. Schneider, M. Matsuoka, M. Takeuchi, J. Zhang, Y. Horiuchi, M. Anpo and D. W. Bahnemann, *Chem. Rev.*, 2014, **114**, 9919–9986.

[49] S. G. Kumar and L. G. Devi, *J. Phys. Chem. A*, 2011, **115**, 13211–13241.

[50] C. Chen, C. Liao, K. Hsu, Y. Wu and J. C. Wu, *Catal. Commun.*, 2011, **12**, 1307–1310.

[51] M. A. Rasheed, R. Rahimullah, S. K. Uddin, N. Khaliq, Y. Khan, A. Waheed, A. Shah, A. Mahmood and G. Ali, *Appl. Nanosci.*, 2019, **9**, 1731–1742.

[52] J. Liu, Y. Li, J. Ke, S. Wang, L. Wang and H. Xiao, *Appl. Catal. B Environ.*, 2018, **224**, 705–714.

[53] M. Wang, Y. Hu, J. Han, R. Guo, H. Xiong and Y. Yin, *J. Mater. Chem. A*, 2015, **3**, 20727–20735.

[54] J. Chen, T. Chen, L. Lai, P. Li, H. Liu, Y. Hong and D. Liu, *Materials (Basel).*, 2015, **8**, 4273–4286.

[55] Q. E. Zhao, W. Wen, Y. Xia and J. M. Wu, *Thin Solid Films*, 2018, **648**, 103–107.

[56] G. Zhang, X. Zhang, H. Huang, J. Wang, Q. Li, L. Chen and Q. Wang, *Adv. Mater.*, 2016, **28**, 4811–4816.

[57] J. Zhang, Q. Xu, M. Li, Z. Feng and C. Li, *J. Phys. Chem. C*, 2009, **113**, 1698–1704.

[58] G. Ai, R. Mo, H. Li and J. Zhong, *Nanoscale*, 2015, **7**, 6722–6728.

[59] M. Regue, K. Armstrong, D. Walsh, E. Richards, A. L. Johnson and S. Eslava, *Sustain. Energy Fuels*, 2018, **2**, 2674–2686.

[60] V. Cremers, R. L. Puurunen and J. Dendooven, *Conformality in atomic layer deposition: Current status overview of analysis and modelling*, 2019.

[61] R. Islam, G. Chen, P. Ramesh, J. Suh, N. Fuchigami, D. Lee, K. A. Littau, K. Weiner, R. T. Collins and K. C. Saraswat, *ACS Appl. Mater. Interfaces*, 2017, **9**, 17201–17207.

[62] B. H. Brandow, *Adv. Phys.*, 1977, **26**, 651–808.

[63] S. Hüfner, *Adv. Phys.*, 1994, **43**, 183–356.

[64] J. Y. Zhang, W. W. Li, R. L. Z. Hoye, J. L. MacManus-Driscoll, M. Budde, O. Bierwagen, L. Wang, Y. Du, M. J. Wahila, L. F. J. Piper, T.-L. Lee, H. J. Edwards, V. R. Dhanak and K. H. L. Zhang, *J. Mater. Chem. C*, 2018, **6**, 2275–2282.

[65] S. Mutsumi, N. Hiroshi, S. Gaku, Y. Aika and F. C. Shigefusa, *Jpn. J. Appl. Phys.*, 2016, **55**, 88003.

[66] Y. R. Denny, K. Lee, C. Park, S. Kun Oh, H. J. Kang, D. Yang and S. Seo, *Thin Solid Films*, 2015, **591**, 255–260.

[67] N. Wang, C. Q. Liu, C. Q. L. B. Wen, H. L. Wang, S. M. Liu, W. W. Jiang, W. Y. Ding and W. P. Chai, *Thin Solid Films*, 2016, **616**, 587–593.

[68] M. Yang, H. Pu, Q. Zhou and Q. Zhang, *Thin Solid Films*, 2012, **520**, 5884–5888.

[69] C. Hsu, H. Su, C. Hou, J. Shyue and F. Tsai, *Nanotechnology*, 2015, **26**, 385201.

[70] S. Seo, I. J. Park, M. Kim, S. Lee, C. Bae, H. S. Jung, N. Park, J. Y. Kim and H. Shin, *Nanoscale*, 2016, **8**, 11403–11412.

[71] W. J. Nam, Z. Gray, J. Stayancho, V. Plotnikov, D. Kwon, S. Waggoner, D. V. Shenai-Khatkhate, M. Pickering, T. Okano, A. Compaan and S. J. Fonash, *ECS Trans.*, 2015, **66**, 275–279.

[72] V. Zardetto, B. L. Williams, A. Perrotta, F. Di Giacomo, M. A. Verheijen, R. Andriessen, W. M. M. Kessels, M. Creatore, F. D. Giacomo, M. A. Verheijen, R. Andriessen, W. M. M. Kessels and M. Creatore, *Sustain. Energy Fuels*, 2017, **1**, 30–55.

[73] Z. Qiu, H. Gong, G. Zheng, S. Yuan, H. Zhang, X. Zhu, H. Zhou and B. Cao, *J. Mater. Chem. C*, 2017, **5**, 7084–7094.

[74] P. Chen and S. Yang, *ACS Appl. Energy Mater.*, 2019, **2**, 6705–6713.

[75] E. Østreng, H. H. Sønsteby, S. Øien, O. Nilsen and H. Fjellvåg, *Dalt. Trans.*, 2014, **43**, 16666.

[76] W. W. Rudolph, G. Irmer and E. Konigsberger, *Dalt. Trans.*, 2008, 900–908.

[77] D. Fischer, G. Irmer and W. W. Rudolph, *Appl. Spectrosc.*, 2006, **60**, 130–144.

Chapter 4

PEALD of Fe_2O_3 and $NiFe_2O_4$

Contents

4.1 Abstract

Nickel ferrite ($Ni_xFe_{2-x}O_4$) is a ferrimagnetic, magnetic insulator with potential application in magnetic data storage and magneto-optics. Given that by varying the relative ratio of Ni:Fe the magnetic and optical properties may be altered, ALD is an ideal tool for the controlled growth and adjustment of nickel ferrite films. However, to date only one nickel ferrite ALD process has been developed. To that end, a new Fe_2O_3 PEALD process utilsing $Fe(MeCp)_2$ was developed and optimised for film growth at 250 °C. The $Fe(MeCp)_2$ PEALD process was supercycled with a $NiCp_2$ PEALD process with Ni:fe ratios of 2:1, 1:1, 1:2 and 1:5 to ascertain whether by altering the Ni:Fe supercycle ratio the film stoichiometry could be controlled. It was determined that a Ni:Fe ratio of 1:5 was optimal for the growth of spinel phase nickel ferrite and the process represents the first PEALD process for the growth of nickel ferrite.

4.2 Introduction

4.2.1 Precursors for the growth of Fe_2O_3

Hematite (Fe_2O_3), like NiO is a p-type semiconductor that is utilised in applications that lend themselves to ALD such as photocatalysis and supercapacitors.[1, 2] Similar to NiO, the ALD of Fe_2O_3 has only a few fundamental processes published to date, many of which utilise the iron metallocenes; ferrocene ($FeCp_2$) and tert-butylferrocene (Fe(^{t}BuCp)Cp).[3–8] From the summary of Fe_2O_3 ALD in **Table 4.1** it is evident that only a few iron precursors have been investigated and that ferrocene has been the focus of many studies. However, ferrocene is limited by its chemical stability and low volatility as evidenced by the fact that no film growth is reported below 200 °C. The reports utilising non-metallocenes can grow films at less than 200 °C but are restricted by narrow thermal windows because the precursors have limited thermal stability.[9–12]

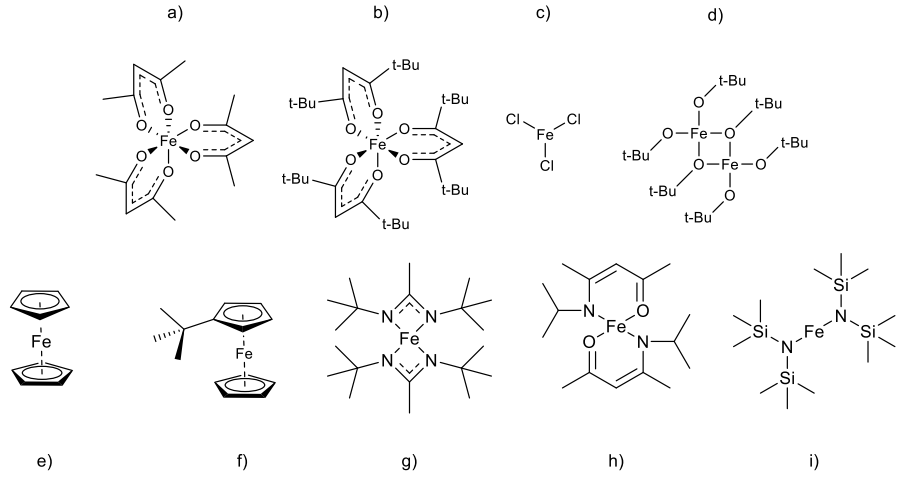

Figure 4.1. *Fe_2O_3 ALD precursors a) Fe(acac)$_3$ b) Fe(THD)$_3$ c) $FeCl_3$ d) Fe(^{t}BuO)$_3$ e) $FeCp_2$ f) Fe(^{t}BuCp)Cp g) Fe(AMD)$_2$ h) Fe(^{i}PrNacAc)$_2$ i) Fe(HMDS)$_2$.*

Iron oxide ALD is limited by slow reaction rates and high deposition temperatures. It is therefore surprising that only one PEALD process has been reported, given that in general PEALD enables low temperature deposition due to the highly reactive radicals present in O_2 plasma.[4] The PEALD process reported by Ramachandran *et al*, had a significant thermal dependency with the growth rate increasing from 0.02-0.12 nm/cycle as the temperature increased 150-350 °C. Though the growth rate varied significantly, it was reported as saturation limited between 150-350 °C and is one of the largest thermal windows for the growth of Fe_2O_3. The deposition at 350 °C cannot be repeated on an o-ring sealed PEALD chamber such as the Beneq TFS-200, as the o-ring is generally made of a thermally sensitive plastic and if it were to melt the chamber vacuum would be compromised. However, similar to the NiO processes discussed in chapter 3, new processes with other iron metallocenes should be possible, which may offer fast growth below

350 °C.

Iron Precursor	Oxygen Source	Deposition Temperature (°C)	Growth Rate (nm/cycle)	Reference
$Fe(acac)_3$	O_2	RT-150	-	[13]
	O_3	230	-	[14]
$Fe(THD)_3$	O_3	186 °C	0.011	[15]
	O_3	186	0.011	[16]
	O_3	160-210	0.011	[17]
	O_3	200	-	[18]
	$O^\bullet$	190-230	0.049	[7]
$FeCl_3$	H_2O	210-360	0.06-0.07	[19]
$Fe(^tBuO)_3$	H_2O	140	0.025	[9]
	H_2O	130-170	0.026	[20]
$Fe(Cp)_2$	O_3	300	0.05	[2]
	O_3	200	0.14	[21]
	O_3	200	0.02	[9]
	O_3	200-350	0.05	[22]
	O_2	350-500	0.14	[23]
	O_2	400	0.016	[24]
	O_2	300	-	[25]
	O_2	400, 500	0.06, 0.16	[26]
	O_2	367-534	0.015	[6]
$Fe(^tBuCp)Cp$	O_2	250	0.045-0.070	[27]
	O_2 Plasma	150-350	0.02-0.12	[4]
$Fe(AMD)_2$	H_2O	150-200	0.055	[11]
$Fe(^iprNacAc)_2$	H_2O	105-150	0.047	[10]
$Fe(HMDS)_2$	H_2O_2	150	0.035	[12]

Table 4.1. *Summary of the growth rate and thermal window of Fe_2O_3 ALD processes.*

Similar to the nickel metallocenes, altering any alkyl-substituents on the $\{C_5H_5\}$ ring alters the volatility of the iron metallocenes. **Table 4.2** compares the cost (STREM chemical) and thermal transition temperatures of ferrocene, 1,1'-dimethylferrocene ($Fe(MeCp)_2$), ethyl ferrocene (Fe(EtCp)Cp) and tert-butylferrocene ($Fe(^tBuCp)Cp$), all of which are commercially available CVD/ALD precursors. From this comparison $Fe(MeCp)_2$ was identified as a potential new precursor for Fe_2O_3 PEALD as at 70 °C vapour pressure should be suitable for precursor carry-over and it is a cost effective alternative to $Fe(^tBuCp)Cp$. Furthermore, given that literature is scarce concerning the CVD/ALD of $Fe(MeCp)_2$ any new deposition processes could be a positive

addition to current ALD literature.[28]

	$FeCp_2$	$Fe(MeCp)_2$	Fe(EtCp)Cp	$Fe(^tBuCp)Cp$
Cost (g^{-1})	£0.37	£14	£15	£46
Boiling Point	249 °C	70-80 °C	364 °C	80 °C

Table 4.2. *Comparison of the cost and relative volatility of iron metallocenes. Relative price taken from current STREM precursor chemical catalogue.*

There were two aims when developing the Fe_2O_3 PEALD process, the first was to expand the literature of Fe_2O_3 ALD and the second was to ensure we had Fe_2O_3 processes PEALD optimised to the BENEQ TFS-200 tool. The intention being to supercycle the new Fe_2O_3 PEALD process with the $NiCp_2$ PEALD processes discussed in chapter 3, to grow nickel ferrite ($Ni_xFe_{3-x}O_4$). Similar to NiO, nickel ferrite can inhibit electron hole recombination and can and significantly enhance photovoltaic efficiency.[29, 30] Furthermore, nickel ferrite has a spinel structure which results in anti-parallel alignment of the local magnetic moments resulting in a net charge of zero. Ferrimagnetic materials such as nickel and cobalt ferrite are magnetic insulators and have potential application in spintronics, magnetic data storage and magneto-optics.[31–34]

A publication by Bratvold *et al* reported the growth of $Ni_xFe_{3-x}O_4$ using $Ni(acac)_2$ and $Fe(Cp)_2$ with O_3 as the oxidant.[35] It was reported that the relative stoichiometry of the film could be altered by varying the ratio of Ni:Fe supercycles and PXRD indicated that depending on the choice of substrate, the overall crystal orientation could be varied as shown by the presence of reflections associated with the (100), (110), and (111) $NiFe_2O_4$ mirror planes.[35] The process is restricted by the ferrocene precursor, which as discussed previously, cannot effectively deposited Fe_2O_3 below 200 °C. Therefore developing an alternative method which utilises another Fe_2O_3 precursor may allow ALD nickel ferrite fabrication at temperatures lower than 200 °C.

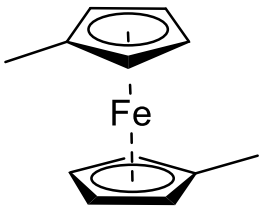

Figure 4.2. *$Fe(MeCp)_2$*

Having identified $Fe(MeCp)_2$ as a potential Fe_2O_3 ALD precursor an investigation was performed utilising the compound in a series of PEALD depositions and a new PEALD method for the growth of Fe_2O_3 was optimised. Films were analysed by ellipsometry, PXRD, GIXRD and XPS and the thermal deposition window investigated. The Fe_2O_3 PEALD process was then

supercycled in a series of depositions with the flow NiO process from chapter 3 and a series of deposition experiments performed whereby the ratio of Ni:Fe cycles was varied to determine whether the $Ni_xFe_{3-x}O_4$ stoichiometry could be controlled.

4.3 Results and Discussion

4.3.1 PEALD of Fe_2O_3

The α-Fe_2O_3 PEALD investigations focused on ensuring a new process could be supercycled with the flow NiO PEALD processes discussed in chapter 3. To ensure the α-Fe_2O_3 process could be combined, the initial investigation utilised the flow set up whereby plasma gases (O_2/N_2) are continuously flowed into the chamber between half-cycles and deposition is initiated by plasma ignition, as illustrated in **Fig 4.3**.

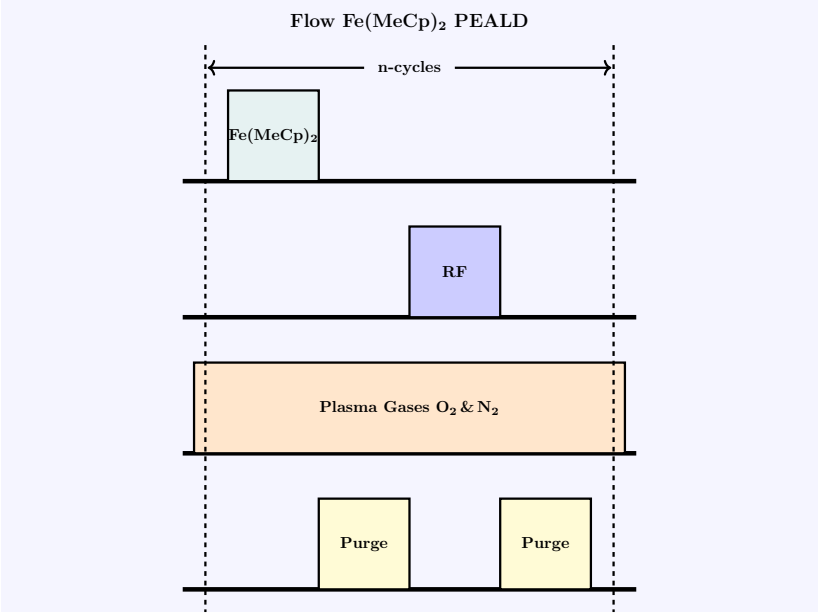

Figure 4.3. *Illustration of the flow PEALD process utilised in the Fe_2O_3 PEALD investigations*

To confirm that α-Fe_2O_3 film growth is plasma initiated, the initial depositions utilised the same precursor delivery steps, however in a control experiment no plasma ignition was completed. For the two depositions the $Fe(MeCp)_2$ was held at 40 °C and the reaction chamber heated to 250 °C. The full PEALD cycle consisted of a 5 s $Fe(MeCp)_2$ pulse followed by a 5 s N_2 purge and a 3 s O_2 plasma exposure ignited with a 100 W RF pulse, followed by a 5 s N_2 purge (5 s/5 s/3 s/5 s). In 300 PEALD cycles a film with an average thickness of 13.20 nm, with no measurable crystallinity, was grown onto SiO_2 substrates. Following the second control experiment, after 300 cycles without plasma ignition no film growth was measurable by ellipsometry. The samples were visually unaffected by the deposition process which confirmed at 250 °C plasma ignition is required to facilitate film growth.

Having confirmed the Fe_2O_3 PEALD process was plasma dependent at 250 °C the process was iteratively altered to ensure that saturated growth had been achieved and the growth rate maximised. Shown in **Fig 4.4** are the optimisation experiments for the $Fe(MeCp)_2$ PEALD process. Optimisation started with the $Fe(MeCP)_2$ delivery pulse, shown in **Fig 4.4a** are the saturation

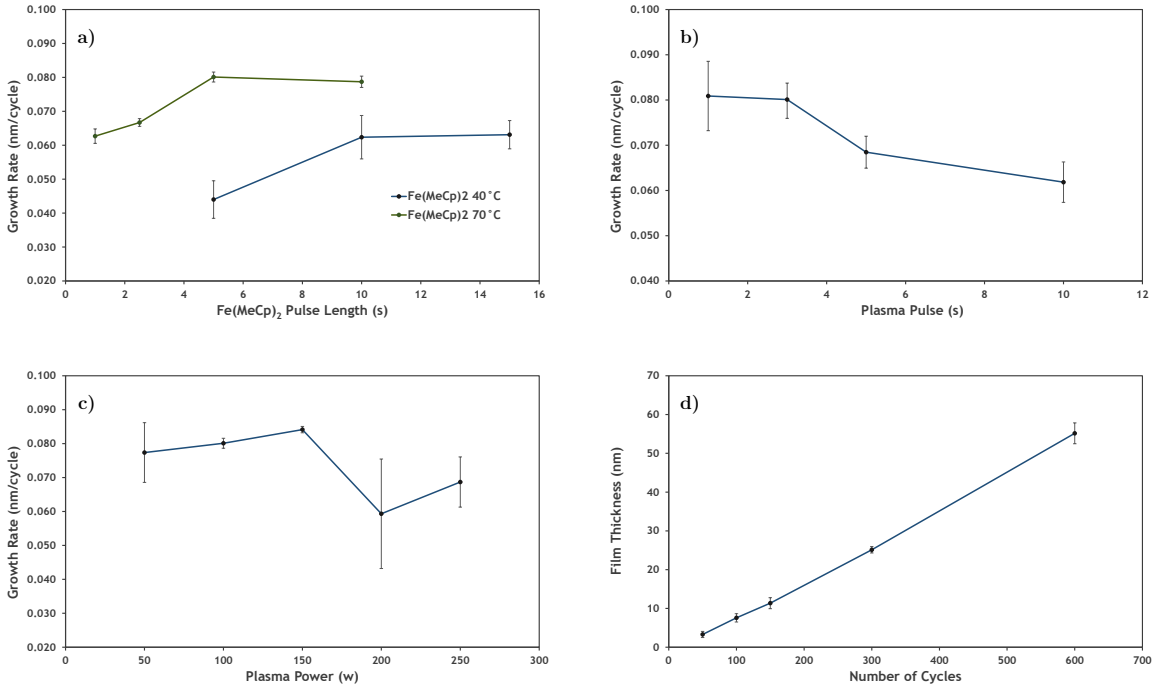

Figure 4.4. *Optimisation experiments of the Fe_2O_3 PEALD process utilising $Fe(MeCp)_2$ at 250 °C a) Effect of $Fe(MeCp)_2$ temperature and pulse length on growth rate, b) effect of plasma pulse length on growth rate, c) Effect of plasma power on growth rate d) Linearity of growth rate at with changes in cycle number at 250 °C*

curves for the delivery pulse completed with the $Fe(MeCp)_2$ held at both 40 °C and 70 °C. At both temperatures the precursor is a liquid, however when the $Fe(MeCp)_2$ is held at 70 °C the increase in volatility results in saturated growth (0.08 nm/cycle) after a 5 s pulse. Furthermore, the overall film uniformity improves as the deviation in film thickness across the deposition chamber reduces from 20% to 5%. From the $Fe(MeCp)_2$ pulse optimisation it can be concluded that a 5 s pulse is sufficient for saturation when the $Fe(MeCp)_2$ is held at 70 °C.

To optimised the second half-cycle, the length of plasma pulse was incrementally increased from 1 s to 10 s, the results of which are shown in **Fig 4.4b**. Interestingly it was observed that the overall growth rate reduced from 0.08-0.06 nm/cycle as the plasma exposure length increased. This may have been a result of either the re-orientation or densification the films. However, the samples showed no crystallinity when analysed by PXRD so the exact mechanism of growth reduction has not been determined. Similarly if the O_2 plasma pulse is held at 3 s and the plasma power varied when more than 150 W is applied there is a reduction in growth rate as shown in **Fig 4.4c**. The experiment performed at 200 W was repeated several times and with each deposition the growth rate was noted to be approximately 0.06 nm/cycle and the films had

a thickness gradient of up to 27%. From these two data sets it can be concluded a 3 s 100 W RF pulse is necessary to grow films at the saturated rate of 0.08 nm/cycle.

From the optimisation experiments the overall $Fe(MeCp)_2$ PEALD process required for maximum growth rate is 5 s $Fe(MeCp)_2$ pulse (held at 70 °C) followed with a 5 s N_2 purge and the second half-cycle consists of a 3 s RF pulse at 100 W followed by a 5 s N_2 purge, (5 s/5 s/3 s/5 s). O_2 and N_2 flows of 50 and 200 sccm can be maintained by mass flow controller throughout the PEALD cycle and no CVD reaction occurs at 250 °C though this was not confirmed for higher temperatures. This process was used in a series of depositions at 250 °C which varied the total cycle number from 50-600 and the overall rate of film growth was found to be linear with respect to the number of cycles as shown in **Fig 4.4d**.

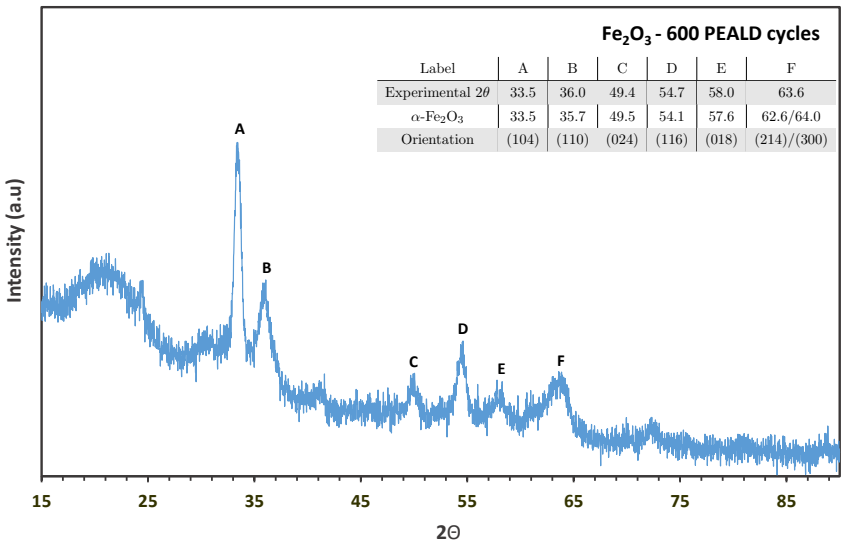

Figure 4.5. *GIXRD of a sample grown from 600 PEALD cycles $Fe(MeCp)_2$ at* 250 °C

A sample grown from 600 $Fe(MeCp)_2$ PEALD cycles was analysed by GIXRD, the resulting reflection data is displayed in **Fig 4.5**. When analysed by XRD the detector was not sensitive enough to detect any crystallinity within the samples however, the GIXRD analysis was able to detect a number of peaks which can be associated with α-Fe_2O_3, as shown by the inset in **Fig 4.5**. From the x-ray analysis it has been determined that the $Fe(MeCp)_2$ PEALD process deposits multiphase α-Fe_2O_3 at 250 °C.

For the final set of $Fe(MeCp)_2$ PEALD depositions the thermal window was examined. A series of depositions were performed between 100-300 °C at 50 °C intervals and the growth rates monitored. The results are displayed in **Fig 4.6**, and similar to the results presented by Ramachandran *et al*, the growth rate varies significantly with deposition temperature.[4] It was observed that the growth rate increased from 0.02-0.10 nm/cycle as the temperature increased

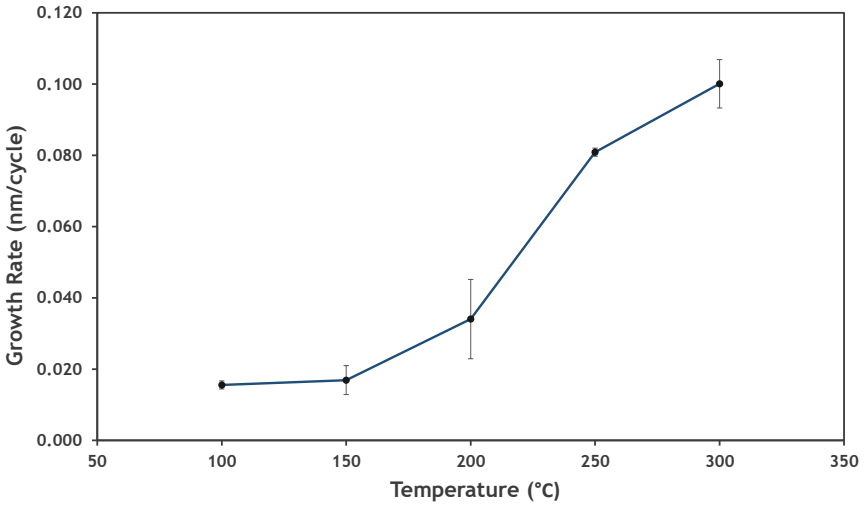

Figure 4.6. *PEALD $Fe(MeCp)_2$ process performed between 100-300 °C*

from 100-300 °C. From the optimisation experiments discussed previously, it is confirmed that the process is saturation limited at 250 °C. However, the increase in growth rate at 300 °C may be a consequence of thermal decomposition though this was not confirmed. Given that Ramachandran *et al*, concluded that saturated growth for the tert-butylferrocene PEALD process occurred between 150-350 °C at a rate of 0.02-0.12 nm/cycle it is plausible that in the range of 100-300 °C the $Fe(MeCp)_2$ PEALD process is also saturation limited.

The $Fe(MeCp)_2$ PEALD process was designed with the intention for it to be supercycled within the NiO PEALD process discussed in chapter 3. The overall stoichiometry was determined by XPS to provide comparison for $Ni_xFe_{3-x}O_4$ films. To quantify the stoichiometry XPS scans of the Fe2p, O1s and C1s regions were completed and fitted in accordance with the method utilised by Grosvenor *et al.*[36] The basic analysis completed from the survey scan determined the Fe:O ratio to be 1:3 and found negligible carbon content within the films. The more accurate high resolution scans are in agreement, with an overall Fe:O ratio of 1:3. Though the high resolution scans show the films have up to 21% carbon contamination. Whilst much of the carbon contamination can be associated with alkyl and aryl groups (284.71 eV), there is a significant amount of carbon-oxygen bonded species which partially account for the excess oxygen content within the films. When re-calculating the Fe:O ratio with only lattice oxygen (529.88 eV), the Fe:O ratio is equal to 2.38, closer to the desired stoichiometric α-Fe_2O_3.

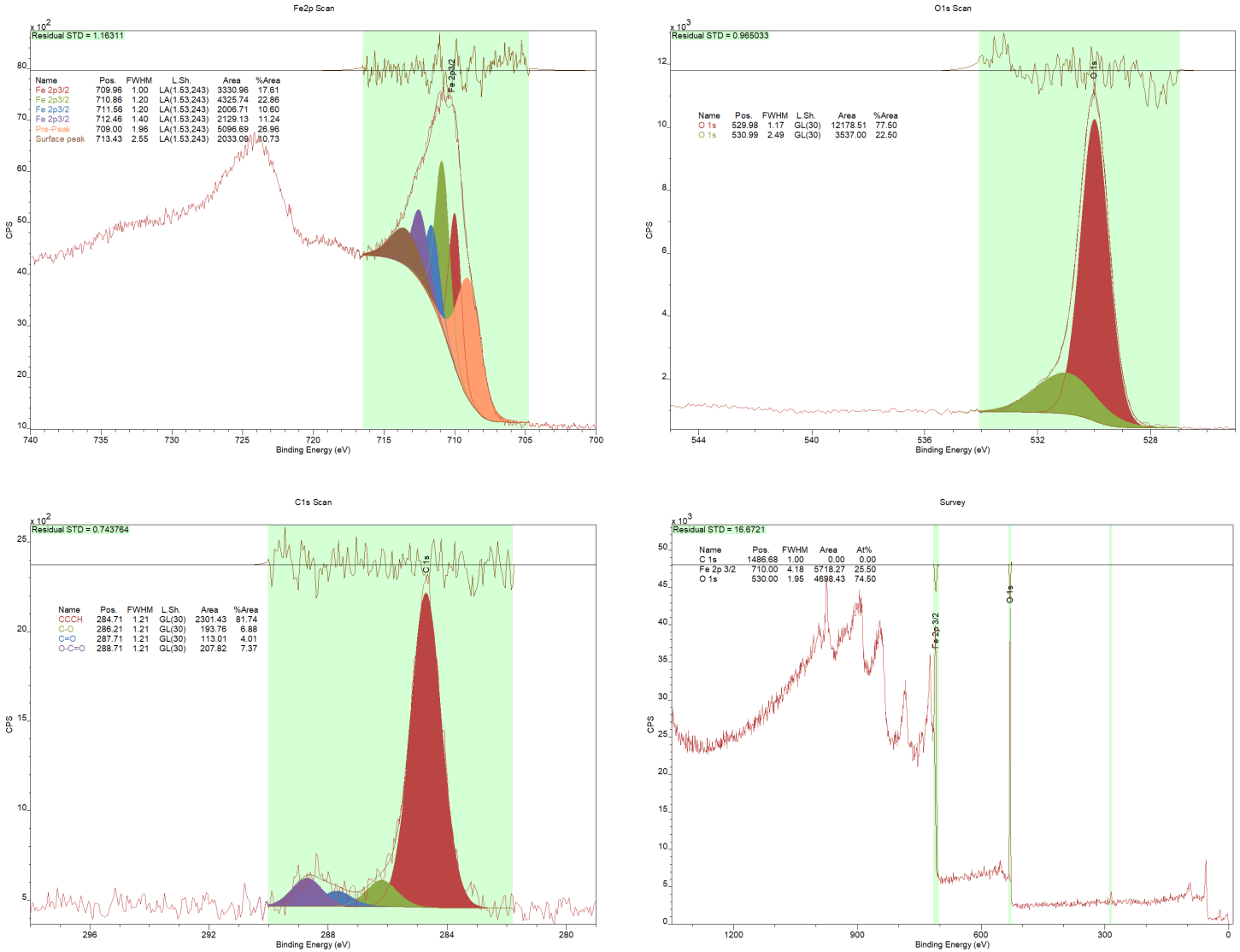

Figure 4.7. *XPS scans of a film grown from 600 PEALD cycles of $Fe(MeCP)_2$*

Fe_2O_3 Conclusions

This is an important study as, to the best of our knowledge, it is only the second α-Fe_2O_3 PEALD process that has been investigated. The growth rate and thermal window match closely with that in literature though importantly, this process utilises a cheaper precursor.[4] The $Fe(MeCp)_2$ PEALD process was found to uniformly deposit α-Fe_2O_3 at a rate of 0.08 nm/cycle at 250 °C. Analysis by GIXRD has shown the material grown at 250 °C is polycrystalline α-Fe_2O_3 and stoichiometric analysis by XPS shows the films to be oxygen rich with a Fe:O ratio of 1:3, though films contained significant carbonyl, carboxyl and alkoxy carbon impurities, which partially account for the excess oxygen content. Despite significant carbon contamination, the $Fe(MeCp)_2$ PEALD process demonstrated excellent reproducibility within the thermal window of the NiO flow PEALD process discussed in chapter 3. Given the alignment of the thermal windows for the $NiCp_2$ and $Fe(MeCp)_2$ PEALD processes, it was hypothesised that the two processes could be supercycled to produce $Ni_xFe_{3-x}O_4$.

Unfortunately, due to project time restrictions, the investigations into the Fe_2O_3 PEALD process were restricted. Left undone where photocatalytic performance tests of the PEALD deposited materials and the mechanism of the etching/reorientation of films by prolonged plasma exposure was not completed. To investigate the plasma mechanism, Fe_2O_3 samples of known thickness, crystallinity and roughness could be exposed to varying numbers of plasma cycles. Any alteration in any parameter may be able to suggest whether the reduction in growth rate, as a result of prolonged plasma pulses, is a consequence of plasma etching or film reorientation. The results of which may influence the processes optimal plasma power and pulse length.

4.3.2 PEALD of $NiFe_2O_4$

Nickel ferrite, $NiFe_2O_4$ is a material of interest for its catalytic and magnetic properties.[29, 30, 37] To date two ALD processes have been designed for the production of $NiFe_2O_4$ and other nickel iron composite films.[35, 38] Both processes utilise O_3 as the oxidant with either $NiCp_2$ or $Ni(acac)_2$ as nickel precursors and $FeCp_2$ as an iron source. In both reports altering the ratio of Ni:Fe in ALD supercycles resulted in the control of the overall film stoichiometry. Literature concerning an equivalent $NiFe_2O_4$ PEALD process is scarce. However, by supercycling the $NiCp_2$ PEALD process discussed in chapter 3 and the $Fe(MeCp)_2$ PEALD process, it was hypothesised that altering the ratio of the Ni:Fe could control film stoichiometry and a film consistent with the formation of $NiFe_2O_4$ could be produced.

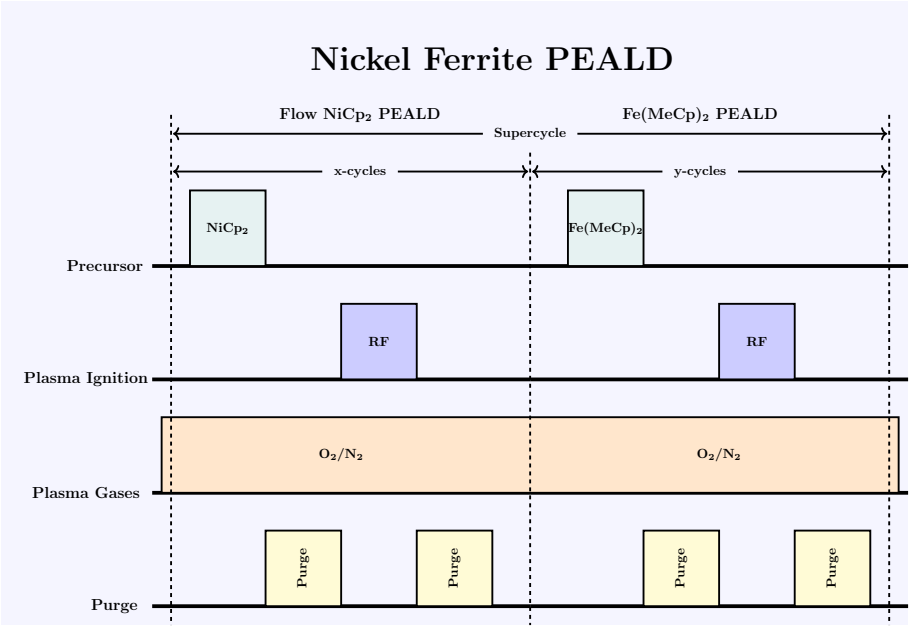

Figure 4.8. *Illustration of the nickel ferrite PEALD supercyle process*

Shown in **Fig 4.8** is an illustration of the $NiFe_2O_4$ PEALD process implemented within this study. All depositions were performed using a total of 600 cycles at 250 °C onto SiO_2, FTO and borosilicate glass substrates. The process growth rates and film uniformity were monitored by ellipsometry and the samples analysed by XRD, GIXRD and XPS. For the individual half-cycles the optimised NiO flow cycle was used (2 s/5 s/2 s/5 s) in combination with the optimised $Fe(MeCp)_2$ process (5 s/5 s/3 s/5 s). Plasma gas flows were maintained by mass flow controllers at 50 sccm for O_2 and 200 sccm for N_2 and the plasma ignited by a 100 W RF pulse. To ascertain whether there was control of the film stoichiometry from alterations in the Ni:Fe supercycle ratios experiments were completed with differing ratios, namely Ni:Fe 2:1, 1:1, 1:2 and 1:5.

Shown in **Fig 4.9** is a comparison of the thicknesses of films grown from 600 cycles of a Fe_2O_3 and NiO PEALD and the 2:1, 1:1, 1:2 and 1:5, Ni:Fe supercycle processes. There is a linear relationship between film growth rate and ratio of Ni:Fe, as the relative number of $Fe(MeCp)_2$

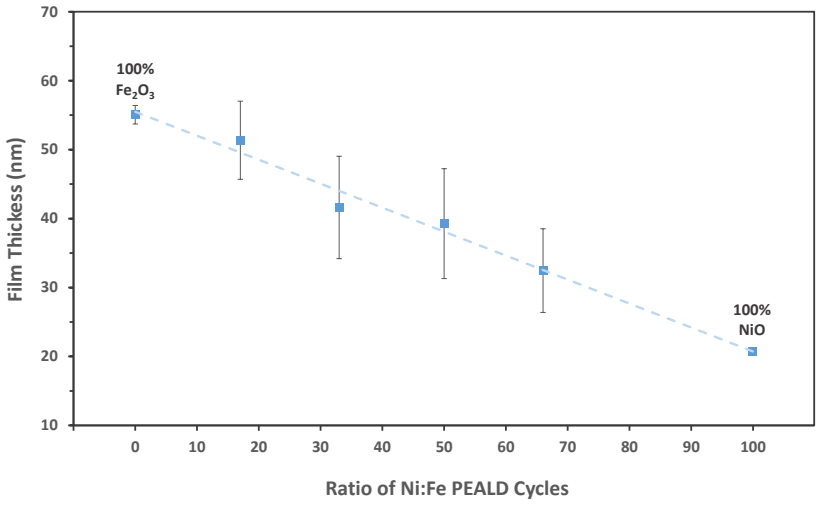

Figure 4.9. *Thickness of films grown from 600 PEALD iron and nickel cycles and supercycles at* 250 °C

pulses is reduced the growth rate reduces to that of the purely NiO process. This demonstrates that the contribution of each precursor pulse to film growth is similar to the optimised growth rate of the individual $NiCp_2$ and $Fe(MeCp)_2$ PEALD processes. This result demonstrates that the two PEALD processes can be controllably cycled to alter the overall film growth and potentially the stoichiometry.

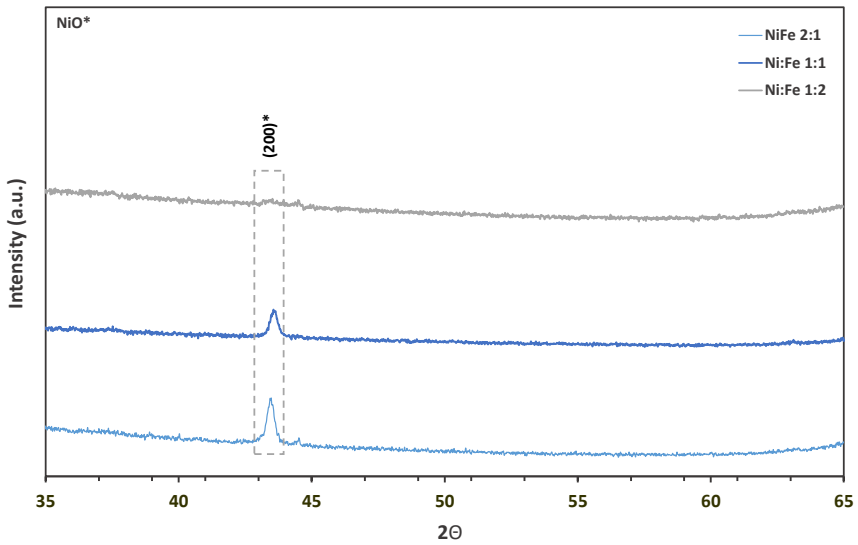

Figure 4.10. *XRD scans of samples grown by supercycled NiO and Fe_2O_3 PEALD process with Ni:Fe ratios of 2:1, 1:1, 1:2*

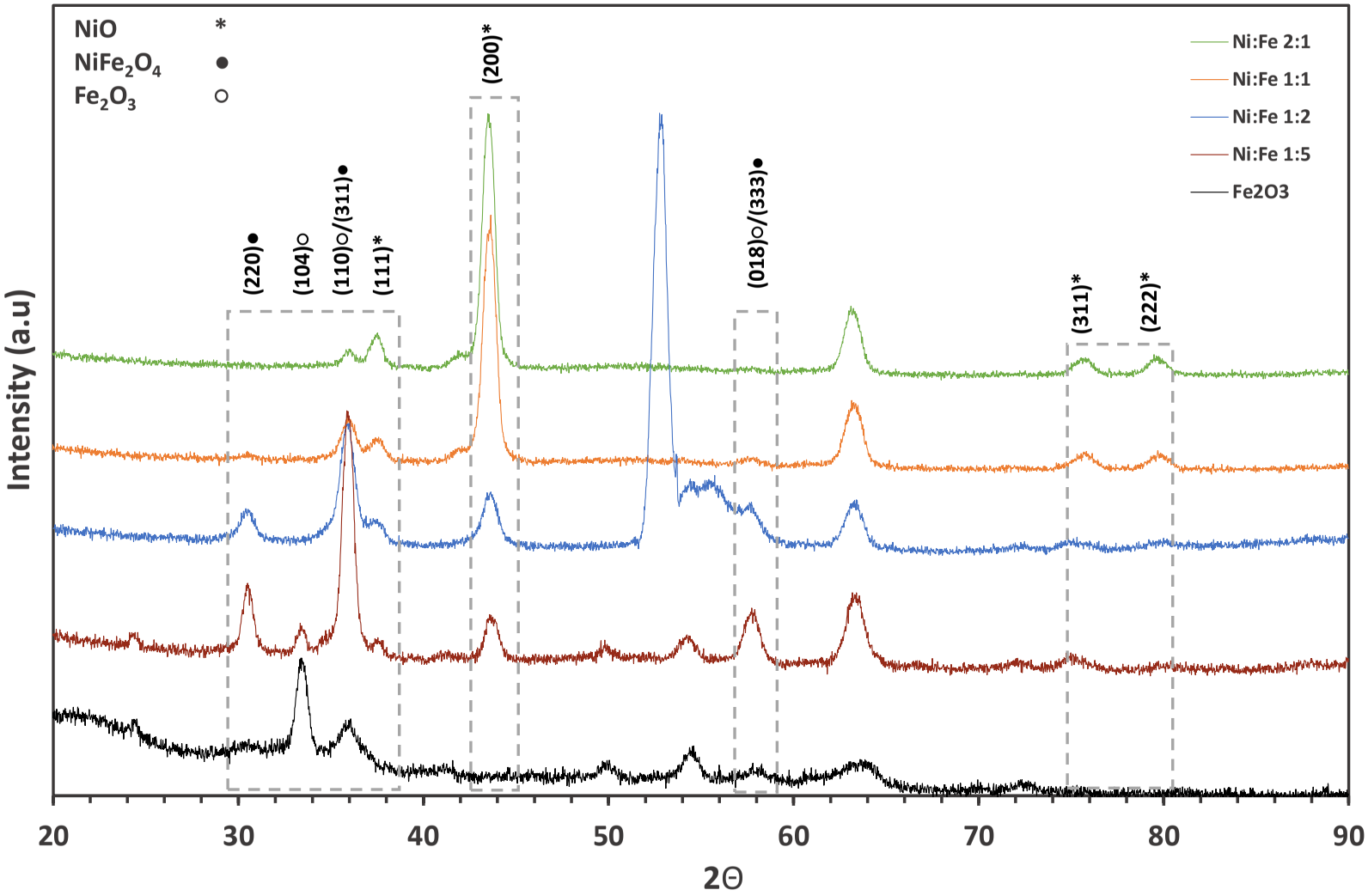

Figure 4.11. *GIXRD scans of samples grown by supercycled NiO and Fe_2O_3 PEALD process with Ni:Fe ratios of 2:1, 1:1, 1:2, 1:5 and only Fe_2O_3*

XRD analysis shows the Ni:Fe, 2:1, 1:1 and 1:2 films show negligible crystallinity. Shown in **Fig 4.10** the Ni:Fe 2:1 and 1:1 films present reflections consistent with the (200) cubic NiO plane, though as the Ni ratio is reduced, such as in the 1:2 sample, the films become amorphous. Further x-ray analysis by GIXRD provides significantly more information on the structural orientation of the films. **Fig 4.11** shows the GIXRD diffraction patterns of the all nickel ferrite deposition and a pattern from a Fe_2O_3 PEALD film. Following a few principal peaks, the Ni and Fe content of the films can be monitored. For example, the reflection associated with the (200) cubic NiO peak is strongly diffracting in the 2:1 and 1:1 films but as the Ni ratio is reduced the peak intensity diminishes, as seen in the 1:2 and 1:5 samples. Further to this, the cubic NiO (311) and (222) reflection peaks are absent in the Fe rich 1:2 and 1:5 processes but detectable in the Ni rich 2:1 and 1:1 process. Alternatively, if the Fe content is tracked by the peaks associated with the (104) *alpha*-Fe_2O_3 diffraction plane, reflections can only be detected in the Fe rich 1:5 sample. For films with greater Ni content the Fe_2O_3 (104) plane is absent. Importantly, the target material $NiFe_2O_4$ can also be detected. The Ni:Fe 1:5 sample has the most $NiFe_2O_4$ character with reflections that can be attributed to the (220), (311) and (333) peaks present. Tracking these peaks across all samples, it is evident that a Ni:Fe ratio of 1:5 is the PEALD process closest to synthesising the target material. However, the process does not preferentially grow $NiFe_2O_4$ as the sample is multiphase with reflections associated to both NiO and Fe_2O_3 also detectable.

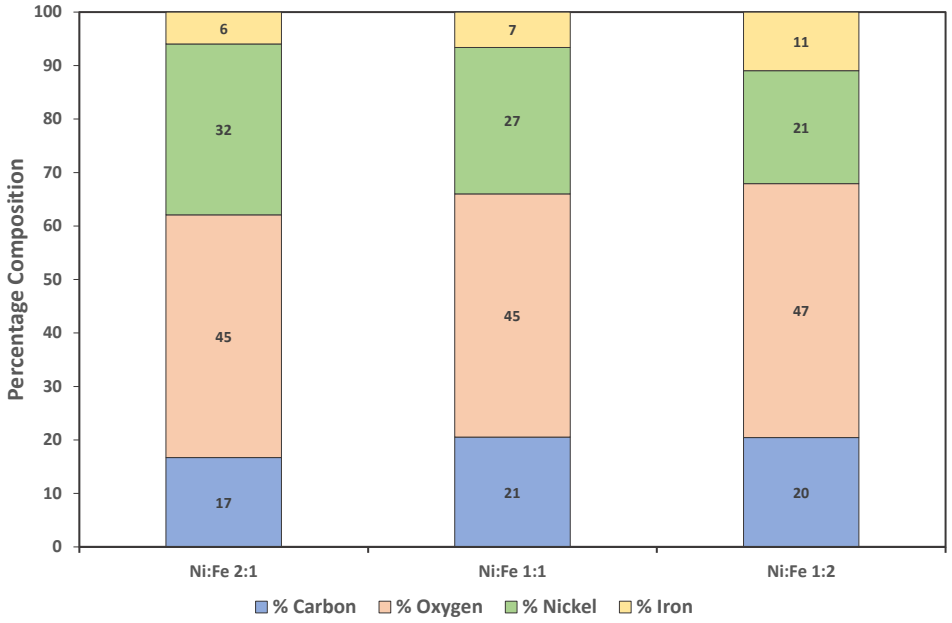

Figure 4.12. *Stoichiometry of the Supercycled NiO and Fe_2O_3 PEALD process 2:1, 1:1, 1:2. As estimated by XPS analysis.*

The $NiFe_2O_4$ PEALD processed samples were analysed by XPS to determine the effect of altering

the ratio of Ni:Fe pulses. Due to the presence of a Ni Auger peak at approximately 716 eV which sits on the shoulder of the Fe $2p_{3/2}$ XPS peak, the precise quantification of the film stoichiometry is challenging. Modelling the Fe $2p_{3/2}$ peak with the method utilised for the Fe_2O_3 XPS discussed previously is no longer possible. Integration of the $2p_{3/2}$ peak area will include the Ni auger peak and the iron content will be overestimated.[36]

Thus XPS analysis can only provide an estimate of the effect of changing the ratio of Ni:Fe on the sample stoichiometry. Shown in **Fig 4.12** are the XPS determined stoichiometries of the 2:1, 1:1 and 1:2 Ni:Fe samples. Overall as the ratio of Ni pulses is reduced there is a slight reduction of the nickel content from 32-21% and an increase in Fe content from 6-11%, proving there is some control of stoichiometry from altering the ratio of Ni:Fe PEALD pulses.

From the combination of GIXRD and XPS analysis, it has been shown that altering the ratio of $NiCp_2$ and $Fe(MeCp)_2$ PEALD cycles in a $NiFe_2O_4$ supercycle can control the stoichiometry and crystallinity of the as deposited films. The results are very promising but due to time constraints the process could not be fully optimised and characterised. There are two significant flaws with the process that could be addressed. The first is that for all supercycled depositions there was a significant growth gradient in the deposition chamber. This has not been attributed to a CVD reaction but could be accounted for with a single experiment mixing the Ni:Fe ratio at 1:1 and not igniting the plasma, if deposition is present then there is a possible thermal decomposition step which was not present in the individual processes. The second concern is the significant carbon content present in the samples. The carbon is persistent from the $Fe(MeCp)_2$ PEALD process and to address the issue an alternative iron precursor may be required.

Despite the $NiFe_2O_4$ process not being fully optimised it does facilitate the growth of spinel phase $NiFe_2O_4$ without further thermal treatment. For future depositions a 1:5 sample shall be grown on sapphire and measured by GIXRD to ascertain whether growth is epitaxial. Also of interest is whether the films can be used as a co-catalyst in photocatalytic water splitting. TiO_2 and Fe_2O_3 photocatalytic films will be used as substrate for nano-layers of the $NiFe_2O_4$ and the photocatalytic water splitting assessed. Overall the process is a viable method for the production of spinel nickel ferrite given some further optimisation the process may easily be adapted to other ALD tools.

4.4 Conclusions and Future Work

Two new PEALD methods for the production of Fe_2O_3 and a multiphase $NiFe_2O_4$ have been developed. The $Fe(MeCp)_2$ PEALD process was developed to be utilised as a co-cycle in a $NiCp_2$:$Fe(MeCp)_2$ PEALD method for the production of multiphase $NiFe_2O_4$. As such the $Fe(MeCp)_2$ PEALD process was optimised to 250 °C where it grows Fe_2O_3 at a rate of 0.08nm/cycle. 250 °C is within the $NiCp_2$ PEALD thermal window and at this temperature the processes were supercycled at a ratio of Ni:Fe 2:1, 1:1, 1:2 and 5:1. It has been shown that by varying the ratio of Ni:Fe cycles the overall stoichiometry and crystallinity of the films can be altered. The 1:5 process was closest to synthesising the target nickel ferrite with multiple reflections which can be associated to $NiFe_2O_4$ present in the GIXRD data.

To the best of our knowledge, only one other Fe_2O_3 PEALD method has been published and no other nickel ferrite PEALD method has been reported in literature. The nickel ferrite process has been interesting to work with and this preliminary study has laid the foundation for a number of studies. Primarily, another iron precursor needs to be trialled because high carbon content noted in the Fe_2O_3 films is also present in the nickel ferrite composites. An alternative precursor may reduce carbon content with Fe(^{t}BuCp)Cp a potential candidate given it has been utilised in Fe_2O_3 PEALD and grows at a similar rate.

Given the sparsity of literature concerning the PEALD of Fe_2O_3 and $NiFe_2O_4$ it is important that the results presented in this chapter are reported. Whilst they are currently being drafted, there are further investigations which may increase the impact of work presented. Due to the restrictions in project time it was not possible to complete magnetic measurements of the nickel ferrite films or collect XPS data for the 1:5 Ni:Fe film. To fully realise the projects potential, future work would require that these gaps in the experimental data are filled.

Another study which is of interest, is to assess the photo-anodic water splitting properties of the nickel ferrite and Fe_2O_3 films. Prior to the lockdown these experiments were planned to be completed with partners at Imperial College London. Samples of both nickel ferrite and Fe_2O_3 have been grown onto FTO and their photoanodic performance will be assessed when the COVID-19 lockdown eases. If the devices can demonstrate photocatalytic activity, both the Fe_2O_3 and nickel ferrite may be optimised by adjusting the film thickness during deposition or crystallinity by post deposition annealing.

4.5 References

[1] Y. Lin, Y. Xu, M. T. Mayer, Z. I. Simpson, G. McMahon, S. Zhou and D. Wang, *J. Am. Chem. Soc.*, 2012, **134**, 5508–5511.

[2] C. Guan, J. Liu, Y. Wang, L. Mao, Z. Fan, Z. Shen, H. Zhang and J. Wang, *ACS Nano*, 2015, **9**, 5198–5207.

[3] A. B. F. Martinson, M. J. DeVries, J. A. Libera, S. T. Christensen, J. T. Hupp, M. J. Pellin and J. W. Elam, *J. Phys. Chem. C*, 2011, **115**, 4333–4339.

[4] R. K. Ramachandran, J. Dendooven and C. Detavernier, *J. Mater. Chem. A*, 2014, **2**, 10662–10667.

[5] J. Bachmann, J. Jing, M. Knez, S. Barth, H. Shen, S. Mathur, U. Gösele and K. Nielsch, *J. Am. Chem. Soc.*, 2007, **129**, 9554–9555.

[6] J. R. Scheffe, A. Francés, D. M. King, X. Liang, B. A. Branch, A. S. Cavanagh, S. M. George and A. W. Weimer, *Thin Solid Films*, 2009, **517**, 1874–1879.

[7] C. D. Pham, J. Chang, M. A. Zurbuchen and J. P. Chang, *Chem. Mater.*, 2015, **27**, 7282–7288.

[8] M. Rooth, A. Johansson, K. Kukli, J. Aarik, M. Boman and A. Hårsta, *Chem. Vap. Depos.*, 2008, **14**, 67–70.

[9] J. Escrig, J. Bachmann, J. Jing, M. Daub, D. Altbir and K. Nielsch, *Phys. Rev. B - Condens. Matter Mater. Phys.*, 2011, **77**, 214421.

[10] D. Peeters, A. Sadlo, K. Lowjaga, O. Mendoza Reyes, L. Wang, L. Mai, M. Gebhard, D. Rogalla, H. Becker, I. Giner, G. Grundmeier, D. Mitoraj, M. Grafen, A. Ostendorf, R. Beranek and A. Devi, *Adv. Mater. Interfaces*, 2017, **4**, 1700155.

[11] J. R. Avila, D. W. Kim, M. Rimoldi, O. K. Farha and J. T. Hupp, *ACS Appl. Mater. Interfaces*, 2015, **7**, 16138–16142.

[12] S. Selvaraj, H. Moon, J. Y. Yun and D. H. Kim, *Korean J. Chem. Eng.*, 2016, **33**, 3516–3522.

[13] M. de Ridder, P. C. van de Ven, R. G. van Welzenis, H. H. Brongersma, S. Helfensteyn, C. Creemers, P. Van Der Voort, M. Baltes, M. Mathieu and E. F. Vansant, *J. Phys. Chem. B*, 2002, **106**, 13146–13153.

[14] K. Zhou, J. Huang, Q. Zhang and F. Wei, *Nanoscale Res. Lett.*, 2010, **5**, 1555–1560.

[15] O. Nilsen, M. Lie, S. Foss, H. Fjellvåg and A. Kjekshus, *Appl. Surf. Sci.*, 2004, **227**, 40–47.

[16] L. Hannevold, O. Nilsen, A. Kjekshus and H. Fjellvåg, *Appl. Catal. A Gen.*, 2005, **284**, 177–184.

[17] M. Lie, H. Fjellvåg and A. Kjekshus, *Thin Solid Films*, 2005, **488**, 74–81.

[18] J. A. Libera, J. W. Elam, N. F. Sather, T. Rajh and N. M. Dimitrijevic, *Chem. Mater.*, 2010, **22**, 409–413.

[19] A. Tanskanen, O. Mustonen and M. Karppinen, *APL Mater.*, 2017, **5**, 056104.

[20] J. Bachmann, J. Jing, M. Knez, S. Barth, H. Shen, S. Mathur, U. Gösele and K. Nielsch, *J. Am. Chem. Soc.*, 2007, **129**, 9554–9555.

[21] A. B. F. Martinson, M. J. DeVries, J. A. Libera, S. T. Christensen, J. T. Hupp, M. J. Pellin and J. W. Elam, *J. Phys. Chem. C*, 2011, **115**, 4333–4339.

[22] X. Li, N. C. Fan and H. J. Fan, *Chem. Vap. Depos.*, 2013, **19**, 104–110.

[23] M. Rooth, A. Johansson, K. Kukli, J. Aarik, M. Boman and A. Hårsta, *Chem. Vap. Depos.*, 2008, **14**, 67–70.

[24] T. M. Onn, M. Monai, S. Dai, L. Arroyo-Ramirez, S. Zhang, X. Pan, G. W. Graham, P. Fornasiero and R. J. Gorte, *Appl. Catal. A Gen.*, 2017, **534**, 70–77.

[25] M. Fondell, T. J. Jacobsson, M. Boman and T. Edvinsson, *J. Mater. Chem. A*, 2014, **2**, 3352–3363.

[26] I. L. Soroka, M. Rooth, J. Lu, M. Boman, P. Svedlindh, J.-O. Carlsson and A. Hårsta, *J. Appl. Phys.*, 2009, **106**, 084313.

[27] J. A. Singh, N. F. W. Thissen, W. Kim, H. Johnson, W. M. M. Kessels, A. A. Bol, S. F. Bent and A. J. M. Mackus, *Chem. Mater.*, 2018, **30**, 663–670.

[28] Y. Tasaki, T. Kanoko, M. Kabeya, N. Chifu and S. Yoshizawa, *Integr. Ferroelectr.*, 2006, **81**, 281–288.

[29] J. L. Domínguez-Arvizu, J. A. Jiménez-Miramontes, J. M. Salinas-Gutiérrez, M. J. Meléndez-Zaragoza, A. López-Ortiz and V. Collins-Martínez, *Int. J. Hydrogen Energy*, 2017, **42**, 30242–30248.

[30] U. Lüders, A. Barthélémy, M. Bibes, K. Bouzehouane, S. Fusil, E. Jacquet, J.-P. Contour, J.-F. Bobo, J. Fontcuberta and A. Fert, *Adv. Mater.*, 2006, **18**, 1733–1736.

[31] M. A. Soler and L. G. Paterno, in *Nanostructures*, Elsevier Inc., 2017, pp. 147–186.

[32] Y. P. Sukhorukov, A. V. Telegin, N. G. Bebenin, A. P. Nosov, V. D. Bessonov and A. A. Buchkevich, *Solid State Commun.*, 2017, **263**, 27–30.

[33] K. J. Kim, H. S. Lee, M. H. Lee and S. H. Lee, *J. Appl. Phys.*, 2002, **91**, 9974–9977.

[34] B. S. Holinsworth, D. Mazumdar, H. Sims, Q. C. Sun, M. K. Yurtisigi, S. K. Sarker, A. Gupta, W. H. Butler and J. L. Musfeldt, *Appl. Phys. Lett.*, 2013, **103**, 082406.

[35] J. E. Bratvold, H. H. Sønsteby, O. Nilsen and H. Fjellvåg, *J. Vac. Sci. Technol. A*, 2019, **37**, 021502.

[36] A. P. Grosvenor, B. A. Kobe, M. C. Biesinger and N. S. McIntyre, *Surf. Interface Anal.*, 2004, **36**, 1564–1574.

[37] D. Y. Li, Y. K. Sun, P. Z. Gao, X. L. Zhang and H. L. Ge, *Ceram. Int.*, 2014, **40**, 16529–16534.

[38] A. P. Espejo, R. Zierold, J. Gooth, J. Dendooven, C. Detavernier, J. Escrig and K. Nielsch, *Nanotechnology*, 2016, **27**, 345707.

Chapter 5

Investigations Into the Development of ALD Precursors for New Ni ALD Processes

Contents

5.1 Abstract

In their current state, the ALD methods available to grow NiO films are hindered by the lack of precursors with sufficient reactivity, volatility and thermal stability to produce NiO efficiently. Consequent processes are restricted to narrow thermal windows or require strong oxidants for film growth. To continue to develop new, scalable and reproducible NiO ALD processes, precursor development is essential. To that end, this chapter details the synthesis and analysis of the compounds investigated as potential ALD precursors of NiO. Though none of the complexes were experimentally trialled as ALD precursors, two nickel(II) pyrrole complexes were found to be volatile and thermally stable and could be a new class of NiO ALD precursor.

Special Acknowledgements

Special thanks go to Max Robson for his hard work and support in the development of the nickel pyrrole complexes.

5.2 Aminoalkoxides

5.2.1 Nickel Aminoalkoxides

The design of ALD and CVD precursors is an interesting avenue of synthetic chemistry. Searching for "Goldilocks" compounds which possess the required stability, reactivity and volatility to be suitable ALD precursors can appear as much as guess work, as it is a systematic investigation. Take for instance the parent compound shown in **Fig 5.1** 2-Dimethylamino-2-methylpropanol (DMAMP) (**6**). Multiple synthetic approaches can be taken to adjust the volatility of ligands. For example, the electronics of a ligand may be adjusted by incorporating CF_3 groups, this may induce greater electrostatic repulsion between molecules, lowering the boiling point and increasing ligand volatility. Alternatively, the asymmetry of the molecule can be adjusted and alkyl substitutions increased in length to disrupt molecular packing and lower van der Waals interactions. It can be one or both of these synthetic routes which result in an optimum precursor. Though, it is this prediction of physical traits brought about by changes in ligand architecture that drives the design process of ALD precursors.

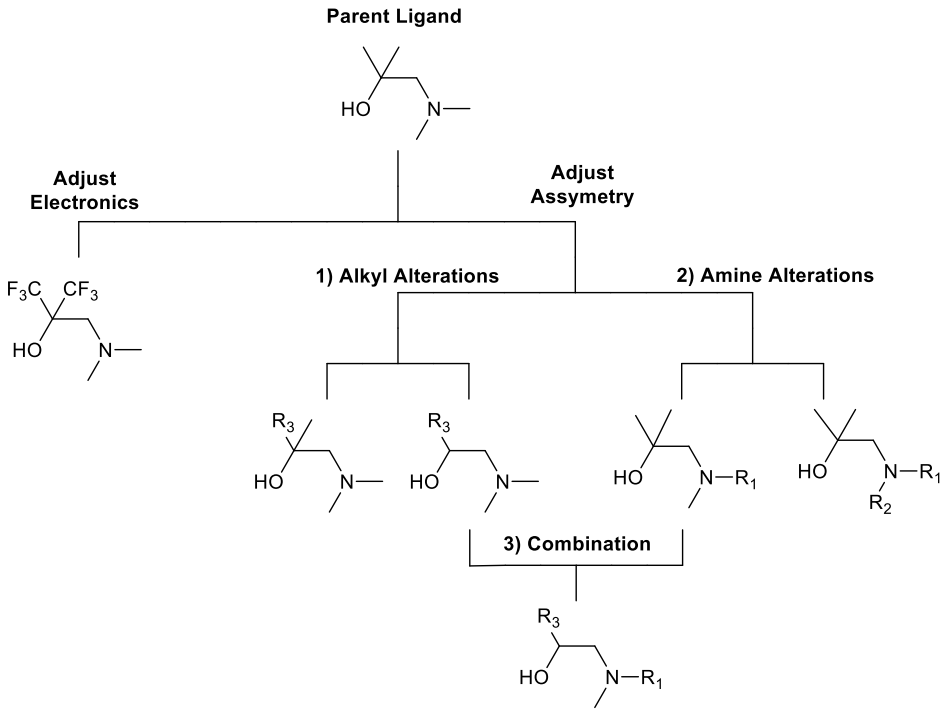

Figure 5.1. *Iterative alteration and Design process of CVD and ALD ligands*

As discussed in Chapter 2, $Ni(DMAMP)_2$ is simple to synthesise, inexpensive and could be easily adjusted by the design principles in **Fig 5.1**. Despite the flaws with $Ni(DMAMP)_2$ as an ALD precursor it was the basis of two lines of investigation. The first was the altering of the ligand architecture to synthesise several nickel compounds two of which could be compared to $Ni(DMAMP)_2$ as precursors, $Ni(FDMAMP)_2$ (**1**) and $Ni(DEA2P)_2$ (**2**). The second investigation

was the synthesis and analysis of four potential group one DMAMP ALD compounds, LiDMAMP (**3**), LiFDMAMP (**7**), NaDMAMP (**4**) and KDMAMP (**5**).

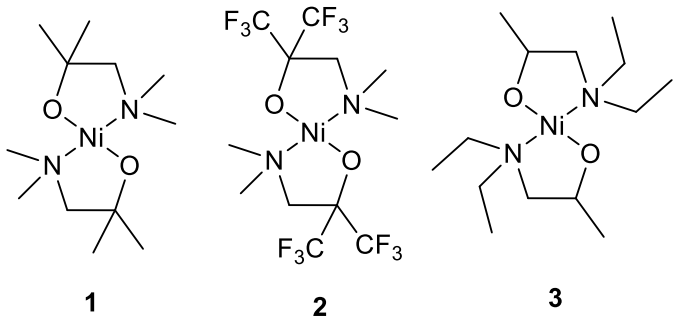

Figure 5.2. *Nickel compounds for application in ALD/CVD 1) Ni(DMAMP)$_2$ 2) Ni(FDMAMP)$_2$ 3) Ni(DEA2P)$_2$.*

Ni(DMAMP)$_2$ research was first reported by Kim *et al* with the publication of the Ni(DMAMP)$_2$ and H_2O ALD process.[1] This report was followed up with two publications featuring more nickel aminoalkoxides variations which have increased asymmetry.[2, 3] The publications demonstrated that by changing the asymmetry of the molecule the physical properties of the compound can be manipulated. Of the complexes reported in these publications, only Ni(DMAMP)$_2$ and Ni(DMAMB)$_2$ have been utilised as ALD precursors.[4–7] Looking to expand on the work by Kim *et al* two further aminoalkoxide variations were targeted, Ni(FDMAMP)$_2$ **1** and Ni(DEA2P)$_2$ **2**. Both compounds were isolated, their crystal structure refined and their thermal properties analysed by thermal gravimetric analysis (TGA).

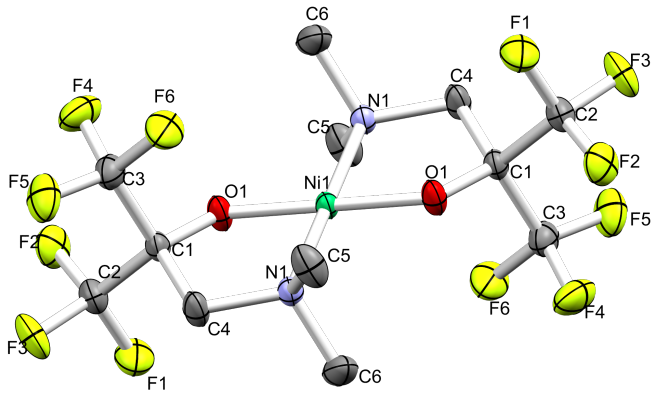

Figure 5.3. *Molecular structure of Ni(FDMAMP)$_2$ (**1**).*

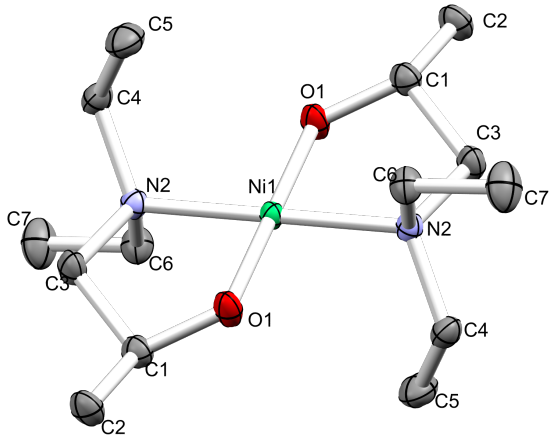

Figure 5.4. *Molecular structure of Ni(DEA2P)$_2$ (**2**).*

Expanding on the nickel aminoalkoxide library, compounds **1** and **2** (**Fig 5.2**) were synthesised by the methodology described by Kim *et al.*[3] The compounds were isolated from THF and their crystal structures refined and thermal properties analysed by TGA. Ni(FDMAMP)$_2$ is shown in **Fig 5.3** and Ni(DEA2P)$_2$ in **Fig 5.4**, both structures have a square planar geometry with the Ni atom positioned as a centre of inversion. The geometry of both structures is compared to the experimentally derived data set for Ni(DMAMP)$_2$ in **Table 5.1**.

	Ni(DMAMP)$_2$	**Ni(FDMAMP)$_2$**	**Ni(DEA2P)$_2$**
Space Group	$P2_{1/n}$	$P2_{1/n}$	P-1
Ni-O(Å)	1.842(8)	1.8322(10)	1.8452(8)
Ni-N(Å)	1.937(10)	1.9326(11)	1.9545(9)
C-F (Å)	-	1.3417(18)	-
C-O (Å)	1.4029(14)	1.3687(16)	1.4004(14)
N-Ni-O(°)	88.09(4)	87.86(4)	88.46(4)
O-C-C(°)	106.55(9)	112.04(11)	107.38(9)
C-C-N(°)	109.76(9)	109.50(11)	108.23(9)

Table 5.1. *Comparison of the structures of the nickel aminoalkoxides Ni(DMAMP)$_2$ (**1**), Ni(FDMAMP)$_2$ (**2**) and Ni(DEA2P)$_2$ (**3**).*

For the TGA analysis of nickel aminoalkoxides each compound was compared to the TGA profile of Ni(DMAMP)$_2$. The TGA profile of Ni(DMAMP)$_2$ was initially collected by two experimental methods. The first collection was completed on a bench top TGA. The sample was contained in a sealed pan which was held under a constant flow of argon. The pan had a pinhole in the lid which ensured it did not over pressurise but because of the pinhole, the sample was exposed to atmosphere during transfer from glove box to argon flow. The second collection

was performed on a TGA within a glovebox. The sample was in an open pan but was kept under an inert atmosphere. The TGA profiles from both experimental set ups are shown in **Fig 5.5**. Keeping the sample in an inert atmosphere ensures no unwanted reactions occur and consequently the TGA profile is improved with a lower residual mass of 2.88% compared to the atmosphere sample 27%. A residual mass of 27% correlates closely to residual NiO (25%) which was likely formed as a consequence of the decomposition of non-volatile species formed as the $Ni(DMAMP)_2$ reacted with atmospheric oxygen and water. All further TGA profiles were completed under an inert atmosphere to ensure the thermal profiles accurately represented the volatilisation and decomposition of each compound.

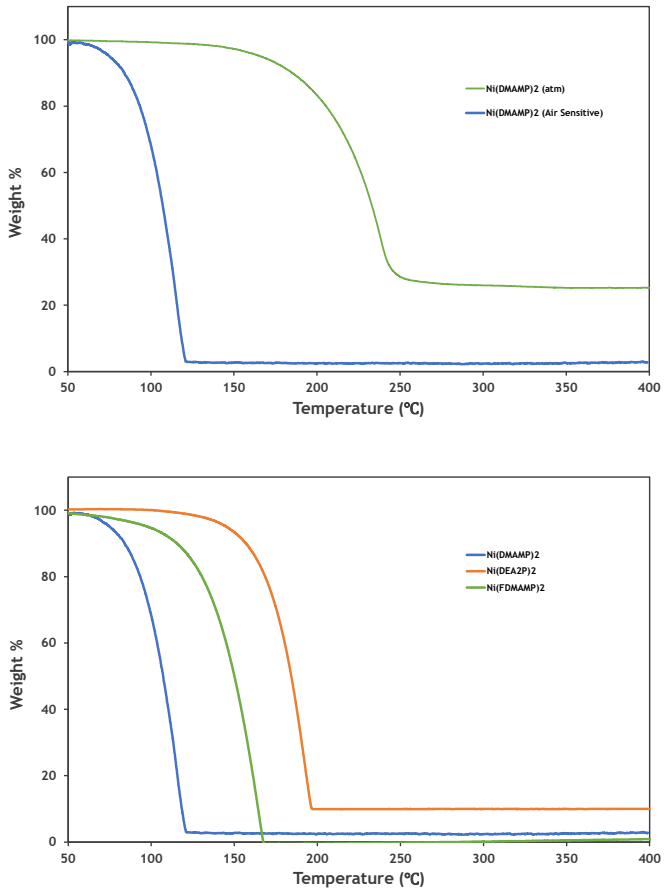

Figure 5.5. *Top:TGA profiles of $Ni(DMAMP)_2$ collected with a heating rate of* $5\,^{\circ}C\,min^{-1}$ *in both atmospheric conditions and in an inert atmosphere. Bottom: TGA profiles of $Ni(DMAMP)_2$, $Ni(FDMAMP)_2$ and $Ni(DEA2)P_2$ collected with a heating rate of* $5\,^{\circ}C\,min^{-1}$.

Shown in **Fig 5.5** are the TGA profiles of $Ni(FDMAMP)_2$ and $Ni(DEA2P)_2$ compared to $Ni(DMAMP)_2$. Both $Ni(FDMAMP)_2$ and $Ni(DMAMP)_2$ have 1% mass loss at 55 °C, however the rate of mass loss for the $Ni(FDMAMP)_2$ is slower and the resulting residual mass is less at 0.6%. Comparatively $Ni(DEA2P)_2$ displayed lower volatility with 1% mass loss at 120 °C and a residual mass of 10%. From the thermal analysis $Ni(FDMAMP)_2$ can be considered a more

appropriate ALD precursor than the $Ni(DEA2P)_2$ as it has shown greater volatility and thermal stability. Unfortunately, the cost of the 2,-2-bis(trifluoromethyl)-oxirane required to synthesise the ligand, is significantly more expensive than the 2,2-dimethyloxirane required for DMAMP synthesis. Consequently, the compound was not used in any ALD deposition experiments.

5.2.2 Group One Aminoalkoxides

Group 1 ALD precursors are relatively limited with only a few precursors published for lithium and metal tert-butoxide complexes (MO^tBu) are the only published precursors for sodium and potassium ALD.[8–15] Generally, ALD processes which utilise Li, Na and K tert-butoxides are restricted by the high temperatures required to volatilise the compounds. Therefore, developing alternative precursors capable of deposition at lower temperature is of interest.

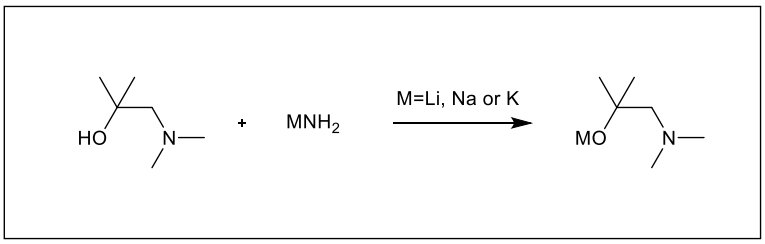

Figure 5.6. *Reaction scheme for the synthesis of a group 1 DMAMP species.*

During the synthesis of $Ni(DMAMP)_2$ a group one MDMAMP intermediate is generated and utilised in a salt metathesis reaction. Initially out of curiosity, the compound NaDMAMP (**4**) was isolated and attempts were made to determine its crystal structure. Handling the compound was challenging as it rapidly decomposes when exposed to atmosphere, which indicated it may have suitable reactivity with water for ALD deposition. The TGA profile of the sample was obtained in an inert atmosphere and the compound was found to be volatile with a 1% mass loss observed at 60 °C and negligible residual mass observed at 270 °C as shown in **Fig. 5.11**. Given the volatility and reactivity of the NaDMAMP the other group one amino alkoxides LiDMAMP (**3**), KDMAMP (**5**) and LiFDMAMP (**7**) were isolated and their crystal structures refined.

The group one MDMAMP compounds are all cubanes and hexamers. Cubanes commonly occur in group one compounds where bonding is dictated by electrostatics, which leads to metal cations and anionic donors with high coordination number.[16] Shown in **Fig 5.7** is the molecular structure of LiDMAMP (**3**). The structure consists of four tetrameric units $[LiDMAMP]_4$ with lithium atoms occupying diagonal corners of the quadratic face. The distorted cubane core of the molecule has average Li-O-Li angles of 81.69° and O-Li-O angle of 97.72°. Each lithium centre has pseudo trigonal bipyramidal geometry with O1 axial and N1, O2 and O3 in equatorial positions (N1-Li1-O2 136.92°, N1-Li1-O3 123.23°).

The LiFMAMP molecular structure shown in **Fig 5.8** has a similar distorted cubane structure

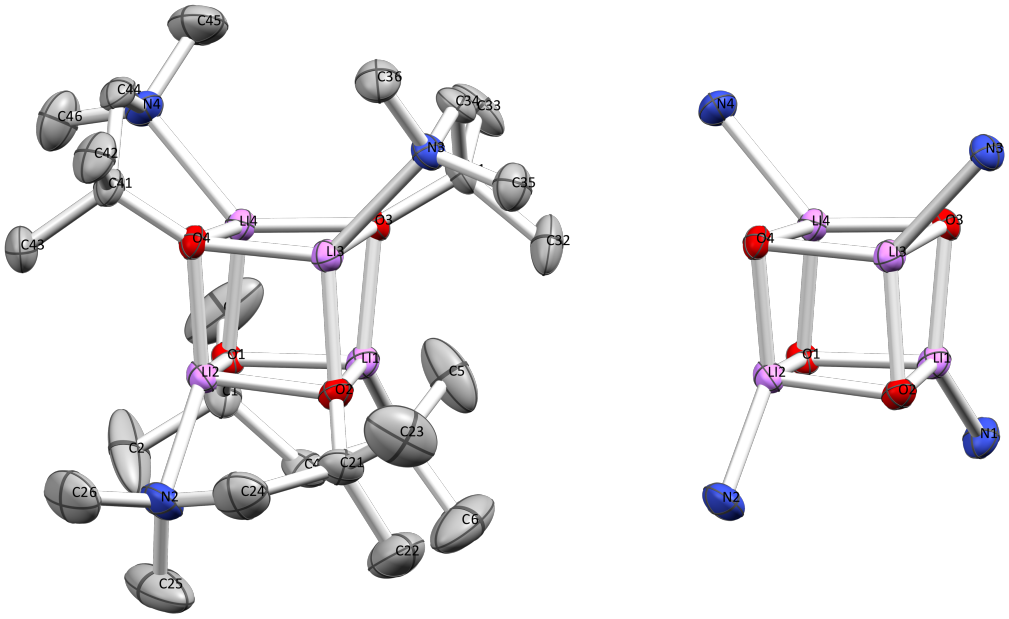

Figure 5.7. *Left: molecular structure of LiDMAMP. Middle: Cubane core of LiDMAMP Right: Structure of a lithium bonding sphere. Hydrogen atoms omitted for clarity and ellipsoids calculated at* 50%.

with the lithium occupying diagonal corners of the quadratic face. The Li-O bonds in the FDMAMP are, on average, longer than those in LiDMAMP at 1.977 Å and 1.934 Å respectively. The distorted cubane of NiFDMAMP is closer to ideal cubic geometry with average Li-O-Li and O-Li-O angles of 85.11° and 94.54° respectively. **Table 5.3** compares the geometry of both complexes, the differences in geometry are likely a consequence of the reduction in electron density on the oxygen, which has been withdrawn by the CF_3 fluorine groups.

X-ray analysis of the LiFDMAMP complex has shown it possesses S_4 symmetry in the solid state.[17, 18] NMR analysis of the complex suggests that in solution it is in equilibrium between S_4 and D_2 symmetry.[17, 18] Observed in the ^{1}H NMR spectra are two singlets which can be attributed to the six protons on the amine substituent, at 2.00 pmm (s, 6H) and 2.07 ppm (s, 6.4H). A further two singlets are observed at 2.49 ppm (s, 2H) and 2.54 ppm (s, 2.1H) which are associated with the protons positioned $OC(CF_3)_2C(\mathbf{H})_2$. Further to this, the ^{7}Li NMR spectrum of the complex displays two lithium peaks, one at 1.25 ppm and the other at 0.52 ppm in a ratio of 1:1.14. This alone is not evidence of the structural equilibria, however by happen stance, another sample of the complex had previously been analysed by both ^{1}H and ^{7}Li NMR. The concentration in the two samples are different which alters the solution equilibrium, as evidenced by a change in the ratio of peaks, as shown in **Table 5.2**. Further analysis is ongoing to evaluate

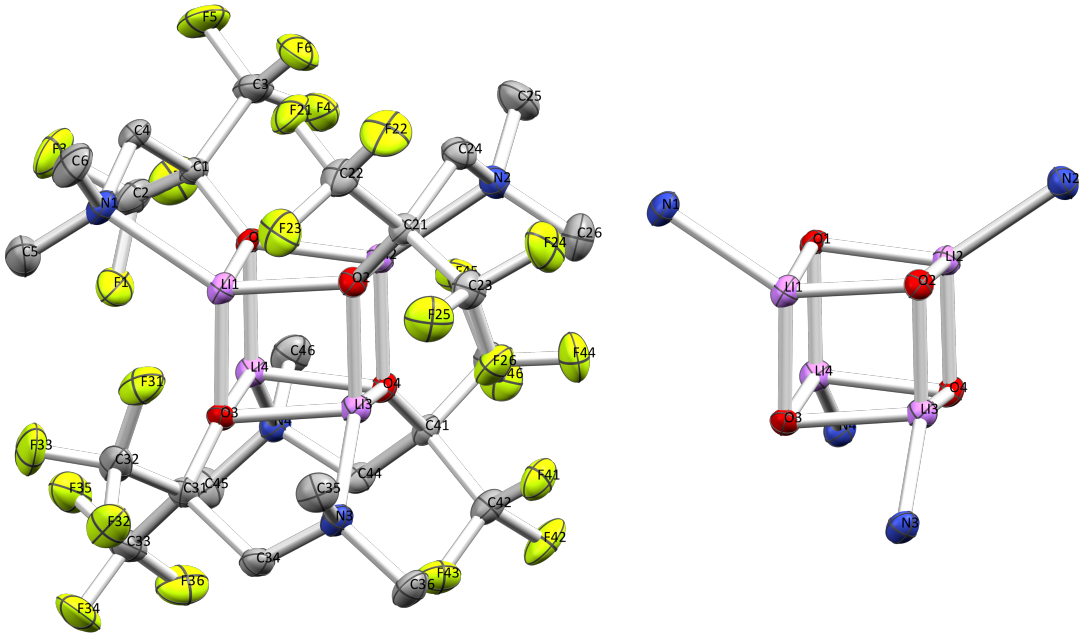

Figure 5.8. *Left: molecular structure of LiFDMAMP. Middle: Cubane core of LiFDMAMP Right: Structure of a lithium bonding sphere. Hydrogen atoms omitted for clarity and ellipsoids calculated at* 50%.

the equilibria and determine whether the D_2 or S_4 structure is favoured in solution.

^{1}H NMR		
Peak Position ppm	**LiFDMAMP Sample 1**	**LiFDMAMP Sample 2**
2.00	6.00	6.00
2.07	6.40	7.78
2.49	1.99	2.01
2.54	2.09	2.69
^{7}Li NMR		
0.52	1.00	1.00
1.25	1.14	0.80

Table 5.2. *Comparison of the relative integration of proton and lithium NMR peaks associated with the S_4 and D_2 LiFDMAMP cubane cores observed in solution.*

Shown in **Fig. 5.9** is the molecular structure of NaDMAMP. The core is a formed from two Na_3O_3 rings staggered with a distorted hexagonal prism structure. The hexagonal Na_3O_3 faces have a high order of symmetry with Na-O-Na and O-Na-O angles of 111.82° and 139.25° respectively. The deviation from ideal hexagonal geometry (120°) off sets the two Na_3O_3 rings,

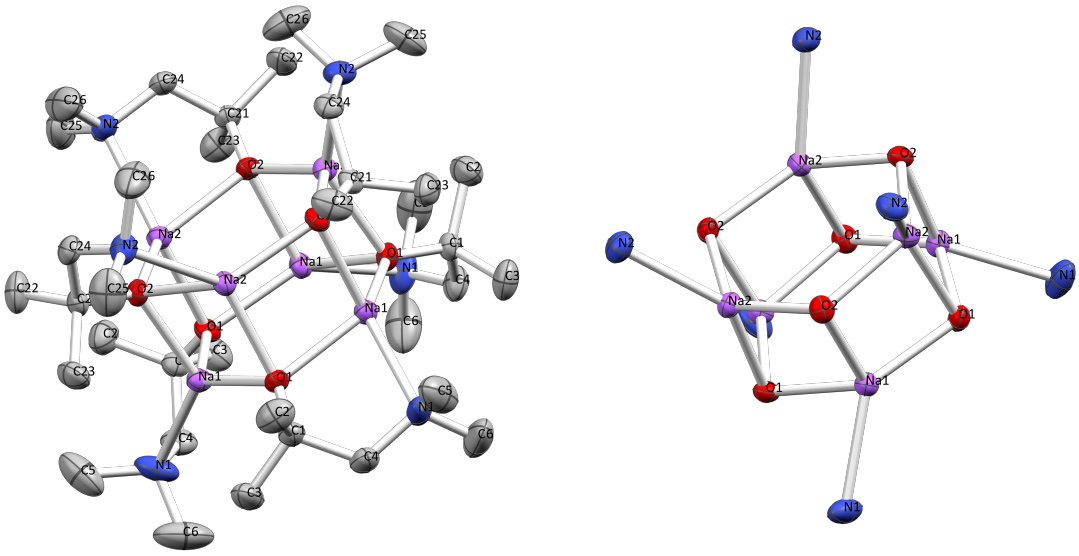

Figure 5.9. *Left: molecular structure of NaDMAMP. Middle: Hexameric Stack of NaDMAMP Right: Structure of the sodium bonding sphere. Hydrogen atoms omitted for clarity and ellipsoids calculated at* 50%.

which consequently distorts the quadrilateral Na_2O_2 face such that the K-O-K and O-K-O angles are 85.37° and 94.09° respectively. The alteration in structure from cubic to hexagonal, Li_4DMAMP_4 to Na_6DMAMP_6, is a consequence of the increase in ion size from Li to Na, 78 ppm and 98 ppm respectively. The co-ordination sphere of Na will be larger due to its greater atomic radii, which allows the structure to expand in order to lower the steric interaction of the DMAMP ligands.

Given the expansion from cubic to hexagonal geometry with increased group one metal ion size, the KDMAMP structure could be predicted as hexagonal. However, the 5-coordinate potassium atoms are arranged in a K_4O_4 cube, with a THF molecule bound to the potassium filling the potassium's co-ordination sphere. The K_4O_4 cube displays near ideal cubic geometry with O-K-O and K-O-K angles of 92° and 87.94° respectively. The co-ordination of the THF molecule introduces steric bulk to the molecule which pinches the O1-K1-N1 angle (63.14°) such that it is narrower than the other group one DMAMPs. The KDMAMP was not isolated from a solvent other than THF, so the structure without THF co-ordinated cannot be compared. Though given the size of the potassium ion and the trend observed from Li to Na, the structure of KDMAMP is predicted to be hexagonal similar to NaDMAMP.

The TGA profiles of LiDMAMP, NaDMAMP and KDMAMP-THF are shown in **Fig 5.11**. The

	LiDMAMP	LiFDMAMP	NaDMAMP	KDMAMP
MDMAMP				
M1-O1 (Å)	1.978	2.004	2.277	2.666
M1-N1 (Å)	2.130	2.132	2.499	2.953
O1-M1-N1 (°)	88.29	86.05	76.52	63.14
M1-O1-C1 (°)	110.73	111.94	114.56	112.96
O1-C1-C4 (°)	110.60	113.35	111.58	112.18
C1-C4-N1 (°)	115.94	113.66	117.71	114.12
C4-N1-M1 (°)	99.05	99.11	101.25	107.74
N1-M1-O3 (°)	123.23	121.70	139.25	63.14
N1-M1-O2 (°)	136.92	145.54	122.84	86.04
O2-M1-O1				111.08
Quadrilateral face				
M-O (Å)	1.934	1.977	2.314	2.629
M-O-M (°)	81.69	85.11	85.37	87.94
O-M-O (°)	97.72	94.54	94.09	92.00
Hexameric Face				
M-O (Å)			2.263	
O-M-O (°)			127.68	
M-O-M (°)			111.82	

Table 5.3. *Comparison of the MDMAMP Structural Geometries. Bond lengths and angles are given as an average of the structure.*

three compounds all demonstrate volatility and good stability with residual masses of 8.54% for Li/KDMAMP and 0.23% for NaDMAMP. The TGA profile of KDMAMP−THF has a two step volatilisation. The first step has a 1% mass loss at 72 °C and rests at 68%. This first step has been attributed to the volatilisation of THF (30% mass loss). The second step is volatilisation of KDMAMP and the residual mass is a result of thermal decomposition of the KDMAMP complex.

The TGA mass balance used for the collection of the MDMAMP thermal profiles is extremely sensitive to changes in mass. When held under the dynamic atmosphere of a glove box the mass balance alters with changes in pressure, hence why the LiDMAMP mass balance exceeds 100%. As such, the TGA profiles shown in **Fig 5.11** have an inconsistent machine error which could not be resolved and the profiles represent the best set of data that could be collected at the time. The Na/KO^{t}Bu thermal profiles in the report by Østreng *et al* cannot be accurately

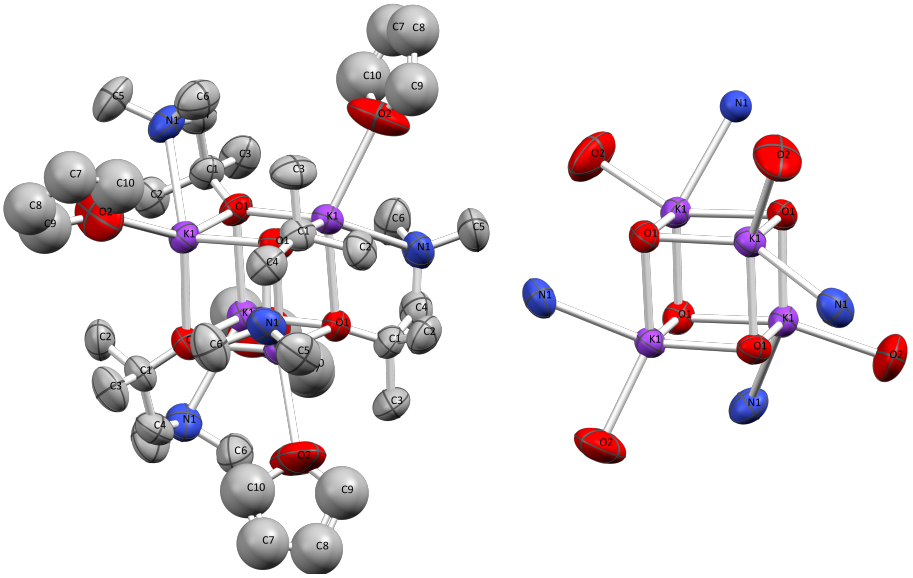

Figure 5.10. *Left: molecular structure of KDMAMP–THF. Middle: Cubane core of KDMAMP Right: Structure of the potassium bonding sphere. Hydrogen atoms omitted for clarity and ellipsoids calculated at* 50%.

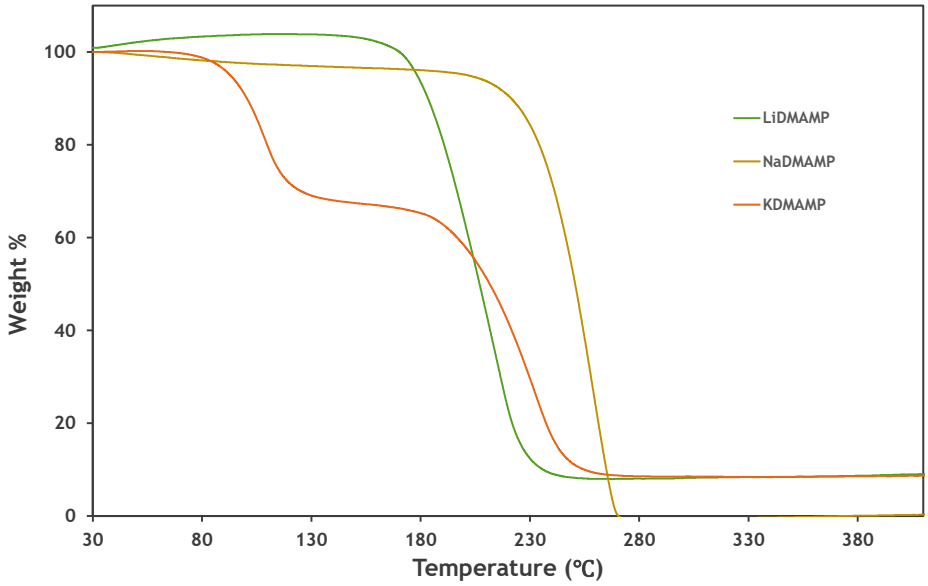

Figure 5.11. *TGA profiles of LiDMAMP (**3**), NaDMAMP (**4**) and KDMAMP (**5**) collected from with heating rate of* $5\,^{\circ}\mathrm{C\,min^{-1}}$.

compared to those in **Fig 5.11** because of the instrument error and a different experimental set up.[11] However, it is interesting that the thermal profiles of Na/KO^{t}Bu are both multi-step and occur at 200 °C, the same as NaDMAMP and KDMAMP. It is therefore probable that the

compounds NaDMAMP and KDMAMP could be used as ALD precursors. As both compounds have limited volatility below 200 °C they would likely require high deposition temperatures to prevent condensation and would not necessarily improve on the Na/KO^{t}Bu ALD processes as they would be limited by volatility and thermal stability.

Conclusions

Several Li, Na and K MDMAMP aminoalkoxides have been synthesised with either cubane or hexameric structures and TGA analysis shows all the complexes have limited volatility at low temperatures.[11] At the time of writing however, there is a scarcity of Na and K ALD precursors with sodium and potassium tertbutoxide the only published processes to date. ALD processes using NaDMAMP and KDMAMP would be potentially hindered by the compounds thermal stability, but it is important to expand the precursor library and provide options for materials processing. Neither NaDMAMP or KDMAMP were tested as precursors in this body of work though their limited ALD potential is worth exploring.

5.3 Nickel Pyrroles

As discussed by Utriainen *et al* in their report concerning the ALD of NiO with water and O_3, nickel precursors generally lack the reactivity to grow crystalline films with mild oxidants.[19] One method of enhancing a gas-surface ALD reactions is to alter the acidity of the ligand system. Consider a reaction between water and a surface chemisorbed metal ligand species in ALD. Ideally, the ligand system will be substituted protonated and the metal forms a new M-OH bond. Either the affinity of the Ni-L bond is weaker than that of M-OH or the L-H bond affinity greater than that of L-M. To enhance the rate of reaction either could be modified. The species (DMAMPH) has an estimated pKa of 10.2, a ligand system with a greater pKa that is more basic may drive the ALD reaction by the formation of the L-H bond. A group of compounds previously investigated within the research group, pyrroles and pyrroldienes, fit these criteria with an estimated pKa of 16.5.[20]

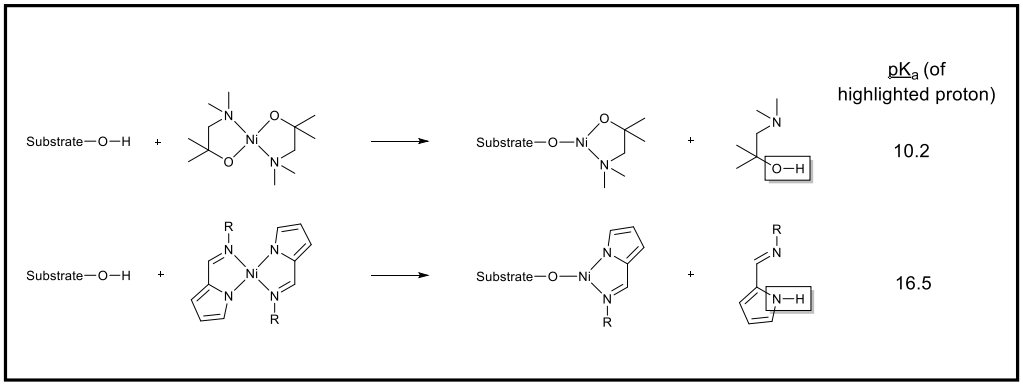

Figure 5.12. *Estimated pKa of Ni(DMAMP)$_2$ and a generic nickel(II) pyrrole.*

Six pyrrolidene pre-ligands were synthesised with varying alkyl and aryl substituents, in an attempt to alter the volatility and reactivity of the subsequent Ni(II) pyrrolide complexes. Each pre-ligand was subsequently coordinated to nickel and the complexes analysed by air-sensitive TGA. The thermal profiles were used to estimate which complexes have potential as NiO ALD precursors. The compounds nickel pyrroles **7-12** are shown in the **Fig 5.13**.

For the initial synthetic route to **7**, the isopropylpyrrolidene pre-ligand was reacted with $NaNH_2$, then a salt-metathesis reaction with $[Ni(NH_3)_6]Cl_2$ was completed the aim of synthesising complex, **7**. However, ammonia generated during synthesis, resulted in further substitution reactions such that an asymmetric complex was also produced as a reaction by-product (**7'**). To avoid making further asymmetric complexes pre-ligands were reacted with NaHMDS before isolation and $NiCl_2$ was utilised in place of $[Ni(NH_3)_6]Cl_2$. This synthetic approach eliminated the synthesis of the asymmetric products.

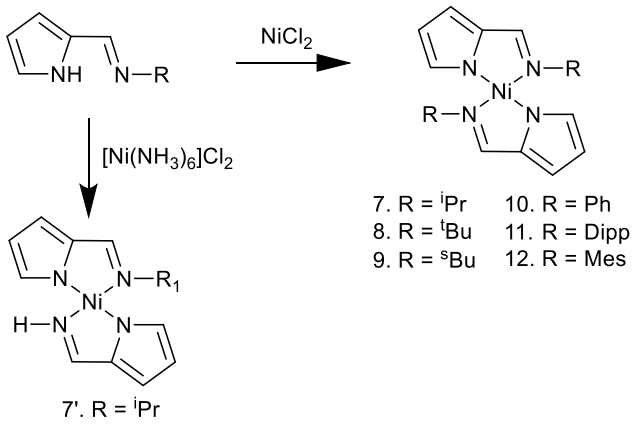

Figure 5.13. *Schematic for the synthesis of nickel(II) pyrrole compounds* ***7-12****.*

Nickel Pyrrole Structures

Single crystals of complexes **7** and **8** were analysed by x-ray diffraction. Complex **8** has previously been reported in literature, though the locations of the ^{t}Bu substituents were not solved and as such, a new experimental structure has been resolved.[21] Crystallographic data for the remaining complexes **10**, **11** and **12** are already present in literature and were not redetermined in this study.[22–24] Compound **9** had significant twinning and its crystal structure could not be resolved. Due to a lack of chemical characterisation data the physical properties of **9** were not pursued.

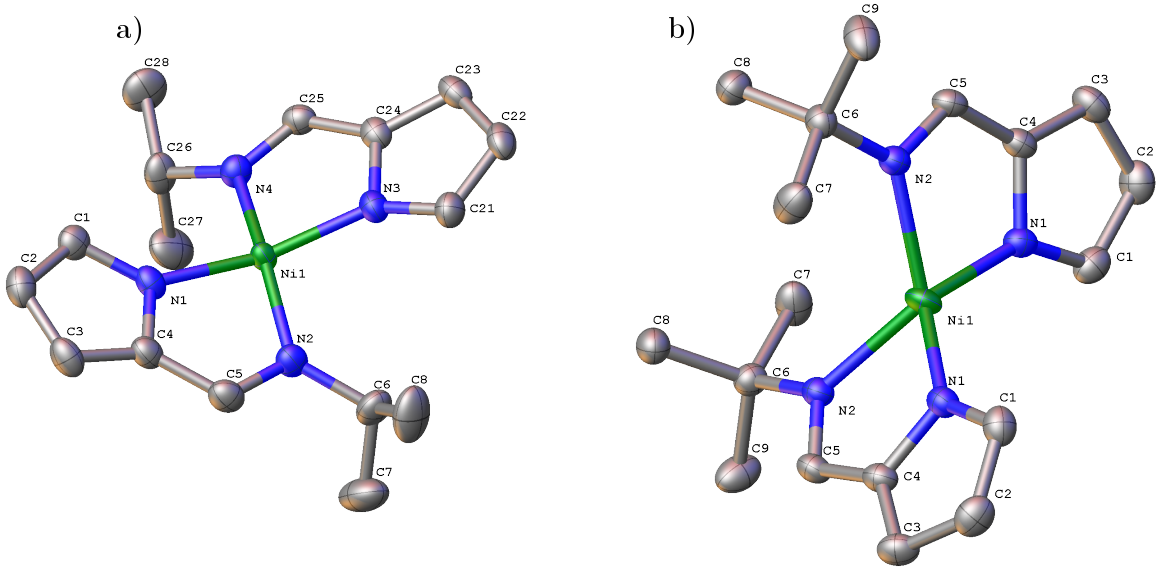

Figure 5.14. *a) Molecular structure of Ni(^{i}PrPyr)$_2$ (**7**), b) Molecular structure of Ni(^{t}BuPyr)$_2$ (**8**). Hydrogen atoms omitted for clarity and ellipsoids calculated at* 50%.

Four co-ordinate nickel(II) (d^8) complexes are versatile and can possess either tetrahedral or square planar geometry about the nickel center. Generally high spin Ni2+ tetrahedral complexes,

are a consequence the Ni-L bonds having ionic character or when ligands are sufficiently large, tetrahedral geometry can be adopted to reduce ligand-ligand repulsion. The complexes **7** and **8** are shown in **Fig 5.14** and possess pseudo square planar and tetrahedral geometry respectively. Comparing the two compounds the variation in structure is a consequence of the steric bulk of the ^{i}Pr and ^{t}Bu substituent. In order to minimise the repulsion between the N_1C_4 rings and the alkyl substituent, the nickel geometry distorts from ideal square planar to tetrahedral. For compound **7**, with the ^{i}Pr substituent, the steric clash is small enough that the complex favours a distorted square planar geometry. The molecule is not entirely planar with a shift out of plane by 28.11°, as shown in the inset in **Fig 5.14a**. Conversely the greater steric bulk of ^{t}Bu forces the nickel to adopt tetrahedral geometry with the two bidentate ligands near perpendicular to one another (90°). **Table 5.4** compares the relative geometries of complexes **7** and **8**.

	Ni(^{i}PrPyr)$_2$ (7)	**Ni(^{t}BuPyr)$_2$ (8)**
N1-Ni1 (Å)	1.8948(14)	1.9612(10)
N2-Ni1 (Å)	1.9129(14)	2.0376(10)
N3-Ni1 (Å)	1.8892(14)	1.9613(10)
N4-Ni1 (Å)	1.9299(14)	2.0376(10)
N1-Ni1-N2 (°)	83.51(6)	82.72(4)
N3-Ni1-N4 (°)	83.57(6)	82.72(4)
N1-Ni1-N4 (°)	98.46(6)	123.90(4)
N2-Ni1-N3 (°)	99.41(6)	127.57(6)
Ligand Bite (°)	28.11	87.88
τ_4	0.24	0.77

Table 5.4. *Comparison of the geometry of Ni(^{i}PrPyr)$_2$ (**7**) and Ni(^{t}BuPyr)$_2$ (**8**).*

A τ_4 analysis, equation **5.1** where α and β are the two largest angles in the four coordinate species, provides a qualitative assessment of four-coordinate geometry and calculates complexes **7** and **8** to have τ_4 values of 0.24 and 0.77 respectively.[25] A τ_4 value of 0 indicates ideal square planar geometry, and a value of 1 indicates ideal tetrahedral geometry. The τ_4 values of complexes **7** and **8** indicate there is out of plane distortion and that they possess neither ideal square planar geometry or ideal tetrahedral geometry.[25]

$$\tau_4 = \frac{360° - (\alpha + \beta)}{141°} \tag{5.1}$$

In solution, nickel complexes can exist in equilibria between diamagnetic (square planar) and paramagnetic (tetrahedral).[26] For complexes **7** and **8** the structures exhibit a structural change, indicated by an alteration in colour, when dissolved into different solvents. Compounds **7** and **8** were prepared in both deuterated THF (OC_4D_8) and deuterated benzene (C_6D_6). Compound **8** which is black in benzene is a pale yellow solution in THF, and compound **7** is a dark purple

in benzene and a lighter red/orange in THF. Given the alteration in colour, it is reasonable to suggest there is an alteration in $d-d$ transition energy, associated with a change in coordination environment about the Ni centre, which is confirmed by proton NMR analysis.

When compound **7** is solvated in C_6D_6 and the ^{1}H NMR analysed, all protons can be accounted for between δ 30.98 to 1.02 ppm, when solvated in OC_4D_8 this broadens to δ 208.2 to 3.22 ppm. Contrastingly, for the NMR analysis of **8** when solvated in C_6D_6 all protons are accounted for between δ 171 to -55 ppm which narrows to δ 8.02 to 3.22 ppm in OC_4D_8. For compound **7** given the broadening of the spectra and increase in paramagnetic quality from C_6D_6 to OC_4D_8, it has been concluded that the complex may have co-ordinated two OC_4D_8 molecules. Consequently, the nickel geometry alters from pseudo square planar to octahedral leaving two unpaired electrons, as illustrated in **Fig 5.15**. Conversely, for compound **8**, diamagnetic character increases as we change solvent from C_6D_6 to OC_4D_8. It is probable that a single THF molecule co-ordinates to the central nickel atom and the complex adopts a square based pyramid geometry. If two THF molecules co-ordinated, the Ni atom would possess octahedral geometry and remain paramagnetic. From the ^{1}H NMR analysis, we can surmise that a second OC_4D_8 molecule is restricted by the steric bulk of the ^{t}Bu substituent.

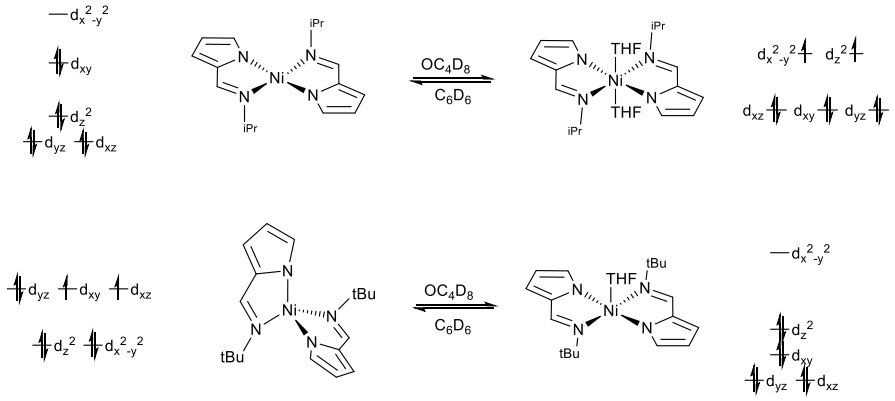

Figure 5.15. *Proposed schematic of the bonding in solution for Ni(^{i}PrPyr)$_2$ (**7**) and Ni(^{t}BuPyr)$_2$ (**8**).*

The magnetic moment of **7** was calculated using NMR susceptibility by Evans' method. The resulting magnetic moment of **7** was calculated as 1.62 BM. This corresponds to the spin of less than a single electron, suggesting in solution the complex is in equilibrium between the square planar and square based pyramid geometries, with the equilibrium favouring pseudo square planar geometry.

Pyrrole Thermal Analysis

As with the aminoalkoxide compounds discussed previously, the thermal analysis of the nickel pyrroles was completed in an inert atmosphere in open pan TGA boats. All samples were heated at a rate of 5 °C min^{-1} between 30-400 °C. The TGA profiles of the aryl pyrroles **10-12** are shown in **Fig 5.17** and the alkyl pyrroles **7, 8** in **Fig 5.16**.

For compounds Ni(^{i}PrPyr)$_2$ (**7**) and Ni(^{t}BuPyr)$_2$ (**8**) the thermal profiles both have a single step volatilisation with residual masses of approximately 2%. Ni(^{i}PrPyr)$_2$ has lost 1% of its mass at 155 °C and in a single volatilisation step it reaches its residual mass of 2% at 236 °C. Similarly Ni(^{t}BuPyr)$_2$ has slightly greater volatility losing 1% of its mass by 140 °C and completing a single step volatilisation to 2% residual mass by 232 °C.

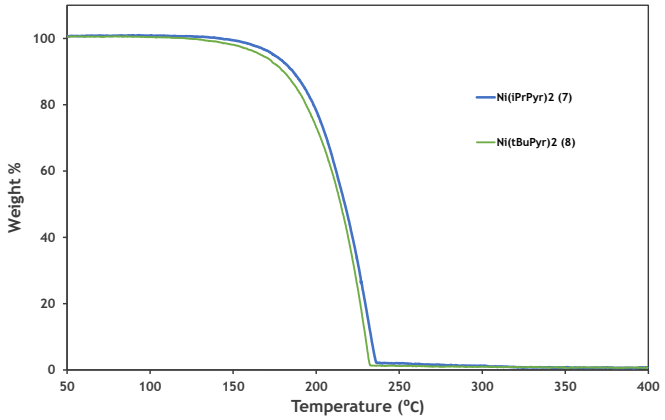

Figure 5.16. *TGA Profiles of compounds Ni(^{i}PrPyr)$_2$ (**7**) and Ni(^{t}BuPyr)$_2$ (**8**) collected at a heating rate of* 5 °C min^{-1}.

In contrast, compounds Ni(PhPyr)$_2$ (**10**), Ni(DippPyr)$_2$ (**11**) and Ni(MesPyr)$_2$ (**12**) do not demonstrate the thermal stability of compounds **7** and **8**. Compounds **10**, **11** and **12** have residual masses of 43%, 10% and 27.5% respectively. Each compound does not have a smooth volatilisation and the profiles are multi-step with the rate of mass loss varying as temperature increases.

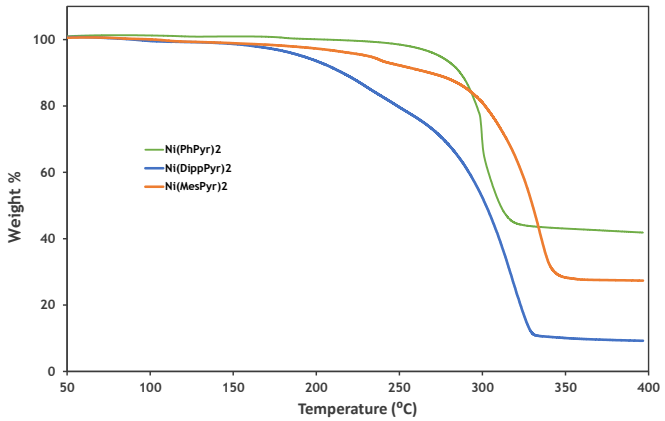

Figure 5.17. *TGA profiles of compounds Ni(PhPyr)$_2$ (**10**), Ni(DippPyr)$_2$ (**9**) and Ni(MesPyr)$_2$ (**10**) collected at a heating rate of* 5 °C min^{-1}.

To assess the potential of the nickel pyrroles as ALD precursors they can be compared to the complex Ni(DMAMP)$_2$ which was discussed in **5.2.2**. Given the poor thermal stability of the complexes Ni(PhPyr)$_2$ (**10**), Ni(DippPyr)$_2$ (**11**) and Ni(MesPyr)$_2$ (**12**) they have poor potential as NiO ALD precursors and will not be discussed further. Conversely, compounds Ni(^{i}PrPyr)$_2$ (**7**) and Ni(^{t}BuPyr)$_2$ (**8**) show greater thermal stability than Ni(DMAMP)$_2$ but demonstrate reduced volatility with Ni(DMAMP)$_2$ losing 1% mass at 55 °C. This is a promising result, the weaknesses of the Ni(DMAMP)$_2$ PEALD process discussed in Chapter 2 are that the thermal window is narrow (100-150 °C) and that films contain carbon impurities which are likely a consequence of thermal decomposition of Ni(DMAMP)$_2$. Given the thermal stability of the nickel pyrroles they may enable NiO deposition at a temperature greater than 150 °C without carbon incorporation. The limited volatility below 150 °C may be problematic, but provided the compound shows sufficient gas phase stability it may be a useful precursor for deposition of NiO at high temperatures.

Nickel Pyrroles Conclusions and Future Work

The nickel pyrroles analsyed in this study have demonstrated interesting thermal and electronic properties. The nickel pyrroles with aryl substiuents have all been previously documented in literature but no analysis of their thermal properties is present. Given that the aryl complexes demonstrate poor thermal stability and limited volatility, they do not have the properties necessary to be ALD precursors. However, the nickel alkyl pyrroles which have greater stability and are volatile above 145 °C, have greater potential as ALD precursors. Ni(^{i}PrPyr)$_2$ (**7**) and Ni(^{t}BuPyr)$_2$ (**8**) have similar thermal properties and so discerning which has greater potential as an ALD precursor from thermal profiles alone is not possible. ALD experimentation would be necessary to differentiate between the two.

The nickel pyrroles Ni(^{i}PrPyr)$_2$ (**7**) and Ni(^{t}BuPyr)$_2$ (**8**) were not prioritised as for ALD depositions during this body of work. Though upon reflection, the two compounds may make for an interesting study. Given that in solution the complexes are in equilibrium between multiple geometries, whether this trait lends itself to greater reactivity in the gas phase may be interesting. By comparing growth rates of films grown with compounds **7** or **8** with water as an oxygen source, it may be possible to discern which complex has greater gas phase reactivity. By comparing this to solution phase equilibria, it may be possible to ascertain whether the properties shown in solution lend themselves to gas phase reactivity.

Though not directly related to the ALD of NiO there is a study which can be completed with compounds **7** and **8**. Given the switching between paramagnetic and diamagnetic structures in differing solvents, determining whether this behaviour is also thermally dependant would be of interest. If either compound exhibits a reversible change in color when heated or cooled in solution the complexes may have potential application as a temperature sensors or temperature

dependant molecular switches.

5.4 Nickel Guanidinates

Similar structurally to amidinate complexes which have been extensively utilised for the ALD deposition of NiO, guanidinates were considered a possible new precursor group.[27–33] Guanidine is an N-donor bidentate ligand which can be altered by varying the substituents on the NCN backbone. By altering the steric bulk of the ligand the volatility of the resulting nickel complex may be altered. Volatile Cu, Co, Ni and Hf guanidinates have been reported for the ALD and CVD of their respective metal oxides.[34–37] However, at the time of investigation we were not aware of the report by Zhang *et al* which had already synthesised the nickel(II) isopropylguanidinate complex and had reported both its structure and thermal properties.[35] The report had noted that the compound is volatile but thermally unstable and it was utilised in the CVD deposition of NiO. The findings of our investigation are in agreement with their study and have found both nickel(II) bis-isopropylguanidinate **(13)** and nickel(II) bis-cyclohexylguanidinate **(**14) unsuitable as ALD precursors.

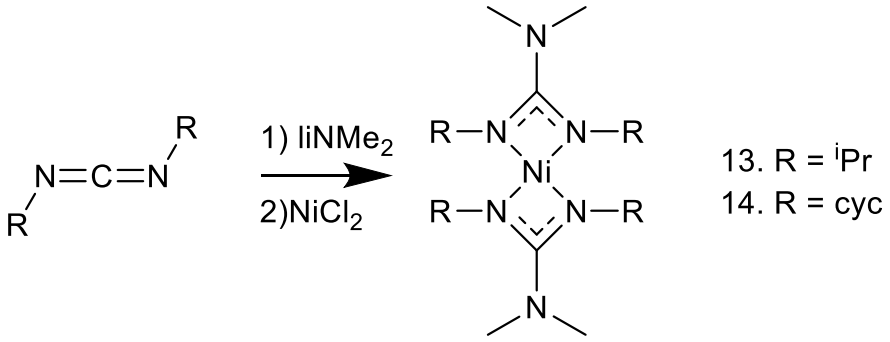

Figure 5.18. *Reaction scheme for the synthesis of the Nickel(II) Guanidinates.*

Nickel (II) Guanidinate Structures

The guanidinate complexes Ni(^{i}PrGu)$_2$ **(13)** and Ni(CycGu)$_2$ **(14)** are mononuclear with the nickel atom surrounded by four N atoms in a pseudo square planer geometry. The average Ni-N bond lengths of **13** and **14** are equal to 1.933 Å and 1.925 Å respectively. The structure of **(13)** is in excellent agreement with that reported by Zhang *et al* and **14** has a similar molecular structure.[35] Notably, in complexes **13** and **14** there is a high degree of symmetry on the carbon atom on the NCN backbone. In complex **14** the the C-N bond lengths (1.333Å and 1.335Å) and C-N-C bond angles (124.67° and 124.85°) suggest there is a high degree of π-electron delocalisation. A τ_4 analysis, which provides a qualitative assessment of four-coordinate geometry, calculates complexes **13** and **14** to have τ_4 values of 0.07 and 0.08 respectively.[25] A τ_4 value of 0 indicates ideal square planar geometry and the τ_4 values of complexes **13** and **14**

indicate there is negligible out of plane distortion and that they possess near ideal square planar geometry.[25]

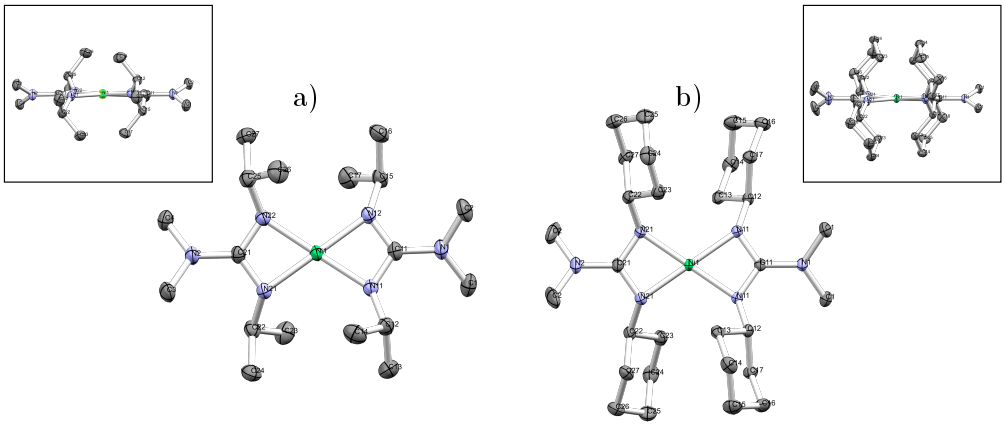

Figure 5.19. *Molecular structure of a) Ni(^{i}PrGu)$_2$* ***(13)*** *and b) Ni(CycGu)$_2$* ***(14)****.*

Ni(^{i}PrGu)$_2$ (13)

Ni1 - N11	1.9351(14)	N11-Ni1-N12	69.14(6)
Ni1 - N12	1.9289(14)	N21-Ni1-N22	69.17(6)
Ni1 - N21	1.9379(14)	N21-C21-N2	124.4(2)
Ni1 - N22	1.9297(14)	N22-C21-N2	125.1(2)
N12 - C11	1.338(2)	N11-C11-N1	125.3(2)
N11 - C11	1.333(2)	N1-C11-N12	124.4(2)
N21 - C21	1.337(2)	N11-C11-N12	110.3(1)
N22 - C21	1.335(2)	N21-C21-N22	110.5(1)

Ni(CycGu)$_2$ (14)

Ni1 - N11	1.9230(10)	N11-Ni1-N11	69.48(6)
Ni1 - N21	1.9271(11)	N21-Ni1-N21	69.41(7)
Ni1 - N11	1.9230(10)	N11-C11-N1	124.84(8)
Ni1 - N21	1.9271(11)	N11-C11-N1	124.84(8)
N21 - C21	1.3332(15)	N11-C11-N11	110.31(15)
N11 - C11	1.3353(14)	N21-C21-N2	124.84(8)
		N21-C21-N2	124.84(8)
		N21-C21-N21	110.77(16)

Table 5.5. *Selected bonds lengths (Å) and angles (°) for Ni(^{i}PrGu)$_2$* ***(13)*** *and Ni(CycGu)$_2$* ***(14)****.*

Guanidinate Thermal Analysis

Both guanidinate complexes had their thermal behaviour analysed by TGA to assess whether they were suitable ALD precursors. All TGAs were performed in an inert atmosphere in open pans between 30-400 °C at a ramp rate of 5 °C min^{-1}. Both compounds Ni(^{i}PrGu)$_2$ **(13)** and Ni(CycGu)$_2$ **(14)** display poor thermal suitability as ALD precursors, with multistep volatilisations and residual masses of 20.1% and 16.3% respectively. The high residual mass suggests that both compounds decompose during volatilisation.

Notably, the TGA profile observed for compound **13** differs than that reported by Zhang *et al.*[35] In our results complex **13** has a higher residual mass (20.1%*vs*12.3%) and contrastingly the published TGA profile is a single step volatilisation. This is partially a consequence of the slower ramp rate used within this study (5 °C min^{-1} vs 10 °C min^{-1}). Because the heating rate is slower within this study, a greater degree of decomposition can occur during the volatilisation step. Interestingly the complex also has a lower T_{50} of 166 °C compared to 176 °C reported by Zhang *et al.*[35] Given the change in evaporation rate at approximately 165 °C, it is plausible that above this temperature is where decomposition begins. Unfortunately, due to the inaccuracy of the equipment no firm conclusions can be drawn.

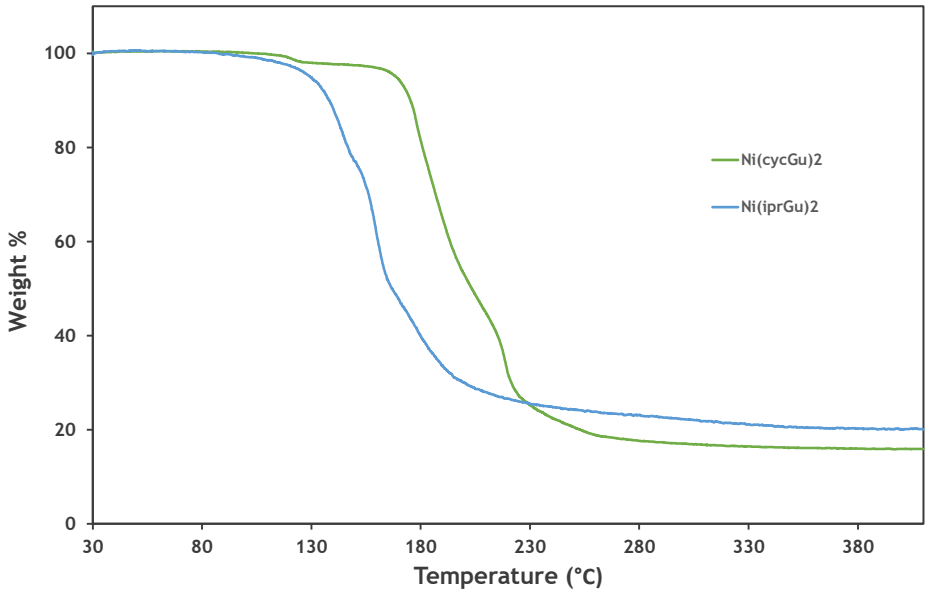

Figure 5.20. *TGA profiles of compounds Ni(^{i}PrGu)$_2$* ***(13)*** *and Ni(CycGu)$_2$* ***(14)****, collected at a heating rate of* 5 °C min^{-1}.

Guanidinate Conclusions

Given the relative success of nickel amidinate as an ALD precursor it was hypothesised that nickel guanidinates may be suitable NiO ALD precursors. Two complexes Ni(^{i}PrGu)$_2$ **(13)** and Ni(CycGu)$_2$ **(14)** were synthesised, their crystal structures analysed and thermal properties examined by TGA. Though volatile, both complexes were found to be unsuitable ALD precursors due to their thermal instability. Given that Ni(^{i}PrGu)$_2$ has been reported as a NiO CVD precursor, Ni(CycGu)$_2$ with similar thermal properties is likely better suited to CVD rather than ALD.

5.4.1 Bis(β-ketoamino)Nickel(II) Complexes

Metal acetylacetonate complexes have been utilised for the deposition of both transition metal and main group films using both ALD and CVD.[38–41] Metal acetylacetonates are however, limited by both poor volatility and low reactivity. Consequently, high temperatures or oxidative species such as O_3 are generally required for film growth.[40, 42] To address this low reactivity nickel(II) β-ketoiminates, which are similar in structure but potentially more reactive than the acetylacetonates, due to the relatively weak M-N bonding, could present a new group of precursors for the CVD/ALD of NiO.

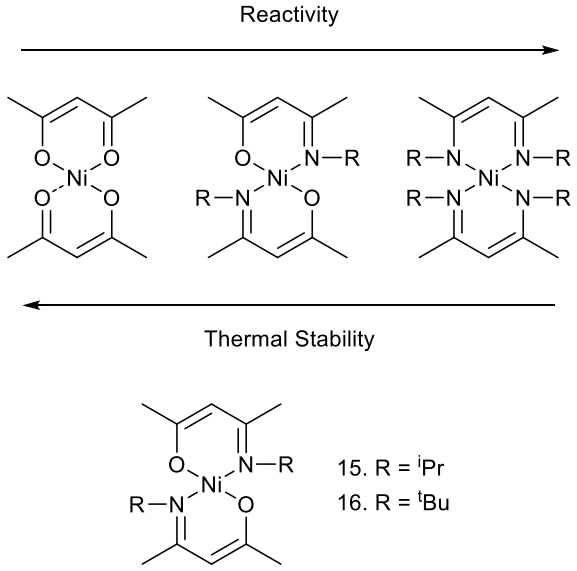

Figure 5.21. *Molecular structures of bis(β-ketoamino)nickel(II) complexes.*

The first nickel(II) β-ketoiminates were reported by Everett *et al* and focused on the solution equilibria between tetrahedral and square planar complexes.[43] These Schiff-base ligands are highly suited to ALD and CVD chemistry because the backbone and side chain can be engineered to vary the resulting metal complexes volatility.[44–46] Though currently only two reports have utilised nickel Schiff Bases for the CVD of NiO.[47, 48] Both investigations utilised sterically encumbered β-iminocarbonylenolato complexes and salicylaldimine ligands which limited the volatility and high deposition temperatures were necessary for film growth.[47, 48] Through the targeted synthesises of low molecular weight nickel(II) β-ketoiminates volatile and reactive Schiff-base complexes for the ALD of NiO may be found. To that end, three complexes Ni(^{i}PrNacAc)$_2$ (**15**), Ni(^{t}BuNacAc)$_2$ (**16**) and Ni(EtNacA)$_2$ (**17**) were synthesised and their potential as ALD precursors assessed by TGA.

5.4.2 Bis(β-ketoamino)Nickel(II) Structures

Similar to iron and cobalt analogues, the three nickel β-ketoamino complexes crystallise as monomers in orthorhombic crystal systems.[44, 45] Like the nickel pyrroles discussed previously,

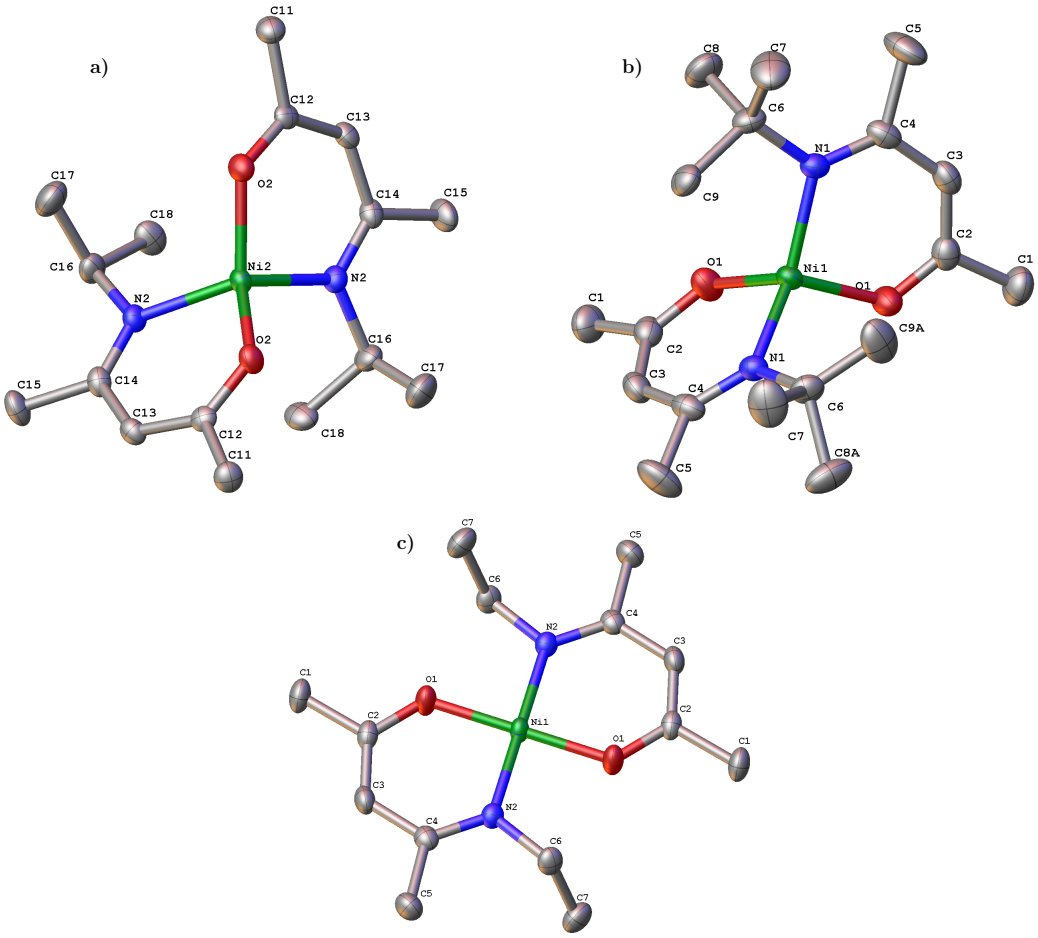

Figure 5.22. *Molecular structures of the Nickel(II)β-ketoamino complexes a) Ni(^{i}PrNacAc)$_2$ (**15**), b) Ni(^{t}BuNacAc)$_2$ (**16**) and c) Ni(EtNacAc)$_2$ (**17**).*

as the bulk of the alkyl substituent is increased the co-ordination geometry of the central nickel atom varies. As the steric bulk increases from Et>^{i}Pr, the geometry is forced from square planar to tetrahedral. The Ni(^{i}PrPyr)$_2$ complex discussed previously is pseudo square planar, in contrast the Ni(^{i}PrNacAc)$_2$ (**15**) is tetrahedral. With increased ring size from the five-membered pyrrole to six-membered β-ketoiminates, there is an increase steric repulsion between the isopropyl substituent and the opposite ligand because the separation has been reduced by 0.3Å, this forces a change in geometry about the nickel centre.

A τ_4 analysis can provide a qualitative assessment of the geometry of four-coordinate complexes.[25] While τ_4 of complex **17** is 0 indicating it is ideal square planar, complexes **15** and **16** have τ_4 values of 0.82 and have deviated from ideal tetrahedral geometry ($\tau_4 = 1$). Whilst less distorted than the Ni(^{t}BuPyr)$_2$ complex ($\tau_4 = 0.76$) they show a similar degree of distortion as other transition metal β-ketoamino complexes.[44, 45]

The Ni-O bond lengths for all the β-ketoamino complexes are between 1.830-1.91Å and the Ni−N between 1.946-1.986Å which is within the range associated with other transition metal

	Ni(EtNacAc)$_2$	**Ni(^{i}PrNacAc)$_2$**	**Ni(^{t}BuNacAc)$_2$**
Ni1-N2	1.9462(11)	1.980(2)	1.9859(16)
Ni-O1	1.8315(10)	1.918(2)	1.9187(15)
N1-C4	1.311(2)	1.303(4)	1.316(3)
O1-C2	1.289(2)	1.301(4)	1.283(3)
C2-C3	1.353(2)	1.375(4)	1.372(3)
C3-C4	1.423(2)	1.424(4)	1.427(3)
N1-Ni1-O1	92.68(5)	94.97(9)	96.60(6)
N1*-Ni1-O1*	92.68(5)	94.97(9)	96.60(6)
N1-Ni1-O1*	87.32(5)	112.33(10)	111.35(6)
N1*-Ni1-O1	87.32(5)	112.33(10)	111.35(6)
N1-Ni1-Ni1*	180	119.93(15)	132.60(10)
O1-Ni1-O1*	180	124.45(15)	106.87(11)
τ_4	0	0.82	0.82

Table 5.6. *Selected bonds lengths (Å) and angles (°) for Ni(^{i}PrNacAc)$_2$ (**15**), Ni(^{t}BuNacAc)$_2$ (**16**) and Ni(EtNacA)$_2$ (**17**)*

β-ketoiminates.[44, 45] Across the backbone of the nickel β-ketoamino complexes the N(1)-C(4) and O(1)-C(2) bond lengths are approximately 1.3Å and 1.29Å respectively. These values are between the ideal single and double bonds lengths for N-C and O-C bonds and suggest that there is delocalisation of the π-electrons on the back bone. This verified by evidence of intermediate C−C bond lengths between C2-C3 (1.29Å) and C3-C4 (1.42Å).

(β-ketoamino)Nickel(II) Thermal Analysis

The thermal gravimetric analysis of the β-ketoiminates was completed in an inert atmosphere in open pan TGA boats. All samples were heated at a rate of 5 °C min^{-1} between 30-400 °C. Shown in **Fig 5.23** are the thermal profiles of Ni(^{i}PrNacAc)$_2$ (**15**) and Ni(^{t}BuNacAc)$_2$ (**16**). The thermal profile of Ni(EtNacAc)$_2$ could not be collected. Despite repeated attempts a fault with the instrument scale, which persisted until this document was written, meant that collecting data which represented the true thermal profile of the complex was not possible.

Complexes **15** and **16** have differing thermal profiles. Complex **15** has a single step volatilisation with a residual mass ranging between $3-6\%$ and a T_{50} of approximately 152 °C. Unfortunately the instrument scale creep, means the mass increases to 103% and slowly fluctuates post evaporation step, the data can only be used an estimation of the compounds thermal properties. Complex **16** completes a two step volatilisation; the first has a 1% mass loss by 60 °C and a residual mass of 90%, the second step has a residual mass of 14% and a T_{50} of 192 °C. The first volatilisation is likely of solvent impurities, possibly hexane (BPT 68 °C) and the second step is

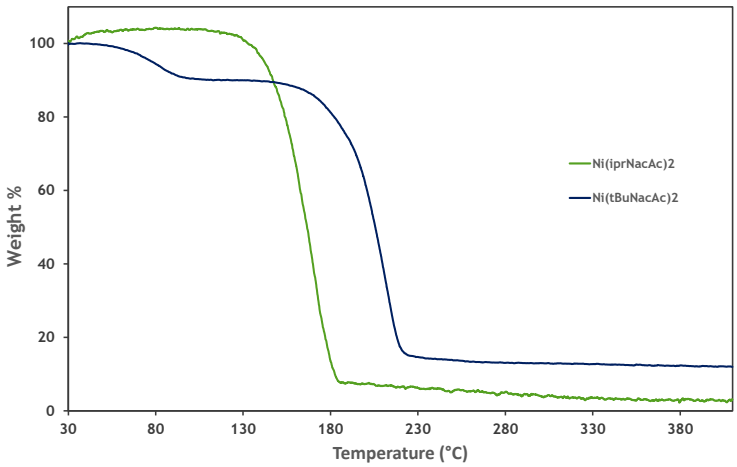

Figure 5.23. *Thermal gravimetric profiles of Ni(^{i}PrNacAc)$_2$ (**15**) and Ni(^{t}BuNacAc)$_2$ (**16**) collecetd with a heating rate of* $5\,^{\circ}\mathrm{C\,min^{-1}}$

likely the volatilisation of complex **16**.

Given its high residual mass and low evaporation temperature, complex **16** is likely better suited as a CVD precursor than ALD, as it does not have the required thermal stability or volatility. Given the low quality TGA data set it is hard to accurately estimate whether complex **15** has the stability for ALD application. However, it is less volatile than Ni(DMAMP)$_2$ and has similar stability. Using Ni(DMAMP)$_2$ as a relative comparison, complex **15** presents few benefits as an ALD precursor and like **16**, is likely better suited to CVD.

Bis(β-ketoamino)Nickel(II) Conclusions and Future Work

Three nickel β-ketoiminates were synthesised, their structures characterised and their thermal properties determined by TGA. It was found that by engineering the size of the ligand side chain the molecular geometry of the nickel could be altered from square planar to tetrahedral. Though the volatility of square planar and tetrahedral complexes could not be compared, Ni(^{i}PrNacAc)$_2$ (**15**) was found to be more volatile than the relatively heavy, Ni(^{t}BuNacAc)$_2$ (**16**). Whilst none of the complexes have suitable volatility or thermal stability for the application as NiO ALD precursors, they may be suited to CVD processes which have less stringent precursor requirements.

The synthesis of the β-ketoiminates was intended as a two part investigation, with the intention to compare the nickel β-ketoiminates to nickel diketiminates (NacNac) complexes. That study still has value as currently, the β-ketoiminates analysed in this investigation remain unpublished and no study has yet reported the synthesis and thermal properties of the nickel diketiminates. Given the increase in the number of Ni-N bonds from NacAc to NacNac, it is plausible that the nickel

diketiminates would display greater reactivity than the β-ketoiminates, yet whether the NacNacs would they have suitable thermal stability for application in ALD remains unanswered.[49]

5.5 Experimental

All chemicals supplied by Sigma Aldrich Inc. or Alfa Aesar with no further purification. Unless stated, all solvents were dried over a purification system (Innovative Technology Incorporated PS-400-7) and freeze-thaw degassed before use. Elemental analyses were performed using an Exeter Analytical CE 440 analyser. All NMR experiments were carried out using J Youngs valve NMR tubes prepared in a glove box. NMR data was collected at 25 °C unless otherwise stated, using either a Bruker Avance AV-300, Avance AV-400 or Avance II+ AV-500 spectrometer. in deuterated benzene, C_6D_6. Chemical shifts, δ, are given in parts per million, ppm, and nJ values in Hertz, Hz. Solid state molecular structures were obtained by Dr. A.L. Johnson, University of Bath, Department of Chemistry, using a RIGAKU SuperNova Dual Spectrometer or a RIGAKU Xcalibur. TGA analysis was performed under nitrogen (20 ml min^{-1}) at a ramp rate of 5 °C min^{-1} between 50 and 600 °C on a PerkinElmer TGA4000 with autosampler; samples were contained in alumina crucibles (open pans). Elemental analysis was performed under inert conditions by the elemental analysis service at the Science Centre, London Metropolitan University, UK.

5.5.1 Aminoalkoxides

2-Dimethylamino-2-methylpropanol, DMAMP (1a)

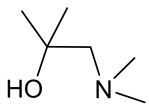

Under an inert atmosphere of argon gas, an excess of dimethylamine (30 mL) was condensed using liquid nitrogen onto lithium trifluoromethanesulfonate (2.0 g, 12.8 mmol). To this 1,2-Epoxy-2-methylpropane (22.75 mL, 0.256 mol) was added via syringe. The reaction mixture was left to stir for twelve hours. The unreacted dimethylamine was allowed to evaporate and 50 mL of water was added. The product was extracted in dichloromethane and dried over $MgSO_4$. After filtration the solvent is removed under vacuum to afford a colourless liquid. (25.60 g, 85%).

^{1}H NMR (300 MHz, Benzene-d_6) δ_{ppm} 1.13 (s, $N(C\mathbf{H}_3)_2$, 6 H), 2.02 (s, $C\mathbf{H}_2N(CH_3)_2$, 2H), 2.10 (s,$C(C\mathbf{H}_3)_2OH$, 6H), 2.78 (br s, $C(CH_3)_3O\mathbf{H}$, 1H).
^{13}C NMR (75 MHz, Benzene-d_6) δ_{ppm} 28.3 ($N(\mathbf{C}H_3)_2$), 48.2 ($HOC(\mathbf{C}H_3)_2$, 69.7 ($HO\mathbf{C}(CH_3)_2$, 70.2 $N\mathbf{C}H_2C(CH_3)_2$.

2-((dimethylamino)methyl)-1,1,1,3,3,3-hexafluoropropan-2-ol, FDMAMP (2a)

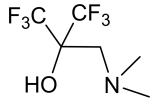

Under an inert atmosphere of argon gas, an excess of dimethylamine (20 mL) was condensed

using liquid nitrogen onto lithium trifluoromethanesulfonate (0.22 g, 14 mmol). To this 2,2-bis(trifluoromethyl)-oxirane (5.00 g, 27 mmol) was added via syringe. The reaction mixture was left to stir overnight. The unreacted dimethylamine is allowed to evaporate and 50 mL of water was added. The product was extracted in dichloromethane and dried over $MgSO_4$. After filtration the solvent is removed under vacuum to afford a colourless liquid.

^{1}H NMR (300 MHz, Benzene-d_6) δ_{ppm} 1.64 (s, (N(C**H**$_3$)$_2$, 6H), 2.27 (s, N(C**H**$_3$)$_2$, 6H).
^{13}C NMR (75 MHz, Benzene-d_6) δ_{ppm} 44.2 (N(**C**H$_3$)$_2$) , 53.7 (N**C**H$_2$), 70.4 (m, C(**C**F$_3$)$_2$), 76.2 (**C**(CF$_3$)$_2$).
^{19}F NMR (470.6 MHz, Benzene-d_6) δ_{ppm} -78.4 (s, C(C**3**), 6F).

1-Ethylmethylamino-2-methylpropanol, EMAMP (1.1a)

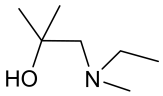

N-Ethylmethylamine (1.19 g, 20 mmol) was added to a suspension of lithium trifluoromethanesulfonate (0.156 g) in 1,2-Epoxy-2-methylpropane (1.43 g) and hexane (100 mL) and the reaction allowed to stir for twelve hours. The solution is washed with water (50 mL) and the product extracted in dichloromethane and dried over $MgSO_4$. After filtration the solvent is removed under vacuum to afford a colourless liquid (1.94 g, 73%).

^{1}H NMR (300 MHz, Benzene-d_6) δ_{ppm} 0.84 (t, NCH$_2$C**H**$_3$, 3H, J = 7.1 Hz), 1.14 (s, HOC(C**H**$_3$)$_2$, 6H), 2.08 (s, NC**H**$_2$C(CH$_3$)$_2$, 2H), 2.11 (s, NC**H**$_3$, 3H), 2.28 (q, NC**H**$_2$CH$_3$, 2H, J = 7.1 Hz).
^{13}C NMR (75 MHz, Benzene-d_6) δ_{ppm} 13.0 (NCH$_2$**C**H$_3$), 20.9 (OC(**C**H$_3$)$_2$), 41.6 (O**C**(CH$_3$)$_2$), 52.2 (N**C**H$_2$C(CH$_3$)$_2$), 63.3 (N**C**H$_3$), 65.7 (N**C**H$_2$C(CH$_3$)).

1-Ethylmethylamino-2-propanol, EMA2P (1.2a)

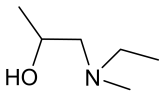

N-Ethylmethylamine (2.00g, 33.8 mmol) was added to a suspension of lithium trifluoromethanesulfonate in propylene oxide (1.96 mL, 33.8 mmol) and hexane (100mL), the solution was refluxed for twelve hours. The solution was washed with water (50 mL) and the product extracted in dichloromethane and dried over $MgSO_4$. After filtration the solvent is removed under vacuum to afford a colourless liquid (2.40 g, 65%).

1^1H NMR (300 MHz, Benzene-d_6) δ_{ppm} 0.81 (t, NCH$_2$C**H**$_3$, 3H, J = 5.5Hz), 1.11 (d, HOCHC**H**$_3$, 3H, J = 6.1Hz), 1.87 (m, NC**H**$_2$CH$_3$, 1H), 1.93 (s, NC**H**$_3$, 3H), 2.07 (m, NC**H**$_2$CH$_3$, 1H), 2.07 (m, NC**H**$_2$CH, 1H), 2.23 (m, NC**H**$_2$CH, 1H), 3.69 (m, HOC**H**CH$_3$, 1H).

^{13}C NMR (75 MHz, Benzene-d$_6$) δ_{ppm} 12.5 (NCH$_2$**C**H$_3$), 19.8 (HOCH(**C**H$_3$), 41.2 O**C**H(CH$_3$), 51.5 N**C**H$_2$CH$_3$, 62.5 N**C**H$_3$, 64.9 (N**C**H$_2$CH(CH$_3$).

1-Diethylamino-2-propanol, DEA2P (1.3a)

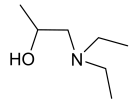

30 mL of diethylamine was added to a solution of suspension of lithium trifluoromethanesulfonate in propylene oxide (5.8g, 0.1 mol) and hexane (100 mL), the solution was refluxed for twelve hours. The solution was washed with water (50 mL) and the product extracted in dichloromethane and dried over $MgSO_4$. After filtration the solvent is removed under vacuum to afford a colourless liquid (10.72 g, 81%).

1^{1}H NMR (300 MHz, Benzene-d$_6$) δ_{ppm} 0.76 (t, N(CH$_2$C**H**$_3$)$_2$, 6H, J = 7.1 Hz), 1.13 (d, HOCH(C**H**$_3$), 3H, J 6.1 = Hz), 2.05 (m, NC**H**$_2$CH, 2H), 2.18 (m, N(C**H**$_2$CH$_3$)$_2$, 2H), 2.35 (m, N(C**H**$_2$CH$_3$)$_2$, 2H), 3.60 (m, HOC**H**CH$_3$, 1H).
^{13}C NMR (75 MHz, Benzene-d$_6$) δ_{ppm} 12.4 (N(CH$_2$**C**H$_3$)$_2$), 20.4 (OCH(**C**H$_3$), 51.9 (N(**C**H$_2$CH$_3$)$_2$), 62.8 (HO**C**H(CH$_3$), 65.1 (N**C**H$_2$).

Lithium DMAMP (3)

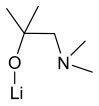

Under an inert atmosphere of argon gas, LiHMDS (7.10 g, 42 mmol) was added to DMAMP (5.00g, 42 mmol) in THF (50 mL). The reaction was the left to stir for twelve hours. Solvent and HMDS was removed in vacuo. To yield an off-white solid. The solid is crystallized in hexane to yield the desired product (3.90 g, 74%).

^{1}H NMR (300 MHz, Benzene-d$_6$) δ_{ppm} 1.31 (s, N(C**H**$_3$)$_2$, 6H), 2.28 (s, NC**H**$_2$, 2H), 2.31 (s, OC(C**H**$_3$)$_2$, 6H).
^{13}C NMR (75 MHz, Benzene-d$_6$) δ_{ppm} 34.4 (N(**C**H$_3$)$_2$, 49.6 (OC(**C**H$_3$)$_2$), 69.9 (O**C**(CH$_3$)$_2$), 76.8 (N**C**H$_2$).
^{7}Li NMR (194.317 MHz, Benzene-d$_6$)δ_{ppm} 1.02 (s, C(CH$_3$)$_2$O**Li**)
Anal. Calc for C$_6$H$_{14}$NLiO: C, 58.53, H, 11.46, N, 11.38, found: C, 58.49, H, 11.40, N, 11.34.

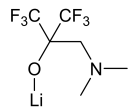

Lithium FDMAMP (4)

Under an inert atmosphere of argon gas, LiHMDS (0.37 g, 2 mmol) was added to FDMAMP (0.5 g, 2 mmol) in THF (30 mL). The reaction was the left to stir for twelve hours. Solvent and HMDS was removed in vacuo. To yield an off-white solid. The solid is crystallized in hexane to yield the desired product (0.40 g, 78%).

^{1}H NMR (300 MHz, Benzene-d$_6$) δ_{ppm} 1.80 (s, (N(C**H**$_3$)$_2$, 6H), 2.35 (s, N(C**H**$_3$)$_2$, 6H).

^{13}C NMR (125.7 MHz, Benzene-d$_6$)δ_{ppm} 127.5 (N(**C**H$_3$)$_2$, 127.7 (OC(**C**H$_3$)$_2$), 127.8 (O**C**(CH$_3$)$_2$), 127.9 (N**C**H$_2$).

Sodium DMAMP (5)

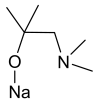

Under an inert atmosphere of argon gas, NaHMDS (1.84 g, 10 mmol) was added to DMAMP (1.18 g, 10 mmol) in THF (10 mL). The reaction was the left to stir for twelve hours. Solvent and HMDS was removed in vacuo to yield an off-white solid. The solid is crystallized in hexane to yield the desired product (1.08 g, 77%).

^{1}H NMR (300 MHz, Benzene-d$_6$) δ_{ppm} 1.26 (s, N(C**H3**)$_2$, 6H), 2.21 (s, NC**H**$_2$, 2H), 2.23 (s, OC(C**H**$_3$)$_2$, 6H).

^{13}C NMR (75 MHz, Benzene-d$_6$) δ_{ppm} 32.6 (N(**C**H$_3$)$_2$, 49.3 (OC(**C**H$_3$)$_2$) , 69.9 (O**C**(CH$_3$)$_2$), 74.9 (N**C**H$_2$).

Anal. Calc for $C_6H_{14}NNaO$: C, 51.78, H, 10.14, N, 10.06, found: C, 51.89, H, 10.20, N, 10.16.

Potassium DMAMP-THF (6)

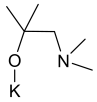

Under an inert atmosphere of argon gas, KHMDS (8.51 g, 42 mmol) was added to DMAMP (5.00 g, 42 mmol) in THF (50 mL). The reaction was the left to stir for twelve hours. Solvent and HMDS was removed in vacuo. To yield an off-white solid. The solid is crystallized in hexane to yield the desired product (7.32 g, 86%).

^{1}H NMR (300 MHz, Benzene-d$_6$) δ_{ppm} 1.17 (s, OC(C**H**$_3$)$_2$, 6H), 2.13 (s, NC**H**$_2$, 2H), 2.19 (s, N(C**H**$_3$)$_2$, 6H).
^{13}C NMR (75 MHz, Benzene-d$_6$) δ_{ppm} 30.9 (N(**C**H$_3$)$_2$), 49.0 (OC(**C**H$_3$)$_2$), 69.9 (O**C**(CH$_3$)$_2$), 73.0 (N**C**H$_2$). Anal. Calc for $C_{10}H_{22}NKO_2$: C, 52.82, H, 9.75, N, 6.16, found: C, 52.75, H, 9.70, N, 6.23.

Ni(DMAMP)$_2$ (1)

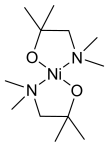

Under an inert atmosphere of argon gas, KHMDS (8.51 g 42.66 mmol) and DMAMP (5 g, 42.6 mmol) were combined in THF (50 mL) and stirred for twelve hours, the solvent was removed in vacuo. The product was redissolved in THF (50 mL) and added to two equivalents of hexaamminenickel(II) chloride (4.93 g, 21.33 mmol). The reaction was heated to 50 °C and left to stir for twelve hours. The solvents were removed in vacuo to leave a mixture of salt and (**1**). The product was dissolved in hexane, filtered through celite® and purified by crystallization to yield green crystals. (2.03 g, 47%).

^{1}H NMR (300 MHz, Benzene-d$_6$) δ_{ppm} 1.36 (s, N(C**H**$_3$)$_2$, 12H), 1.73 (s, NC**H**$_2$, 4H), 2.31 (s, C(C**H**$_3$)$_2$, 12H).
^{13}C NMR (75 MHz, Benzene-d$_6$) δ_{ppm} 23.4 (N(**C**H$_3$)$_2$), 51.3 (**C**(CH$_3$)$_2$), 73.4 (C(**C**H$_3$)$_2$), 78.1 (N**C**H$_2$).

Ni(FDMAMP)$_2$ (2)

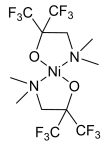

Compound (**2**) was prepared by the same method as (1) with FDMAMP (1.20 g, 5.3 mmol), KHMDS (1.06 g, 5.3 mmol) and hexaamminenickel(II) chloride in THF, to yield red crystals of (2) (0.871 g, 65%).

^{1}H NMR (300 MHz, Benzene-d$_6$) δ_{ppm} 1.91 (s, N(C**H**$_3$)$_2$, 6H), 2.04 (s, NC**H**$_2$, 2H).
^{13}C NMR (75 MHz, Benzene-d6) δ_{ppm} 50.5 (s, N(**C**H$_3$)$_2$, 66.1 (s, (N**C**H$_2$) ^{19}F NMR (75 MHz, Benzene-d$_6$) δ_{ppm} -78.1 (s, C(C**F**$_3$), 6F)
Anal. Calc for $C_{12}H_{16}F_{12}N_2NiO_2$: C, 28.43, H, 3.18, N, 5.53, found: C, 28.36, H, 2.99, N, 5.46.

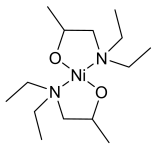

Ni(DEA2P)$_2$ (1.3)

The compound was prepared by the same method as (1) with DEA2P (2.62 g, 20 mmol), KHMDS (3.99 g, 20 mmol) and hexammine nickel(II) chloride (2.3178 g, 10 mmol) in THF. The reaction yielded dark red crystals (2.02 g, 63%).

^{1}H NMR (300 MHz, Benzene-d$_6$) δ_{ppm} 0.98 (m, OCHC**H**$_3$, 6H), 1.47 (m, NC**H**$_2$CH$_3$, 4H), 1.56 (m, NCH$_2$C**H**$_3$, 6H), 1.98 (m, NC**H**$_2$CH$_3$, 2H), 2.02 (m, NCH$_2$C**H**$_3$, 6H), 2.46 (m, NCH$_2$C**H**$_3$, 2H), 3.10 (m, NC**H**$_2$CH(CH$_3$), 2H), 3.18 (m, NC**H**$_2$CH(CH$_3$), 2H), 3.68 (m, OC**H**(CH$_3$), 2H).
^{13}C NMR (75 MHz, Benzene-d$_6$) δ_{ppm} 10.2 (NCH$_2$**C**H$_3$), 10.8 (NCH$_2$**C**H$_3$), 12.1 (NCH$_2$**C**H$_3$), 12.5 (NCH$_2$**C**H$_3$), 22.9 (NCH$_2$**C**H$_3$), 23.1 (NCH$_2$**C**H$_3$), 50.58 (N**C**H$_2$CH$_3$), 50.65 (N**C**H$_2$CH$_3$), 51.42 (N**C**H$_2$CH(CH$_3$), 51.8 (N**C**H$_2$CH(CH$_3$), 66.7 (N**C**H$_2$CH$_3$), 66.0 (N**C**H$_2$CH$_3$), 68.0 (O**C**H(CH$_3$)), 68.1 (O**C**H(CH$_3$)).
Anal. Calc for C$_{14}$H$_{32}$N$_2$NiO$_2$: C, 52.69, H, 10.11, N, 8.78, found: C 52.64, H, 10.38, N, 8.79.

5.5.2 Pyrroles

N-(2-pyrrolidene) iso-propylamine (7a)

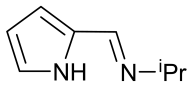

This was carried out in accordance with the method published in literature and a yield of 69% was obtained.[50]

^{1}H NMR (300 MHz, Benzene-d$_6$) δ_{ppm} 1.15 (d, J = 6.3 Hz, CH**Me$_2$**, 6H), 3.18 (hept, J = 6.3, 0.7 Hz, C**H**Me$_2$, 1H), 6.36 (m, Py-C**H**, 1H), 6.19 (m, Py-C**H**, 1H), 6.40 (m, Py-C**H**, 1H), 7.77 (s, NC(**H**), 1H), 9.31 (s, Py-N**H**, 1H).

^{13}C NMR (75 MHz, Benzene-d$_6$) δ_{ppm} 24.6 (CH**Me$_2$**), 61.3 (**C**HMe$_2$), 109.8 (Py-**C**H), 114.2 (Py-**C**H), 122.1 (Py-**C**H), 133.0 (Py-**C**CH), 150.2 (C**C**HN).

N-(2-pyrrolidene) tert-butylamine (8a)

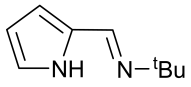

This was carried out in accordance with the method published in literature and a yield of 49% was obtained.[50]

^{1}H NMR (300 MHz, Benzene-d$_6$) δ_{ppm} 1.17 (s, NC**Me$_3$**, 9H), 6.22 (m, Py-C**H**, 1H), 6.37 (m, Py-C**H**, 1H), 6.43 (m, Py-C**H**, 1H), 7.94 (s, NC(**H**), 1H), 8.31 (s, Py-N**H**, 1H).

^{13}C NMR (75 MHz, Benzene-d$_6$) δ_{ppm} 30.1 (C**Me$_3$**), 66.3 (**C**Me$_3$), 110.9 (Py-**C**H), 119.4 (Py-**C**H), 123.6 (Py-**C**H), 132.6 (Py-**C**CH), 154.6 (C**C**HN).

N-(2-pyrrolidene) sec-butylamine (9a)

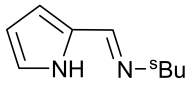

This was carried out in accordance with the method published in literature and a yield of 40% was obtained.[50].

^{1}H NMR (300 MHz, Benzene-d$_6$) δ_{ppm} 0.83 (t, J = 7.4 Hz, ^{s}Bu−CH$_2$C**H$_3$**, 3H), 1.18 (d, J = 6.3 Hz, ^{s}Bu−CH(C**H$_3$**), 3H), 1.67 – 1.37 (m, ^{s}Bu−C**H$_2$**CH$_3$, 2H), 2.99 – 2.82 (m, ^{s}Bu−C**H**(CH$_3$), 1H), 6.20 (m, Py-C**H**, 1H), 6.38 (m, Py-C**H**, 1H), 6.42 (m, Py-C**H**, 1H), 7.80 (s, C**H**N, 1H), 9.25 (s, Py-N**H**, 1H).

^{13}C NMR (75 MHz, Benzene-d$_6$) δ_{ppm} 11.2 (CH$_2$**C**H$_3$), 22.7 (CH**C**H$_3$), 31.1 (**C**H$_2$CH$_3$), 67.8 (**C**HCH$_3$), 109.7 (Py-**C**H), 114.0 (Py-**C**H), 121.9 (Py-**C**H), 130.9 (Py-**C**CH), 150.6 (C**C**HN).

N-(2-pyrrolidene) phenylamine (10a)

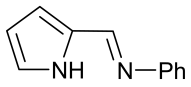

This was carried out in accordance with the method published in literature and a yield of 28% was obtained.[51]

^{1}H NMR (500 MHz, Benzene-d$_6$) δ_{ppm} 6.15 (m, Py-C**H**, 1H), 6.28 (m, Py-C**H**, 1H), 6.46 (m, Py-C**H**, 1H), 7.07 – 7.02 (m, Ph-C**H**, 1H), 7.15 – 7.13 (m, Ph-C**H**, 2H), 7.23 – 7.18 (m, Ph-C**H**, 2H), 7.94 (s, C**H**N, 1H), 9.11 (s, Py-N**H**, 1H).

^{13}C NMR (75 MHz, Benzene-d$_6$) δ_{ppm} 110.3 (Py-**C**H), 116.9 (Py-**C**H), 120.9 (Ph-**C**H), 123.5 (Ph-**C**H), 125.4 (Pr-**C**H), 129.2 (Ph-**C**H), 130.65 (Py-**C**CH), 150.2 (N**C**H), 151.8 (Ph-**C**H).

N-(2-pyrrolidene) 2,6-diisoproyl-phenylamine (11a)

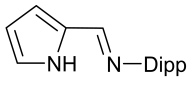

This was carried out in accordance with the method published in literature and a yield of 33% was obtained.[51]

^{1}H NMR (300 MHz, Benzene-d$_6$) δ_{ppm} 1.14 (d, J = 6.9 Hz, ^{i}Pr-(C**H$_3$**)$_2$, 12H), 3.15 (h, J = 6.9 Hz, ^{i}Pr-C**H**, 2H), 6.09 (m, Py-C**H**, 1H), 6.17 (m, Py-C**H**, 1H), 6.40 (m, Py-C**H**, 1H), 7.08 – 7.20 (m, Ph-C**H**, 3H), 7.74 (s, C**H**N, 1H), 9.75 (s, Py-N**H**, 1H).

^{13}C NMR (75 MHz, Benzene-d$_6$) δ_{ppm} 24.0 (CH**Me$_2$**), 28.4 (**C**HMe$_2$), 110.3 (Py-**C**H), 117.1 (Py-**H**), 123.7 (Py-**C**H), 124.6 (Ph-**C**H), 125.0 (Ph-**C**H), 130.3 (Py-**C**CH), 139.4 (Ph-**C**H), 148.9 (Ph-**C**N), 153.2 ppm (C**C**HN).

N-(2-pyrrolidene) 2,4,6-trimethyl-phenylamine (12a)

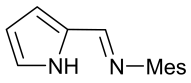

This was carried out in accordance with the method published in literature and a yield of 72% was obtained.[51]

^{1}H NMR (500 MHz, Benzene-d$_6$) δ_{ppm} 2.13 (d, J = 3.0 Hz, (o)Ph-**Me**, 6H), 2.21 (d, J = 1.9 Hz, (p)Ph-**Me**, 3H), 6.13 (m, Py-C**H**, 1H), 6.27 (m, Py-C**H**, 1H), 6.40 (m, Py-C**H**, 1H), 6.85 (d, J = 2.6 Hz, Ph-C**H**, 2H), 7.61 (s, CC**H**N, 1H), 9.62 (s, Py-N**H**, 1H).

^{13}C {^{1}H} NMR (75 MHz, Benzene-d$_6$) δ_{ppm} 18.5 (o-Ph-**Me**), 21.0 (p-Ph-Me), 109.9 (Py-**C**H), 117.0 (Py-**C**H), 124.5 (Py-**C**H), 128.4 (o-Ph-**C**Me), 129.0 (Ph-**C**H), 130.1 (*p*-Ph-**Me**), 133.4 (Py-**C**C), 148.3 (Ph-**C**N), 153.8 (C**C**HN).

Nickel bis(N-(2-pyrrolide) iso-propylamine) (7)

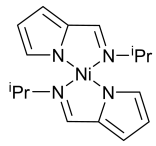

In an argon atmosphere, sodium hexamethyldisilazide (NaHMDS) (4.82 g, 0.026 mol) was dissolved in toluene (30 ml) and ligand **7a** (3.95 g, 0.026 mol) added. The mixture was then stirred at room temperature for 16 hours before removing the toluene in vacuo to yield an off-white solid product. A 100% yield was assumed and the sodiated ligand was combined with $[Ni(NH_3)_6]Cl_2$ (1.78 g, 0.009 mol). These were then dissolved in THF (40-50 ml) and stirred for 48 hours. The resulting dark brown-black solid was isolated by removal of all solvent in vacuo. The nickel complex was then solvated in toluene (40-50 ml) and the NaCl filtered off. Toluene was slowly removed in vacuo to yield crystals of (**7**). The crystals were heated back into solution and slowly cooled to $-28\,^{\circ}C$ to allow further crystallisation. After 24 hours the crystals were isolated from all solvent to yield 1.48 g (50%) of product.

^{1}H NMR (500 MHz, Benzene-d$_6$) δ_{ppm} 1.02 (s, C**H**Me$_2$, 2H), 1.61 (s, CH**Me$_2$**, 12H), 10.72 (s, Py-C**H**, 2H), 13.05 (s, Py-C**H**, 2H), 27.71 (s, Py-C**H**, 2H), 30.98 (s, CC(**H**)N, 2H).
^{13}C NMR (126 MHz, Benzene-d$_6$) δ_{ppm} 34.3 (-CH(**C**H$_3$)$_2$), 97.7 (Py-**C**H), 102.8 (Ph-**C**H), 114.7 (Py-**C**H), 152.7 (-**C**H(CH$_3$)$_2$), 162.7 (Py-**C**H).
Anal. Calc for $C_{16}H_{22}N_4Ni$: C, 58.40, H, 6.74, N, 17.03, found: C, 59.2, H, 6.76, N, 17.13.

Nickel bis(N-(2-pyrrolide) tert-butylamine) (8)

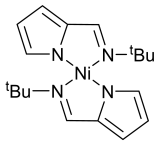

The same method of preparation was utilised as **7**, except $NiCl_2$ was used in place of $[Ni(NH_3)_6]Cl_2$. Sodium hexamethyldisilazide (4.85 g, 0.026 mol) was added to toluene (30 ml). Ligand 8a (3.95 g, 0.026 mol) was added. A 100% yield was assumed. Nickel(II) chloride (1.68 g, 0.013 mol) was then added to the isolated ligand. These were then dissolved in toluene (40-50 ml). The same method of isolation as 7 was utilised to yield 1.99 g (43%).

^{1}H NMR (500 MHz, Benzene-d$_6$) δ_{ppm} -55.55 (s, 1H), 14.36 (s, ^{t}Bu–C(C**H$_3$**)$_3$, 9H), 51.47 (s, Py-C**H**,1H), 74.30 (s, Py-C**H**, 1H), 171.18 (s, Py-C**H**, 1H).
^{13}C NMR (126 MHz, THF) δ_{ppm} 1.2 (s, ^{t}Bu–C(**C**H$_3$)$_3$, 9H), 6.1 (m, Py-**C**H, 1H), 6.3 (m, Py-**C**H, 1H), 6.8 (m, Py-**C**H, 1H), 8.0 (s, -C**C**HN, 1H).
Anal. Calc for $C_{18}H_{26}N_4Ni$: C, 60.54, H, 7.34, N, 15.69, found: C, 60.45, H, 7.18, N, 15.65.

Nickel bis(N-(2-pyrrolide) sec-butylamine) (9)

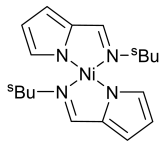

The same method as for that of preparation of **8**. Sodium hexamethyldisilazide (4.85 g, 0.026 mol) was added to toluene (30 ml). Ligand **9a** (3.97 g, 0.026 mol) was added. A 100% yield was assumed. Nickel(II) chloride (1.68 g, 0.013 mol) was added to the isolated ligand. These were then dissolved in toluene (40-50 ml). The same method of isolation as **7** was utilised. No yield was measured.

^{1}H NMR (500 MHz, Benzene-d$_6$) δ_{ppm} 1.77 – 0.59 (m,^{s}Bu–CH(CH$_3$)CH$_2$CH$_3$, 8H), 2.90 (s, ^{s}-C**H**, 1H), 6.37 (s, CC**H**N, Py-C**H**, 2H), 7.81 (s, Py-C**H**, 1H), 8.65 (s, Ph-C**H**, 1H).

Nickel bis(N-(2-pyrrolide) phenylamine) (10)

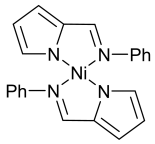

The same method as for that of preparation of **8**. Sodium hexamethyldisilazane (2.02 g, 0.011 mol) was added to toluene (40 ml). Ligand 10a (1.88 g, 0.011 mol) was added. A 100% yield was assumed. Nickel(II) chloride (0.71 g, 0.0055 mol) was added to the sodiated ligand. These were then dissolved in toluene (40-50 ml). The same method of isolation as **7** was utilised to yield 1.99 g (8%).

^{1}H NMR (126 MHz, Benzene-d$_6$) δ_{ppm} 5.52 (s, Ph-C**H**, 2H), 6.11 (s, Py-C**H**, 2H), 6.56 (s, Py-C**H**, 2H), 6.62 (m, -CC**H**N, 2H), 6.91 (m, Ph-C**H**, 6H), 7.15 – 7.11 (m, Ph-C**H**, 4H).
^{13}C NMR (126 MHz, Benzene-d$_6$) δ_{ppm} 114.1 (Py-**C**H), 119.8 (-C**H**HN), 124.9 (Ph-**H**H), 126.3 (Ph-**H**H), 128.9 (Ph-**H**H), 140.0 (Py-**H**H), 160.0 (Py-**H**H).

Nickel bis(N-(2-pyrrolide) 2,6-diisopropyl-phenylamine (11)

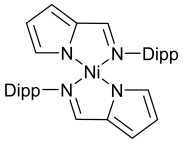

The same method as for that of preparation of **8**. Sodium hexamethyldisilazide (2.020 g, 0.011 mol) was added to toluene (40 ml). Ligand **11a** (2.79 g, 0.011 mol) was added. A 100% yield

was assumed. Nickel(II) chloride (0.71 g, 0.0055 mol) was added to the sodiated ligand. These were then dissolved in toluene (40-50 ml). The same method of isolation as **7** was utilised to yield 1.38 g (45%).

^{1}H NMR (500 MHz, Benzene-d$_6$) δ_{ppm} 1.17 (d, J = 6.7 Hz, ^{i}Pr−CH(C**H$_3$**)$_2$, 12H), 1.26 (d, J = 6.8 Hz, ^{i}Pr−CH(C**H$_3$**)$_2$, 12H), 4.47 (hept, J = 6.9 Hz, ^{i}Pr−C**H**(CH$_3$)$_2$, 4H), 5.13 – 5.06 (m, Py-C**H**, 2H), 5.94 (m, Py-C**H**, 2H), 6.55 (m, Py-C**H**, 2H), 6.58 (s, -CC**H**N, 2H), 7.02 (d, J = 7.7 Hz, Ph-C**H**, 4H), 7.15 (m, Ph-C**H**, 2H).
^{13}C NMR (126 MHz, Benzene-d$_6$) δ_{ppm} 24.0 (^{i}Pr−CH(**C**H$_3$)$_2$), 25.1 (^{i}Pr−CH(**C**H$_3$)$_2$)), 129.0 (^{i}Pr−**C**H(CH$_3$)$_2$), 113.9 (Py-**C**H), 120.0 (Py-**C**H), 124.6 (Ph-**C**H), 139.0 (Py-**C**H), 161.9 (-C**C**HN).

Nickel bis(N-(2-pyrrolide) 2,4,6-trimethyl-phenylamine) (12)

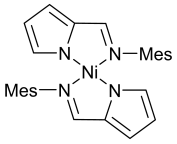

The same method as for that of preparation of **8**. Sodium hexamethyldisilazide (4.22 g, 0.023 mol) was added to toluene (40 ml). Ligand **11a** (4.96 g, 0.023 mol) was added. A 100% yield was assumed. Nickel(II) chloride (1.49 g, 0.00115 mol) was added to the sodiated ligand. These were then dissolved in toluene (40-50 ml). The same method of isolation as **7** was utilised to yield 1.38 g (45%).

^{1}H NMR (500 MHz, Benzene-d$_6$) δ_{ppm} 2.06 (s, *p*Ph-C**Me**, 6H), 2.48 (s, *o*Ph-C**Me**, 12H), 5.20 (s, -CC**H**N, 2H), 6.02 (m, Py-C**H**, 2H), 6.20 (s, Py-C**H**, 2H), 6.58 (m, Py-C**H**, 2H), 6.67 (s, (m)Ph-C**H**, 4H).
^{13}C NMR (126 MHz, Benzene-d$_6$) δ_{ppm} 20.7 (*o*Ph-**C**Me), 21.9 (*p*Ph-**C**Me), 114.4 (Py-**C**H), 120.1 (Py-**C**H), 131.0 (*m*Ph-CH), 138.0 (-C**C**HN), 163.6 (Py-**C**H).

5.5.3 Nickel Guanidinates

Ni(^{i}PrGu)$_2$ (13)

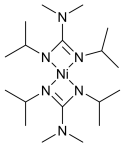

This was carried out in accordance with the method published in literature.[36] Under an inert atmosphere, diisopropyl-carbodiimide (2.00 g, 0.016 mol) was added to a suspension of with lithiumamide (0.81 g, 0.016 mol) in THF. The reaction was stirred for 2 hours before adding nickel(II) chloride (1.027 g, 0.008 mol) after stirring for 12 hours all solvent was removed in vacuo, the solid dissolved into hexanes and filtered through celite. hexanes were slowly removed in vacuo to yield crystals of (**14**). The crystals were heated back into solution and slowly cooled to $-28\,^{\circ}$C to allow further crystallisation. After 24 hours the crystals were isolated from all solvent to yield 2.11 g (70%) of **13**.

NMR analysis was in agreement with that of literature.[35].

^{1}H NMR (500 MHz, Benzene-d$_6$) δ_{ppm} 1.59 (d, N(C**H**3)2), 12H), 2.34 (s, N**Me**$_2$, 12H), 3.52 (m, NC**H**(CH$_3$)$_2$, 4H).

^{13}C NMR (126 MHz, Benzene-d$_6$) δ_{ppm} 26.0 (CH(**Me**2)), 38.8 (N(**Me**)$_2$), 50.27 (N**C**H).

Ni(CycGu)$_2$ (14)

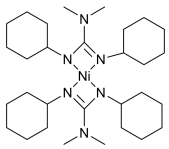

This was carried out in accordance with the method published in literature.[36] Under an inert atmosphere, dicycloxehyl-carbodiimide (2.00 g, 0.01 mol) was added to a suspension of with lithiumamide (0.5 g, 0.01 mol) in THF. The reaction was stirred for 2 hours before adding nickel(II) chloride (0.63 g, 0.005 mol) after stirring for 12 hours all solvent was removed in vacuo, the solid dissolved into hexanes and filtered through celite. hexanes were slowly removed in vacuo to yield crystals of (**14**). The crystals were heated back into solution and slowly cooled to $-28\,^{\circ}$C to allow further crystallisation. After 24 hours the crystals were isolated from all solvent to yield 2.11 g (78%) of **14**.

^{1}H NMR (500 MHz, Benzene-d$_6$) δ_{ppm} 1.32 ((m, o/m-NC$_6$H$_{11}$, 8H), 1.32 (m, NC**H**, 4H), 1.60 (m, NC**H**, 4H), 1.96 (m, o/m-NC$_6$H$_{11}$, 8H), 2.06 (m, NC**H**, 8H), 2.36 (s, N**Me**$_2$, 12H), 2.45 (m, o/m-NC$_6$H$_{11}$, 8H), 3.36 (m, NC**H**, 4H).

^{13}C NMR (126 MHz, Benzene-d$_6$) δ_{ppm} 26.0 (N**C**H), 27.1 (o/m-NC$_6$H$_{11}$) 36.7 (o/m-NC$_6$H$_{11}$), 39.1 (N**Me**$_2$), 60.6 (N**C**H).

Anal. Calc for $C_{30}H_{56}N_6Ni$: C, 64.40, H, 10.09, N, 15.02, found: C, 63.82, H, 10.12, N, 14.69.

5.5.4 Nickel β-ketoiminates

Ni(^{i}PrNacAc)$_2$ (15)

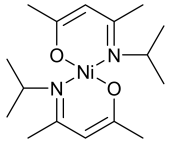

In an argon atmosphere, N-isopropyl-4-amino-3-penten-2-one (^{i}PrNacAc) (1.60 g, 0.013 mol) was added to a suspension of sodium amide (0.49 g, 0.013 mol) in toluene (50 mL). The mixture was then stirred for 12 hours before the addition of hexamminenickel chloride (2.41 g, 0.007 mol). The mixture was stirred for a further 24 hours before all toluene was removed in vacuo. The dark solid was redissolved into hexanes (40-50 mL) and the NaCl removed by filtration. The hexanes were slowly removed in vacuo to yield crstals of **15**. The crystals were heated into solution before cooling to $-28\,^{\circ}$C to allow further crystallisation. After 24 hours the crystals were isolated from solvent to yield 2.64 g (62 %) of product.
^{1}H NMR (500 MHz, Benzene-d$_6$) δ_{ppm} 21.80 (s, NC(**Me**)$_2$, 12H), -22.40 (s, OC(**CH3**)C(H), 6H), -33.99 (s, NC(**CH3**)C(H), 6H)
Anal. Calc for $C_{16}H_{28}N_2NiO_2$: C, 56.67, H, 8.32, N, 8.26, found: C, 56.20, H, 8.18, N, 8.43.

Ni(^{t}BuNacAc)$_2$ (16)

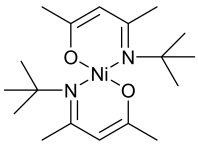

The same method as for that of preparation of **15**. Sodium amide (0.49 g, 0.013 mol) was added to toluene (40 ml). 4-(tert-butyl)-amino-3-pentene-2-one (1.94 g, 0.013 mol) was added. A 100% yield was assumed. Nickel(II) chloride (1.46 g, 0.007 mol) was added to the sodiated ligand. The same method of isolation as **15** was utilised to yield 1.71 g (37%).
^{1}H NMR (500 MHz, Benzene-d$_6$) δ_{ppm} 50.43 (s, NC(**Me**)$_3$, 18H), -8.14 (s, OC(**CH3**)C(H), 6H), -19.99 (s, NC(**CH3**)C(H), 6H)
Anal. Calc for $C_{18}H_{32}N_2NiO_2$: C, 58.88, H, 8.79, N, 7.63, found: C, 59.18, H, 8.92, N, 7.82.

Ni(EtNacAc)$_2$ (17)

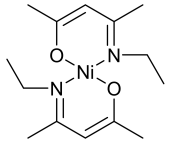

The same method as for that of preparation of **15**. Sodium amide (0.49 g, 0.013 mol) was suspended in toluene (40 ml) and 4-(ethylamino)penten-2-one (1.60 g, 0.013 mol) was added.

A 100% yield was assumed. Nickel(II) chloride (1.46 g, 0.007 mol) was added to the sodiated ligand. The same method of isolation as **15** was utilised to yield 2.41 g (62%).
^{1}H NMR (500 MHz, Benzene-d_6) δ_{ppm} 26.21 (s, NC(**H**$_2$)C(H$_3$), 4H), 2.45 (s, NC(H$_2$)C(**H**$_3$), 6H), -1.11 (s, OC(C**H**$_3$)C(H), 6H), -2.36 (s, NC(C**H**$_3$)C(H), 6H), -4.56 (s, C(CH$_3$)C(H)C(CH$_3$), 2H).
^{13}C NMR (126 MHz, Benzene-d_6) δ_{ppm} 30.51 (C(CH$_3$)**C**(H)C(CH$_3$)), 10.81 (NC(**C**H$_3$)C(H), 1.01 (OC(**C**H$_3$)C(H).
Anal. Calc for $C_{14}H_{24}N_2NiO_2$: C, 54.06, H, 7.78, N, 9.01, found: C, 54.10, H, 7.80, N, 9.12.

[1] T. S. Yang, W. Cho, M. Kim, K. S. An, T. M. Chung, C. G. Kim and Y. Kim, *J. Vac. Sci. Technol. A Vacuum, Surfaces, Film.*, 2005, **23**, 1238–1243.

[2] S. H. Yoo, H. Choi, H. Kim, B. K. Park, S. S. Lee, K. An, Y. K. Lee, T. Chung and C. G. Kim, *Eur. J. Inorg. Chem.*, 2011, **2011**, 1833–1839.

[3] T. Chung, S. S. Lee, W. Cho, M. Kim, Y. K. Lee, J. Hwang, K. An and C. G. Kim, *Korean Chem. Soc.*, 2011, **32**, 783–784.

[4] H. B. R. Lee, S. H. Bang, W. H. Kim, G. H. Gu, Y. K. Lee, T. M. Chung, C. G. Kim, C. G. Park and H. Kim, *Jpn. J. Appl. Phys.*, 2010, **49**, 05FA11.

[5] K. C. Min, M. Kim, Y. H. You, S. S. Lee, Y. K. Lee, T. M. Chung, C. G. Kim, J. H. Hwang, K. S. An, N. S. Lee and Y. Kim, *Surf. Coatings Technol.*, 2007, **201**, 9252–9255.

[6] P. A. Premkumar, M. Toeller, C. Adelmann, J. Meersschaut, A. Franquet, O. Richard, H. Tielens, B. Brijs, A. Moussa, T. Conard, H. Bender, M. Schaekers, J. Kittl, M. Jurczak and S. Van Elshocht, *Chem. Vap. Depos.*, 2012, **18**, 61–69.

[7] M. Ko, B. Shong and J. Hwang, *Ceram. Int.*, 2018, **44**, 16342–16351.

[8] M. Putkonen, T. Aaltonen, M. Alnes, T. Sajavaara, O. Nilsen and H. Fjellvåg, *J. Mater. Chem.*, 2009, **19**, 8767.

[9] J. Liu, M. N. Banis, X. Li, A. Lushington, M. Cai, R. Li, T. Sham and X. Sun, *J. Phys. Chem. C*, 2013, **117**, 20260–20267.

[10] E. Østreng, H. H. Sønsteby, T. Sajavaara, O. Nilsen and H. Fjellvåg, *J. Mater. Chem. C*, 2013, **1**, 4283–4290.

[11] E. Østreng, H. H. Sønsteby, S. Øien, O. Nilsen and H. Fjellvåg, *Dalt. Trans.*, 2014, **43**, 16666.

[12] N. Hornsveld, B. Put, W. M. M. Kessels, P. M. Vereecken and M. Creatore, *RSC Adv.*, 2017, **7**, 41359–41368.

[13] A. Ruud, V. Miikkulainen, K. Mizohata, H. Fjellvåg and O. Nilsen, *J. Vac. Sci. Technol. A Vacuum, Surfaces, Film.*, 2017, **35**, 01B133.

[14] J. R. Bickford, H. Sønsteby, N. A. Strnad, P. Zavalij and R. C. Hoffman, *J. Vac. Sci. Technol. A*, 2019, **37**, 020904.

[15] H. H. Sønsteby, A. Yanguas-Gil and J. W. Elam, *J. Vac. Sci. Technol. A*, 2020, **38**, 020804.

[16] A. D. Bond, *Cryst. Growth Des.*, 2005, **5**, 755–771.

[17] P. A. van der Schaaf, J. T. B. H. Jastrzebski, M. P. Hogerheide, W. J. J. Smeets, A. L. Spek, J. Boersma and G. van Koten, *Inorg. Chem.*, 1993, **32**, 4111–4118.

[18] T. Gietz and R. Boeré, *Inorganics*, 2017, **5**, 30.

[19] M. Utriainen, M. Kröger-Laukkanen and L. Niinistö, *Mater. Sci. Eng. B*, 1998, **54**, 98–103.

[20] J. D. Parish, M. W. Snook, A. L. Johnson and G. Kociok-Köhn, *Dalt. Trans.*, 2018, **47**, 7721–7729.

[21] C. H. Wei and J. R. Einstein, *Acta Crystallogr. Sect. B Struct. Crystallogr. Cryst. Chem.*, 1972, **28**, 2591–2598.

[22] C. S. Gomes, M. T. Duarte and P. T. Gomes, *J. Organomet. Chem.*, 2014, **760**, 167–176.

[23] P. Pérez-Puente, E. de Jesús, J. C. Flores and P. Gómez-Sal, *J. Organomet. Chem.*, 2008, **693**, 3902–3906.

[24] C. E. Anderson, A. S. Batsanov, P. W. Dyer, J. Fawcett and J. A. Howard, *J. Chem. Soc. Dalt. Trans.*, 2006, 5362–5378.

[25] L. Yang, D. R. Powell and R. P. Houser, *Dalt. Trans.*, 2007, 955–964.

[26] Y. Mori, H. Shirase and Y. Fukuda, *Bull. Chem. Soc. Jpn.*, 2008, **81**, 1108–1115.

[27] B. S. Lim, A. Rahtu, J. Park and R. G. Gordon, *Inorg. Chem.*, 2003, **42**, 7951–7958.

[28] B. S. Lim, A. Rahtu and R. G. Gordon, *Nat Mater*, 2003, **2**, 749–754.

[29] R. Zhao, S. Xiao, S. Yang and X. Wang, *Chem. Mater.*, 2019, **31**, 5172–5180.

[30] W. J. Nam, Z. Gray, J. Stayancho, V. Plotnikov, D. Kwon, S. Waggoner, D. V. Shenai-Khatkhate, M. Pickering, T. Okano, A. Compaan and S. J. Fonash, *ECS Trans.*, 2015, **66**, 275–279.

[31] J. W. Shim, C. Fuentes-Hernandez, A. Dindar, Y. Zhou, T. M. Khan and B. Kippelen, *Org. Electron.*, 2013, **14**, 2802–2808.

[32] E. Thimsen, A. B. F. Martinson, J. W. Elam and M. J. Pellin, *J. Phys. Chem. C*, 2012, **116**, 16830–16840.

[33] K. M. Young and T. W. Hamann, *Chem. Commun.*, 2014, **50**, 8727–8730.

[34] J. P. Coyle, W. H. Monillas, G. P. A. Yap and S. T. Barry, *Inorg. Chem.*, 2008, **47**, 683–689.

[35] Y. Zhang, L. Du, X. Liu and Y. Ding, *Polyhedron*, 2018, **156**, 218–222.

[36] Y. Zhang, L. Du, X. Liu and Y. Ding, *New J. Chem.*, 2018, **42**, 9110–9115.

[37] K. Xu, A. P. Milanov, H. Parala, C. Wenger, C. Baristiran-Kaynak, K. Lakribssi, T. Toader, C. Bock, D. Rogalla, H. Becker, U. Kunze and A. Devi, *Chem. Vap. Depos.*, 2012, **18**, 27–35.

[38] T. J. Knisley, L. C. Kalutarage and C. H. Winter, *Coord. Chem. Rev.*, 2013, **257**, 3222–3231.

[39] A. Devi, *Coord. Chem. Rev.*, 2013, **257**, 3332–3384.

[40] M. E. Alnes, E. Monakhov, H. Fjellvåg and O. Nilsen, *Chem. Vap. Depos.*, 2012, **18**, 173–178.

[41] S. Kannan Selvaraj, A. Feinerman and C. G. Takoudis, *J. Vac. Sci. Technol. A Vacuum, Surfaces, Film.*, 2014, **32**, 01A112.

[42] E. Lindahl, M. Ottosson and J. O. Carlsson, *Chem. Vap. Depos.*, 2009, **15**, 186–191.

[43] G. W. Everett and R. H. Holm, *J. Am. Chem. Soc.*, 1965, **87**, 2117–2127.

[44] K. Junge Puring, D. Zywitzki, D. H. Taffa, D. Rogalla, M. Winter, M. Wark and A. Devi, *Inorg. Chem.*, 2018, **57**, 5133–5144.

[45] D. Peeters, A. Sadlo, K. Lowjaga, O. Mendoza Reyes, L. Wang, L. Mai, M. Gebhard, D. Rogalla, H. Becker, I. Giner, G. Grundmeier, D. Mitoraj, M. Grafen, A. Ostendorf, R. Beranek and A. Devi, *Adv. Mater. Interfaces*, 2017, **4**, 1700155.

[46] X. Su, T. Kim, K. A. Abboud and L. McElwee-White, *Polyhedron*, 2019, **157**, 548–557.

[47] M. Basato, E. Faggin, C. Tubaro and A. C. Veronese, *Polyhedron*, 2009, **28**, 1229–1234.

[48] M. Chandrakala, S. Raj Bharath, T. Maiyalagan and S. Arockiasamy, *Mater. Chem. Phys.*, 2017, **201**, 344–353.

[49] I. Kazadojev, D. J. Otway and S. D. Elliott, *Chem. Vap. Depos.*, 2013, **19**, 117–124.

[50] V. V. Grushin and W. J. Marshall, *Adv. Synth. Catal.*, 2004, **346**, 1457–1460.

[51] C. E. Anderson, A. S. Batsanov, P. W. Dyer, J. Fawcett and J. A. Howard, *J. Chem. Soc. Dalt. Trans.*, 2006, 5362–5378.

5.6 Appendix

Table 5.7. *Inert atmosphere TGA analysis completed between 30-600 °C at a ramp rate of 5 °C min^{-1} with an Ar gas flow rate of 20 ml min^{-1}. ∗Sample measured in atmospheric conditions.*

Compound	T^{99}(°C)	T^{50}(°C)	**Residual Mass%**
$Ni(DMAMP)_2$	58	106	0.0
$Ni(DMAMP)_2$∗	111	232	26.0
$Ni(DEA_2P)_2$	120	185	9.9
$Ni(FDMAMP)_2$	52	150	0.0
LiDMAMP	173	207	8.4
NaDMAMP	58	250	0.0
KDMAMP(THF)	73	204	8.4
$Ni(iPrPyr)_2$	154	217	0.1
$Ni(tBuPyr)_2$	140	214	0.1
$Ni(PhPyr)_2$	241	310	42.1
$Ni(DippPyr)_2$	139	302	9.6
$Ni(MesPyr)_2$	146	330	27.5
$Ni(iPrCu)_2$	92	153	20.3
$Ni(cycGu)_2$	106	202	15.9
$Ni(iPrNacAc)_2$	121	152	12.3
$Ni(tBuNacAc)_2$	47	192	3.2

Table 5.8. *Crystal data and structure refinement for* ***1****.*

	$Ni(DMAMP)_2$
Identification code	s16alj35
Empirical formula	C12 H28 N2 Ni O2
Formula weight	291.07
Temperature	150.00(10) K
Wavelength	1.54184 Å
Crystal system	Monoclinic
Space group	$P2_{1/n}$
Unit cell dimensions	a = 5.78180(10)Å α= 90°.
	b = 18.0979(3) Å β = 111.676(2)°.
	c = 7.59290(10) Å γ = 90°.
Volume	738.33(2) angstrom^3
Z	2
Density (calculated)	1.309 Mg/m^3
Absorption coefficient	1.845 mm^{-1}
F(000)	316
Crystal size	0.220 x 0.200 x 0.180 mm^3
Theta range for data collection	6.734 to 73.099°
Index ranges	$-7 <= h <= 7; -22 <= k <= 21; -6 <= l <= 9$
Reflections collected	8560
Independent reflections	1482 [R(int) = 0.0213]
Completeness to theta = 67.684°	99.8%
Absorption correction	Semi-empirical from equivalents
Max. and min. transmission	1.00000 and 0.80998
Refinement method	Full-matrix least-squares on F2
Data / restraints / parameters	1482 / 0 / 83
Goodness-of-fit on F2	1.08
Final R indices [$I > 2\sigma(I)$]	R1 = 0.0237 wR2 = 0.0610
R indices (all data)	R1 = 0.0264 wR2 = 0.0615
Extinction coefficient	n/a
Largest diff. peak and hole	0.270 and -0.288 e. Å^{-}3

Table 5.9. *Crystal data and structure refinement for* ***2****.*

	$Ni(FDMAMP)_2$
Identification code	s17alj05
Empirical formula	C12 H16 F12 N2 Ni O2
Formula weight	506.98
Temperature	150.00(10) K
Wavelength	1.54184 Å
Crystal system	Monoclinic
Space group	P21/n
Unit cell dimensions	a = 6.27080(10) Å $\alpha = 90°$
	b = 11.7760(2) Å $\beta = 90.156(2°$
	c = 11.7667(2) Å $\gamma = 90°$
Volume	868.91(3) $Å^3$
Z	2
Density (calculated)	1.938 Mg/m^3
Absorption coefficient	2.941 mm^{-1}
F(000)	508
Crystal size	0.200 x 0.110 x 0.090 mm^3
Theta range for data collection	5.314 to 73.481 °
Index ranges	$-7 <= h <= 7; -14 <= k <= 10; -14 <= l <= 13$
Reflections collected	8139
Independent reflections	1758 [R(int) = 0.0275]
Completeness to theta = 67.684°	99.9%
Absorption correction	Semi-empirical from equivalents
Max. and min. transmission	1.00000 and 0.70778
Refinement method	Full-matrix least-squares on F2
Data / restraints / parameters	1758 / 0 / 135
Goodness-of-fit on F2	1.064
Final R indices $[I > 2\sigma(I)]$	R1 = 0.0265 wR2 = 0.0697
R indices (all data)	R1 = 0.0279 wR2 = 0.0709
Extinction coefficient	n/a
Largest diff. peak and hole	0.360 and -0.301 e.$Å^{-3}$

Table 5.10. *Crystal data and structure refinement for* ***3****.*

	$Ni(DEA2P)_2$
Identification code	s17alj10
Empirical formula	C14 H32 N2 Ni O2
Formula weight	319.12
Temperature	150.01(10) K
Wavelength	0.71073 Å
Crystal system	Triclinic
Space group	P-1
Unit cell dimensions	a = 7.2724(4) Å α=100.218(4)°
	b = 7.5126(4) Å β= 105.097(4)°
	c = 8.8143(4) Å γ=111.588(5)°
Volume	411.82(4) $Å^3$
Z	1
Density (calculated)	1.287 Mg/m^3
Absorption coefficient	1.179 mm^{-1}
F(000)	174
Crystal size	0.300 x 0.300 x 0.120 mm^3
Theta range for data collection	3.061 to 31.753°
Reflections collected	7261
Independent reflections	2560 [R(int) = 0.0318]
Completeness to theta = 25.242°	99.9%
Absorption correction	Semi-empirical from equivalents
Max. and min. transmission	1.00000 and 0.83352
Refinement method	Full-matrix least-squares on F2
Data / restraints / parameters	2560 / 0 / 91
Goodness-of-fit on F2	1.068
Final R indices [$I > 2\sigma(I)$]	R1 = 0.0261 wR2 = 0.0652
R indices (all data)	R1 = 0.0280 wR2 = 0.0656
Extinction coefficient	n/a
Largest diff. peak and hole	0.578 and -0.498 e.$Å^{-3}$

Table 5.11. *Crystal data and structure refinement for* ***4****.*

	LiFDMAMP
Identification code	s16alj31
Empirical formula	C24 H32 F24 Li4 N4 O4
Formula weight	924.29
Temperature	150.00(10) K
Wavelength	1.54184 Å
Crystal system	Triclinic
Space group	P-1
Unit cell dimensions	a = 10.2062(5) Å α= 82.225(3)°
	b = 12.0158(5) Å β= 73.261(4)°
	c = 16.4956(6) Å γ = 68.782(4)°
Volume	1804.81(15) Å^3
Z	2
Density (calculated)	1.701 Mg/m^3
Absorption coefficient	1.780 mm^{-1}
F(000)	928
Crystal size	0.150 x 0.120 x 0.050 mm^3
Theta range for data collection	3.949 to 73.047°
Index ranges	$-12 <= h <= 12; -11 <= k <= 14; -15 <= l <= 20$
Reflections collected	13222
Independent reflections	7096 [R(int) = 0.0336]
Completeness to theta = 25.242°	100%
Absorption correction	Semi-empirical from equivalents
Max. and min. transmission	1.00000 and 0.68250
Refinement method	Full-matrix least-squares on F2
Data / restraints / parameters	7096 / 0 / 549
Goodness-of-fit on F2	1.04
Final R indices [$I > 2\sigma(I)$]	R1 = 0.0504 wR2 = 0.1414
R indices (all data)	R1 = 0.0587 wR2 = 0.1489
Extinction coefficient	n/a
Largest diff. peak and hole	0.446 and -0.332 e.Å^{-3}

Table 5.12. *Crystal data and structure refinement for* ***5****.*

	NaDMAMP
Identification code	s19alj11
Empirical formula	C36 H84 N6 Na6 O6
Formula weight	835.03
Temperature	150.00(10) K
Wavelength	1.54184 Å
Crystal system	Trigonal
Space group	R-3
Unit cell dimensions	a = 20.0253(3) Å α= 90°
	b = 20.0253(3) Å β= 90°
	c = 21.8683(3) Å γ=120°
Volume	7594.6(3) $Å^3$
Z	6
Density (calculated)	1.095 Mg/m^3
Absorption coefficient	1.027 mm^{-1}
F(000)	2736
Crystal size	0.686 x 0.349 x 0.241 mm^3
Theta range for data collection	4.416 to 73.733°
Index ranges	$-20 <= h <= 24; -24 <= k <= 24; -26 <= l <= 25$
Reflections collected	5909
Independent reflections	3258 [R(int) = 0.0161]
Completeness to theta = 25.242°	98%
Absorption correction	Semi-empirical from equivalents
Max. and min. transmission	1.00000 and 0.75758
Refinement method	Full-matrix least-squares on F2
Data / restraints / parameters	3258 / 0 / 171
Goodness-of-fit on F2	1.055
Final R indices [$I > 2\sigma(I)$]	R1 = 0.0487 wR2 = 0.1415
R indices (all data)	R1 = 0.0531 wR2 = 0.1459
Extinction coefficient	n/a
Largest diff. peak and hole	0.471 and -0.272 e.$Å^{-3}$

Table 5.13. *Crystal data and structure refinement for* ***6****.*

	KDMAMP-THF
Identification code	s16alj34
Empirical formula	C40 H88 K4 N4 O8
Formula weight	909.54
Temperature	150.00(10) K
Wavelength	1.54184 Å
Crystal system	Tetragonal
Space group	I41/acd
Unit cell dimensions	a = 16.62270(10) Å α= 90°
	b = 16.62270(10) Å β= 90°
	c = 39.0510(5) Å γ=90°
Volume	10790.35(19) Å3
Z	8
Density (calculated)	1.120 Mg/m^3
Absorption coefficient	3.290 mm^{-1}
F(000)	3968
Crystal size	0.220 x 0.200 x 0.200 mm^3
Theta range for data collection	4.391 to 73.838°
Index ranges	$-20 <= h <= 20; -20 <= k <= 19; -31 <= l <= 48$
Reflections collected	76900
Independent reflections	2742 [R(int) = 0.0347]
Completeness to theta = 25.242°	100%
Absorption correction	Semi-empirical from equivalents
Max. and min. transmission	1.00000 and 0.66979
Refinement method	Full-matrix least-squares on F2
Data / restraints / parameters	2742 / 429 / 222
Goodness-of-fit on F2	1.131
Final R indices [$I > 2\sigma(I)$]	R1 = 0.0581 wR2 = 0.1656
R indices (all data)	R1 = 0.0662 wR2 = 0.1772
Extinction coefficient	n/a
Largest diff. peak and hole	0.215 and -0.279 e.Å^{-3}

Table 5.14. *Crystal data and structure refinement for* ***7****.*

	Ni(^{i}PrPyr)$_2$
Identification code	s17alj32
Empirical formula	C16 H22 N4 Ni
Formula weight	329.08
Temperature	150.00(10) K
Wavelength	1.54184 Å
Crystal system	Monoclinic
Space group	C2/c
Unit cell dimensions	a = 21.2358(3) Å α=90°
	b = 15.6067(2) Å β=91.8320(10)°
	c = 9.81960(10) Å γ=90°
Volume	3252.76(7) Å^3
Z	8
Density (calculated)	1.344 Mg/m^3
Absorption coefficient	1.698 mm^{-1}
F(000)	1392
Crystal size	0.200 x 0.160 x 0.150 mm^3
Theta range for data collection	3.515 to 73.157°
Index ranges	$-25 <= h <= 26; -12 <= k <= 19; -12 <= l <= 11$
Reflections collected	13993
Independent reflections	3242 [R(int) = 0.0193]
Completeness to theta = 25.242°	100%
Absorption correction	Semi-empirical from equivalents
Max. and min. transmission	1.00000 and 0.85488
Refinement method	Full-matrix least-squares on F2
Data / restraints / parameters	3242 / 0 / 194
Goodness-of-fit on F2	1.086
Final R indices [$I > 2\sigma(I)$]	R1 = 0.0328 wR2 = 0.0842
R indices (all data)	R1 = 0.0334 wR2 = 0.0846
Extinction coefficient	n/a
Largest diff. peak and hole	0.595 and -0.215 e.Å^{-3}

Table 5.15. *Crystal data and structure refinement for* ***8****.*

	$Ni(^tBuPyr)_2$
Identification code	s17alj40
Empirical formula	C18 H26 N4 Ni
Formula weight	357.14
Temperature	150.00(10) K
Wavelength	1.54184 Å
Crystal system	Orthorhombic
Space group	Pbcn
Unit cell dimensions	a = 17.01380(10) Å α= 90°
	b = 7.02050(10) Å β= 90°
	c = 15.09180(10) Å γ = 90°
Volume	1802.65(3) $Å^3$
Z	4
Density (calculated)	1.316 Mg/m^3
Absorption coefficient	1.573 mm^{-1}
F(000)	760
Crystal size	0.020 x 0.020 x 0.020 mm^3
Theta range for data collection	5.199 to 73.391°
Index ranges	$-21 <= h <= 21; -8 <= k <= 8; -18 <= l <= 17$
Reflections collected	32629
Independent reflections	1825 [R(int) = 0.0233]
Completeness to theta = 25.242°	100.00
Absorption correction	Semi-empirical from equivalents
Max. and min. transmission	1.00000 and 0.74382
Refinement method	Full-matrix least-squares on F2
Data / restraints / parameters	1825 / 0 / 108
Goodness-of-fit on F2	1.095
Final R indices [$I > 2\sigma(I)$]	R1 = 0.0260 wR2 = 0.0708
R indices (all data)	R1 = 0.0264 wR2 = 0.0711
Extinction coefficient	n/a
Largest diff. peak and hole	0.240 and -0.363 e.$Å^{-3}$

Table 5.16. *Crystal data and structure refinement for* ***13****.*

	$Ni(iPrGu)_2$
Identification code	s18alj11
Empirical formula	C18 H40 N6 Ni
Formula weight	399.27
Temperature	150.00(10) K
Wavelength	1.54184 Å
Crystal system	Orthorhombic
Space group	Pbca
Unit cell dimensions	a = 20.5221(2)Å α= 90°
	b = 15.97110(10) Å β= 90°
	c = 27.7402(2)Å γ= 90°
Volume	9092.14(12) $Å^3$
Z	16
Density (calculated)	1.167 Mg/m^3
Absorption coefficient	1.310 mm^{-1}
F(000)	3488
Crystal size	0.463 x 0.245 x 0.138 mm^3
Theta range for data collection	3.186 to 73.032°
Index ranges	$-25 <= h <= 25; -12 <= k <= 19; -34 <= l <= 34$
Reflections collected	67440
Independent reflections	9071 [R(int) = 0.0414]
Completeness to theta = 25.242°	100%
Absorption correction	Semi-empirical from equivalents
Max. and min. transmission	1.00000 and 0.41321
Refinement method	Full-matrix least-squares on F2
Data / restraints / parameters	9071 / 24 / 534
Goodness-of-fit on F2	1.058
Final R indices [$I > 2\sigma(I)$]	R1 = 0.0401 wR2 = 0.1033
R indices (all data)	R1 = 0.0452 wR2 = 0.1068
Extinction coefficient	n/a
Largest diff. peak and hole	0.709 and -0.394 e.$Å^{-3}$

Table 5.17. *Crystal data and structure refinement for* ***14****.*

	$Ni(CycGu)_2$
Identification code	e18alj10
Empirical formula	C30 H56 N6 Ni
Formula weight	559.51
Temperature	150.01(10) K
Wavelength	0.71073 Å
Crystal system	Monoclinic
Space group	I2/a
Unit cell dimensions	a = 8.7490(4)Å α= 90°
	b = 16.8830(7) Å β= 100.756(4)°
	c = 21.6752(9)Å γ = 90°
Volume	3145.4(2)$Å^3$
Z	4
Density (calculated)	1.182 Mg/m^3
Absorption coefficient	0.644 mm^{-1}
F(000)	1224
Crystal size	0.400 x 0.210 x 0.180 mm^3
Theta range for data collection	3.393 to 29.191°
Index ranges	$-7 <= h <= 11; -22 <= k <= 21; -29 <= l <= 28$
Reflections collected	12509
Independent reflections	3700 [R(int) = 0.0250]
Completeness to theta = 25.242°	99.8
Absorption correction	Semi-empirical from equivalents
Max. and min. transmission	1.00000 and 0.87226
Refinement method	Full-matrix least-squares on F2
Data / restraints / parameters	3700 / 0 / 172
Goodness-of-fit on F2	1.049
Final R indices [$I > 2\sigma(I)$]	R1 = 0.0276 wR2 = 0.0676
R indices (all data)	R1 = 0.0364 wR2 = 0.0715
Extinction coefficient	n/a
Largest diff. peak and hole	0.372 and -0.276 e.$Å^{-3}$

Table 5.18. *Crystal data and structure refinement for* ***15****.*

	$Ni(^{i}PrNacAc)_2$
Identification code	s18alj38
Empirical formula	C16 H28 N2 Ni O2
Formula weight	339.11
Temperature	150.00(10) K
Wavelength	1.54184Å
Crystal system	Orthorhombic
Space group	Iba2
Unit cell dimensions	a = 10.5327(3)Å α= 90°
	b = 15.7704(5)Å β= 90°
	c = 20.5285(6)Å γ= 90°
Volume	3409.88(18)$Å^3$
Z	8
Density (calculated)	1.321 Mg/m^3
Absorption coefficient	1.682 mm^{-1}
F(000)	1456
Crystal size	0.626 x 0.143 x 0.030 mm^3
Theta range for data collection	4.307 to 73.061°
Index ranges	$-12 <= h <= 12; -19 <= k <= 15; -17 <= l <= 25$
Reflections collected	4001
Independent reflections	2411 [R(int) = 0.0183]
Completeness to theta = 67.684°	99.9%
Absorption correction	Gaussian
Max. and min. transmission	1.000 and 0.658
Refinement method	Full-matrix least-squares on F2
Data / restraints / parameters	2411 / 1 / 199
Goodness-of-fit on F2	1.042
Final R indices [$I > 2\sigma(I)$]	R1 = 0.0315 wR2 = 0.0820
R indices (all data)	R1 = 0.0358 wR2 = 0.0854
Absolute structure parameter	-0.12(5)
Extinction coefficient	n/a
Largest diff. peak and hole	0.328 and -0.458 e.$Å^{-3}$

Table 5.19. *Crystal data and structure refinement for* ***16****.*

	Ni(^{t}BuNacAc)$_2$
Identification code	s19alj03
Empirical formula	C18 H32 N2 Ni O2
Formula weight	367.16
Temperature	150.00(10) K
Wavelength	1.54184Å
Crystal system	Orthorhombic
Space group	Aba2
Unit cell dimensions	a = 11.0392(2)Å α= 90°
	b = 15.3900(4)Å β= 90°
	c = 11.2693(2)Å γ= 90°
Volume	1914.58(7)Å^3
Z	4
Density (calculated)	1.274 Mg/m^3
Absorption coefficient	1.536 mm^{-1}
F(000)	792
Crystal size	0.180 x 0.173 x 0.032 mm^3
Theta range for data collection	5.750 to 73.434°
Index ranges	$-9 <= h <= 13; -19 <= k <= 19; -13 <= l <= 14$
Reflections collected	8489
Independent reflections	1905 [R(int) = 0.0218]
Completeness to theta = 67.684°	100%
Absorption correction	Gaussian
Max. and min. transmission	1.000 and 0.735
Refinement method	Full-matrix least-squares on F2
Data / restraints / parameters	1905 / 1 / 141
Goodness-of-fit on F2	1.074
Final R indices [$I > 2\sigma(I)$]	R1 = 0.0222 wR2 = 0.0590
R indices (all data)	R1 = 0.0225 wR2 = 0.0592
Absolute structure parameter	0.02(2)
Extinction coefficient	n/a
Largest diff. peak and hole	0.149 and -0.119 e.Å^{-3}

Table 5.20. *Crystal data and structure refinement for* ***17****.*

	$Ni(EtNacAc)_2$
Identification code	s19alj33
Empirical formula	C14 H24 N2 Ni O2
Formula weight	311.06
Temperature	150.00(10) K
Wavelength	1.54184 Å
Crystal system	Orthorhombic
Space group	Pccn
Unit cell dimensions	a = 18.0026(2)Å α= 90°
	b = 12.35010(10)Å β= 90°
	c = 6.83230(10)Å γ = 90°
Volume	1519.05(3) $Å^3$
Z	4
Density (calculated)	1.360 Mg/m^3
Absorption coefficient	1.840 mm^{-1}
F(000)	664
Crystal size	0.270 x 0.104 x 0.047 mm^3
Theta range for data collection	4.341 to 72.954°
Index ranges	$-22 <= h <= 22; -15 <= k <= 15; -5 <= l <= 8$
Reflections collected	11894
Independent reflections	1521 [R(int) = 0.0279]
Completeness to theta = 25.242°	100%
Absorption correction	Gaussian
Max. and min. transmission	1.000 and 0.717
Refinement method	Full-matrix least-squares on F2
Data / restraints / parameters	1521 / 0 / 91
Goodness-of-fit on F2	1.068
Final R indices [$I > 2\sigma(I)$]	R1 = 0.0284 wR2 = 0.0773
R indices (all data)	R1 = 0.0309 wR2 = 0.0798
Extinction coefficient	n/a
Largest diff. peak and hole	0.297 and -0.285 e.$Å^{-3}$